FACULTY OF ENGINEERING
AND ARCHITECTURE

Experimental Study on Stability of Scour Protection around Offshore Monopile Foundations

Minghao Wu

Doctoral dissertation submitted to obtain the academic degree of
Doctor of Civil Engineering

Supervisors
Prof. Peter Troch, PhD - Vicky Stratigaki, PhD

Department of Civil Engineering
Faculty of Engineering and Architecture, Ghent University

November 2021

GHENT
UNIVERSITY

FACULTY OF ENGINEERING
AND ARCHITECTURE

Experimental Study on Stability of Scour Protection around Offshore Monopile Foundations

Minghao Wu

Doctoral dissertation submitted to obtain the academic degree of
Doctor of Civil Engineering

Supervisors
Prof. Peter Troch, PhD - Vicky Stratigaki, PhD

Department of Civil Engineering
Faculty of Engineering and Architecture, Ghent University

November 2021

GHENT
UNIVERSITY

ISBN 978-94-6355-549-4
NUR 956
Wettelijk depot: D/2021/10.500/97

Members of the Examination Board

Chair

Prof. Filip De Turck, PhD, Ghent University

Other members entitled to vote

Prof. Erik Damgaard Christensen, PhD, Danmarks Tekniske Universitet, Denmark
Prof. Tom De Mulder, PhD, Ghent University
Leen De Vos, PhD, Vlaamse Overheid, Departement Mobiliteit en Openbare Werken
Prof. Wim De Waele, PhD, Ghent University
Prof. Francisco Taveira Pinto, PhD, Universidad do Porto, Portugal

Supervisors

Prof. Peter Troch, PhD, Ghent University
Vicky Stratigaki, PhD, Ghent University

Acknowledgements

The research work presented in this thesis could only be completed with the help and support of many friends and colleagues. Their contributions in this thesis are immense and significant. Therefore, I would like to express my thanks sincerely.

First and foremost, I would like to express my sincere gratitude to my supervisors, Prof. Peter Troch and Dr. Vicky Stratigaki for your strong supports, patient supervisions and valuable suggestions throughout the my entire PhD track. Thank you for providing me opportunities to investigate such an interesting topic and join various attractive projects. I learnt many from you in these years. Without your support and encouragement, I would not be able to present this manuscript for the readers.

I would like to thank Ghent University (UGent) BoF for funding my PhD research, especially after an extremely difficult time due to the coronavirus crisis. It is a precious asset for my life being a student in UGent.

I would like to thank the examination board members for your careful reviews and comments. You have pointed out many critical problems of the thesis and helped to improve the quality of the manuscript a lot. These valuable comments also enlighten me to think deeper and wider on the topic.

I would like to sincerely thank the professional technician team, Mr. Herman Van Der Elst, Mr David Derynck and Mr. Tom Versluys, in assisting the experiments in the UGent wave flume. You are the great magicians who build a miniature world full of fantastic phenomena in coastal and ocean engineering.

I would like to thank all colleagues in the Hydralab+ PROTEUS project. It was an unforgettable joyful memory working with you handling the amazing large scale model, as well as the disgusting heavy stones and sands. I always appreciate every discussion with you in Wallingford, which enlightens me the road to the finale of the thesis.

I would like to offer my special thanks to Dr. Leen De Vos. As Issac Newton said, If I have seen further, it is by standing on the shoulders of giants, then you are the real giant in front of me. I deeply appreciate your hand-on-hand instructions and patient guidance during the entire research and the thesis work.

I would like to express my gratitude to all the colleagues in the Coastal Engineering Research Group. Every moment when I feel discouraged, you are the ones who give me strength, happiness and confidence. Thanks for teaching me so many during the last four years, I see a more gorgeous and colorful world from you.

I would sincerely thank my beloved parents for your immense encouragement during these years. Although you are thousands of miles away, your support is my biggest reassurance during the hard days. Your contribution to this thesis is irreplaceable.

Minghao Wu
November, 2021

Contents

List of Figures

List of Tables

Nomenclature

Latin symbols (I)

A	wave amplitude	m
A_i	area of overlapped subarea	m^2
A_w	near-bed peak wave orbital velocity	m
C	cost function	$-$
C_1	constant in cost function	$-$
C_a	Cauchy number	$-$
D	sieve diameter	m
D_n	nominal sieve diameter	m
D_{n50}	nominal median diameter of armour stone	m
D_P	diameter of cylindrical pile	m
D_s	diameter of armour stone	m
D_{t50}	median diameter of top layer material	m
D_{50}	median diameter of armour stone	m
D_*	dimensionless particle size	$-$
d	water depth	m
d_f	sieve diameter of filter layer material	m
d_b	sieve diameter of base material	m
d_s	sieve diameter of sediment	m
d_{50}	median diameter of sediment	m
F	flatness coefficient of scour protection	$-$
F_D	drag force	N
F_L	lift force	N
F_N	time scale factor	$-$
F_r	Froude number	$-$
$F_{r,d}$	Froude number of water depth	$-$
F_{r,D_P}	Froude number of pile	$-$
$F_{r,D_{n50}}$	Froude number of armour stone	$-$
F_{rc,D_P}	Froude number of pile using current velocity	$-$
F_{rw,D_P}	Froude number of pile using wave orbital velocity	$-$
F_{r,U_c}	densimetric Froude number using current velocity	$-$
F_{r,U_m}	densimetric Froude number using wave orbital velocity	$-$
F_{r,u_*c}	densimetric Froude number using current-induced shear velocity	$-$

Latin symbols (II)

F_{r,u_*w}	densimetric Froude number using wave-induced shear velocity	$-$
$\mathcal{F}$	complex potential	m^2/s
f	frequency	s^{-1}
f_c	bed friction coefficient due to current	$-$
f_s	sampling frequency	s^{-1}
f_t	turbulence frequency	s^{-1}
f_v	vortex shedding frequency	s^{-1}
f_w	bed friction coefficient due to wave	$-$
G	gravity	N
g	acceleration due to gravity = 9.81	m/s^2
H	wave height	m
H_{m0}	spectral significant wave height	m
H_{max}	maximum wave height	m
H_s	significant wave height	m
$H_{1/10}$	1/10 significant wave height	m
I	hydraulic gradient	$-$
K	criterion number $K = K_1 K_2 K_3$	$-$
K_1	criterion number for flow velocities	$-$
K_2	criterion number for θ/θ_{cr}	$-$
K_3	criterion number for armour layer thickness	$-$
KC	Keulegen-Carpenter number	$-$
K_D	K-factor for pier diameter to bed material ratio	$-$
K_e	K-factor for scour protection area	$-$
K_S	K-factor for pier shape	$-$
K_t	K-factor for armour layer thickness	$-$
K_Y	K-factor for pier placement depth	$-$
K_α	K-factor for pier alignment	$-$
$K_{\alpha 1}$	longitudinal slope factor	$-$
$K_{\alpha 2}$	lateral slope factor	$-$
k	wave number	m^{-1}
k_p	coverage factor of uncertainty	$-$
k_s	surface roughness	m
L	characteristic length	m
L_e	extension length of edge scour hole at wake area	m
L_s	significant wave length	m
L_w	wave length	m
M_s	data number in a subarea of FFT analysis	$-$
m	number of points for calculating scour protection flatness	$-$
N	number of waves in a wave duration	$-$
N_{char}	characteristic number of waves	$-$
n	number of tests, observations or measurements	$-$
n_a	layers of armour stones of scour protection	$-$
n_f	porosity coefficient	$-$
P	probability	$-$

Latin symbols (III)

P_f	failure probability	$-$
p	pressure	N/m^2
p_s	number of subseries in FFT analysis	$-$
p_∞	pressure at far side	N/m^2
Q	combined measured quantity	$-$
q	parameters, measured quantities	$-$
r	radial coordinate in polar coordinate system	m
r_c	correlation coefficient	$-$
r_{cr}	reduction coefficient of critical Shields parameter	$-$
r_0	radius of cylinder	m
R	hydraulic radius	m
R_e	Reynolds number	$-$
$R_{e\delta_*}$	Reynolds number of boundary layer thickness	$-$
R_{e,D_P}	Reynolds number of pile	$-$
$R_{e,D_{50}}$	Reynolds number of armour stone	$-$
R_{e*}	Reynolds number of sediment	$-$
s	relative density $= \rho_s/\rho$	$-$
S	scour depth around a pile	$-$
$STAB$	Opti-pile STAB parameter	$-$
S_{3D}	damage number of scour protection	$-$
$S_{3D,i}$	damage number of subarea in scour protection	$-$
S_{e1}	edge scour depth at two sides	$-$
S_{e2}	edge scour depth at wake area	$-$
S_P	sectional area of monopile	m^2
S_t	Strouhal number	$-$
$S(f)$	wave spectral density function	m^2s
$S_U(f)$	wave orbital velocity spectral density function	m^2/s
T	wave period	s
T_d	overlapped data length in an FFT analysis	
$T_{m-1,0}$	spectral mean wave energy period	s
T_i	turbulent intensity	$-$
T_P	peak wave period	s
T_r	total recorded data number in a FFT analysis	$-$
t	time	s
t_a	armour layer thickness	m
t_e	time to reach equilibrium scour depth	s
t_f	filter layer thickness	m
t^*	equilibrium time scale, $=Ut_e/D_P$	$-$
U	flow velocity	m/s
U_c	current velocity	m/s
U_{cr}	critical current velocity	m/s
U_{cw}	relative ratio between current and wave velocities	m/s
U_m	mean wave orbital velocity	m/s

Latin symbols (IV)

U_{max}	maximum velocity	m/s
U_r	Ursell number	$-$
U_{rms}	root-mean-square wave orbital velocity	m/s
U_w	wave orbital velocity	m/s
U_∞	flow velocity at far side	m/s
u	standard uncertainty	$-$
u_A	Type A standard uncertainty	$-$
u_B	Type B standard uncertainty	$-$
u_C	combined standard uncertainty	$-$
u_E	expanded uncertainty	$-$
u_r	radial component of flow velocity	m/s
u_ϕ	tangential component of flow velocity	m/s
u_*	shear velocity	m/s
u_{*c}	shear velocity due to current	m/s
u_{*cr}	critical shear velocity	m/s
u_{*cs}	critical shear velocity for sediment	m/s
u_{*w}	shear velocity due to wave	m/s
u_{*max}	maximum shear velocity	m/s
$u^{'}$	velocity perturbation	m/s
V_i	eroded volume in subarea i	m^3
W_{50}	median stone weight	kg
W_a	width or extension of armour layer	m
W_b	width or extension of filter layer	m
W_e	Weber number	$-$
X	coordinate in x-axis	m
x_s	horizontal distance of horseshoe vortex separation point	m
x_v	horizontal distance of horseshoe vortex center	m
Y	coordinate in y-axis	m
Z	coordinate in z-axis	m
z	vertical height above bottom	m
z_0	roughness length	m

Greek symbols (I)

α	amplification factor	$-$
α_{down}	downstream scour slope	$^\circ$
α_{k_s}	bed roughness factor $= k_s/D_{50}$	$-$
α_{up}	upstream scour slope	$^\circ$
δ	boundary layer thickness	m
δ_*	boundary layer displacement thickness	m
ϵ_q	error range of quantity q	$-$
γ	peak enhancement coefficient of JONSWAP spectrum	$-$
γ_s	safety factor	$-$
γ_{str}	current enhancement coefficient	$-$
κ	von Karman constant = 0.4	$-$
λ	geometrical scale ratio	$-$
μ	mean value	$-$
ν	degree of freedom	$-$
ν_{eff}	effective degree of freedom	$-$
Φ	potential function	m^2/s
ϕ	angle in polar coordinate system	$^\circ$
φ	cross angle between current and wave	$^\circ$
Ψ	stream function	m^2/s
ρ	density of fluid	kg/m^3
ρ_f	density of filter layer material	kg/m^3
ρ_b	density of based material	kg/m^3
ρ_s	density of sediment or armour stone	kg/m^3
σ	standard deviation	$-$
σ_g	sediment uniformity	$-$
τ_b	bed shear stress	N/m^2
τ_{bl}	local bed shear stress	N/m^2
τ_c	bed shear stress due to current	N/m^2
τ_{cr}	critical bed shear stress	N/m^2
τ_m	mean bed shear stress	N/m^2
τ_{max}	maximum bed shear stress	N/m^2
τ_w	bed shear stress due to wave	N/m^2
τ_∞	bed shear stress at far side	N/m^2
θ	Shields parameter	$-$
θ_{cr}	critical Shields parameter	$-$
$\theta_{cr,modified}$	modified critical Shields parameter	$-$
υ	kinematic viscosity of fluid, $\approx 1 \times 10^{-6}$ for water	m^2/s
η	wave surface elevation	m

Subscripts

m	model
$meas$	measured value
p	prototype
$pred$	predicted value

Abbreviations

ADV	Acoustic Doppler Velocity meter
FFF	Fast Flow Facility
FFT	Fast Fourier Transformation
GBF	Gravity-Based Foundation
IPCC	Intergovernmental Panel on Climate Change
JCGM	Joint Committee for Guides in Metrology
PROTEUS	PRotection of Offshore wind Turbine monopilEs against scoUring
SBD	Simulation Based Design
SDF	Statically stable, Dynamically stable or Failure
TLP	Tensional Leg Platform
UNFCCC	United Nations Framework Convention on Climate Change
WG	Wave Gauge

Samenvatting

Offshore wind, als een veelbelovende koolstofarme energieoplossing, groeit snel over de hele wereld. Nieuwe generatie offshore windturbines hebben grotere turbine- en funderingsafmetingen, zodat de grotere windenergie verder van het land kan worden opgevangen. Van alle soorten funderingen wordt de monopaal of paalfundering het meest toegepast in ondieper water. Een belangrijk punt voor de stabiliteit van de monopaal-fundering is het voorkomen van erosie rond de paal ten gevolge van de grote oceaangolven en sterke stroming. Veldonderzoek en laboratoriumstudies hebben aangetoond dat de erosiediepte rond de monopaal kan oplopen tot 2 keer de paaldiameter, wat de ontwerpfrequentie van de paalfundering aanzienlijk kan beïnvloeden. Daarom wordt er meestal een erosiebescherming, met name een laag stortsteen aangebracht op de zeebodem rond de paal, om dit erosie effect te verminderen.

De stabiliteit van de erosiebescherming rond een monopaal is een belangrijke aspect bij het ontwerp van de paalfunderingen, en kan worden onderverdeeld in statische stabiliteit en dynamische stabiliteit. De statische stabiliteit laat geen verplaatsing van de stortsteen nabij de monopaal toe ten gevolge van de hydrodynamische belasting. De dynamische stabiliteit laat beperkte verplaatsingen van de stortsteen toe, terwijl de functionaliteit tegen erosie behouden blijft. Verschillende ontwerpbenaderingen voor de afmetingen van de stortsteen worden voorgesteld in de literatuur, op basis van kleinschalige laboratoriumexperimenten, maar de inherente model- en schaaleffecten in hydraulische experimenten zullen de toepasbaarheid van deze methoden voor prototypeontwerp beïnvloeden. Er ontstaan daarom technische uitdagingen, aangezien de erosiebescherming voor nieuw gebouwde windparken zowel conservatief als onvoldoende kan zijn, wat kan leiden tot een duur of onveilig ontwerp. Voor deze problemen zijn grootschalige experimenten nodig om de mechanismen nauwkeuriger te onderzoeken.

Om het ontwerp van erosiebescherming rond monopaals van offshore windturbines te verbeteren en ze toekomstbestendig te maken tegen de gevolgen van klimaatverandering, werd het PROTEUS-project (bescherming van monopaals van offshore windturbines tegen erosie) uitgevoerd in het kader van HYDRALAB- PLUS van het Europese Horizon 2020-programma. In dit project werden grootschalige golfgootexperimenten uitgevoerd naar de schade van de erosiebescherming rond een monopaal, ten gevolge van gecombineerde golven en stromingens, met modelschalen van 1:16.667 en 1:8.333 in de Fast Flow Facility in HRWallingford. Op basis van de dataset verkregen uit dit project, wordt in dit proefschrift de toepas-

baarheid van bestaande ontwerpmethoden voor erosiebescherming op grootschalige modellen onderzocht. Voor het geval van de statische stabiliteit, overschatten bestaande ontwerpmethoden de steenbeweging van stortsteen in vergelijking met grootschalige modelresultaten. De voorspelde kritische schuifspanningen zijn groter dan de gemeten waarden in de grootschalige modellen, en de gemeten versterkingsfactoren van de schuifspanning in de grootschalige modellen zijn kleiner dan de voorspelde waarden. De experimentele resultaten tonen het conservatief karakter van de statische ontwerpmethoden. Voor het geval van de dynamische stabiliteit, wordt in dit proefschrift het driedimensionale schadegetal (S_{3D}) toegepast voor de evaluatie. De resultaten laten zien dat de voorspelde S_{3D} veel groter zijn dan de gemeten waarden in de grootschalige modellen, wat ook aangeeft dat de voorspelling conservatief kan zijn. Daarnaast wordt de schadediepte van de erosiebescherming vergeleken met bestaande voorspellingsformules. Ook de gemeten schadedieptes blijken kleiner te zijn dan de voorspelde waarde. Deze verschillen tussen grootschalige experimentele resultaten en voorspellingen op basis van bestaande ontwerpmethoden worden toegeschreven aan de schaaleffecten. Daarom wordt geconcludeerd dat prototyperesultaten afwijken van de ontwerpwaarden ten gevolge van een nog groter schaalverschil.

Om de schaaleffecten in monopaal erosiebeschermingsexperimenten verder te kwantificeren, is een reeks correct verkleinde laboratorium experimenten nodig, terwijl de modeleffecten van dergelijke experimenten a priori moeten worden onderzocht. Dit deel van het werk is uitgevoerd in de golfgoot in de Coastal Engineering Research Group aan de Universiteit Gent, met behulp van een 1:50 kleinschalig model. De testomstandigheden van het kleinschalige experiment worden verkleind ten opzichte van enkele testgevallen in het PROTEUS-project en bepaald door de Best Model-schaalregel. Door herhaalde tests zijn de standaarddeviaties van S_{3D} ($\sigma(S_{3D})$) en deelgebiedschade $S_{3D,i}$ ($\sigma(S_{3D,i})$)) verkregen. De resultaten laten verder zien dat $\sigma(S_{3D})$ 20.3% bereikt van het gemiddelde schadegetal, $\overline{S_{3D}}$, terwijl $\sigma(S_{3D,i})$ maximaal 33.1% van $\overline{S_{3D}}$ kan zijn. Herhaalbaarheids- en onzekerheidsanalyses worden uitgevoerd om de mogelijke redenen voor de hoge modeleffecten te vinden. Een reden is dat een dergelijk experiment nauwelijks kan worden herhaald vanwege de aanwezigheid van stromingsturbulentie en de onmogelijkheid om een identieke beschermingslaag tegen erosie te bouwen in een herhaalde test, hoewel de statistische golven en stromingsparameters een ideale herhaalbaarheid hebben. De andere reden wordt verondersteld de hoge gepropageerde onzekerheid van metingen tot de uiteindelijke resultaten te zijn. Omdat het hydraulische model sterk niet-lineair is, zal een kleine onzekerheid in de testinvoer zich uiteindelijk ontwikkelen tot een grote en oncontroleerbare afwijking in het testresultaat, waardoor het moeilijk is om een bepaald experimenteel resultaat te verkrijgen.

Nu we de invloeden van modeleffecten kennen, kunnen de schaaleffecten van het monopaal erosiebeschermingsexperiment worden gekwantificeerd door vergelijkbare testresultaten op kleine en grote schaal te vergelijken. Vergelijking van schadeprofielen en schadegetallen leidt tot de conclusie dat kleinschalige experimenten vaak leiden tot grote schadegetallen. Gegevens uit de ene vergelijkingsgroep tonen S_{3D}=1.208 voor kleinschalige tests en S_{3D}=0.602 voor vergelijkbare grootschalige tests, en de andere vergelijkingsgroep geeft S_{3D}=1.269 voor kleinschalige tests en S_{3D}=1.082 voor grootschalige tests. De schaaleffecten worden voornamelijk veroorzaakt door onvolkomenheden in de schaalverdeling, omdat de vergelijkbaarheden tussen het Reynoldsgetal, de kritische Shields-parameter en het Strouhal-getal niet kunnen worden bereikt met behulp van de schaalregel voor het Best Model. Verder worden de progressieve kenmerken van monopaal erosiebeschermingsschade onderzocht. Voor een grootschalig model bereikt het schadeprofiel een geschatte evenwichtstoestand na 3000 golven. Maar voor een vergelijkbaar kleinschalig model blijft de schade zich ontwikkelen na 5000 golven in een stroming-tegen-golf toestand. De studie benadrukt de noodzaak van aanpassingen van de huidige ontwerpmethoden, zodat ze kunnen worden toegepast op nieuwe generatie grote windturbinefunderingen, rekening houdend met de schaaleffecten.

Op basis van de beschikbare kleinschalige en grootschalige experimentele gegevens van de testen van de stabiliteit van monopile erosiebescherming, wordt een synthetische data analyse uitgevoerd. Deze studie past dimensieloze parameters toe om de stabiliteit van de monopaal erosiebeschermings te beschrijven. Volgens het onderzoek zijn de meest beïnvloedende parameters: (1) densimetrisch Froude-getal van stroomsnelheid; (2) densimetrisch Froude-getal van gemiddelde golforbitaalsnelheid nabij de bodem; (3) verhouding tussen Shields-parameter en kritische Shields-parameter; (4) verhouding tussen stroom- en golfsnelheden; (5) dimensieloze dikte van de ersiebeschermingslaag. Een criteriumgetal K wordt verhoogd om de stabiliteit van de monopaal erosiebescherming te evalueren. Dit getal K wordt berekend via de vermelde beïnvloedende parameters. Bij $K \geq 1$ is de bescherming tegen erosie van de monopaal stabiel. Dit K-getal wordt voorlopig toegepast in ontwerpvoorbeelden met behulp van bestaande windparkgegevens. De resultaten laten zien dat kleinere stortsteenformaten kunnen worden verkregen wanneer aan $K \geq 1$ wordt voldaan.

Summary

Offshore wind, as a promising low-carbon energy solution, is growing fast all around the world. New generation offshore wind turbines have larger turbine and foundation size so that to capture the larger wind energy further away from land. Monopile, among all types of foundation, is mostly applied in shallow water areas. An important issue for the stability of the monopile foundation is the prevention of scouring around the pile due to strong ocean wave and current condition. Field surveys and laboratory studies have shown that the scour depth around monopile can reach up to 2 times the pile diameter, which can significantly affect the design frequency of the pile foundation. Therefore, a scour protection layer, in particular a layer of armour stones, is usually applied at the seabed around the pile to mitigate this scour effect, namely the scour protection.

The stability of the scour protection around monopile is an important aspect in the design of pile foundation and can be categorised into static stability and dynamic stability. The static stability does not allow any displacement of armour stones near the monopile due to the hydrodynamic loading. The dynamic stability allows limited displacements of armour stones while the functionality against scouring is maintained. Various design approaches for the sizes of armour stones are proposed in the literature based on small scale laboratory experiments, however the inherent model and scale effects in hydraulic experiments will affect the applicability of these methods for prototype design. Engineering challenges therefore arise as the scour protections for newly build wind farms might be either conservative or insufficient, which may lead to a costly or unsafe design. Towards these problems, large scale experiments are necessary to explore the mechanisms more accurately.

In order to improve the design of scour protection around offshore wind turbine monopiles, as well as future-proofing them against the impacts of climate change, the PROTEUS project (PROtection of offshore wind turbine monopilEs against scoUring) was carried out within the framework of HYDRALAB-PLUS of the European Horizon 2020 programme. In this project, large scale wave flume experiments on the damage of the scour protection around a monopile due to combined waves and current conditions were carried out with model scales of 1:16.667 and 1:8.333 in the Fast Flow Facility in HRWallingford. Based on the dataset obtained from this project, in this thesis, the applicability of existing scour protection design methods on large scale models is investigated. For the case of the static stability, existing design approaches overestimate the stone movement for large scale model results. The predicted critical shear stresses are larger than the measured

values in the large scale models, and the measured shear stress amplification factors in large scale models are smaller than the predicted values. Experimental results show the conservative characteristics of the static design methods. For the case of the dynamic stability, the three-dimensional damage number (S_{3D}) is applied for the evaluation in the thesis work. Results show that the predicted S_{3D} are much larger than the measured values for large scale models, which also indicate the prediction can be conservative. In addition, the damage depth of the scour protection is compared to existing prediction formulas. The measured damage depths are found to be smaller than predicted value as well. These differences between large scale experimental results and predictions based on existing design methods are attributed to the scale effects. Therefore, it is inferred that prototype results deviate from the design values as a result of an even larger scale difference.

To further quantify the scale effects in monopile scour protection experiments, a series of correctly scaled-down laboratory experiments are necessary while the model effects of such experiments should be investigated a priori. This part of work is carried out in the wave flume in the Coastal Engineering Research Group at Ghent University using a 1:50 small scale model. The test conditions of the small scale experiment are scaled down from some test cases in the PROTEUS project and determined by the Best Model scaling rule. Through repeated tests, the standard deviations of S_{3D} ($\sigma(S_{3D})$) and subarea damage number $S_{3D,i}$ ($\sigma(S_{3D,i})$) are obtained. The results further show that $\sigma(S_{3D})$ reaches 20.3% of the mean damage number, $\overline{S_{3D}}$, meanwhile, $\sigma(S_{3D,i})$ can be up to 33.1% $\overline{S_{3D}}$. Repeatability and uncertainty analysis are performed to find the possible reasons for the high model effects. One reason is that such experiment can hardly be repeated due to the presence of flow turbulence and the impossibility to build an identical scour protection layer in a repeated test, albeit the statistical waves and currents parameters have ideal repeatability. The other reason is assumed to be the high propagated uncertainty from measurements to the final results. Since the hydraulic model is highly nonlinear, a small uncertainty in test input will eventually develop to a large and uncontrollable deviation in the test result, which makes it difficult to obtain a certain experimental result.

Knowing the influences of model effects, the scale effects of monopile scour protection experiment can then be quantified by comparing similar small scale and large scale test results. Comparisons of damage profiles and damage numbers lead to a conclusion that small scale experiments tend to end up in large damage numbers. One comparison group data shows S_{3D}=1.208 for small scale test and S_{3D}=0.602 for similar large scale test, and the other comparison group gives S_{3D}=1.269 for small scale test and S_{3D}=1.082 for large scale test. The scale effects are mainly caused by imperfections of scaling, since the similarities of Reynolds number, critical Shields parameter and Strouhal number are not able to be attained using the Best Model scaling rule. Furthermore, the progressive characteristics of monopile scour protection damage are investigated. For a large scale model, the damage profile reaches an approximate equilibrium status after 3000 waves. But for similar small scale model, the damage continues to develop after 5000 waves in a current against wave condition. The study highlights the necessity for modifications of current design methods such that they can be applied to new generation large wind turbine foundations taking account the scale effects.

On the basis of the available small and large scale experimental data of monopile scour protection stability tests, a synthetic data analysis is carried out. This study applies dimensionless parameters to describe the stability of the monopile scour protection layer. According to the investigation, the most influencing parameters are: (1) densimetric Froude number of current velocity; (2) densimetric Froude number of mean bottom wave orbital velocity; (3) ratio between Shields parameter and critical Shields parameter; (4) ratio between current and wave velocities; (5) dimensionless thickness of the scour protection layer. A criterion number K is raised to evaluate the stability of monopile scour protection. This number K is calculated via the listed influencing parameters. When $K \geq 1$, the monopile scour protection is stable. The K value is tentatively applied in design examples using existing wind farm data. The results show that smaller amour stone sizes can be obtained when satisfying $K \geq 1$.

Chapter 1

Introduction

1.1 Background

1.1.1 Development of offshore wind energy

The fast developing human society significantly influences the climate since mid-20th century. The vast emission of greenhouse gas due to increasing utilization of fossil fuels is concerned as the major contributor to the global average surface temperature warming. In order to take actions against climate change, the Paris Agreement was signed under the United Nations Framework Convention on Climate Change (UNFCCC) with a goal of limiting the rise of global temperatures to preferably 1.5°C compared to pre-industrial levels in long term. This requires the greenhouse gas emission reaches a climate neutral status as soon as possible (UNFCCC, 2015). According to IPCC (Intergovernmental Panel on Climate Change), the sustainable pathways of mitigating global warming requires a shift of energy supply from fossil fuels to renewables. It is estimated with high confidence that the renewable energy needs to take a share of 52-67% of the total energy supply for achieving the target of limiting the global warming to 1.5°C above pre-industrial levels (Rogelj et al., 2018).

Wind energy as one of the most competitive renewables in energy market is expanding rapidly over the recent decade. The annual global net wind installation capacity additions reach 60 GW in 2020, and are expected to hit a record of 68 GW by 2021. In the newly installed capacity, offshore renewable energy takes a share of 5.3 GW in 2020, and is expected to reach 7.3 GW in 2021 (IEA, 2020). Compared with onshore wind, offshore wind has many advantages (Colmenar-Santos et al., 2016): (1) The offshore wind resource is more abundant. (2) The available space in marine is more than inland. (3) The visual and acoustic impacts for offshore wind are lower which allows bigger machines, faster rotation speeds and more efficient wind turbine arrays. (4) Higher offshore wind turbine makes it possible to exploit the high density wind resources at higher heights. According to the statistics given by WindEurope (2020b), the weighted average power rating of onshore turbines is about 3 MW, while the average rated capacity of newly installed offshore turbines was 7.2 MW in 2019. Large offshore wind turbines are recently tested or commercially applied, such as the MHI Vestas V164 turbine (164m rotor diameter, 9.5 MW) and the GE's Haliade-X (12 MW). According to Sánchez et al. (2019), the costs of foundation and electric installations of a wind farm are mainly affected by distances from shore, water depths and metocean conditions, which remain stable during the last years. This makes wind energy generated from larger and more efficient offshore wind turbines more cost competitive in the market.

1.1.2 Offshore wind turbine foundation

The foundation is a key component for the offshore wind turbine, which contributes to 20-30% of the total construction cost of an offshore wind farm (Wu et al., 2019). It withholds the loads from the turbine and the supporting structure as well as the loads from wind, waves and currents, and has to provide a stable operating condition for the rotor. There exist various types of foundations, see Figure 1.1, including: (a) gravity-based foundation (GBF) ; (b) monopile; (c) tripod; (d) jacket; (e) tensional leg platform (TLP); (f) spar-buoy; (g) semi-submersible, as sketched in Figure 1.1, where (a) to (d) are bottom-fixed structures and (e) to (g) are floating structures.

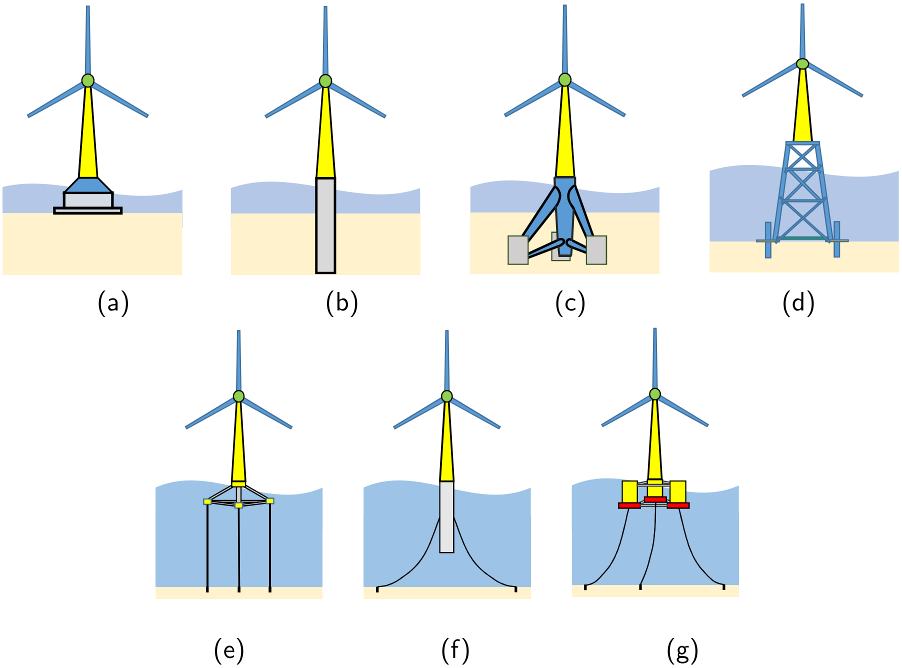

Figure 1.1: Foundations types of offshore wind turbines: (a) GBF ; (b) monopile; (c) tripod; (d) jacket; (e) TLP; (f) spar-buoy; (g) semi-submersible

The economical foundation solution depends on the water depth and marine environment of the site. Normally, as for the bottom-fixed structures, GBF is suitable for water depth less than 10 m, monopile and tripod are suitable for 10-40 m and the jacket can be used for 50 m water depth condition. Recently, Esteban et al. (2019a) report that GBF foundation is also deployed in water area up to 60 m depth, which can hold 8 MW turbines. Hermans and Peeringa (2016) and Steelwind Nordenham (2020) have also discussed the possibility of installing monopiles at deep water areas with 50-65 m water depth. The floating wind foundations are mostly used in deeper water areas ($>$ 60 m). Nowadays, the manufacturing and installation cost of bottom-fixed structure is much cheaper than floating structure thanks to the relatively mature technology and engineering experience (Wu et al., 2019), while the floating wind solution is also promising in the near future as more and more deep water offshore wind farms are planned, such as the Hywind Tampen windpark in Norway and Kincardine wind farm in the UK (WindEurope, 2020a).

Recent statistics provided by WindEurope (2020a) show that monopile is the most preferable wind foundation among all types of foundation structures in the year of 2019, which takes a share of 80.9% (4258/5258) in all installed foundations in 2019. The wide application of monopile is mainly attributed to its low installation cost and simple installation procedures. General comparisons are made in the studies by NREL (2016) and Gonzalez-Rodriguez (2017) and reveal the advantages of monopile regarding the cost of the wind foundation.

1.1.3 Scour protection of offshore wind foundation

Exposed to harsh sea conditions, the wind turbine system faces many engineering risks. The complex sea loads induced by wind, wave and current can lead to damages or failures of turbine components, supporting structures and foundations. For bottom-fixed foundation, one important risk comes from the scour problem at the seabed around the foundation. The wave and current induced hydrodynamic loads will initiate the sediment motion in the area near the foundation base, resulting in a local scour hole around the foundation structure. The depth of this scour hole depends on the characteristics of sediments, the shape of supporting structure and the sea conditions, but is usually with the same order of the size of the supporting structure. Typical scour patterns around offshore wind foundations are displayed in Figure 1.3.

As for monopile, the scouring hole developed around an unprotected foundation can cause safety issues for the upper structure (Sørensen and Bo Ibsen, 2013). On one hand, the high scour depth shortens the buried height of the monopile and reduces its stiffness, which leads to 10% decrease of natural frequency of the pile foundation. Figure 1.2 shows the typical wave and wave spectra, rotational frequency bands (1P) and blade-passing (3P) frequency bands and natural frequencies of some existing offshore wind turbines. It can be a dangerous scenario when the natural frequency significantly deviates from the design status and appears close to the rotational frequency (1P frequency). On the other hand, the lateral and axial bearing capacity is deteriorated with the development of scour, due to the growing bending moment and the loss of skin friction at the foundation base (Wu et al., 2019). If no countermeasures are adopted, a deeper pile penetration length will be required, which may significantly increase the foundation cost due to the pile fabrication, transportation and installation. Therefore, a protection layer against scour is usually necessary, namely the scour protection layer or scour protection. Such scour protection layer is mostly built with riprap, and can also be installed using concrete mattress (Chen et al., 2014), geotextile sand container (Corvaro et al., 2018), anti-scour collar (Subcon, 2021) and other flow-altering devices attached to the pile, such as spiral threading and submerged vanes around the pile (Tafarojnoruz et al., 2012). New concepts of anti-scouring measures are also investigated recently, for example, using fishnet around monopile (Yang et al., 2019) and utilizing a tidal current turbine at the base of the pile (Yang et al., 2021). Figure 1.4 shows a few scour protection solutions for offshore wind foundations.

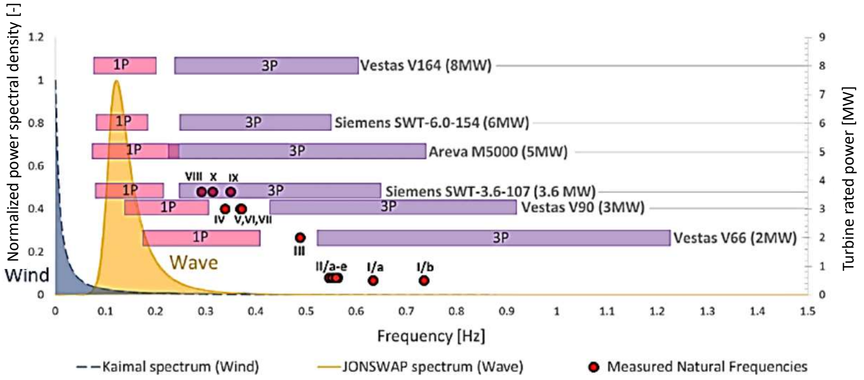

Figure 1.2: Typical wind and wave spectra, rotational frequency bands (1P), blade passing frequency bands (3P) and natural frequencies of the offshore wind turbines (Arany et al., 2016).

The riprap, also known as the rock armour, is the mostly used scour protection material (Esteban et al., 2019b) in offshore wind foundation installation. Two ways of installing protection materials are suggested by CIRIA (2007): one is to dump the rocks near the pile before a scour hole develops, the other is to lay the rocks after the scour hole reaches an equilibrium depth. For offshore installation of scour protection, the former way is more adopted so that the monopile foundation is hammered to the seabed after the scour protection is prepared (Asgarpour, 2016). The scour protection and foundation installation takes a considerable proportion of the total cost of an offshore turbine. This cost, as concluded in Gonzalez-Rodriguez (2017), increases as the operation water depth increases and the turbine size grows. With a rise of new generation large-size offshore wind turbine, reducing the installation cost and enhancing the reliability of scour protection layer become more significant.

(a) Monopile (HRWallingford, 2021)

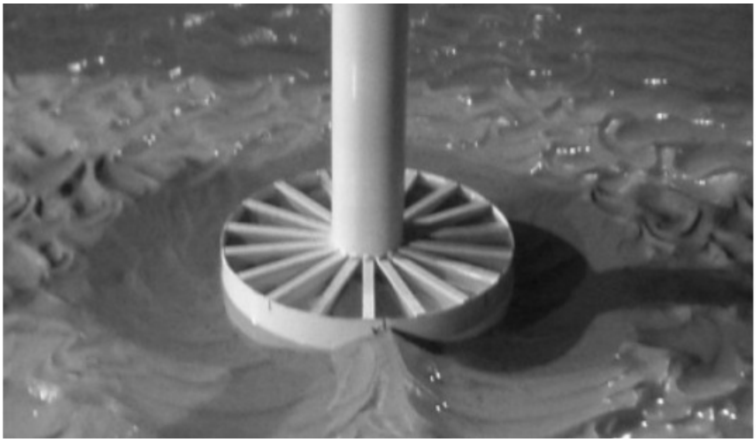

(b) GBF (Whitehouse, 2004)

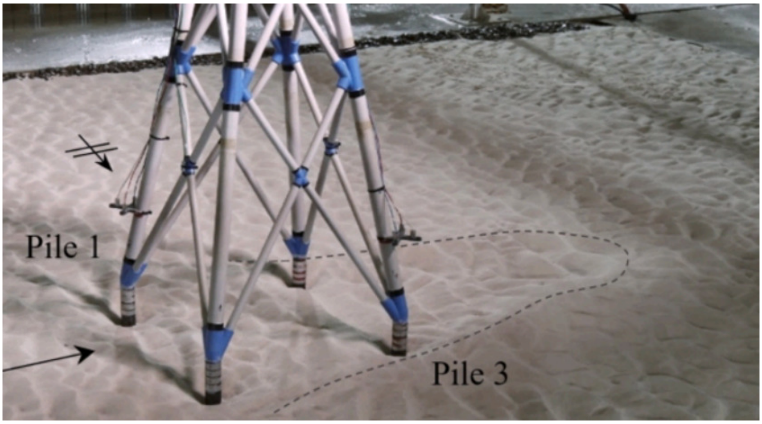

(c) Jacket (Welzel et al., 2019)

Figure 1.3: Scour patterns around offshore wind foundations for: (a) monopile; (b) GBF; (c) jacket.

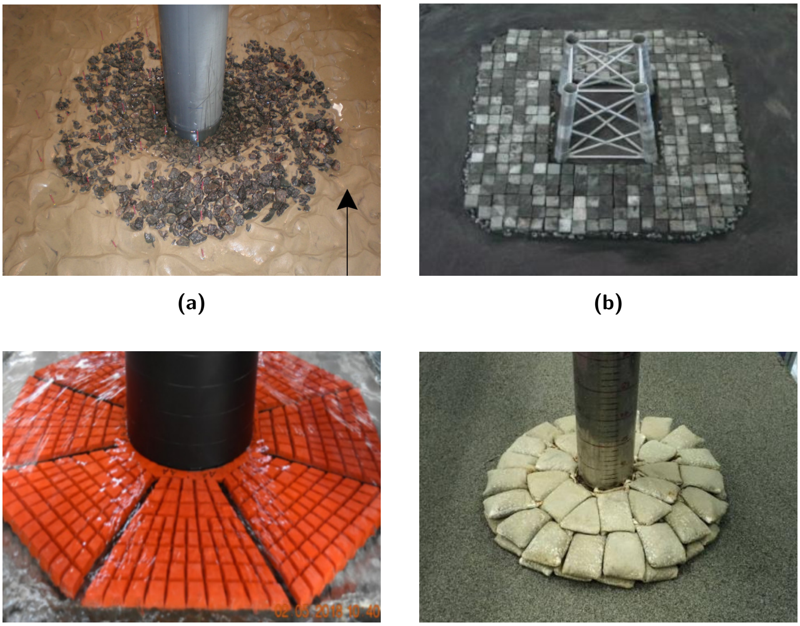

(a) (b) (c) (d)

Figure 1.4: Scour protection solutions for offshore wind foundations: (a) riprap (Nielsen, 2011); (b) concrete units (Chen et al., 2014); (c) Scour collar (Subcon, 2021) (d) Geobags (Corvaro et al., 2018).

1.2 Motivations and objectives

The present thesis work is primarily motivated by the engineering problems in the offshore wind industry, specifically, the scour problems around monopile foundation. Laboratory studies show that the scour depth around an unprotected monopile foundation at sea can reach an average value of approximately 1.3 times the pile diameter. Some field surveys show that the scour depth around a monopile can be up to 1.47 times the pile diameter, while the absolute value can be in the order of 7 meters (Whitehouse et al., 2011). Reliable scour protection is indispensable to reduce the engineering risks due to scour, but new technical requirements arise along with the surge of planned offshore wind farms. Firstly, as the turbine size grows bigger and the offshore wind installation zones locate further away from the coast, the existing wind foundation scour protection design methods might have many limitations either due to an overuse of scour protection materials or an understable scour protection system. It is crucial to identify these limitations, evaluate the applicability of these design methods and make adjustments in new foundation designs. Secondly, considering the increasing impacts from climate change on the ocean conditions, more investigations and new design methods are necessary for enhancing the reliability of these heavy offshore investments as well as improving the cost competitiveness of the clean energy from sea. Therefore, driven by the motivations stated above, the main aim of this research is to gain more knowledge on the design of scour protection of offshore monopile foundations, specifically, by means of laboratory experiments and with a focus on the erosion stability of armour layer.

On the basis of the description of specific scientific problems, five study objectives are proposed in this thesis as following:

- Objective 1: Existing design methods of monopile scour protection against erosion failure were proposed based on small scale experiments as they are efficient and convenient. But using such methods may bring deviations of scour protection stability when applied to large scale models and prototype. To explore this issue, a large scale experiment of monopile scour protection is carried out and the first objective is to investigate the applicabilities of existing design methods to the large scale experiment.

- Objective 2: As small scale experiments are widely adopted in monopile scour protection design, the model effects of such small scale experiments are rarely discussed. The quantification of model effects is important for understanding the characteristics of data distribution. For this issue, the second objective of this thesis is to quantify the model effects in small scale experiments of monopile scour protection.

- Objective 3: Uncertainties in experiments are usually inevitable. A formal analysis of the associated experimental uncertainties for monopile scour protection experiments can help to know the experimental accuracy and its potential sources. It will also provide experiences for raising data accuracy in future experimental studies. Therefore, the third objective of this thesis is to carry out a standard uncertainty analysis of monopile scour protection experiments, by means of small scale experiments.

- Objective 4: Due to the impossibility to achieve perfect similarities between scaled tests and prototype, scale effects in hydraulic experiments should always be concerned as they may cause serious deviation between model test result and prototype performance. As field test of prototype is very expensive, time-consuming and difficult, a more approachable way is to adopt similar large and small scale experiments to analyse the scale effects. For this issue, the fourth objective of this thesis is to quantify the scale effects in monopile scour protection experiments and understand the key reasons for such scale effects.

- Objective 5: Gathering the available results from the existing small scale experiments and the new large scale experiment, the fifth objective of the thesis is to carry out a synthetic analyse of the key dimensionless parameters that may lead to erosion failure of a monopile scour protection.

1.3 Outline of the thesis

The thesis applies 10 chapters to elaborate the new findings in laboratory study of offshore monopile foundation scour protection. The content and targeting objective of each chapter is outlined in Table 1.1.

Table 1.1: Outline of the thesis

Chapter	Main content	Objective
Chapter 1	This chapter introduces the technical background, defines the scope and specifies the objectives of the thesis work.	
Chapter 2	This chapter reviews the theories and physics of scour around monopile, which includes the flow field around a vertical pile and the mechanism of scouring.	
Chapter 3	This chapter reviews the state-of-the-art of the monopile scour protection study with focuses on the experimental modelling and the existing design methods.	
Chapter 4	This chapter introduces the principles and procedures of analysing experimental uncertainties and scale effects that exist in physical modelling of monopile scour protection.	
Chapter 5	This chapter presents the experimental results of large scale physical modelling of monopile scour protection under combined wave and current conditions. The applicability of existing design methods for large scale experiments is analysed.	Objective 1
Chapter 6	This chapter describes a scaled-down experiment together with a thorough analysis of the associated measurement and model effects.	Objective 2
Chapter 7	This chapter carries out a formal analysis of the experimental uncertainties due to measurement in such hydraulic experiments.	Objective 3
Chapter 8	This chapter analyses the scale effects that are inherent in the experimental modelling of monopile scour protection with proper scaling schemes. The obtained results and conclusions add values to the state-of-the-art of the topic.	Objective 4
Chapter 9	This chapter compiles existing laboratory monopile scour protection experimental data and analyses the most important parameters which may influence the stability of the scour protection. A new criterion is proposed to evaluate the erosion failure.	Objective 5
Chapter 10	As a closure of the study, conclusions and recommendations for future study are given in this chapter.	

Chapter 2

Literature review of the physical process analysis of scour around monopile

2.1 Flow around a vertical cylindrical pile

Cylindrical structures are widely applied in offshore engineering. Exposed to the marine environment of wind, waves and current, the flow field around a cylinder becomes complex as a result of the combined tidal-current-induced steady flow and wave-induced oscillatory flow. The flow field characteristics triggers various engineering problems, including the scour around a monopile. For a vertically mounted cylindrical pile, when a steady incoming flow approaches, the streamlines deflect and contract around the pile, as skechted in Figure 2.1. A pressure stagnation point is formed in the upstream side of the pile. The adverse horizontal pressure gradient leads to a basic acceleration of flow velocity at the two sides of the pile. Furthermore, the surface roughness and fluid viscosity introduce boundary layers above the pile surface and the seabed, and vortices are often formed due to the high velocity gradient in the boundary layer. One vortex is called the horseshoe vortex. It is caused by the adverse vertical velocity gradient in the upstream side of the pile. Blocked by the blunt surface of the pile, the incoming flow streamlines tend to converge downwards to the pile base, hence, the vortex structure is created due to the boundary layer separation in front of the pile. The vortex develops from the pile to downstream and gives rise to an increased flow velocity around the pile. Another vortex structure originates from the boundary layer separation at the two sides of the pile due to the adverse horizontal pressure gradient, develops to the lee side and the wake region, and emerges by pairs. This is the well-known lee-wake vortex (vortices). As a result, the flow velocity is accelerated due to the vorticity of the lee-wake vortex structure.

The flow acceleration near the pile base leads to an amplification of local bed shear stress. Note the near bed flow velocity at far side as u_∞ and at local place

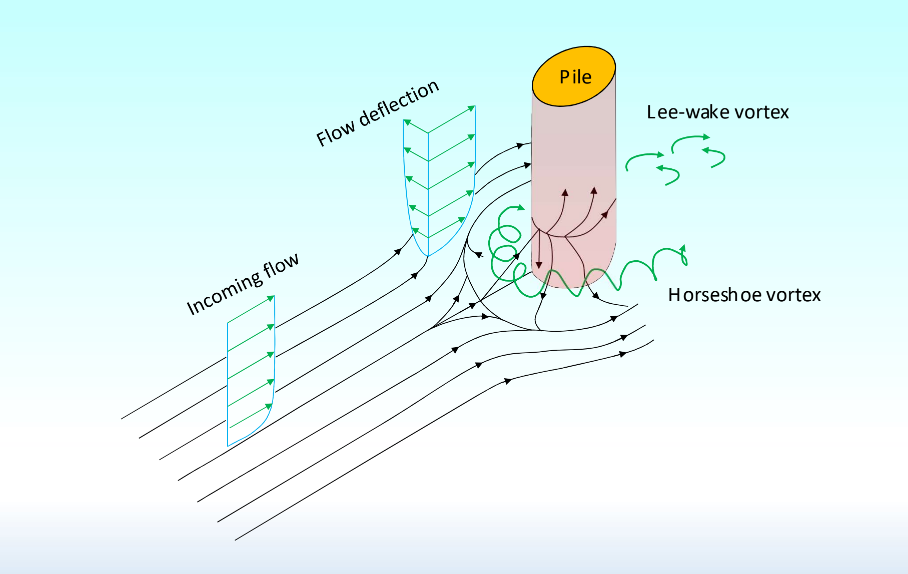

Figure 2.1: Sketch of flow structure around a vertical cylindrical pile, modified after Hjorth (1975).

as u_{*l}, the far side bed shear stress $\tau_\infty = \rho {u_\infty}^2$ and the local bed shear stress is $\tau_{bl} = \rho {u_{*l}}^2$, where ρ is the fluid density. The amplification factor α is defined as Eq.(2.1).

$$\alpha = \frac{\tau_{bl}}{\tau_\infty} = \left(\frac{u_{*l}}{u_\infty}\right)^2 \tag{2.1}$$

The amplification factor is important for the scour and scour protection around a monopile. $\alpha > 1$ indicates that the local bedload is larger than the far side bedload. A larger α value leads to a higher local bedload around the pile, which is able to initiate the scour around pile easier and create deeper scour hole. The estimation and measurement value of α will be introduced in the following text of this section. For scour protection of a monopile, the armour stone resistance against the local bedload around the pile has to be sufficient to maintain a stability in design conditions, and α also becomes a key factor for the design. The design of scour protection around monopile will be introduced in Chapter 3.

2.1.1 Potential flow solution

Starting with a simplified approach to get insight in the fluid-structure interaction of flow passing a cylindrical pile, the potential flow theory can be applied to solve the basic two dimensional (2D) flow field around a cylinder (Spurk and Aksel, 2020) assuming that the cylinder is smooth and the fluid is ideal and non-viscous. The 2D flow passing a cylinder section is shown in Figure 2.2, where O is the centre point of the cylinder section, r_0 is the radius of the cylinder, r and ϕ are the polar coordinates of a point inside the flow field, $r \geq r_0$. Denoting the $\varPhi$ and $\varPsi$ as the potential and stream functions, the complex potential $\mathcal{F}$ is written as,

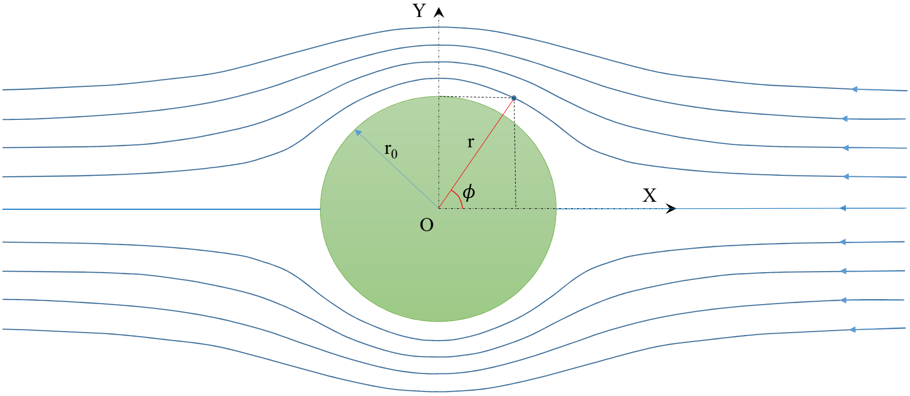

Figure 2.2: Sketch of 2D non-viscous flow structure around a cylinder.

$$\mathcal{F}(z) = \varPhi + i\varPsi = -U_\infty \left(z + \frac{r_0^2}{z} \right) \tag{2.2}$$

U_∞ is the incoming flow velocity, $z = re^{i\phi}$, is the polar coordinate in the complex plane. Therefore,

$$\mathcal{F} = -U_\infty \left(r + \frac{r_0^2}{r} \right) \cos\phi - iU_\infty \left(r - \frac{r_0^2}{r} \right) \sin\phi \tag{2.3}$$

$$\varPhi = -U_\infty \left(r + \frac{r_0^2}{r} \right) \cos\phi \tag{2.4}$$

$$\varPsi = -U_\infty \left(r - \frac{r_0^2}{r} \right) \sin\phi \tag{2.5}$$

The radial and tangential velocity components in a flow field point can be written as u_r and u_ϕ, respectively.

$$u_r = \frac{\partial \varPhi}{\partial r} = -U_\infty \left(1 - \frac{r_0^2}{r^2} \right) \cos\phi \tag{2.6}$$

$$u_\phi = \frac{1}{r}\frac{\partial \varPhi}{\partial \phi} = U_\infty \left(1 + \frac{r_0^2}{r^2} \right) \sin\phi \tag{2.7}$$

The magnitude of velocity, u, near the cylinder is given in Eq. (2.8).

$$u = \sqrt{u_r^2 + u_\phi^2} = U_\infty \sqrt{1 + \frac{r_0^4}{r^4} - 2\frac{r_0^2}{r^2}\cos 2\phi} \tag{2.8}$$

Therefore, the maximum velocity $u_{max} = 2U_\infty$ is obtained on the surface of the cylinder ($r = r_0$) and at the two sides when $\phi = 90°$ or $270°$. Referring to Eq.(2.1), the maximum amplification factor is obtained by Eq. (2.9).

$$\alpha = \left(\frac{u_{max}}{U_\infty}\right)^2 = 4 \tag{2.9}$$

The pressure on the cylinder surface can be derived by the Bernoulli equation as Eq. (2.10),

$$\begin{aligned} p &= p_\infty + \frac{1}{2}\rho U_\infty^2 - \frac{1}{2}\rho u^2|_{r=r_0} \\ &= p_\infty + \frac{1}{2}\rho U_\infty^2(1 - 4\sin^2\phi) \end{aligned} \tag{2.10}$$

The tangential pressure gradient over the angle ϕ is then,

$$\frac{\partial p}{\partial \phi} = -\frac{4}{r_0}\rho U_\infty^2 \cos\phi \sin\phi \tag{2.11}$$

which shows that the maximum pressure gradient occurs for $\phi = 45°$ and $135°$.

2.1.2 Lee-wake vortices

Beyond the scope of 2D potential flow assumption, lee-wake vortices are generated when flow passing a pile due to the existence of fluid viscosity and pile surface roughness. The structure of lee-wake vortices around a cylinder in 2D or 3D flow have been extensively investigated for many decades and can be dated back to von Kármán and Rubach (1912). The properties and regimes of the lee-wake vortices are strongly dependent on the Reynolds number of the flow around the cylinder (Sumer and Fredsøe, 1997). Various classic studies have investigated the flow characteristics and hydrodynamic forces under different Reynolds number conditions, such as Delany and Sorensen (1953), Roshko (1961), Bearman (1969), Gaster (1971) and Williamson (1989). The Reynolds number R_e is defined as Eq. (2.12), where D_P is the diameter of the cylindrical pile, U is the characteristic flow velocity and υ is the kinematic viscosity of the fluid. The flow regimes around the cylinder in steady current are concluded in Figure 2.3 by Sumer and Fredsøe (1997).

$$R_e = \frac{UD_P}{\upsilon} \tag{2.12}$$

The asymmetrical vortices generated in the condition of $R_e > 40$ can lead to a vortex-shedding phenomenon, which introduces periodic forces acting on the cylinder and an unsteady flow field in the wake region. The shedding frequency f_v is normalized into the Strouhal number, S_t, as Eq. (2.13). S_t is a function of the Reynolds number and the surface roughness of the cylinder, as illustrated in Figure 2.4.

$$S_t = \frac{f_v D_P}{U} = S_t(R_e, k_s/D_P) \tag{2.13}$$

For an oscillatory flow passing the cylinder, such as a pile in sinusoidal waves, the lee-wake vortices also depend on the Keulegen-Carpenter number, KC, as defined in Eq. (2.14),

$$KC = \frac{U_{max} T}{D_P} \tag{2.14}$$

where U_{max} is the maximum velocity of the oscillatory flow in a period T. KC number depicts the ratio between the oscillatory flow amplitude and the cylinder diameter. Small KC number means the water particle motion amplitude is relatively small to the cylinder size so that flow separation does not often occur. Large KC number indicates that the water particle motion amplitude is relatively large, resulting in periodic flow separation and vortex shedding. Very large KC number can be regarded as a scenario of steady current passing the cylinder in half an oscillation period. Extensive experimental and theoretical studies have been carried out decades ago, such as in Sarpkaya (1976, 1986), Williamson (1985) and Bearman et al. (1985). A conclusive figure depicting the regimes of oscillatory flow passing a smooth cylinder is given in Figure 2.5 by Sumer and Fredsøe (1997).

2.1.3 Horseshoe vortex

The horseshoe vortex structure near the pile base is plotted in Figure 2.6. In front of the pile, streamlines of incoming flow detach with bed at the separation point. The separated boundary layer rolls up downstream of the separation line to form the vortex. The horizontal distance between the separation point and the pile is x_s and the horizontal distance between the primary vortex centre and the pile is x_v. Experimental studies have revealed regimes and dimensions of the horseshoe vortex near the pile base in steady flow, e.g. by Baker (1979, 1980, 1985, 1991) and Dargahi (1989). With an increase of the Reynolds number of the incoming flow, the number of vortices increases and the structure of the vortex system becomes complex. The distances of x_v and x_s are related to the relative boundary layer displacement thickness (D_P/δ_*) and the Reynolds number (R_e in Eq. 2.12), as described in Figure 2.7 (Baker, 1985). It is also discussed in Sumer and Fredsøe (2002) that the separation distance x_s in steady flow induced horseshoe vortex increases as the relative incoming flow boundary layer thickness δ/D_P increases. In a turbulent flow condition, the upstream pressure distribution is found to be insensitive with the R_e number according to the observations done by Baker (1980) and Dargahi (1989), while the pressure distribution downstream increases in the region close to the pile, causing the primary wake vortices (Dargahi, 1989).

In case of oscillatory flow, the horseshoe vortex near the pile base can occur periodically and alternatively upstream and downstream of the pile. The occurrence and lifespan of the horseshoe vortex is related to whether and how long a sufficiently large flow velocity exist in an oscillation period. Sumer et al. (1997) provide a detailed analysis of a horseshoe vortex near a pile in wave and current conditions. For wave alone condition, it is found that the horseshoe vortex exists when $KC > 6$ and the lifespan increases as KC increases, as shown in Figure 2.8. When a current is superposed, the horseshoe vortex lifespan increases as U_c/U_m increases, while the horseshoe vortex can occur at a lower KC number condition.

Despite the vortex structure, the characteristics of the down-flow in front of a pile is also important for the scour around pile as described in Raudkivi (1986). The down-flow velocity can be up to 40% of the approaching mean flow velocity in flat bed condition, and can increase as the scour depth increases around the pile. Many investigations of the down-flow characteristics as well as the horseshoe vortex near the pile are presented, such as Hjorth (1975), Graf and Yulistiyanto (1998) and Unger and Hager (2007). A recent summary of the horseshoe vortex can be referred to Gazi and Afzal (2020).

The horseshoe vortex affects the bed shear stress and the amplification factor distribution near the pile base. The distribution of α under current and wave conditions are presented in the experiments from Hjorth (1975) and Sumer et al. (1997), respectively. According to Sumer et al. (1997), the amplification factor α in front of the pile increases as KC increases and can be as large as $\alpha = O(6)$ in a steady current condition (KC is infinite). While the maximum α happens at about 45° position toward the incoming flow, which can be up to $\alpha = O(11)$. This large α is also reproduced in numerical simulations from such as Roulund et al. (2005) and Baykal et al. (2015) (see Figure 2.9).

Miles et al. (2017) measures the flow velocity amplification around a pile using a 1:25 scale model in current-only, wave-only and current-orthogonal-to-wave conditions. In a current-only condition, the maximum current velocity at both sides of the pile is 1.35 times the incoming current velocity. In a wave-only condition, the wave orbital oscillatory flow velocity is enhanced up to 1.85 times the wave orbital velocity far from the pile. When wave and current are orthogonally combined, the combined maximum flow velocity near the pile is 1.2 times the combined velocity far from the pile. The maximum velocity occurs at the current incoming side of the pile.

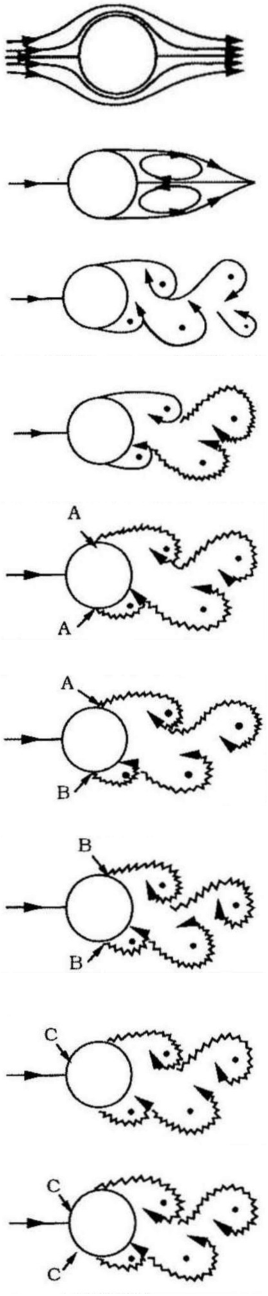

No separation, creeping flow	Re < 5
A fixed pair of symmetric vortices	5< Re < 40
Laminar vortex street	40 < Re < 200
Transition to turbulence in the wake	200 < Re < 300
Wake completely turbulent. A: Laminar boundary layer separation	$300 < Re < 3 \times 10^5$ Subcritical
A: Laminar boundary layer separation B: Turbulent boundary layer separation, but boundary layer laminar	$3 \times 10^5 < Re < 3.5 \times 10^5$ Critical (Lower transition)
B: Turbulent boundary layer separation; The boundary layer partly laminar and partly turbulent	$3.5 \times 10^5 < Re < 1.5 \times 10^6$ Upper transition
C: Boundary layer completely turbulent at one side	$1.5 \times 10^6 < Re < 4 \times 10^6$ Supercritical
C: Boundary layer completely turbulent at two sides	$4 \times 10^6 < Re$ Transcritical

Figure 2.3: Lee-wake flow regimes around a smooth circular cylinder in steady current, after Sumer and Fredsøe (1997).

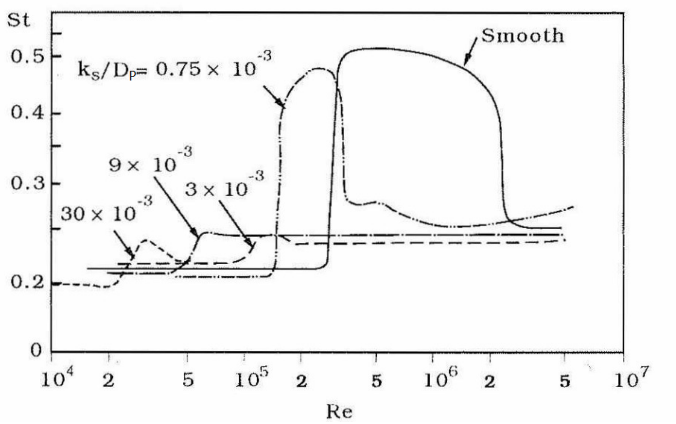

Figure 2.4: Relationship between S_t number and R_e with varied surface roughness of the cylinder, after Sumer and Fredsøe (1997).

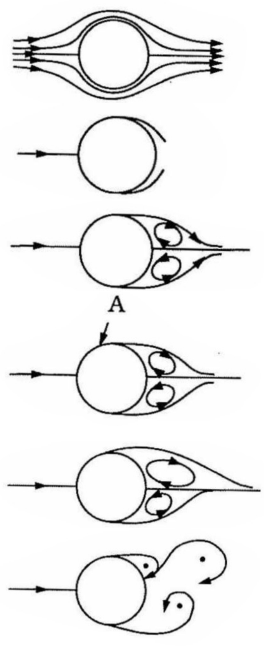

No separation Laminar flow	KC < 1.1
Separation with Honji vortices	1.1 < KC < 1.6
A pair of symmetric vortices	1.6 < KC < 2.1
A pair of symmetric vortices. Turbulence over the cylinder surface (A)	2.1 < KC < 4
A pair of asymmetric vortices	4 < KC < 7
Vortex shedding	KC > 7

Figure 2.5: Regimes of oscillatory flow passing a smooth cylinder in $R_e = U_{max}D_P/\upsilon = 10^3$ condition, after Sumer and Fredsøe (1997).

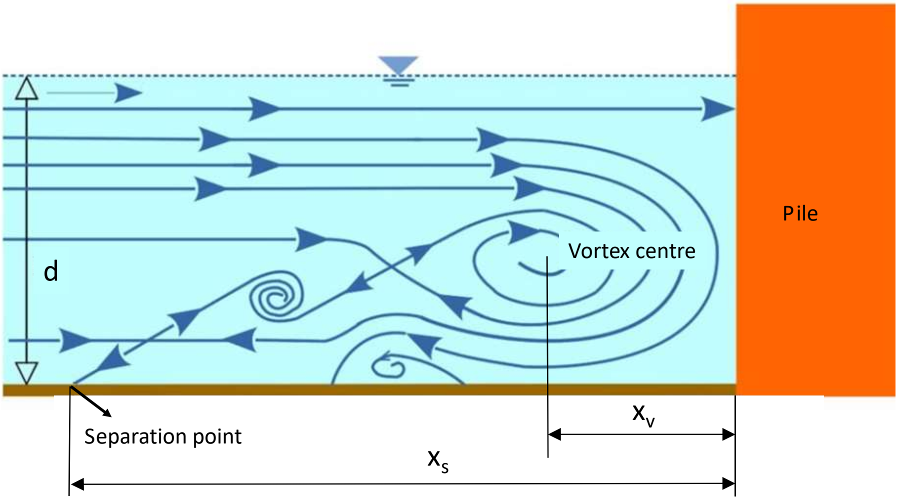

Figure 2.6: Horseshoe vortex near the pile base, modified from Gazi and Afzal (2020).

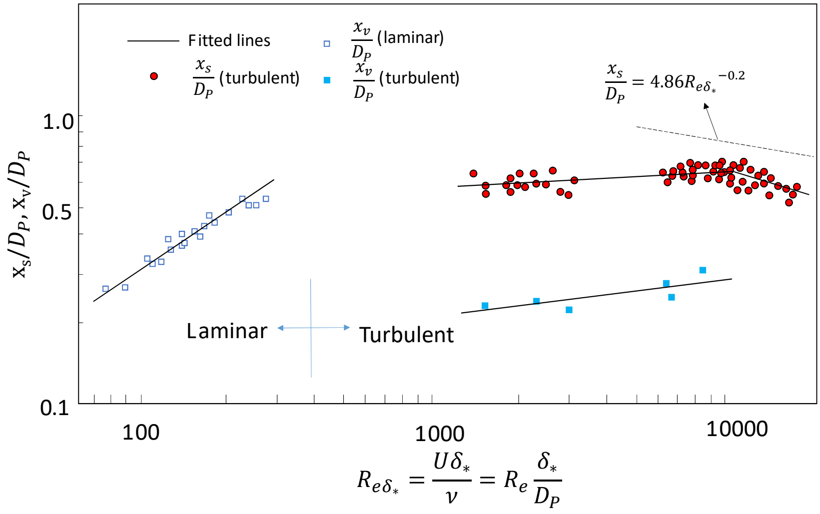

Figure 2.7: Horseshoe vortex dimensions, modified from Baker (1985).

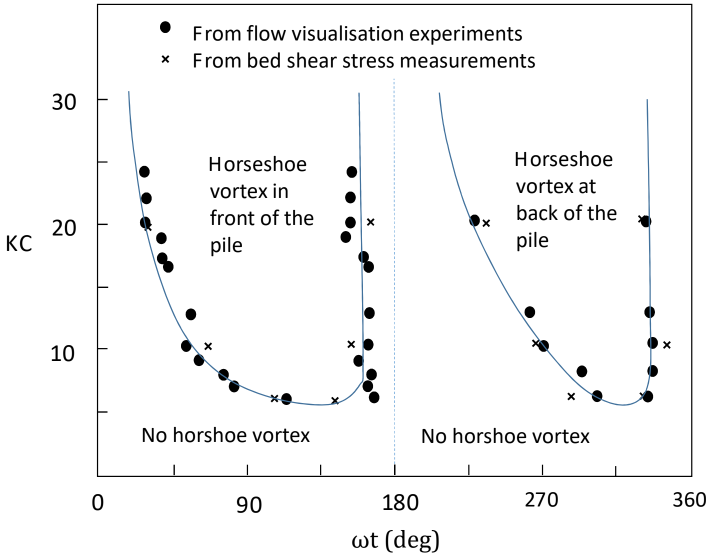

Figure 2.8: Horseshoe vortex occurrence in phase space, modified from Sumer et al. (1997).

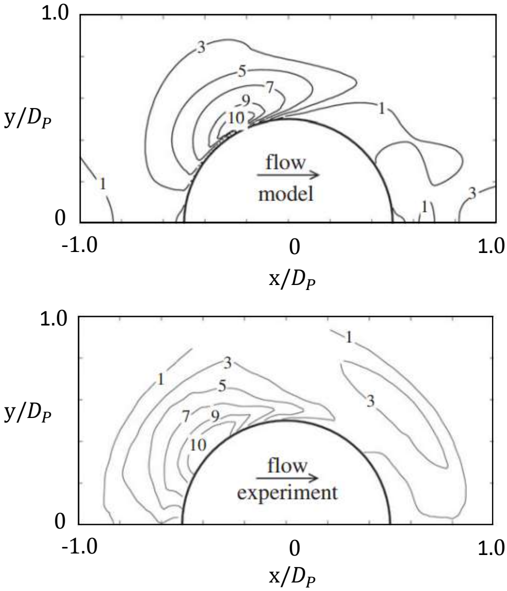

Figure 2.9: Bed shear stress amplification factor distribution around a pile, after Baykal et al. (2015).

2.2 Mechanism of scour around a vertical pile

2.2.1 Initiation of sediment motion

The sediment particle in flat river or sea bed will move when the instantaneous fluid force acting on a particle is larger than the instantaneous resistance. As sketched in Figure 2.10, particles on the bed are subjected to submerged gravity (G), drag force (F_D) and lift force (F_L). The moment relationship around the contact point determines the motion status of the sediment particle. A sketch is plotted in Eq. (2.15) following van Rijn (1993).

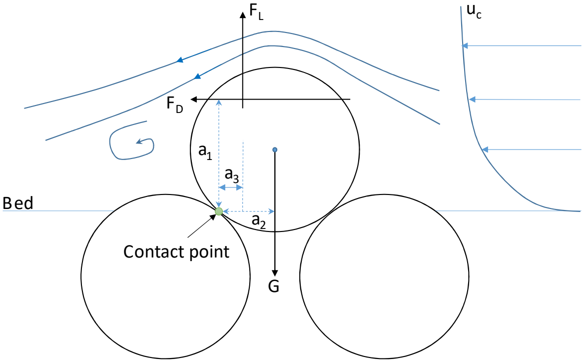

Figure 2.10: Forces acting on the sediment particles, modified from van Rijn (1993).

$$a_1 F_D + a_3 F_L > a_2 G \tag{2.15}$$

The left side of Eq. (2.15) represents the loading on the particle and the right side of Eq. (2.15) is the resistance. According to Shields (1936), the loading is related to the size of the particle (d_s), the shear velocity (u_*), the Reynolds number near the bed ($R_{e*} = u_* d_s / \upsilon$) and the shape of the particle, The resistance is related to the densities of the particle material (ρ_s) and the fluid (ρ) as well as the size of the particle. These relationships are expressed by Eq. (2.16) and (2.17), respectively,

$$a_1 F_D + a_3 F_L = C_1 \rho u_*^2 d_s^2 \tag{2.16}$$

$$a_2 G = C_2 (\rho_s - \rho) g d_s^3 \tag{2.17}$$

where g is the acceleration due to gravity. The criterion in Eq. (2.15) is then simplified into the form in Eq. (2.18),

$$\frac{\rho u_*^2}{\rho (s-1) g d_s} > \frac{C_2}{C_1} \tag{2.18}$$

where the coefficients are $C_1 = f_1(R_{e*}, shape)$ and $C_2 = f_2(shape)$. The term ρu_*^2 is the bed shear stress, (τ_b, in $[N/m^2]$). The left side term of Eq. (2.18) is the Shields parameter, or the mobility parameter as named after van Rijn (1993), which is denoted with the symbol θ ($\theta = \tau_b/[\rho(s-1)gd_s]$). When the bed shear stress τ_b exceeds a critical value τ_{cr}, the particle starts to move. This gives a Shields criterion for a threshold of motion shown as in Eq. (2.19).

$$\frac{\tau_b}{\rho(s-1)gd_s} \geq \frac{\tau_{cr}}{\rho(s-1)gd_s} \tag{2.19}$$

The right side term of Eq. (2.19) is the critical Shields parameter and is expressed by θ_{cr} ($\theta_{cr} = \tau_{cr}/[\rho(s-1)gd_s]$). θ_{cr} is a function of R_{e*} as shown in Figure 2.11, where R_{e*} is represented with the critical shear velocity $u_{*,cr}$. The Shields criterion can be simply written by $\theta \geq \theta_{cr}$ for a sediment particle starting to move.

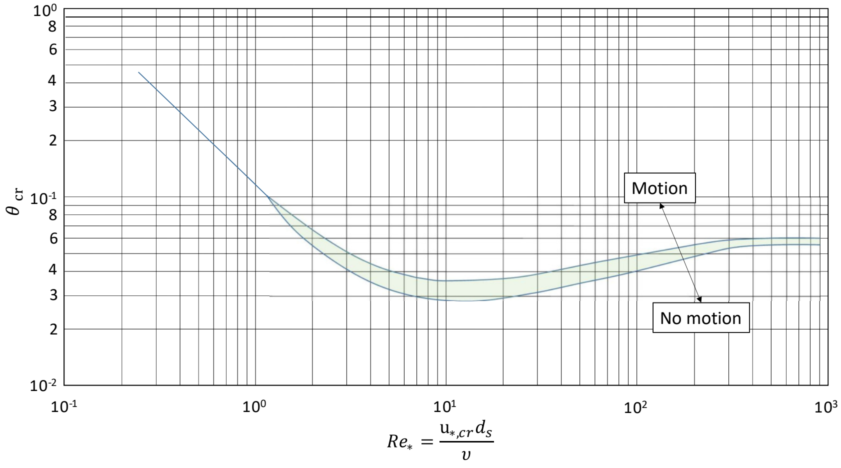

Figure 2.11: Shields curve for threshold of motion in steady current, after van Rijn (1993).

θ_{cr} plotted in Figure 2.11 is implicit with regard to the particle size and only valid for current flow condition. The classic work of Shields is extended to wave only and combined wave and current condition by Soulsby and Whitehouse (1997) with a diagram of explicit relationship between θ_{cr} and the dimensionless sediment particle size D_*, as shown in Figure 2.12. A regression formula to calculate θ_{cr} is given as Eq. (2.20),

$$\theta_{cr} = \frac{0.30}{1+1.2D_*} + 0.055[1 - \exp(-0.020D_*)] \tag{2.20}$$

D_* is calculated by Eq. (2.21),

$$D_* = \left[\frac{g(s-1)}{\upsilon^2}\right]^{\frac{1}{3}} d_s \tag{2.21}$$

and $s = \rho_s/\rho$, is the relative density of sediment in water. For sediments with various particle sizes, the median particle size is used for the calculation, $d_s = d_{50}$. The critical shear stress τ_{cr} is calculated by Eq. (2.22).

$$\tau_{cr} = \theta_{cr} g(\rho_s - \rho) d_{50} \tag{2.22}$$

When $D_* > 200$, θ_{cr} approaches an approximate constant value of 0.056. This value is obtained from experiments. A physical indication of this constant is that the inertia force is dominant for large grains and the resistance for sediment incipience of motion is not governed by the Reynolds number around the grain.

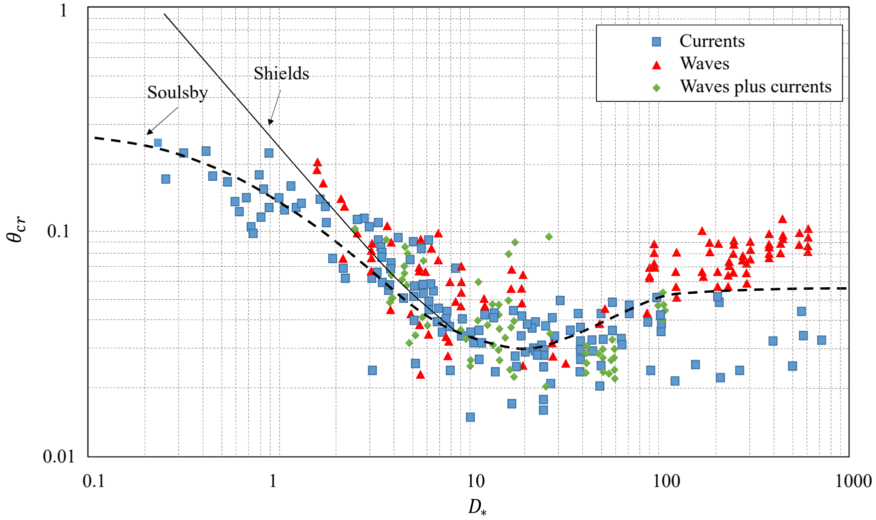

Figure 2.12: Soulsby curve for threshold of motion, modified from Soulsby (1997).

As analysed in van Rijn (1993), the incipience of sediment motion is a highly stochastic process which contains randomness from both the flow (e.g. waves, turbulence, local flow around particle) and the sediment particles (shape and gradation), therefore, θ_{cr} may vary within a wide range with the same D_* value, as shown on Figure 2.12. The differences between the maximum and minimum measured θ_{cr} values can be up to tenfold.

In addition, according to Deltares (1972), the definition of threshold of motion also leads to different θ_{cr} values. As seen in Figure 2.13, if the threshold of motion is defined strictly as occasional particle movement at some locations, a lower θ_{cr}

value will be observed. On the contrary, if the threshold of motion is defined by frequent particle movement at all locations, θ_{cr} can be much higher.

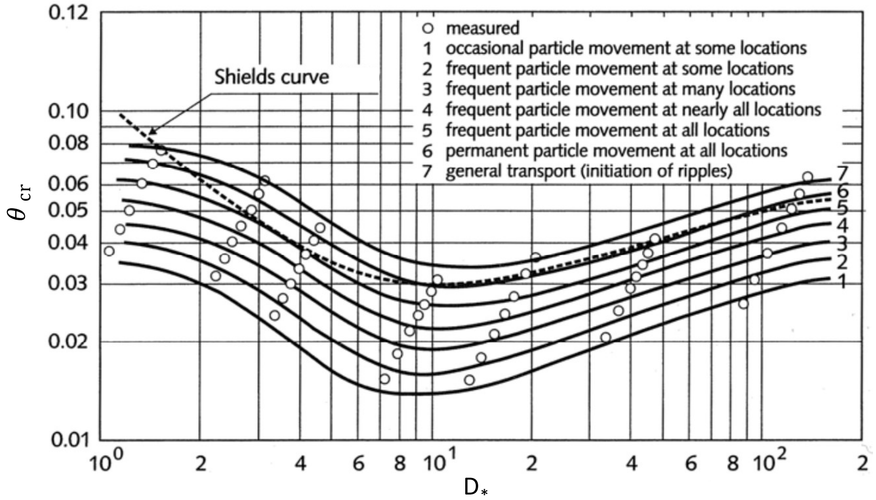

Figure 2.13: Modified Shields diagram using various definitions of threshold of motion, from Hoffman and Verheij (1997).

2.2.2 Bed shear stress due to wave and current

The bed shear stress τ_b over an undisturbed seabed in an ocean environment is composed of two parts: τ_c, the bed shear stress due to the steady current and τ_w, the bed shear stress due to the waves. τ_c is expressed by Eq. (2.23),

$$\tau_c = \frac{1}{2}\rho f_c U_c^2 \tag{2.23}$$

where f_c is the dimensionless current friction coefficient. For the steady flow condition and assuming a logarithmic velocity profile above the seabed as shown in Eq. (2.24), the depth averaged current velocity U_c can be derived by Eq. (2.25). The flow shear velocity u_{*c} then is $(\tau_c/\rho)^{1/2}$. Combined with Eq. (2.23), f_c is obtained via Eq. (2.26),

$$U(z) = \frac{u_{*c}}{\kappa} ln\left(\frac{z}{z_0}\right) \tag{2.24}$$

$$U_c = \frac{1}{d}\int_{z_0}^{d} U(z)dz \tag{2.25}$$

$$f_c = 2\left(\frac{\kappa}{ln\left(\frac{d}{z_0}\right)-1}\right)^2 \tag{2.26}$$

where κ is the von Karman constant, $\kappa = 0.4$, e is the Euler's number and is approximately equal to 2.718. z_0 is the roughness length, as expressed by Christoffersen and Jonsson (1985) in Eq. (2.27)

$$z_0 = \frac{k_s}{30}\left[1-\exp\left(\frac{-u_* k_s}{27\upsilon}\right)\right] + \frac{\upsilon}{9u_*} \tag{2.27}$$

For a hydraulically rough flow when $u_{*c}k_s/\upsilon \geq 70$, Eq. (2.28) is simplified to Eq. (2.28).

$$z_0 = \frac{k_s}{30} \tag{2.28}$$

k_s is the Nikuradse roughness. For a flat and non-rippled sand bed, $k_s = 2.5d_{50}$ (van Rijn, 1993).

The wave induced bed shear stress, τ_w, is calculated by Eq. (2.29),

$$\tau_w = \frac{1}{2}\rho f_w U_m^2 \tag{2.29}$$

where U_m is the mean wave orbital velocity near bed. U_m for regular wave is obtained from linear wave theory as Eq. (2.30) given the wave period T, the wave height H and the water depth d.

$$U_m = \frac{\pi H}{T}\frac{1}{\sinh{(kd)}} \tag{2.30}$$

k is the wave number which satisfies the dispersion relation (Eq. 2.31):

$$\frac{4\pi^2}{T^2} = kg\tanh(kd) \tag{2.31}$$

And for irregular waves, U_m can be derived using spectral analysis method as Eq. (2.32),

$$\begin{aligned} U_m &= \sqrt{2}U_{rms} = \sqrt{2}\sqrt{\int_0^\infty S_U(f)df} \\ &= \sqrt{2}\sqrt{\int_0^\infty \left(\frac{2\pi}{T\sinh(k(f)d)}\right)^2 S(f)df} \end{aligned} \tag{2.32}$$

where U_{rms} is the root-mean-square wave orbital velocity, f is the wave frequency, $f = T^{-1}$. $S(f)$ and $S_U(f)$ are wave spectrum and bottom velocity spectrum respectively. $k(f)$ is the wave number as a function of the wave frequency.

Various methods have been proposed to estimate the dimensionless wave friction coefficient f_w, for example, by Nielsen (1992)(Eq. 2.33), Soulsby (1994)(Eq. 2.34) and Dixen et al. (2008)(Eq. 2.35).

$$f_w = \exp\left[5.5\left(\frac{A}{k_s}\right)^{-0.2} - 6.3\right] \tag{2.33}$$

$$f_w = 1.39\left(\frac{A}{z_0}\right)^{-0.52} \tag{2.34}$$

$$f_w = 0.32\left(\frac{A}{k_s}\right)^{-0.8}, \quad \text{for} \;\; 0.2 < \frac{A}{k_s} < 10 \tag{2.35}$$

A stands for the amplitude of wave orbital motion at the bed, $A = H/2\sinh(kd)$ for regular waves and $A = U_m T/2\pi$ for irregular waves. T is the wave period of the equivalent monochromatic wave, which equals to the peak period T_p referring to Soulsby (1997).

When waves and currents coexist, the wave and current induced bed shear stresses are nonlinearly superposed due to the nonlinear turbulent shear stress (Soulsby et al., 1993). Figure 2.14 sketches the interactions between wave and current bed shear stresses and the mechanism of the superposition.

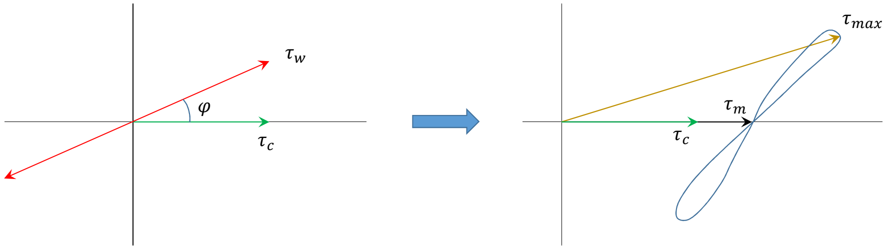

Figure 2.14: Bed shear stresses interactions between wave and current, modified from Soulsby (1997). τ_m is the mean bed shear stress within a wave period and τ_{max} is the maximum combined bed shear stress. φ is the cross angle between wave and current.

Various analytical and numerical models are proposed to solve the bed shear stress in combined wave and current boundary layer, such as by Grant and Madsen (1979), Christoffersen and Jonsson (1985), Myrhaug and Slaattelid (1990), Davies et al. (1988) and Olabarrieta et al. (2010). Meanwhile laboratory data is provided in Bakker and van Doorn (1978), Kemp and Simons (1982, 1983), etc. A review of methodologies on solving wave-current boundary layers can be retrieved from Soulsby et al. (1993). As for the sediment transport problems, the time-mean bed shear stress τ_m and maximum bed shear stress τ_{max} is more important. Most of the theoretical models are too computationally expensive or too complex to use directly, an empirical method is proposed by Soulsby (1995) as a direct fit to laboratory measurements and field measurements. The formulas for τ_m and τ_{max} are given in Eq. (2.36) and (2.37), which are known as the DATA2 method.

$$\tau_m = \tau_c \left[1 + 1.2 \left(\frac{\tau_w}{\tau_c + \tau_w} \right)^{3.2} \right] \tag{2.36}$$

$$\tau_{max} = \left[\left(\tau_m + \tau_w |cos\varphi| \right)^2 + \left(\tau_w |sin\varphi| \right)^2 \right]^{\frac{1}{2}} \tag{2.37}$$

The corresponding shear velocities are then achieved by Eq. (2.38) to Eq. (2.40).

$$u_{*c} = \sqrt{\frac{\tau_c}{\rho}} \tag{2.38}$$

$$u_{*w} = \sqrt{\frac{\tau_w}{\rho}} \tag{2.39}$$

$$u_{*max} = \sqrt{\frac{\tau_{max}}{\rho}} \tag{2.40}$$

2.2.3 Scour around pile

When the near bed flow velocity around a pile induces a local bed shear stress exceeding the critical shear stress of the bed sediment, scouring will occur and form a scour hole around the pile. The depth of this scour hole is usually marked as S and non-dimensionalised using a ratio between the depth and the pile diameter, simply, S/D_P, as sketched in Figure 2.15.

Depending on the bed shear stress due to incoming flow and the critical shear stress of the sediment, two scour phenomena are often defined: (a) clear water scour, when $\theta < \theta_{cr}$; (b) live-bed scour, when $\theta \geq \theta_{cr}$. The two phenomena show different scour depth variations in time and different equilibrium scour depths, as depicted in Figure 2.16.

The investigations on scour depth around pile have been quite extensive in recent decades. Reviews of the subject can be found in the books of Breusers and Raudkivi (1991), Hoffman and Verheij (1997), Whitehouse (1998) and Melville and Coleman (2000). The engineering problems are often analysed with regard to the type of the structure and the environment where it locates. Specifically, for the mechanics of scour around pile in ocean environment, Sumer and Fredsøe (2002) has provided a comprehensive analysis. The scour behaviour around pile at sea is discussed in two scenarios, (a) slender pile when $D_P/L_w < 0.2$ and (b) large pile when $D_P/L_w > 0.2$, based the different diffraction regimes around the pile. L_w is the wave length. In offshore wind engineering, monopiles at sea are mostly with D_P of around 5 m to 10 m, which are regarded as slender piles. A general introduction of scour around pile in various flow conditions is presented here after.

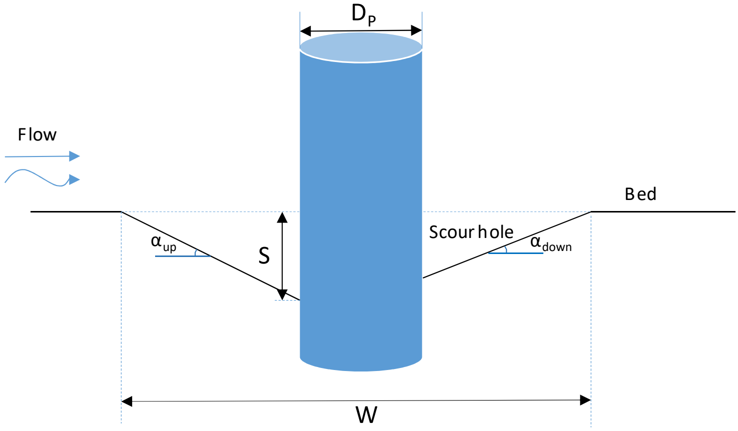

Figure 2.15: Definition of scour hole dimensions. S - Scour depth; α_{up} - Upstream slope; α_{down} - Downstream slope; W - Extension of scour hole.

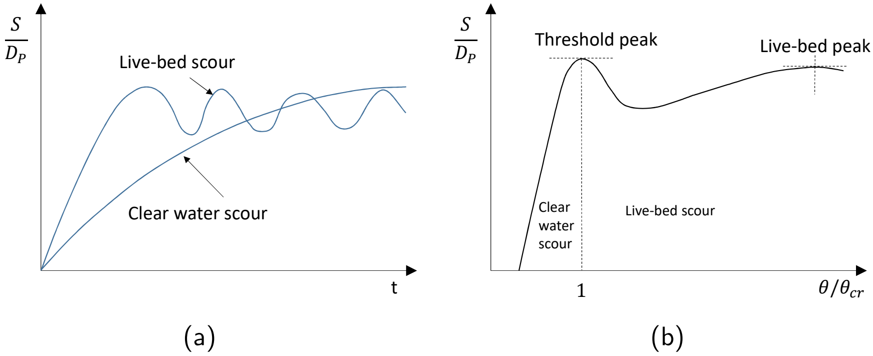

Figure 2.16: Scour depth in clear water and live-bed conditions: (a) S/D_P vs. time (t); (b) S/D_P vs. θ/θ_{cr}. Modified from Melville (2008).

2.2.3.1 Scour around pile in river current condition

As for scour around bridge pile in river current condition, the dominant parameters that affecting the equilibrium S/D_P are concluded in Melville (2008) as listed below:

(1) Flow intensity, U/U_{cr}. In clear water condition, the scour depth increases as U/U_{cr} increases and will reach a maximum value called threshold peak when $U/U_{cr} = 1$ for uniform sediment condition. When U/U_{cr} is large enough in a live-bed condition, the second maximum scour depth, named the live-bed peak, will occur as U/U_{cr} increases.

(2) Shallowness, d/D_P. Small d/D_P is equivalent to a wide pier condition and

leads to a small S/D_P compared to a narrow pier condition when d/D_P is large. S/D_P approaches to a maximum value as $d/D_P > 1.4$.

(3) Euler number, U^2/gD_P. This parameter can be interpreted as an energy of eddies shed from the pier. According to Ettema et al. (1998), S/D_P increases as the Euler number increases.

(4) Reynolds number, UD_P/υ. This parameter is related to the shed eddies frequency. S/D_P decreases as the Reynolds number increases (Ettema et al., 2006).

(5) Sediment coarseness, D_P/d_{50}. Smaller D_P/d_{50} represents coarser sediment relative to the pier. S/D_P increases as D_P/d_{50} increases till $D_P/d_{50} \approx 50$. When $D_P/d_{50} > 50$, S/D_P decreases as sediment becomes finer (Sheppard and Glasser, 2004).

(6) Sediment uniformity, σ_g. Higher σ_g provides more stability to the sediment around pile in current and reduces S/D_P with the same U/U_{cr}, especially in clear-water condition.

(7) Time, t. The relationship of S/D_P varying to t is shown in Figure 2.16(a). But the time to reach equilibrium S/D_P varies with U/U_{cr}, D_P/d_{50} and d/D_P. The maximum equilibrium time scale $t^* = 2.5 \times 10^{-6}$. $t^* = Ut_e/D_P$ and t_e is the absolute equilibrium time.

(8) Pier shape and alignment. The influences from pier shape and alignment are generalised to a K-factor, as described in Hoffman and Verheij (1997). S/D_P increases proportionally to this K-factor. Typically, elliptic piers or rectangular piers with sharp noses have lower K-factor than cylindrical piers. A larger alignment angle of a rectangular pile results in a higher K-factor.

(9) Superstructure submergence. The submerged bridge causes higher bed erosion than an unsubmerged one due to the pressure scour effects.

2.2.3.2 Scour around pile in wave-only condition

For scour depth around slender pile in wave-only condition, the most important factor is the KC number as it governs the process of horseshoe vortex generation. A prediction formula is given Sumer et al. (1992) (Eq. 2.41).

$$\frac{S}{D_P} = 1.3\{1 - \exp\left[-0.03(KC - 6)\right]\}; KC \geq 6 \tag{2.41}$$

The formula indicates S/D_P approaches a maximum equilibrium value when KC number is infinite, which is equivalently a steady flow condition. $KC \geq 6$ is the prerequisite condition for horseshoe vortex occurrence in every wave period. Eq. (2.41) is practically applied in the design of offshore wind foundations as guided in DNV (2014). In addition, the influence of pile shape is then discussed in Sumer et al. (1993) and the influence of breaking waves is studied by Nielsen et al. (2012).

2.2.3.3 Scour around pile in wave and current condition

Regarding a combined wave and current condition, Sumer and Fredsøe (2001a) have proposed prediction formulas as in Eq. (2.42) to Eq. (2.44),

$$\frac{S}{D_P} = \frac{S_c}{D_P}\{1 - \exp\left[-A(KC - B)\right]\}; KC \geq 4 \tag{2.42}$$

$$A = 0.03 + \frac{3}{4}U_{cw}^{2.6} \tag{2.43}$$

$$B = 6\exp(-4.7U_{cw}) \tag{2.44}$$

where S_c is the scour depth in steady current alone condition. $S_c/D_P = 1.3$ and the standard deviation is 0.7. U_{cw} is the relative current velocity, as defined in Eq. (2.45),

$$U_{cw} = \frac{U_c}{U_c + U_m} \tag{2.45}$$

For low KC numbers, Rudolph and Bos (2006) proposed a modified scour depth prediction equation in combined wave and current condition, which is fitted using a series of experimental data within the range of $1 < KC < 10$, as shown in Eq. (2.46) to Eq. (2.49).

$$\frac{S}{D_P} = 1.3\{1 - \exp[-A(KC - B)](1 - U_{cw})^C\} \tag{2.46}$$

$$A = 0.03 + 1.5U_{cw}^4 \tag{2.47}$$

$$B = 6\exp(-5U_{cw}) \tag{2.48}$$

$$C = 0.1 \tag{2.49}$$

It is also discussed in Qi and Gao (2014) for a lower KC number condition when $0.4 < KC < 4$. All the studies reveal that S/D_P increases as U_{cw} and KC number increase.

2.2.3.4 Scour for large piles

When the pile size is large and when the ratio between pile diameter and wave length $D_P/L_w > 0.2$, the wave diffraction becomes significant. For this scenario, the KC number is very small (less than 3) and will not cause flow separation around the pile, according to Sumer and Fredsøe (2001b). Hence, no horseshoe vortex will develop. However, the bed boundary layer near the base of the pile will react to the wave diffraction around the pile, and a so-called steady streaming will develop. Figure 2.17 illustrates the steady streaming around a pile. The velocity of this steady streaming is a resultant of the period-averaged tangential and radial velocities. The magnitude of the steady streaming velocity can be 20% to 25% of the maximum bottom wave orbital velocity. The scour depth of large pile in waves is mainly governed the KC number and D_P/L_w. Investigation from Sumer and Fredsøe (2001b) shows that S/D_P increases as D_P/L_w and KC increase, this is because the steady streaming velocity increases as KC and D_P/L_w increase.

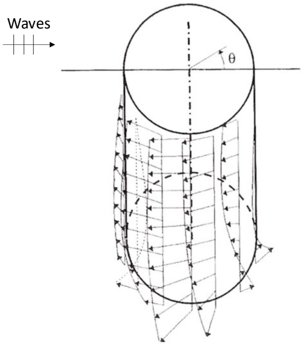

Figure 2.17: Illustration of steady streaming around pile, modified after Sumer and Fredsøe (2001b).

2.3 Conclusions

This chapter has briefly introduced the background theories of scouring around monopile. The mechanism can be explained into two parts: (a) the complex vortex structures around pile lead to an amplification of local bed shear stress. (b) when the local bed shear stresses exceeds the critical shear stresses of the sediments around pile, the sediments start to move and form a scour hole. Laboratory studies show that the scour depth around an unprotected monopile foundation at sea can reach an average value of approximately $1.3D_P$ with a standard deviation of $0.7D_P$, while field survey from Whitehouse et al. (2011) confirms the order of the scour depth data: S/D_P for unprotected monopile foundation can be maximum 1.47, the absolute value of S can be in the order of 7 meters. For the purpose of reducing the risks due to scour around pile, it is important to design reliable scour protections in newly installed windfarms.

Chapter 3

State-of-the-art of the monopile scour protection study

3.1 Failure modes of scour protection

The rip-rap type scour protection is commonly used in civil engineering for preventing scour around structures in river and ocean environment. It usually contains an armour layer, which refers to several sublayers of coarse armour stones to resist the shear load, and a filter layer, which consists of fine stones and/or geotextile to resist the loss of bed materials. Figure 3.1 sketches the layout of a scour protection layer around a pile.

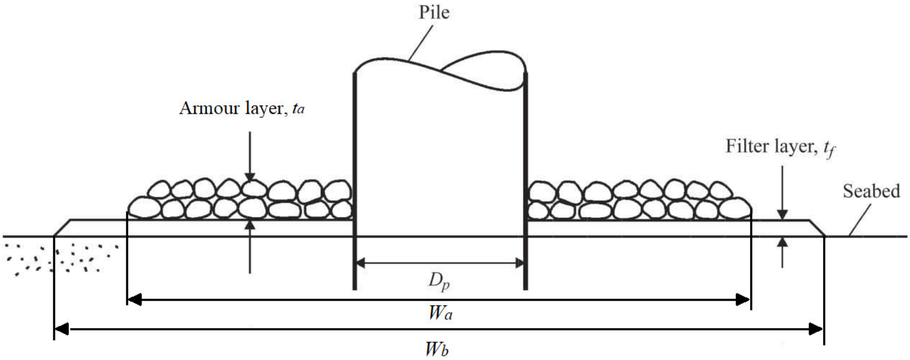

Figure 3.1: Layout of scour protection around pile, D_P - pile diameter; t_a - thickness of armour layer; t_f - thickness of filter layer; W_a - width/extension of armour layer; W_b - width/extension of filter layer. Modified from Sumer and Nielsen (2013).

Similar to the physics of scour around pile, the amplified bed shear stress can lead to the displacement of armour stones, so that the scour protection layer destabilises and fails to maintain its functionality. Therefore, it is necessary to study the stability of scour protection layer and the mechanism of its failure.

Regarding the stability of scour protection around bridge piers, systematic investigations are presented by such as Quazi and Peterson (1973), Breusers et al. (1977), Parola (1993), Chiew (1995), Chiew and Lim (2000), Lim and Chiew (2001), Lauchlan and Melville (2001), Chiew (2004) and Unger and Hager (2006). Three main failure modes are defined by Chiew (1995) to explain the mechanism of destabilisation of a scour protection layer, which are:

(1) Shear failure. The armour stones are not large and heavy enough to withstand the amplified shear stress near the pile due to the downflow and the horseshoe vortex. This mode is also known as the erosion failure.

(2) Winnowing failure. The finer sediment beneath the scour protection layer is sucked out by the above low pressure through the pores between armour stones. This mode is also known as the sinking failure.

(3) Edge failure. A scour hole is formed at the edge of a scour protection layer therefore armour stones roll and fall into the scour hole due to the large exposed slope.

(4) Bed feature destabilisation. When very large sand dunes and ripples pass the pile, the bed fluctuation causes the armour stones losing support, and therefore destabilise (Chiew, 2002). This mode is named by Chiew and Lim (2000) and identified in live-bed condition.

Figure 3.2 briefly depicts the physics of the listed four failure modes. Despite the bed feature destabilisation failure, the other three modes can happen both in clear water condition and live-bed condition. A summary of the failure conditions is provided by Lauchlan and Melville (2001), as shown in Figure 3.3.

The failure modes of scour protection layer are also extended to the application of offshore structures, especially monopiles. The problem becomes more sophisticated as the ocean environment is a combination of waves and currents, while the hydrodynamic loading can be cyclic, multi-directional and extremely high in stormy conditions. Different from what is concerned in river engineering, the bed form destabilisation is not very important as the bed deformation at sea is not as large as that in river current (Nielsen, 2011). According to a field survey of 36 monopile wind turbine foundations in the Dutch offshore windpark Egmond aan Zee (Raaijmakers, 2009), the scour protection performance around a monopile ($D_P = 4.6m$) can be affected in the following patterns:

(1) Most of the wind turbines suffered 25 to 30 cm loss of the scour protection armour materials due to a possible settlement/compaction effect.

(2) Scour protection that is located 0.5-$1.0D_P$ from the pile was more lowered than the average value. The deformation of scour protection layer is possibly induced by stormy weather.

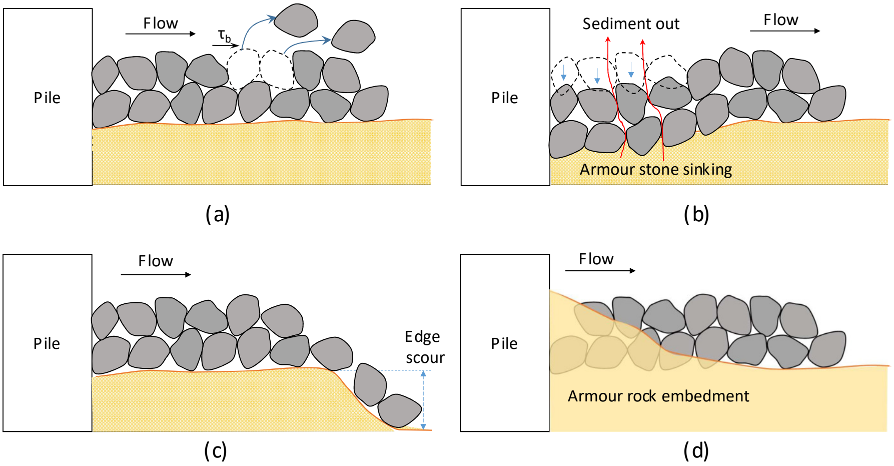

Figure 3.2: Failure modes of scour protection around pile: (a) shear failure; (b) winnowing failure; (c) edge failure; (d) bed feature destabilisation.

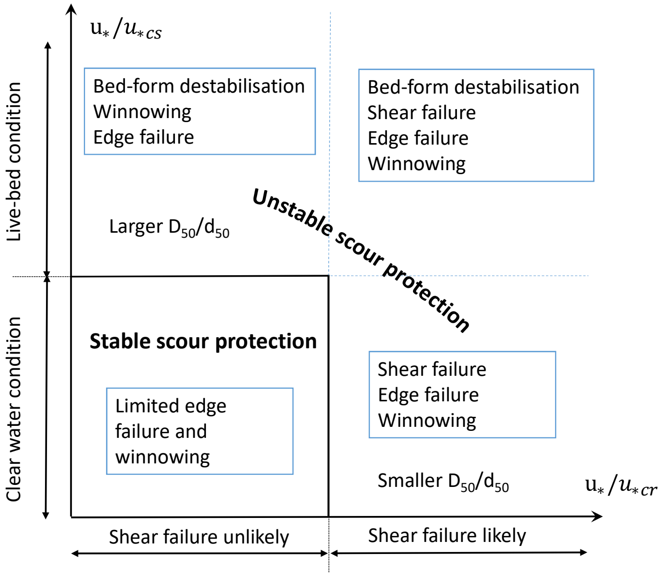

Figure 3.3: Failure modes of scour protection around pile in various conditions: u_* is the near bed shear velocity, u_{*cr} is the critical shear velocity for armour stones, u_{*cs} is the critical shear velocity for sediment. Modified from Lauchlan and Melville (2001).

(3) Filter layer materials can loss near the major edge scour holes. The depth of the edge scour hole can be up to 2 m.

The associated engineering problems attract many interests from academia regarding different possible failure scenarios of the scour protection around monopile as well as the design methods. A brief list of relative literature is provided and categorised as below:

- Shear load and shear failure. See Den Boon et al. (2004), De Vos (2008), Raaijmakers et al. (2010), De Vos et al. (2011, 2012), Looseveldt and Vannieuwenhuyse (2012), Whitehouse et al. (2014), Schendel et al. (2014), De Schoesitter et al. (2014) and Nielsen and Petersen (2019).
- Sand suction process and sinking failure. See Nielsen et al. (2010), Nielsen et al. (2011), Nielsen et al. (2013), Sumer and Nielsen (2013), Nielsen et al. (2015) and Nielsen and Petersen (2018).
- Edge scour. See Petersen (2014) and Petersen et al. (2015).

These investigations come to practical countermeasures tackling with the failures of scour protection. For example, (a) increasing the size of armour stones can improve the stability of scour protection layer against shear failure; (b) increasing the layers of armour stones and applying a filter layer with certain thickness can significantly reduce the sinking depth; (c) building an armour layer and a filter layer with a large extension helps to reduce the risk of edge failure. However, considerations on engineering cost limit the application of an over-stable scour protection layer with relatively large sized armour stones and large amount of rock materials. The problem develops toward the design of a stable and economical scour protection layer.

3.2 Approaches to determine armour stone size

General design requirements and guidelines of a pile scour protection are available in various sources, such as Lagasse et al. (2006) (Chapter 3), CIRIA (2007) (Chapter 6) and Kirby et al. (2015). The stability of scour protection described in CIRIA (2007) should satisfy:

- the external stability of the protection should be adequate, which means that the protection should remain stable under the specified design conditions;
- the internal stability of the protection should be adequate, which means there should be no loss of bed material through the protection;
- the protection should be able to adjust itself adequately to the foreseen bed level fluctuations near the edge of the protection.

The most important design parameter is the median size of armour stones, D_{50}. There exist several design methods towards D_{50} in bridge pier scour protection. For example, a classic design method was proposed by Breusers et al. (1977) which used the Izbash formula (Izbash, 1935) to estimate the boulder diameter (Eq. 3.1).

$$0.85\sqrt{\frac{2gD_{50}(\rho_s-\rho)}{\rho}}=2U_{max} \tag{3.1}$$

Lauchlan (1999) proposed a relationship between D_{50}, water depth d and various factors, as expressed in Eq. (3.2).

$$\frac{D_{50}}{d}=K_YK_DK_eK_tK_SK_\alpha F_{r,d}^2 \tag{3.2}$$

$F_{r,d}^2=U^2/gd$, is the square of water depth Froude number. The K-factors in the formula describe the influences from various parameters: K_Y for placement depth, K_D for the pier diameter-to-bed material ratio, K_e for scour protection area, K_t for armour layer thickness, K_S for pier shape and K_α for pier alignment. The obtained required D_{50} ensures a minimal local scour at a bridge pier, while the applied critical state allows a protected local scour depth less than 20% of an unprotected scour depth during the experimental period.

However, the definition of critical states can significantly affect the required D_{50}, as discussed in Lauchlan and Melville (2001). Some experiments adopt strict criteria for scour protection failure, such as Quazi and Peterson (1973). While some allow a certain deformation or scour beneath, such as Parola (1993) and Chiew and Lim (2000). Depending on the specific construction conditions, it is recommended in CIRIA (2007) that the design of armour layer can be achieved from two approaches: (a) static approach, the scour protection is statically stable which allows no displacement of armour stones; (b) dynamic approach, the scour protection is dynamically stable which allows a certain level of damage of the armour layer but no failure occurs. Therefore, the design methods regarding monopile scour protection are developed on the basis of the two different criteria. The static design approach has been widely applied commercially, but according to De Vos et al. (2012), the statically stable scour protection is usually conservative and results in large grain sizes. A thick filter layer is also needed to prevent large armour stones from sinking, which is an important cost in offshore installation. So a relatively short return period of storm conditions is sometimes applied in the design to reduce the cost of foundation (De Vos et al., 2012). As an alternative way to reduce the foundation cost, recently, the dynamically stable scour protection is getting more and more concerned. By this way the armour stone size can be reduced up to 80% (Fazeres-Ferradosa et al., 2021). In addition, it was also reported that using wide-graded armour stones can reduce the monopile foundation cost by 30%. This cost reduction is mainly due to the fact that such a wide-graded scour protection is formed by only one armour layer without a filter layer, because the small stones can act as a filter to prevent sinking failure. The rest content in this section will give an overview of the existing design methods on the determination of armour stone size used in monopile scour protection.

3.2.1 Soulsby method

Soulsby (1997) derives a method to determine the armour stone size in wave and current environment based on the threshold of motion relationship. For current over an immobile or mobile beds, the shear velocity u_* satisfies a power-law fit (Eq. 3.3),

$$\frac{u_*}{U} = \frac{1}{7}\left(\frac{D_{50}}{d}\right)^{\frac{1}{7}} \tag{3.3}$$

where U is the depth-averaged current velocity, d is the water depth and D_{50} is the median grain size. The sizes of scour protection armour materials usually appear $D_{50} > 10$ mm. Referring to the Soulsby's diagram (Figure 2.12), the critical shear stress for large grain sizes ($D_* > 200$) approaches $\theta_{cr} = 0.056$, which gives

$$\frac{\rho u_{*cr}^2}{\rho(s-1)gD_{50,cr}} = 0.056 \tag{3.4}$$

Hence, combined with Eq. (3.3) and Eq. (3.4), the critical stone size is derived as Eq. (3.5).

$$D_{50,cr} = \frac{0.25U^{2.8}}{d^{0.4}\left[(s-1)g\right]^{1.4}} \tag{3.5}$$

For wave only condition, the critical stone size satisfies:

$$\frac{f_w \rho U_w^2}{2\rho(s-1)gD_{50,cr}} = 0.056 \tag{3.6}$$

where f_w can be obtained from Eq. (2.34). Replacing the bed roughness length z_0 with $z_0 = 2.5D_{50,cr}/30$, Eq. (3.6) develops to Eq. (3.7),

$$\frac{1.39}{2}\left[\left(\frac{U_w T}{2\pi}\right)\left(\frac{30}{2.5D_{50,cr}}\right)\right]^{-0.52} U_w^2 = 0.056(s-1)gD_{50,cr} \tag{3.7}$$

therefore,

$$D_{50,cr} = \frac{97.9U_w^{3.08}}{T^{1.08}\left[(s-1)g\right]^{2.08}} \tag{3.8}$$

where T is the wave period, U_w is the wave orbital velocity amplitude at seabed.

The method is explicit and convenient to apply, but the amplification of bed shear stress around pile when wave and current coexist is not taken into consideration.

3.2.2 STAB method

Den Boon et al. (2004) present an Opti-pile design tool, where a STAB parameter is introduced to describe the damage and failure of the scour protection. The STAB parameter is defined with a simple expression (Eq. 3.9),

$$STAB = \frac{\theta_{max}}{\theta_{cr}} \tag{3.9}$$

where θ_{max} is the maximum Shields parameter in combined wave and current condition, calculated by

$$\theta_{max} = \frac{\tau_{max}}{\rho(s-1)gD_{50}} \tag{3.10}$$

In accordance with the Opti-Pile project experimental results (model scale 1:47.25), it is observed that no movement of armour stones occurs when $STAB < 0.415$, some movement but no failure occurs when $0.415 < STAB < 0.46$, and failure occurs when $STAB > 0.46$. The failure is defined as when the armour layer materials disappear and expose the filter layer over a minimum area of 4 armour stones $(4D_{50}^2)$ for a static design, or an equivalent volume of armour stones disappear for a dynamic design without a filter layer. It can be derived from Eq. (3.10) that when the armour stones are at critical state $(\theta_{cr} = \theta = \alpha\theta_{max})$, the amplification factor $\alpha = 1/0.415 = 2.4$.

The Opti-Pile $STAB$ parameter is very easy to be used in estimating the damage level of a monopile scour protection, but through small-scale model tests under wave and current conditions, it was noticed by De Vos et al. (2012) and Fazeres-Ferradosa (2018) that the same STAB parameter may result in different damage levels, as shown in Figure 3.4. Seen from Figure 3.4(b) and Figure 3.4(c), quite a few failure cases have been reported in the sensitive range of $0.415 < STAB < 0.46$ where the scour protection is assumed to be dynamically stable.

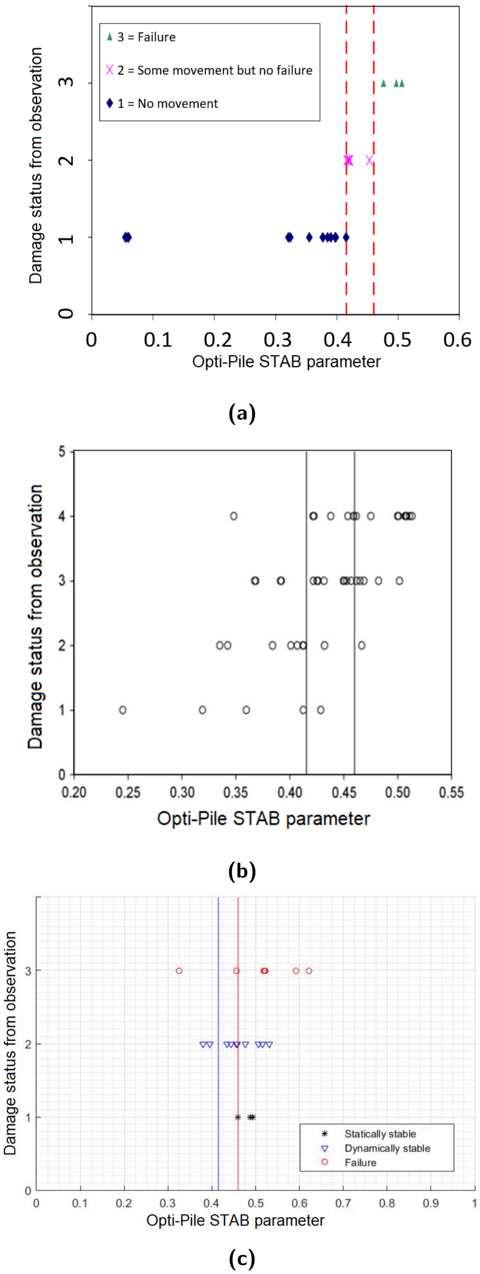

Figure 3.4: $STAB$ parameter and observed damage levels of monopile scour protections in various experiments: (a) Den Boon et al. (2004); (b) De Vos et al. (2012); (c) Fazeres-Ferradosa (2018). In De Vos et al. (2012), damage status is categorised as damage levels - 1 is statically stable, 2 and 3 are dynamically stable and 4 is failure.

3.2.3 De Vos method

A modified judgement regarding the damage levels of a monopile scour protection layer has been suggested by De Vos (2008). In this study, four damage levels are categorized based on visual observation: (1) no movement of armour stones, (2) limited armour stone movement but no failure, (3) significant armour stone movement but no failure, and (4) failure. Two design approaches are introduced by De Vos et al. (2011) and De Vos et al. (2012) which focus on the static and dynamic stability of the monopile scour protection, respectively.

3.2.3.1 Static stability approach

The static stability design approach complies to the design criteria that no armour stone is moved by the hydrodynamic loading, which corresponds to visual damage level 1. In contrast to the STAB parameter which assumes a fixed amplification factor of the bed shear stress, this method considers the critical bed shear as a combination of weighted current induced bed shear stress and wave induced bed shear stress. A linear relationship is obtained through data regression, by Eq. (3.11), for a 1:50 scale model ($D_P = 0.1m$),

$$\tau_{cr,pred} = 1.659 + 3.569\tau_c + 0.765\tau_w \tag{3.11}$$

where $\tau_{cr,pred}$ denotes the predicted local critical bed shear stress, τ_c is the bed shear stress due to steady current, and τ_w is the bed shear stress due to waves. For a prototype scale monopile scour protection, $\tau_{cr,pred}$ is calculated by taking into account the actual scale ratio. If the geometrical scale ratio between prototype pile diameter and 0.1 m pile model is λ, the predicted shear stress should be Eq. (3.12). The friction coefficient of τ_w is suggested to be calculated via Eq. (2.35) (Dixen et al., 2008).

$$\tau_{cr,pred} = 1.659\lambda + 3.569\lambda\tau_c + 0.765\lambda\tau_w \tag{3.12}$$

The predicted critical shear stress $\tau_{cr,pred}$ is comprehended as a load on the armour stone, while the actual critical shear stress τ_{cr} is a resistance. When $\tau_{cr,pred} > \tau_{cr}$, the armour stones are predicted to start moving. Using a strict definition of threshold of motion as Figure 2.13, the regression in De Vos et al. (2011) applies $\theta_{cr} = 0.035$ for occasional particle movement scenario. Meanwhile, considering the interactions between small and large grains in well-graded materials, the method applies a stone size of $D_{67.5}$ to calculate τ_{cr} (Eq. 3.13).

$$\tau_{cr} = 0.035\rho(s-1)gD_{67.5} \tag{3.13}$$

The advantage of this static design method is that it can be applied to the determination the scour protection armour stone easily. Both the stone size, density and gradings can be considered. The main problem of this method is that the applicability to prototype is not fully understood. As described in De Vos et al. (2012), the static design method is prone to give a large stone size and tends to be conservative.

3.2.3.2 Dynamic stability method

For the dynamic stability design which allows armour stone movement but no failure, a three-dimensional damage number, S_{3D}, is defined to quantify the damage, as Eq. (3.14). The total area of the scour protection layer is divided into 24 subsections, as shown in Figure 3.5. Each subsection has the same area as the pile area S_P, $S_P = \pi D_P^2/4$. V_i is the eroded volume of the rock material in each subsection. The damage number for each subsection can be comprehended as the amount of armour stone layers which have been removed,

$$S_{3D} = \max\left(\frac{V_i}{D_{n50} S_P}\right) \tag{3.14}$$

where D_{n50} is the nominal diameter of the armour stone, $D_{n50} = 0.84 D_{50}$ (De Vos et al., 2012).

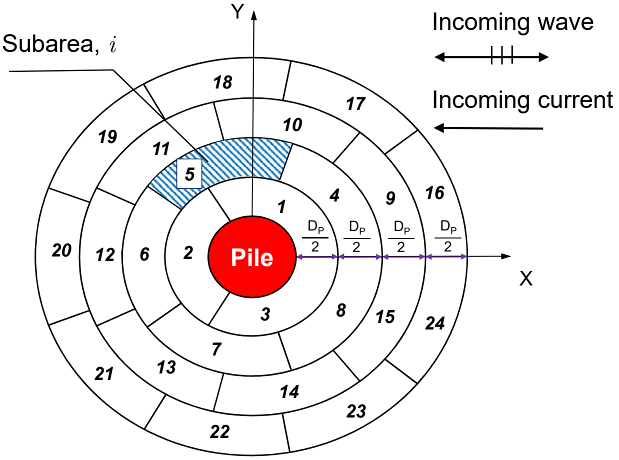

Figure 3.5: Subarea division of monopile scour protection layer.

The concept of the S_{3D} number derives from the two dimensional damage number defined for breakwaters by van der Meer (1988). Applying this value it is easy to assess the damage level of the scour protection. It is concluded in De Vos et al. (2012) that: (1) when $S_{3D} < 0.25$ (damage level 1), no movement of stones is observed; (2) when $0.25 < S_{3D} < 1$ (damage level 2 or 3), some movement of stones without failure occurrence and (3) $S_{3D} > 1$ (damage level 4), significant movement of stones and failure of the protection layer. In model experiments and field survey, the subarea damage $S_{3D,i}$ can also be used in assessing the damage location. In addition, an explicit formula (Eq. 3.15) is presented to predict the damage level of the scour protection layer under combined wave and current conditions based on a series of small scale (1:50) scour protection dynamic stability experiments,

$$S_{3D,pred} = N^{b_0} \times \left(a_0 \frac{{U_m}^3 T_{m-1,0}^2}{\sqrt{gd}(s-1)^{3/2} D_{n50}^2} + a1 \left(a2 + a3 \frac{\left(\frac{U_c}{w_s}\right)^2 \left(|U_c| + a_4 U_m\right)^2 \sqrt{d}}{g {D_{n50}}^{3/2}} \right) \right) \tag{3.15}$$

- d, water depth [m],
- U_c, depth averaged current velocity [m/s],
- U_m, mean bottom wave orbital velocity [m/s], calculated by Eq. (2.32),
- w_s, particle settling velocity [m/s],
- $T_{m-1,0}$ the wave spectrum period [s],
- $s = \rho_s/\rho$, relative density of rock material [-],
- N, number of waves.

- a_0, a_1, a_2, a_3, a_4, and b_0 are parameters obtained from regression, $b_0 = 0.243$, $a_0 = 0.00076$, $a_2 = -0.022$ and $a_3 = 0.0079$. $a_1 = 0$ for $U_c/\sqrt{gD_{n50}} < 0.92$ and wave following current condition, $a_1 = 1$ for $U_c/\sqrt{gD_{n50}} \geq 0.92$ or wave opposing current condition. $a_4 = 1$ for wave following current condition and $a_4 = U_r/6.4$ for wave opposing current condition, where U_r is the Ursell number as defined in Eq. (3.16),

$$U_r = \frac{L_w^2 H}{d^3} \tag{3.16}$$

L_w is the wave length (calculated using $T_{m-1,0}$ for irregular waves), H is the wave height (H_{m0} for irregular waves) and d is the water depth.

$T_{m-1,0}$ is calculated by Eq. (3.17),

$$T_{m-1,0} = \frac{\int_0^\infty f^{-1} S(f) df}{\int_0^\infty S(f) df} \tag{3.17}$$

$S(f)$ is the wave spectrum. If $S(f)$ is a JONSWAP spectrum with a peak enhancement factor $\gamma = 3.3$, $T_{m-1,0}$ can be approximately calculated with the peak period T_p by $T_{m-1,0} = 0.903 T_p$. $T_{m-1,0}$ is also known as the energy period, which is often adopted to describe the processes like wave run-up, overtopping and armour layer stability (Van Gent et al., 2003; Hofland et al., 2017).

The particle settling velocity is calculated using the equation of van Rijn (1984) for particle size larger than 1 mm (Eq. 3.18).

$$w_s = 1.1 \left[(s-1) g D_{50}\right]^{0.5} \tag{3.18}$$

Regarding the time scale, the factor N^{b_0} from De Vos et al. (2012) indicates an increasing S_{3D} as number of waves increases. Raaijmakers et al. (2010) proposes to use an adapted factor to describe the time evolution of S_{3D} in a wave storm as Eq. (3.19),

$$\frac{S_{3D}}{N^{b_0}} \approx \frac{S_{3D}}{b_1\left[1-\exp\left(-\frac{N}{N_{char}}\right)\right]} \tag{3.19}$$

the values are fitted to $b_1 = 7.6$ and $N_{char} = 855$. The number of waves N is bounded from 1000 to 5000 waves. The adapted time scale factor indicates an equilibrium damage at around 3000 waves. Both the two time scale factors are validated in Looseveldt and Vannieuwenhuyse (2012), which state that an equilibrium damage can be approximately reached after 5000 waves, and therefore a higher N_{char} is suggested.

The dynamic design method is validated by Looseveldt and Vannieuwenhuyse (2012) with a wide range of test conditions. It is noticed that the method corresponds well with the designated armour stone size, but may over-predict the damage when the armour stone size is out of the range used in De Vos et al. (2012). Similar to the static design method in De Vos et al. (2011), it is not clear whether the method is applicable to prototype conditions.

3.2.4 Fazeres-Ferradosa method

Recently, Fazeres-Ferradosa et al. (2020) pointed out that in scour protection damage prediction, S_{3D} number may encounter problems that two distinct damage patterns may end up with the same S_{3D}, since it is only a maximum damage number of each subarea. However, the risks of failure are different when the maximum damage occur in the vicinity of pile or far from the pile. Meanwhile, the subarea division is not suitable for non-cylindrical piles or foundations with complex geometry. To improve the scour protection damage evaluation, Fazeres-Ferradosa et al. (2020) propose to use an overlapping way to discretise the scour protection into subarea. As illustrated in Figure 3.6, the overlapped subareas can be created by rotating and refining the subareas defined by De Vos et al. (2012). By tuning the rotating angle and refinement layer, it is more flexible to select a desired subarea size, which does not need to be the same as the pile size. Similar to De Vos et al. (2012), the damage number S_{3D} is defined as the maximum of all subareas, as Eq. (3.20). Where i is the subarea index, V_i is the erode volume in this subarea and A_i is the area or size of the overlapped subarea. D_{n50} is the nominal median stone size.

$$S_{3D} = \max\left(\frac{V_i}{D_{n50}A_i}\right) \tag{3.20}$$

It is found that the shape and overlapping algorithm of the subarea does not have a major influence on the S_{3D} number, but the area A_i can play a major role. When the A_i is less than $4{D_{n50}}^2$ (4 times the nominal stone projection area), the S_{3D} number converges to stable. At this moment, the method does not receive

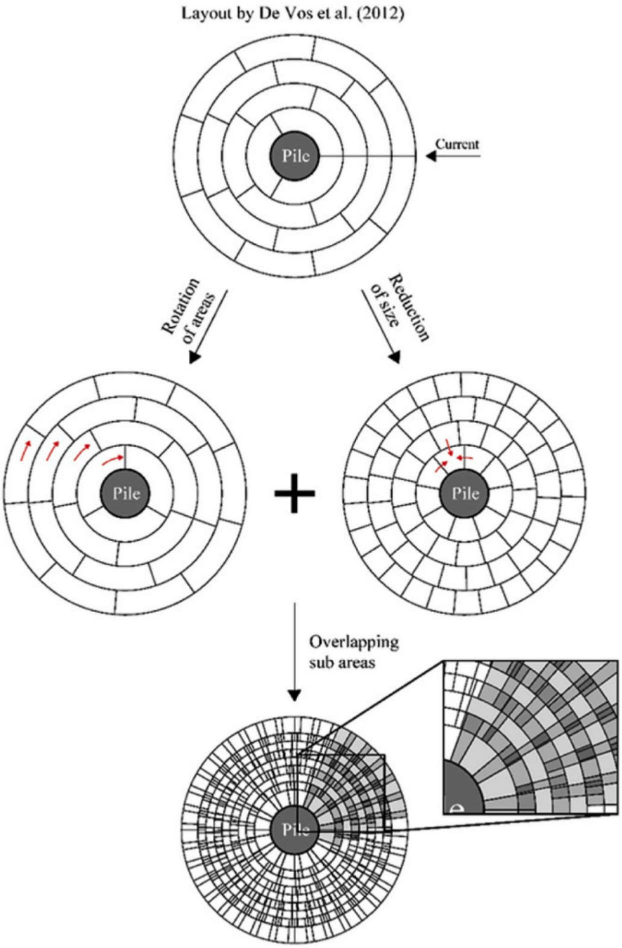

Figure 3.6: Overlapping subarea division of monopile scour protection layer, after Fazeres-Ferradosa et al. (2020).

many validations and it is not able to be used in the determination of D_{50} yet, mainly due to its novelty. However, it is promising to be applied in the future foundation scour protection design as it is suitable for complex foundations such as jacket or tripod.

3.2.5 van Rijn method

For large rocks used for bed protection or monopile scour protection, van Rijn (2019) proposes a method to determine D_{50}. As introduced in Figure 2.13, the frequency of particle movement will lead to a modified Shields parameter. If the particle movement frequency is low, this Shields parameter, $\theta_{cr,modified}$, is usually smaller than the θ_{cr} value observed by Shields (1936). In this case, $\theta_{cr,modified}$ can be written by Eq. 3.21.

$$\theta_{cr,modified} = r_{cr}\theta_{cr} \tag{3.21}$$

r_{cr} is the reduction coefficient of critical Shields parameter, which means how much the critical Shields parameter is reduced when considering the frequency of particle movement as shown in Figure 2.13. If occasional particle movements at some locations happen, about 0.1% of surface is moving, then $r_{cr} = 0.4$, indicating smaller bed load will initiate the incipience of motion. The r_{cr} value ranges from 0.4 to 1.0. For static or dynamically stable scour protection, $r_{cr} =$ 0.5, indicating the stone movement occurs in less than 1% surface area. The critical Shields parameter for large rocks can be regarded as a constant as it is Reynolds independent. van Rijn (2019) suggests to use $\theta_{cr} = 0.05$.

In the case of a sloping bed, the modified critical Shields parameter is defined by Eq. (3.22),

$$\theta_{cr,modified} = K_{\alpha_1}K_{\alpha_2}r_{cr}\theta_{cr} \tag{3.22}$$

where $K_{\alpha 1}$ is the longitudinal slope factor, $K_{\alpha 1} = 1$ stands for a horizontal bed. $K_{\alpha 2}$ is the lateral slope factor. $K_{\alpha 2} = 1$ for a horizontal bed. Please refer to van Rijn (2019) for the calculations of these two parameters in a slope bed condition.

Different from the DATA2 method by Soulsby (1995) introduced previously in Eq. (2.37), van Rijn (2019) proposes to calculate the combined wave and current bed shear stress (τ_b) using a linear superposition approach as shown in Eq. (3.23),

$$\tau_b = \tau_c + \tau_w \tag{3.23}$$

where,

$$\tau_c = 0.125\rho f_c(\gamma_{str}U_c)^2 \tag{3.24}$$

$$\tau_w = 0.25\rho f_w(\gamma_{str}U_w)^2 \tag{3.25}$$

U_c is the mean depth velocity in SI unit, U_w is the bottom peak wave orbital velocity in SI unit. With the given water depth d, wave peak wave period (T_p), significant wave height (H_s) and significant wave length (marked as L_s), U_w can be calculated by Eq. (3.26),

$$U_w = \frac{\pi H_s}{T_p \sinh\left(\frac{2\pi d}{L_s}\right)} \tag{3.26}$$

ρ is the density of fluid. f_c and f_w are the friction coefficients due to current and waves respectively. In van Rijn (2019) two approximate expressions are applied (Eqs. 3.27 and 3.28).

$$f_c \approx 0.11\left(\frac{d}{k_s}\right)^{-0.3} \tag{3.27}$$

$$f_w \approx 0.1 \left(\frac{A_w}{k_s} \right)^{-0.3} \tag{3.28}$$

A_w is the near-bed peak wave orbital amplitude, $A_w = (0.5T_p/\pi)U_w$ where T_p is the wave peak period. k_s is the bed roughness, which can be expressed as $k_s = \alpha_{k_s} D_{50}$. α_{k_s} is the bed roughness factor, α_{k_s} = 1.5 to 2 as suggested by van Rijn (2019).

γ_{str} is a current enhancement coefficient which can reflect the maximum flow velocity considering the turbulent velocity fluctuation. It is calculated on the basis of the standard deviation of flow velocity ($\sigma(U_c)$) and a factor n_c as Eq. (3.29).

$$\gamma_{str} = \frac{U_c + n_c \sigma(U_c)}{U_c} \tag{3.29}$$

Assuming the velocity magnitude over time follows a normal distribution, n_c = 2 to 3 indicates that the probability an instantaneous flow velocity magnitude smaller than $U_c + n_c \sigma(Uc)$ is approximately 97.5% to 99%. In a fully turbulent condition, $\sigma(U_c) = 0.2U_c$ to $0.3U_c$. Therefore, γ_{str} = 1 to 2.

Combining Eq. (3.21) and Eq. (3.23), we have a relationship between the stone size, the bed shear stress and the critical Shields parameter,

$$\frac{\tau_b}{\rho g (s-1) D_{50}} = r_{cr} \theta_{cr} \tag{3.30}$$

where s is relative density, $s = \rho_s/\rho$. Hence, the stone size is expressed by Eq. (3.31),

$$D_{50} = \frac{\tau_w + \tau_c}{\rho (s-1) g r_{cr} \theta_{cr}} \tag{3.31}$$

Inserting Eq. (3.27), Eq. (3.28), $A_w = (0.5T_p/\pi)U_w$ and $k_s = \alpha_{k_s} D_{50}$ into Eq. (3.31), the required stone size can be derived (Eq. 3.32).

$$D_{50} = \frac{\left[0.013 \left(\frac{d}{\alpha_{k_s}} \right)^{-0.3} (\gamma_{str} U_c)^2 + 0.045 \left(\frac{T_p}{\alpha_{k_s}} \right)^{-0.3} (\gamma_{str} U_w)^{1.7} \right]^{1.4}}{\left[(s-1) g r_{cr} \theta_{cr} \right]^{1.4}} \tag{3.32}$$

Adding a safety factor (marked as γ_s) to the design, the required D_{50} is obtained by Eq. (3.33).

$$D_{50} = \gamma_s \frac{\left[0.013 \left(\frac{d}{\alpha_{k_s}} \right)^{-0.3} (\gamma_{str} U_c)^2 + 0.045 \left(\frac{T_p}{\alpha_{k_s}} \right)^{-0.3} (\gamma_{str} U_w)^{1.7} \right]^{1.4}}{\left[(s-1) g r_{cr} \theta_{cr} \right]^{1.4}} \tag{3.33}$$

This method is verified using the dynamically stable monopile scour protection test data of De Vos et al. (2012). The reduction coefficient of critical Shields parameter is selected as r_{cr} = 0.5. In the design, it is found that for monopile scour protections, γ_{str} ranges between 1.1 to 1.6 and the best value is 1.4. The method is explicit and can be flexibly used in estimating the armour stone size of monopile scour protection. But as the method is new, there lack some experiences of how to select suitable r_{cr} and γ_{str} with the respect to different wave and current conditions.

3.2.6 Probabilistic design method

Based on the static and dynamic design method introduced in Section 3.2.3, a probabilistic design approach is raised by Fazeres-Ferradosa et al. (2018b). The approach regards the static and dynamic failure of scour protection layer as the limit state functions as Eq. (3.34) and Eq. (3.35)

$$f(\tau_{cr};\tau_w;\tau_c) = \tau_{cr} - \tau_{max} \tag{3.34}$$

$$f(U_m;U_c;T_{m-1,0};D_{50};\rho_s;\rho;d;g;w_s) = 1 - S_{3D,pred} \tag{3.35}$$

Considering the joint distribution of wave height, wave period and current conditions, the Monte-Carlo method can be applied to estimate the probability of failure, P_f, expressed in Eq. eq3.21,

$$P_f = \frac{(\#f(X_i) < 0)}{n} = \frac{\Sigma_1^n I(f(X_i))}{n} \tag{3.36}$$

where $I(f(X_i)) = 1$ when $f(X_i) < 0$. This approach gives a reliability based estimation of D_{50} considering the failure in long term operation.

3.3 Approaches for filter layer design

The monopile scour protection system typically includes a filter layer, which selects either a geotextile fabric or a granular layer compatible with the sediment beneath. The application of filter layer can significantly mitigate the suction process of subsoil and alleviate the sinking of armour stones. Sumer and Nielsen (2013) state that a filter layer thickness equivalent to the fifth of the pile diameter, $t_f = 0.2D_P$ helps to limit the maximum sinking depth to 0.2 times armour stone size (D_{50}). The design considerations and approaches are briefly introduced in this section.

Lagasse et al. (2006) give a few considerations for geotextile selection, such as permeability, pore size, porosity, percent open area, thickness, grab strength and elongation, tear strength and puncture strength. Generally, the geotextile should have a much higher water permeability than the underlying material and enough strength to resist the long-term loads from flow and cover stones. Please refer to CIRIA (2007) for a more detailed geotextile design requirements and guidelines.

The granular filter layer can be categorised into two types: geometrically closed filter (or geometrically tight filter) and geometerically open filter. The geometrically closed filter is designed such that the openings in the filter layer are small enough to prevent transport of the underlying sediment. The geometrically open filter layer allows larger openings in the filter layer but the hydraulic loads are too small to initiate the movement of the underlying sediment.

The design criteria for geometrically closed filter are introduced in CIRIA (2007), Verheij et al. (2012), and Kirby et al. (2015). One well-known design criterion is provided by Terzaghi and Peck (1948), as Eq. (3.37), where d_{f15} is the particle diameter of the filter layer with 15% passing rate and d_{b85} is the sediment diameter with 85% passing rate.

$$\frac{d_{f15}}{d_{b85}} < 4 \tag{3.37}$$

The geometrically open filter provides possibility to reduce the installation cost, but is not widely investigated in monopile scour protection. Early design formula for a stable geometrically open filter is provided by Wörman (1989) as Eq. (3.38),

$$\frac{t_f}{d_{f15}} = 0.16\frac{n_f}{n_f - 1} \cdot \frac{d_{f85}}{d_{b85}} \cdot \frac{\rho_f/\rho - 1}{\rho_b/\rho - 1} \tag{3.38}$$

where t_f is the thickness of the filter layer, n_f is the porosity of filter layer. ρ_f and ρ_b are the densities of the filter material and base material respectively.

CIRIA (2007) recommends a simplified equation from Bakker et al. (1994) to describe the relationship among the material sizes of top layer, filter layer and base in a geometrically open filter, see Eq. (3.39).

$$\frac{d_{f15}}{d_{b50}} = \frac{15.3R}{C_0 D_{t50}} \tag{3.39}$$

The hydraulic radius R can be assumed equal to the water depth, d_{f15} is the sieve size of 15% pass rate for filter layer, d_{b50} is the median size of base material and D_{t50} is the median size of top layer material. The coefficient C_0 can be conservatively set to 30.

The application of geometrically open filter attracts more recent discussions on the possibility of using a single-layer wide graded material in monopile scour protection, such as Schendel et al. (2016) and Petersen et al. (2018). With such design the grading coefficient D_{85}/D_{15} can be 3 to 6 compared with the traditional armour stone grading of 1.5 to 2.5. The concept of using single-layer wide graded material is embraced by the industry as it significantly reduce the installation cost, according to a report from DHI (2019). More investigations and applications of such type of scour protection are foreseen in the future for offshore monopiles.

3.4 Edge scour

Due to the presence of a scour protection around a monopile, edge scour holes will develop as a result of the horseshoe vortex and the wake vortices around the scour protection layer under waves and current. As shown in Figure 3.7, the edge scour occurs at two sides of the scour protection and in the wake area downstream. The maximum depth of the edge scour holes at two sides is S_{e1}. The depth and the extension length of the edge scour hole in the wake area are S_{e2} and L_e, respectively. The armour layer thickness of the scour protection is t_a and the extension width is W_a.

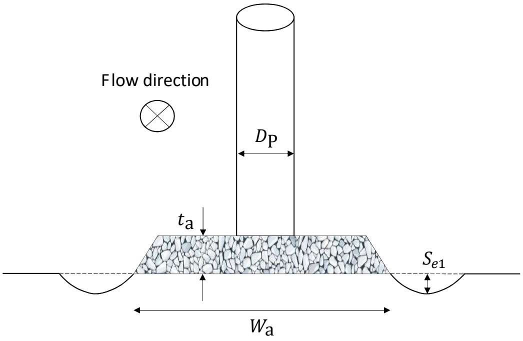

(a) Edge scour at two sides of the pile

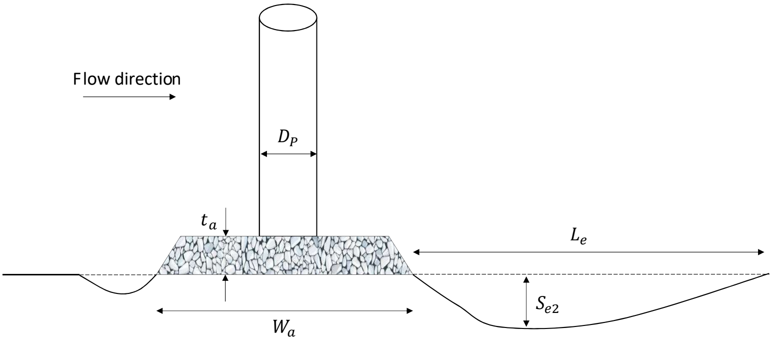

(b) Edge scour at wake area of the pile

Figure 3.7: Sketch of edge scour around a monopile scour protection layer, after Petersen et al. (2015).

The dimensions of the equilibrium S_{e1}, S_{e2} and L_e are depending on the pile size and the parameters of the scour protection according to the investigation from Petersen et al. (2015), as described in Eq. (3.40) to Eq. (3.42). Here, D_{50} is the median stone diameter of the armour layer, θ is the Shields parameter of the sediment outside the scour protection area.

$$\frac{S_{e1}}{t_a} = f(\theta, \frac{W_a}{D_P}, \frac{t_a}{W_a}, \frac{t_a}{D_{50}}) \tag{3.40}$$

$$\frac{S_{e2}}{D_P} = f(\theta, \frac{t_a}{W_a}) \tag{3.41}$$

$$\frac{L_e}{D_P} = f(\theta, \frac{t_a}{W_a}) \tag{3.42}$$

Figure 3.8 plots the magnitude of S_{e1}/t_a with respect to θ and W_a/D_P after Petersen et al. (2015). The test results were obtained from the steady current test. The results show that the edge scour depth S_{e1} increases as the bed load θ increases. Using a wider armour layer extension W_a reduces the size of S_{e1} as it lowers the flow acceleration and deviation at the two sides of the scour protection. Figure 3.9 plots the edge scour depth in the wake area, S_{e2}/D_P, with respect to θ and t_a/W_a (Petersen et al., 2015). The results show that increasing the thickness of the armour layer will lead to a higher S_{e2}. Compared to the pile-only condition, using a thick armour layer means the flow is more disturbed and blocked by the scour protection. This leads to a stronger flow acceleration and deviation in the wake area downstream. In addition, from Figure 3.9, the increased armour layer thickness will lead to a longer edge scour hole extension.

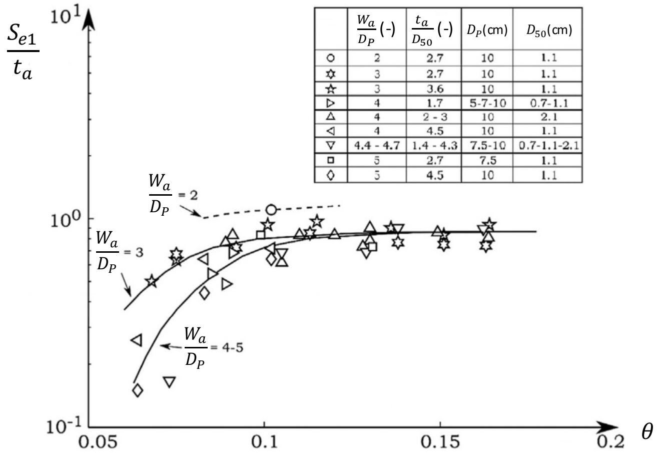

	$\frac{W_a}{D_P}$ (-)	$\frac{t_a}{D_{50}}$ (-)	D_P(cm)	D_{50}(cm)
○	2	2.7	10	1.1
✡	3	2.7	10	1.1
☆	3	3.6	10	1.1
▷	4	1.7	5-7-10	0.7-1.1
△	4	2 - 3	10	2.1
◁	4	4.5	10	1.1
▽	4.4 - 4.7	1.4 - 4.3	7.5-10	0.7-1.1-2.1
□	5	2.7	7.5	1.1
◇	5	4.5	10	1.1

Figure 3.8: Equilibrium edge scour depth S_{e1} in steady current and live-bed conditions, Petersen et al. (2015).

Vandepitte (1979) and De Vos (2008) stated that the occurrence of edge scour can induce a loss of the lateral bearing capacity of the pile. According to the review of De Vos (2008), the value of W_a is suggested to be at least $5D_P$. Petersen et al. (2015) confirmed that W_a should be sufficiently large to reduce the size of the edge scour holes. Breusers and Raudkivi (1991) even suggested to use $W_a = 9D_P$. But this may lead to a significant raise of installation cost. Meanwhile, increasing the armour layer thickness t_a/W_a is beneficial for the stability of a scour protection

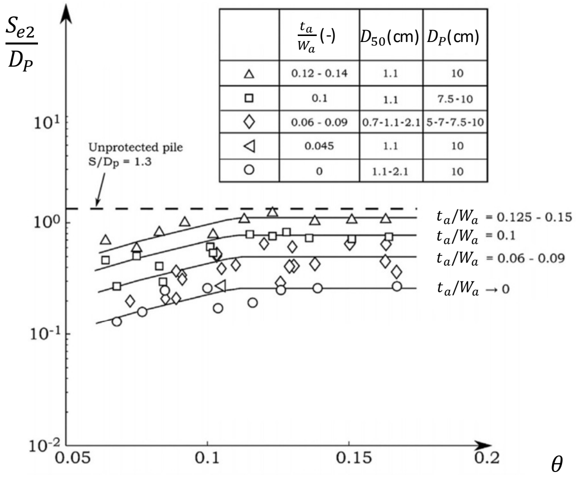

Figure 3.9: Equilibrium edge scour depth S_{e2} in steady current and live-bed conditions, Petersen et al. (2015).

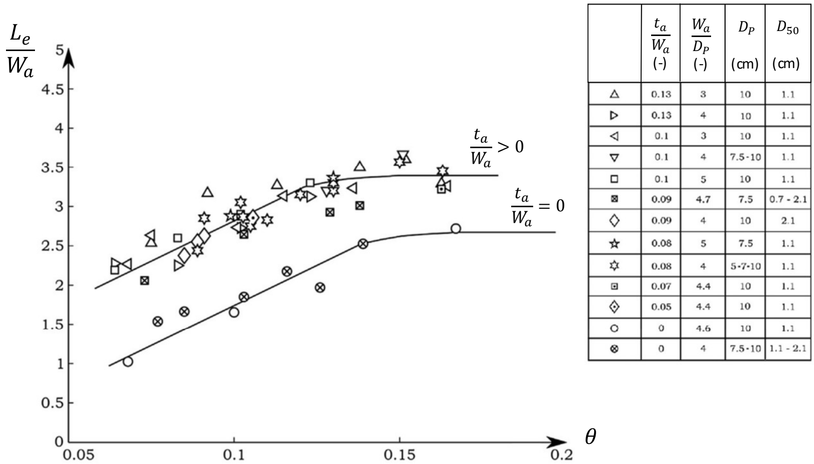

Figure 3.10: Equilibrium edge scour extension length L_e in steady current and live-bed conditions, Petersen et al. (2015).

against erosion failure, but will also lead to a larger edge scour hole size. This means that several engineering trade-offs have to be considered during the design phase when taking account the edge scour.

To mitigate the edge scour, Petersen et al. (2015) suggest to use a wider filter layer extension W_b (as shown in Figure 3.1). With a filter layer extending $2D_P$ further from the edge of the scour protection, the edge scour depth is decreased to $S_{e2} = 0.1D_P$. Esteban et al. (2019b) provided a study of the scour protection parameters of five existing wind farms, where the armour layer extension is 4 to 6 m wider than the filter layer extension.

3.5 Conclusions

This chapter briefly reviews the state-of-the-art regarding the scour protection around pile, including the failure modes, the design methods for armour layer, the design considerations for filter layer and the edge scour problem. Studies of bridge piles and offshore monopiles reveal the failure modes of a rip-rap scour protection around pile, which are (1) shear (erosion) failure, (2) winnowing (sinking) failure (3) edge failure and (4) destabilisation due to large bed form deformation. Besides the failure mode (4), the other failure modes are observed and investigated in field surveys and laboratory tests of offshore monopile foundation scour protection in wave and current conditions.

For the erosion failure mode, the determination of armour stone sizes is mainly based on whether the monopile scour protection is statically stable or dynamically stable. The static stability design method would result in a relatively larger armour stone size and the dynamic stability design method can significantly reduce the designed armour stone size. Several design methods are introduced in this chapter, for example, the Isbash formula, the critical state formula by Soulsby (1997) and the three-dimensional damage number formula by De Vos et al. (2012). A recent study from Esteban et al. (2019b) has compared the listed three methods with some existing wind farm data, however, the conclusion shows that it is yet not clear which formula performs better in real design. Therefore, more studies are required to better understand the pros and cons of the existing design methods and their suitable scenarios.

It is as well noticed that most of the experimental studies of monopile scour protection are carried out using small scale models, as listed in Table 3.1. Knowing the scale effects of model tests is extremely necessary for predicting the scour protection performance of monopile prototype. But there is very little discussion about the scale effects, mainly because a prototype test is very costly. Using large scale models becomes a more approachable way to understand the key parameters that cause the scale effects.

In Chapter 5, a series of large scale monopile scour protection experiment is introduced. Using this experiment, the applicability of existing design methods is discussed. Moreover, for the readers' interest, the scale effects in monopile scour protection experiments are introduced in Chapter 8.

Table 3.1: An overview of model sizes in recent experimental works

Sources	Model pile diameter [m]	Prototype pile diameter [m]	Scale ratio
Chiew and Lim (2000)	0.025 to 0.07		
Lauchlan and Melville (2001)	0.07 to 0.2		
Den Boon et al. (2004)	0.089	4.2	1:47.25
Nielsen et al. (2010)	0.075 to 0.2	4.2	
De Vos et al. (2011, 2012)	0.1	5.0	1:50
Looseveldt and Vannieuwenhuyse (2012)	0.05 to 0.125		
De Schoesitter et al. (2014)	0.1	5.0	1:50
Whitehouse et al. (2014)	0.1	5.0	1:50
Schendel et al. (2014)	1.0	4.0	1:4
Nielsen et al. (2015)	0.05 to 0.2		
Riezebos et al. (2016)	0.2		
Nielsen and Petersen (2018)	0.05		
Nielsen and Petersen (2019)	0.04 to 0.2		

Chapter 4

Experimental uncertainties in monopile scour protection experiments

4.1 Measurement, model and scale effects

Laboratory scale hydraulic experiments provide essential details of the physical processes and are applied to data prediction and design for prototype hydraulic structures. However, the accuracy of reproducing test conditions in laboratory experiment can cause significant differences between scale model and prototype.

For monopile scour protection, most of the experimental studies are done with small scale models, the associated issues of experimental uncertainties related to scale effects may significantly limit the application of small scale dataset in full scale model prediction. The reason has been pointed out by Ettema et al. (1996) and Mayall et al. (2020) that a similitude for flow field, sediment transport and fluid-structure dynamics cannot be satisfied at the same time. Though some hydraulic tests are accomplished in large scale wave flumes (Schendel et al., 2016; Arboleda Chavez et al., 2019), there remains a scarcity of quantitative analysis of the experimental uncertainty and the scale effects as well as the uncertainty in prototype design (Negro et al., 2013).

Kortenhaus et al. (2005) attribute the sources of such differences into measurement effects, model effects and scale effects, see Figure 4.1. These effects constitute the experimental uncertainties in a model test in ocean engineering (Qiu et al., 2014), which are essential for evaluating the quality of experimental results (Wahlin et al., 2005). A brief description of the measurement, model and scale effects in monopile scour protection test is listed below.

- Measurement effects
  The measurement effects are caused by the different configurations of the measurement system, which refer to error or inaccuracy of the measurement

system due to the resolution of data sampling, the location of probes and the quality of measurement. In monopile scour protection tests, the measurement effects are mainly caused by the accuracy of wave gauges, velocity meters, distance sensors, bed profile scanner or pressure gauges. Despite the accuracy information provided in the specification of the instrument, the measurement effects can be caused by calibration, human manipulation and environment condition variation, such as light, humidity, temperature, etc. It is sometimes necessary to use a statistic analysis method and repeated measurements to check the applicability and the uncertainty level of using such instruments (Kortenhaus et al., 2005). According to De Vos (2008) and Debaveye and De Riemacker (2020), the set-up of the bed profiler is considered to be the major source of inaccuracy that contributes to the measurement effects in monopile scour protection experiments.

- Model effects
  The model effects originate from the incorrect reproduction of the prototype situation in the laboratory facility. They are significantly associated with the reliability of the experimental results based on a single test. In experiments for modelling monopile scour protections, the model effects are mainly caused by wave and current generation, armour layer construction, sediment and pile construction. When the experiments are carried out in different wave flumes, model effects may also be introduced by different flume side walls, wave paddles and wave absorption systems. In comparison to the scale effects, the model effects often have less impact, but can sometimes be considerably high, especially when there is observed non-repeatability of the experimental conditions. For example, (1) due to the presence of turbulence and interactions between waves and currents, the instantaneous pressure and velocity distributions around the pile are different; (2) the impossibility of building an identical armour layer makes the results of one test deviating from the results from a repeated test. Kortenhaus et al. (2005) suggest to apply repeated tests, such as re-constructing the armour layer several times, to obtain the model effects in small scale tests.

- Scale effects
  The scale effects are induced by the incorrect reproduction of prototype fluid-particle-structure interactions in the scale model. The factors that lead to potential scale effects in monopile scour protection experiment include: model geometry, actions of wave and current, armour stone configuration and sediment. Unique scaling rules are applied to each factor to obtain the maximum similarities between prototype and scale model, however, a full similarity is impossible to achieve due to the fact that the similarities for flow field, sediment and fluid-particle-structure dynamics cannot be satisfied at the same time (Hughes, 1993; Ettema et al., 1996; Heller, 2011; Mayall et al., 2020).

A systematic approach to quantify scale effects in hydraulic model test is described in Figure 4.2 by Kortenhaus et al. (2005). The procedure explicitly provides a fundamental sequence for experimental data analysis that reliable model effects can be quantified only after the measurement accuracy is certain and the scale effects can only be determined after the model effects are quantified. Two or more different facilities and scale models are needed for separating scale effects from other effects.

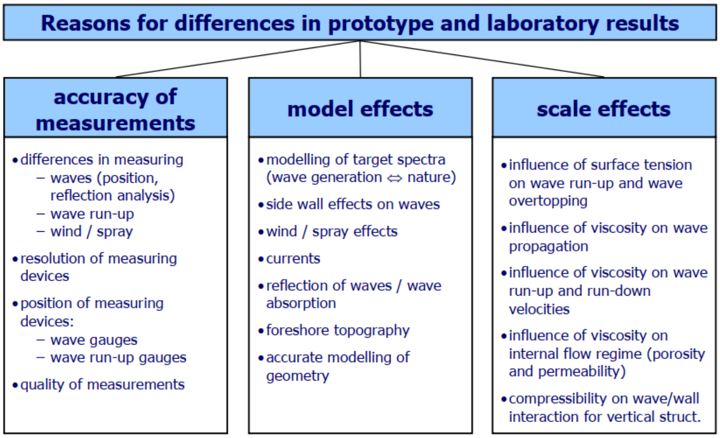

Figure 4.1: Overview of possible reasons for differences in prototype and laboratory results, from Kortenhaus et al. (2005).

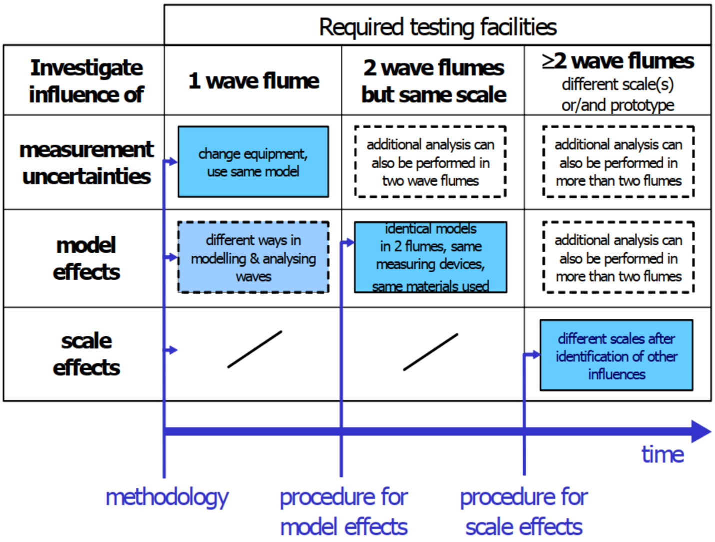

	Required testing facilities		
Investigate influence of	**1 wave flume**	**2 wave flumes but same scale**	**≥2 wave flumes** different scale(s) or/and prototype
measurement uncertainties	change equipment, use same model	additional analysis can also be performed in two wave flumes	additional analysis can also be performed in more than two flumes
model effects	different ways in modelling & analysing waves	identical models in 2 flumes, same measuring devices, same materials used	additional analysis can also be performed in more than two flumes
scale effects	/	/	different scales after identification of other influences

Figure 4.2: Systematic approach to quantify scale effects, from Kortenhaus et al. (2005).

4.2 Analysis of experimental uncertainties in measurement

Each measurement in an experiment comes along with errors due to imperfections of the measurement, which contains two components, a systematic error and a random error. The concepts of these errors are defined based on assumed infinite repeated measurements of a measurand. The systematic error refers to the deviation between the mean result of repeated measurements and the true value. The random error refers to the deviation between the mean result of repeated measurements and each random measurement. The random and systematic errors contribute to an uncertainty in measurement, which reflects the lack of knowledge of the exact value in the experiment.

The Joint Committee for Guides in Metrology (JCGM) publishes a Guidance for Uncertainties in Measurement (GUM) (JCGM, 2008) and provides a formal analysis procedure of the experimental uncertainties in measurement. According to this guide, the uncertainties due to measurement can be categorised into standard uncertainty, combined standard uncertainty and expanded uncertainty. The definitions are explained as below.

(1) Standard uncertainty
The standard uncertainty refers to an uncertainty of the measurement which is expressed as a standard deviation.

(2) Combined standard uncertainty
When the result is obtained from the values of a number of other quantities, the combined standard uncertainty is the square root of a sum of each weighted variances. It also takes the correlations between the quantities into account.

(3) Expanded uncertainty
The expanded uncertainty is an interval about the result of a measurement which is expected to cover a large fraction of the distribution of values.

The standard uncertainty may be evaluated by two ways: Type A evaluation and Type B evaluation. The Type A evaluation of uncertainty refers to an uncertainty result which is obtained by the statistical analysis of series repeated observations. The Type B evaluation of uncertainty refers to an uncertainty result which is obtained with the methods other than a direct statistical analysis. The Type B evaluation of uncertainty is often used when repeated observations are not approachable where knowledge of the distribution of measured data is necessary. A short description of the methodologies used for evaluating each uncertainty component is given in following text. The detailed definitions and procedures for the experimental uncertainty analysis can be referred to JCGM (2008).

4.2.1 Type A uncertainty

Assuming a measured quantity, q, is obtained through n times repetition of independent measurements under the same conditions, the arithmetic mean is defined as Eq. (4.1).

$$\bar{q} = \frac{1}{n}\sum_{a=1}^{n} q_a \tag{4.1}$$

q_a differs in each observation due to the random effects and complies to a probability distribution, the variance of which is expressed as,

$$\sigma^2(q_a) = \frac{1}{n-1}\sum_{a=1}^{n}(q_a - \bar{q})^2 \tag{4.2}$$

The positive square root of $\sigma^2(q_a)$ is the experimental standard deviation, which describes the dispersion about the mean value $\bar{q}$. The variance of the mean is given by,

$$\sigma^2(\bar{q}) = \frac{\sigma^2(q_a)}{n} \tag{4.3}$$

The positive square root of $\sigma^2(\bar{q})$ equals to $\sigma(\bar{q})$ and is defined as the experimental standard deviation of the mean. The Type A standard uncertainty, marked as $u_A(q)$, can be obtained by Eq. 4.4.

$$u_A(q) = \sigma(\bar{q}) \tag{4.4}$$

It should be noted, the more times of repeated measurements, the more reliable the Type A uncertainty is. If the distribution of q is normal, the uncertainty of the uncertain (marked as $u[u_A(q)]$) relative to the obtained uncertainty $(u_A(q))$, written as $u[u_A(q)]/u_A(q)$, is approximately $[2(n-1)]^{-1/2}$. When $n = 10$, this relative uncertainty of uncertainty can be up to 24%.

4.2.2 Type B uncertainty

The Type B uncertainty is obtained from available information other than repeated observations. The information can be either previous measurement data, user experience, manufacturer's specification, etc. On the basis of an instrumental specification, according to JCGM (2008), the evaluation of Type B uncertainty should be based on an error range expression. Take a measured quantity q as example, an expression of its mid value and error range is $Q \pm \epsilon_q$. If $\pm\epsilon_q$ stands for a coverage of 99% confidence interval of a normally distributed q, the Type B uncertainty of q is given by Eq. (4.5), where $k_p = 2.58$.

$$u_B(q) = \frac{\epsilon_q}{k_p} \tag{4.5}$$

If $\pm\epsilon_q$ covers a 95% confidence interval, $k_p = 1.96$.

If the measured value q averagely lies in the range of $-\epsilon_q$ and $+\epsilon_q$, the Type B standard uncertainty can be expressed as

$$u_B(q) = \epsilon_q/\sqrt{3} \tag{4.6}$$

4.2.3 Combined standard uncertainty

For a quantity Q which is not measured directly, but is determined from K other quantities (q_1, q_2 ..q_K)as Eq. (4.7),

$$Q = f(q_1, q_2, ..., q_K) \tag{4.7}$$

if these quantities are uncorrelated, the combined variance can be calculated according to the law of propagation by Eq. (4.8).

$$u_C^2(Q) = \sum_{i=1}^{K} \left(\frac{\partial f}{\partial q_i}\right)^2 u^2(q_i) \tag{4.8}$$

$u_C(Q)$ is the combined standard uncertainty, which is the positive square root of $u_C^2(Q)$. $u(q_i)$ is the standard uncertainty of each measured quantities q_i.

If the measured quantities are correlated, the expression of combined uncertainty has to consider the correlation,

$$u_C^2(Q) = \sum_{i=1}^{K} \left(\frac{\partial f}{\partial q_i}\right)^2 u^2(q_i) + 2\sum_{i=1}^{K-1}\sum_{j=i+1}^{K} \frac{\partial f}{\partial q_i}\frac{\partial f}{\partial q_j} u(q_i, q_j) \tag{4.9}$$

where $u(q_i, q_j) = r_c(q_i, q_j)u(q_i)u(q_j)$. r_c is the correlation coefficient, obtained from Eq. (4.10),

$$r_c(q_i, q_j) = \frac{\sigma(q_i, q_j)}{\sigma(q_i)\sigma(q_j)} \tag{4.10}$$

$\sigma(q_i, q_j)$ defines the covariance of q_i and q_j and $\sigma(q_i), \sigma(q_j)$ are separately the standard deviations.

The partial derivative $\partial f/\partial q_i$ is called sensitivity coefficient. As the analytical form of the partial derivative can be complex, it can also be computed numerically as Eq. (4.11).

$$\frac{\partial f}{\partial q_i} = \frac{1}{2u(q_i)}\{f\left[q_1, q_2, ...q_i + u(q_i), ...q_K\right] - f\left[q_1, q_2, ...q_i - u(q_i), ...q_K\right]\} \tag{4.11}$$

4.2.4 Expanded uncertainty

An expanded uncertainty u_E is obtained by multiplying combined uncertainty with a coverage factor, k_p, as Eq. (4.12).

$$u_E(Q) = k_p u_C(Q) \tag{4.12}$$

With the expanded uncertainty, the measured value Q_{meas} should be bounded between $Q - U_E(Q) \leq Q_{meas} \leq Q + U_E(Q)$. If Q follows a normal distribution, the value of k_p describes the confidence interval of the measured Q, which has a similar meaning to k_p in Eq. 4.5. $k_p = 1.96$ means a coverage of 95% confidence interval of measured Q and $k_p = 2.58$ gives a coverage of 99% confidence interval. If Q follows a rectangular distribution, $k_p =$ 1.94 and 2.38 for a coverage of 95% and 99% confidence interval respectively.

If n times repeated measurements are performed, a t-distribution is derived for $(Q - Q_{meas})/u_C(Q)$. This gives a bounded measured value of $Q - k(\nu)u_C(Q) \leq Q_{meas} \leq Q + k(\nu)u_C(Q)$, where $k(\nu)$ is the coverage factor taking account the degree of freedom ν, $\nu = n - 1$. When $u_C(Q)$ is obtained via K measured quantities q_i as Eq. (4.8), the effective degree of freedom ν_{eff} is achieved from Eq. (4.13),

$$\nu_{eff} = \frac{\sum_{i=1}^{K} \left(\frac{\partial f}{\partial q_i}\right)^4 u^4(q_i)}{\sum_{i=1}^{K} \frac{\left(\frac{\partial f}{\partial q_i}\right)^4 u^4(q_i)}{\nu_i}} \tag{4.13}$$

$\nu_i = n_i - 1$ for $u(q_i)$ obtained from Type A evaluation, and can be calculated through Eq. (4.14) when $u(q_i)$ is obtained from Type B evaluation,

$$\nu_i = \frac{1}{2}\left[\frac{\delta u(q_i)}{u(q_i)}\right]^{-2} \tag{4.14}$$

where $\delta u(q_i)/u(q_i)$ is a relative uncertainty based on experience. The value of the coverage factor $k(\nu_{eff})$ can be looked up in JCGM (2008), it reduces as the number of observation n increases, meaning the expanded uncertainty level reduces. $k(\nu_{eff})$ approaches to k_p for a normal distribution of the measured quantity when $n \to \infty$. And the extended uncertainty is finally estimated by Eq. (4.15)

$$u_E(Q) = k(\nu_{eff})u_C(Q) \tag{4.15}$$

4.3 Scaling rules applied in monopile scour protection tests

The hydraulic modelling of monopile scour protection is a typical "movable-bed model" according to the definition of Hughes (1993). Due to the complexity of the physical processes, it is crucial to apply the appropriate scaling rules to the model tests. This requires a clear analysis of the dominant forces that are acting on each governing factor of the monopile scour protection model. Though the scale effects are usually not cancellable for scale model test, proper scaling rules are needed as significantly high scale effects will eventually make the physical modelling invalid and wasted if incorrect scale test conditions are used. This section briefly introduces the applied scaling rules for the monopile scour protection model.

4.3.1 Geometry

In most of the cases, geometrical similarity should be satisfied, meaning the model size ratio between scale and prototype model in both vertical and horizontal directions are the same. This reads the scale factor, λ, as Eq. (4.16),

$$\lambda = \frac{L_{X,m}}{L_{X,p}} = \frac{L_{Y,m}}{L_{Y,p}} = \frac{L_{Z,m}}{L_{Z,p}} \tag{4.16}$$

where L_X, L_Y and L_Z are the characteristic sizes of the model in three directions. Subscriptions m and p represent values for scale model and prototype, respectively. Applying this uniform scale ratio, the pile diameter and the extension and thickness of the scour protection layer in scaled model can be determined. Sometimes the geometrically distorted model is also applied in hydraulic tests under the specific conditions that (1) facility limitation; (2) vertical flow velocity or acceleration are much smaller than horizontal ones. This gives scale factors different in three dimensions, but is not appropriate in monopile scour protection tests. In addition, the surface roughness of the geometry (k_s) is important when it significantly affects the flow regime around the structure. For example, k_s in scale model should be large enough to stimulate a turbulent flow field similar to that in prototype.

4.3.2 Wave

The scaling rules of modelling waves acting on structures are introduced in Hughes (1993) and Kortenhaus et al. (2005). Different scaling rules are used for specific scenarios, for example, Froude number similarity (F_r) is essential in modelling the wave induced pressure distribution, Weber (W_e), Cauchy (C_a) and Reynolds (R_e) numbers are required to be similar for wave breaking and impact on structure, Reynolds and Weber numbers are suggested to be similar in wave run-up modelling, and Reynolds scaling is needed for bottom friction scenario. The Froude similarity is mostly applied to correctly model the wave pressure field (Heller, 2011), which reads as Eq. (4.17),

$$\left[\frac{U}{\sqrt{gL}}\right]_m = \left[\frac{U}{\sqrt{gL}}\right]_p \tag{4.17}$$

where U is the fluid velocity, g is the acceleration due to gravity, L is the characteristic length.

As stated in Hughes (1993) and Heller (2011), the adoption of the Froude similarity might bring conflicts with other similarities, such as Reynolds, Weber and Cauchy scaling, which leads to an incorrect modelling of forces due to viscosity, surface tension and elasticity in scale model. In addition, for modelling wave field around monopile, when the Froude similarity is applied, the Keulegan–Carpenter number (KC) similarity is usually automatically satisfied. KC is defined in Eq. (2.14) and can be written to $KC = 2\pi A/D_P$, where A is the wave amplitude and D_P is the diameter of pile.

4.3.3 Current

The current induced flow regime around a monopile is introduced in Sumer and Fredsøe (1997) (see Chapter 2). The boundary layer separation and the turbulence level in the flow field around the pile are dominated by the viscous hydrodynamic forces. This requires a similarity of R_e number between scale model and prototype, which is shown in as Eq. (4.18),

$$\left[\frac{UL}{\upsilon}\right]_m = \left[\frac{UL}{\upsilon}\right]_p \tag{4.18}$$

where U is the flow velocity, L is the characteristic length (usually the pile diameter) and υ is the kinematic viscosity.

When $R_e > 40$, the lee-wake vortex due to current becomes asymmetric and forms a shedding regime. The frequency of the vortex shedding f_v is often described with the Strouhal number S_t, $S_t = f_v L/U$. S_t is strongly dependent on the R_e number and the surface roughness of the pile, as described in Eq. (2.13) and Figure 2.4. Meanwhile, the horseshoe vortex structure due to current is also believed to be R_e dominated, as seen from Figure 2.7 (Baker, 1980; Sumer and Fredsøe, 2002).

Despite the R_e number, it is also discussed in Ettema et al. (1996) and Ettema et al. (2006) that the F_r number is important for the stagnation head, the flow pressure gradient as well as the vorticity of wake vortices.

Another commonly used scaling rule in scour test around a pile is to attain similar U/U_{cr} between prototype and scale models (Melville, 2008), where U_{cr} is a critical shear velocity of the sediment, which is governed by the R_e number of the sediment. This ratio describes the flow intensity and is important for obtaining similar dimensionless scour depth between scale model and prototype.

4.3.4 Armour stone

The mobility of an armour stone is mainly determined by the bottom shear stress (τ_b) induced by the near-bed flow. Given the sieve diameter of the armour stone D_s, the Shield parameter, θ, is written as Eq. (4.19),

$$\theta = \frac{\tau_b}{\rho\left(s-1\right)gD_s} \tag{4.19}$$

where ρ is the density of fluid, s is the relative density of the armour stone, $s = \rho_s/\rho$. As introduced, θ_{cr} is a function of the Reynolds number of armour stone, R_{e*}. $R_{e*} = u_* D_s/\upsilon$ and $u_* = \sqrt{\tau_b/\rho}$. When $\theta > \theta_{cr}$, the armour layer becomes movable. Then another scaling is suggested by Oumeraci (1994), which applies a similarity of the ratio between flow velocity U and particle settling velocity, w_s, in prototype and scaled model, see Eq. (4.20).

$$\left[\frac{U}{w_s}\right]_m = \left[\frac{U}{w_s}\right]_p \tag{4.20}$$

According to van Rijn (1984), the particle settling velocity can be calculated with Eqs. (4.21-4.23) depending on D_s.

$$w_s = \frac{1}{18}\frac{(s-1)gD_s^2}{\upsilon}, \quad \text{for } D_s \leq 0.1mm \tag{4.21}$$

$$w_s = 10\frac{\upsilon}{D_s}\left\{\left[1+\frac{0.01(s-1)gD_s^3}{\upsilon^2}\right]^{0.5}-1\right\}, \text{ for } 0.1mm < D_s \leq 1mm \tag{4.22}$$

$$w_s = 1.1\left[(s-1)gD_s\right]^{0.5}, \quad \text{for } D_s > 1mm \tag{4.23}$$

Oumeraci (1994) concludes that w_s should be modelled following a Froude scaling rule, therefore, $w_{s,m} = \sqrt{\lambda} \cdot w_{s,p}$, where λ is the scale ratio of sediment size between scale model and prototype. If the material density and the fluid viscosity are kept the same in both the scaled model and prototype, it can be derived from Eq. (4.20) that when $D_{s,p}$ and $D_{s,m}$ are larger than 1 mm, $D_{s,m} = \lambda \cdot D_{s,p}$, meaning the particles are scaled geometrically, and, when $D_{s,p}$ and $D_{s,m}$ are smaller than 0.1 mm, particles are scaled with a scaling relationship of $D_{s,m} = \lambda^{1/4} \cdot D_{s,p}$. For most of the scour protection armour stones, the prototype grain size is larger than 10 cm (Esteban et al., 2019b). This makes it reasonable to use geometrical scaling in a small scale test with a minimum scale ratio of 1:100.

Another important consideration of the armour material size is the porous flow inside the armour layer pores. The hydraulic gradient inside core materials can be written according to the Engelund equation (Eq. 4.24) (Engelund, 1953).

$$I = \alpha_0\frac{(1-n_f)^3}{n_f^2}\frac{\upsilon}{gD_s^2}U + \beta_0\frac{1-n_f}{n_f^3}\frac{U^2}{gD_s} \tag{4.24}$$

The first term depicts the laminar flow pressure gradient and the second term depicts the turbulent component, where α_0 and β_0 are constants dependent on the grain shape, $\alpha_0 \approx 780 - 1500$ and $\beta_0 \approx 1.8 - 3.6$. n_f is the porosity of the armour material and D_s is the grain size.

I is also proposed by Le Méhauté (1957) using Eq. (4.25),

$$I = 14\frac{1}{n_f^5}\frac{\upsilon}{gD_s^2}U + 0.1\frac{1}{n_f^5}\frac{U^2}{gD_s} \tag{4.25}$$

Due to the Froude scaling of the waves, the porous flow regime in small scale model can be a laminar or a mixing of laminar and turbulent flow, and may deviate from that in prototype, which is often turbulent. This may lead to a scale effect when considering the pressure variation or the sand removal process due to the dissimilarity of viscous forces. If the turbulent component is dominant, $D_{s,m} = D_{s,p}/\lambda$. For small prototype $R_{e,D}$ number situation, the laminar component is more important, it can be derived that $D_{s,m} = D_{s,p}/\lambda^{1/4}$ (Juul Jensen and Klinting, 1983). This leads to a much larger grain size than applying the particle settling velocity similarity.

The discussions over the scaling rule of armour size in monopile scour protection experiment considering the porous flow are rarely seen from literature, but are abundant for breakwater armour stability tests, for example in Dai and Kamel (1969), Thomsen et al. (1972), Burcharth et al. (1999), Burcharth and Lykke Andersen (2009) and Vanneste and Troch (2014).

4.3.5 Sediment

The scaling issues related to sediment transport and scour are thoroughly discussed in Sutherland and Whitehouse (1998). The main considerations are hydrodynamic loading acting on the bed, sediment size, morphological feature and bed response. These issues are crucial for monopile scour protection tests that focus on sand suction process (sinking failure), edge scour and sand ripples around a monopile scour protection. Firstly, the hydrodynamic loading acting on the bed is related to the bed roughness due to the size and shape of the sediments. This may introduce a smaller R_{e*} number and a laminar boundary layer in small scale tests that are different from a prototype condition. Secondly, the sediment size scaling can be determined by the settling velocity or the Shields parameter depending on the interested scenarios. For a problem considering the threshold of motion of sediment, for example, the scour near a pile in a clear water condition, the Shields parameter should be considered. For a sediment transport problem, the sediment size can be determined by the particle fall velocity as Eqs. (4.20-4.23). Thirdly, the morphological feature of sand depends on the sediment size scaling. For example, the size of ripples cannot be scaled geometrically in a small scale model if the sand size is not geometrically scaled down from prototype. Moreover, high scale effects related to bed response usually occur in lightweight sediment model.

4.3.6 Best Model scaling approach

Due to the difficulty of achieving a perfect similitude between scaled model and prototype in a hydraulic experiment, it is crucial to focus on the most important physical processes and maintain the key similarities between model and prototype. Considering the sediment transport problem, the dimensionless products in Eq. (4.26) are used, (Hughes, 1993; Kamphuis, 1996):

$$\Pi_S = f\left[\frac{u_* D_s}{\upsilon}, \frac{\rho {u_*}^2}{\gamma_i D_s}, \frac{\rho_s}{\rho}, \frac{L}{D_s}, \frac{w_s}{u_*}\right] = f\left[R_{e*}, M_*, \rho_*, G_*, W_*\right] \tag{4.26}$$

where,
u_* – shear velocity,
D – grain size,
ρ_s – density of sediment,
ρ – density of fluid,
$\gamma_i = (\rho_s - \rho)g$ – sediment weight in fluid,
L – characteristic length,
w_s – fall velocity of sediment,
$R_{e*} = \frac{u_* D_s}{\upsilon}$ – Reynolds number of grain size,

$M_* = \frac{\rho {u_*}^2}{\gamma_i D_s}$ – grain mobility number or densimetric Froude number,
$\rho_* = \frac{\rho_s}{\rho}$ – relative density,
$G_* = \frac{L}{D_s}$ – geometrical relationship between sediment and wave,
$W_* = \frac{w_s}{u_*}$ – relative sediment fall velocity.

Using these dimensionless products, Hughes (1993) proposes four imperfect models that can be used in scale hydraulic model test for bedload and sediment transport problem (Table 4.1), where the imperfection indicates that the similarities of several parameters in Eq. (4.26) have to be omitted during the modelling.

Table 4.1: Four imperfect bedload models (Hughes, 1993)

Model	$\frac{u_* D_s}{v}$	$\frac{\rho {u_*}^2}{\gamma_i D_s}$	$\frac{\rho_s}{\rho}$	$\frac{L}{D_s}$	$\frac{w_s}{u_*}$
Best Model	○	×	×	×	○
Lightweight model	×	×	○	○	○
Densimetric Froude Model	○	×	○	○	○
Sand Model	○	○	×	○	○

In Table 4.1, "×" means the similarity is achieved and "○" means the similarity is not achieved.

Among the listed models, the Lightweight Model preserves the similarities of the grain size Reynolds number R_{e*} and the densimetric Froude number M_*, which offers a flexibility of using available light weight model materials to correctly model phenomena dominated by the R_{e*} and M_* numbers between model and prototype, such as the initiation of sediment motion and the formation of ripples at seabed. Once the modeller selects either model sediment density, model sediment diameter or model length scale, the scale ratios of other parameters can be determined (Hughes, 1993). The Densimetric Froude Model is similar to the Lightweight Model but it neglects the R_{e*} number, therefore, it can provides more flexibility to use the available model sediment materials. The modeller can select two factors among model sediment size, model sediment diameter and model length scale, then can the scale ratios of other parameters be determined. However, according to Hughes (1993), the Lightweight Model, the Densimetric Froude Model cannot maintain the Froude scaling of current velocity if the modeller pursues the same scale ratio of both wave and current induced bed loads. In addition, scale effects occur when using lightweight materials, for example, suspension may happen earlier in model test due to an incorrect reproduction of relative density, relatively more wave energy will be absorbed in model test due to the different porosity between model and prototype. The Densimetric Froude Model also introduces more scale effects than the Lightweight Model due to incorrect reproduction of R_{e*} number.

The Sand Model only preserves the similarity of model sediment density, which can depict the suspension of sediment process without considering the fall velocity of sediment particle and can be used in longshore sediment transport modelling.

The Sand Model is not suitable for the monopile scour protection experiments as the initiation of armour stone movement, the armour stone size and relative particle fall velocity are crucial.

The Best Model can obtain the similarities of three parameters, that are the mobility of sediment, the relative density and the geometrical relationship between sediment and wave. Hughes (1993) stated that this model can apply the Froude scaling for the hydrodynamic conditions and the undistorted geometrical scaling of the structure and sediment, while the sediment density is assumed to be the same between scale model and prototype. The Best Model is a reasonable scaling scheme to reduce the scale effects in monopile scour protection experiments.

Denoting the scale ratio of each parameter q between scale model and prototype as N_q, $N_q = q_m/q_p$. Applying an undistorted geometrical similarity (Eq. 4.16), we obtain the ratios of the water depth d and the pile diameter D_P as Eq. (4.27).

$$N_d = N_{D_P} = \lambda \tag{4.27}$$

Applying a Froude scaling of the depth averaged velocity U_c, we have the scale ratio of U_c (Eq. 4.28).

$$N_{U_c} = (N_g N_d)^{\frac{1}{2}} = (N_g N_{D_P})^{\frac{1}{2}} = \lambda^{\frac{1}{2}} \tag{4.28}$$

Assuming the scale ratios of wave height H and wave period T as Eq. (4.29) and (4.30),

$$N_H = \lambda \tag{4.29}$$

$$N_T = \lambda^{\frac{1}{2}} \tag{4.30}$$

and considering a linear wave theory, where the bottom horizontal amplitude of wave orbital velocity can be written as Eq. (4.31),

$$U_m = \frac{\pi H}{T} \cdot \frac{1}{sinh(2\pi d/L)} \tag{4.31}$$

the bottom wave orbital velocity has a scale ratio as Eq. (4.32).

$$N_{U_m} = \lambda^{\frac{1}{2}} \tag{4.32}$$

This satisfies the Froude scaling rule.

The armour stone size can be scaled geometrically as the grain size is usually larger than 1 mm, this is written as Eq. (4.33).

$$N_{D_{50}} = \lambda \tag{4.33}$$

The current induced shear stress acting on the armour layer can be referred to Eq. (2.23), where f_c is expressed by Eq. (2.26). We restate these two formulas in Eq. (4.34) and Eq. (4.35).

$$\tau_c = \frac{1}{2}\rho f_c {U_c}^2 \tag{4.34}$$

$$f_c = 2\left(\frac{\kappa}{ln\left(\frac{d}{z_0}\right) - 1}\right)^2 \tag{4.35}$$

For hydraulically rough flow ($u_{*c}k_s/\upsilon \leq 70$), $z_0 = k_s/30$. As suggested in De Vos et al. (2011), $k_s = 2.5D_{50}$, therefore, $N_{k_s} = \lambda$ and $N_{f_c} = 1$. Using fresh water as the fluid in laboratory, the scale ratio of the fluid density is approximately $N_\rho \approx 1$. This gives a scale ratio of the current induced shear stress as shown in Eq. (4.36).

$$N_{\tau_c} = \lambda \tag{4.36}$$

The current induced shear velocity u_{*c}, is calculated through $u_{*c} = \sqrt{\tau_c/\rho}$, hence, the scale ratio of u_{*c} can be derived (Eq. 4.37).

$$N_{u_{*c}} = \lambda^{\frac{1}{2}} \tag{4.37}$$

The wave induced shear stress acting on the armour layer, τ_w, can be retrieved from Eq. (2.29), and the associated wave friction coefficient f_w can be calculated using Eq. (2.33) to Eq. (2.35). We restate the expression of τ_w in Eq. (4.38) and the Soulsby's expression of f_w (Soulsby, 1997) in Eq. (4.39),

$$\tau_w = \frac{1}{2}\rho f_w {U_m}^2 \tag{4.38}$$

$$f_w = 1.39\left(\frac{A}{D_{50}/12}\right)^{-0.52} \tag{4.39}$$

A is the wave amplitude, $N_A = N_H = \lambda$. This gives $N_{f_w} = 1$. Therefore, the scale ratio of the wave induced bed shear stress τ_w and the wave shear velocity u_{*w} are obtained in Eq. (4.40) and Eq. (4.41), separately.

$$N_{\tau_w} = \lambda \tag{4.40}$$

$$N_{u_{*w}} = \lambda^{\frac{1}{2}} \tag{4.41}$$

The maximum combined wave and current shear stress over the armour layer has been introduced by Eq. (2.36) and Eq. (2.37). We restate the formulas in Eq. (4.42) and Eq. (4.43)

$$\tau_m = \tau_c\left[1 + 1.2\left(\frac{\tau_w}{\tau_w + \tau_c}\right)^{3.2}\right] \tag{4.42}$$

$$\tau_{max} = \left[(\tau_m + \tau_w|cos\varphi|)^2 + (\tau_w|sin\varphi|)^2\right]^{\frac{1}{2}} \tag{4.43}$$

So the scale ratio of τ_{max} is derived in Eq. (4.44).

$$N_{\tau_{max}} = \lambda \tag{4.44}$$

Using Eq. (4.19), the Shields parameter for the armour stone has a scale ratio as Eq. (4.45).

$$N_{\theta} = 1 \tag{4.45}$$

Though the Best Model is not intended to achieve a similarity of the ratio between the shear velocity and the fall velocity, it can derived from Eq. (4.23), Eq. (4.37) and Eq. (4.41) that,

$$N_{\frac{w_s}{u_*}} = 1 \tag{4.46}$$

therefore, the similarities of four parameters in Table 4.1 are attained. This shows that the Best Model is a potentially ideal model in monopile scour protection experiments.

However, it should also be concerned that the similarities of the following important R_e numbers cannot be satisfied. They are (1) R_e of pile, R_{e,D_P}; (2) R_e of incoming flow, $R_{e,R}$, where R is the hydraulic radius of the incoming flow and (3) R_e of armour stone, $R_{e,D_{50}}$. The scale ratio factors for (1) and (3) are given in Eq. (4.47) and Eq. (4.48).

$$N_{R_{e,D_P}} = \frac{N_U N_L}{N_\upsilon} = \lambda^{\frac{3}{2}} \tag{4.47}$$

$$N_{R_{e,D_{50}}} = \frac{N_U N_{D_{50}}}{N_\upsilon} = \lambda^{\frac{3}{2}} \tag{4.48}$$

The difference between R_{e,D_P} in model and prototype indicates the flow regime around the pile would possibly be different, leading a potential scale effect in the wake flow. As the similarity of $R_{e,D_{50}}$ cannot be satisfied, the critical shear stress θ_{cr} will not be similar between model and prototype. This can be verified from Eq. (2.20) and Eq. (2.21), $N_{D*} = \lambda$ and $N_{\theta_{cr}} \neq 1$. This indicates that applying the Best Model will also introduce different U/U_{cr} values in model and prototype, which makes the threshold of motion of the armour stone not being precisely modelled.

In addition, regarding the sediment beneath the scour protection layer, the grain size is usually smaller than 1 mm and can be limited by the available sand material in laboratory, the similarity requirements on the threshold of motion, the ripples and the sediment transport can hardly be satisfied simultaneously. Potential scale effects exist in the bed response due to the presence of scour protection layer.

4.4 Conclusions

For a hydraulic test in laboratory, the deviations between small scale test and prototype arouse concerns over the reliability and uncertainties in physical experiments. This chapter briefly introduces the concepts and causes of measurement effects, model effects and scale effects in the hydraulic modelling of monopile scour protection layer stability. A general introduction of experimental uncertainty in measurement is provided referring to JCGM (2008). According to Kortenhaus et al. (2005), it is important to distinguish measurement and model effects prior to a decent analysis of potential scale effects by comparing different scale ratio models. The measurement and model effects will be analysed in Chapter 6. The analysis of the experimental uncertainties in monopile scour protection test will be introduced in Chapter 7.

A study of scale effects requires a correct and reasonable scaling rule of the experimental conditions. The scale rules are established taking consideration of the dominant forces that are acting on the physical models. However, a perfect similitude is not possible for a complex hydraulic experiment, such as the monopile scour protection test, due to the contradictions of achieving similarities between viscous force, pressure force, surface tension and inertia force simultaneously with the same scale ratio. The compromised Best Model is described referring to Hughes (1993) and will be applied in differently scaled scour protection models in order to investigate the associated scale effects of monopile scour protection physical modelling. The analysis of the scale effects will be introduced in Chapter 8.

Chapter 5

Large scale scour protection test - PROTEUS project

5.1 Introduction

The study of monopile scour protection over decades provides physical insight and data support to industries regarding the design and installation of armour materials. However, with the rising design concepts of new generation extra large wind turbines, the foundation size increases a lot. The economical design of monopile foundation requires an optimal armour layer setting considering static or dynamic stability under high hydrodynamic loading associated with potential climate change effect. As introduced, small scale experiment may be associated with strong scale effects and lead to either a conservative or unsafe design. The data, knowledge and experience on the performance of large scale monopile scour protection model in hydraulic laboratory will be precious for the future development on the design methodologies. For this sake, the PROTEUS (Protection of offshore wind turbine monopiles against scouring) project is launched under the framework of the European HYDRALAB-PLUS program. The project is a collaborative effort between international partners, including the Department of Civil Engineering of Ghent University (Belgium), Ludwig Franzius Institute for Hydraulic, Estuarine and Coastal Engineering at the University of Hannover (Germany), the Faculty of Engineering of University of Porto (Portugal), International Marine and Dredging Consultants (Belgium), the Geotechnics division of the Belgian Department of Mobility and Public Works (Belgium) and HR Wallingford (UK). This chapter briefly introduces the project test campaign and presents part of the experimental data. The data analysis focuses on evaluating the performance and applicability of existing methodologies to large scale scour protection model. The author of this thesis is involved in the execution of the tests.

5.2 Experimental setup

5.2.1 Description

The experimental study was conducted in the fast flow facility (FFF) of HR Wallingford in UK. The sketch of the experimental set-up is shown in Figure 5.1. The wave flume consists of a main channel and a returning flow channel. The main channel is 57 m long and 4 m wide, and the operational water depth can be adjusted between 0.8 m and 2.0 m. The hinged flap type wave generation system is installed in the main channel. A reversible current generation system is used to simulate the uni-directional flow following or opposing the wave propagation direction. The maximum current speed is 2.0 m/s. A 4 m × 4 m × 1 m square sandpit, located in the middle part of the wave flume, is filled with fine sands (median sediment diameter $d_{50} = 0.21$ mm).

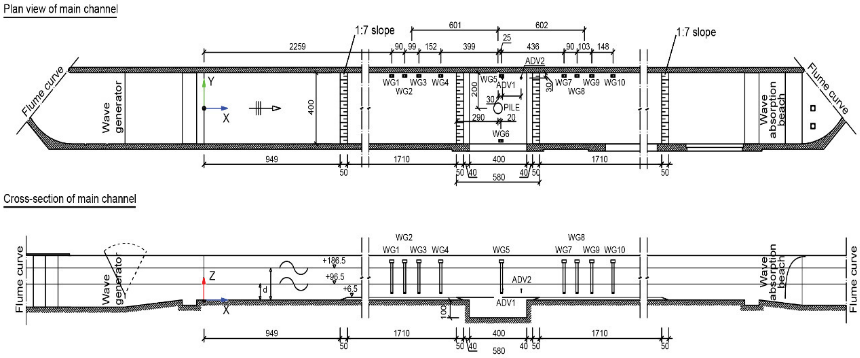

Figure 5.1: Experimental set-up of PROTEUS project (not to scale)

In the experiments described in the present chapter, two model scales, λ=1:16.67 and λ=1:8.33, are applied. The corresponding pile diameters in model scale are D_P = 0.3 m and D_P = 0.6 m, respectively. This results both in a prototype scale diameter of 5 m. The extension of scour protection is 5 times D_P. The pile model and the scour protection is installed in the center of the sandpit. The Froude similarity is applied in order to maintain a correct scaling of the inertia hydraulic forces due to waves and currents. The geometrical scaling is applied to the armor material as suggested in CIRIA (2007) and Sutherland and Whitehouse (1998). The measurement system of these experiments is described in Arboleda Chavez et al. (2019) in detail. The water surface elevations are acquired by 10 resistive wave gauges (abbreviated as WGs, sampling frequency of 100 Hz and accuracy of 1 mm), in which 4 are installed in front of the pile, 4 are placed downstream the pile and 2 are on each side of the pile. The velocity is measured by two Acoustic Doppler Velocity meters (ADVs, sampling frequency 100 Hz) and an acoustic Doppler velocity profiler (Aquadopp, sampling frequency of 1 Hz). An underwater camera is installed in front of the scour protection to capture the movement of the armor stones. In addition, the ULS-200 underwater laser scanner is applied to measure the three-dimensional profiles of the scour protection, the vertical accuracy is 1 mm, and the operational frequency is 7 Hz. The measuring probes are shown in Figure 5.2.

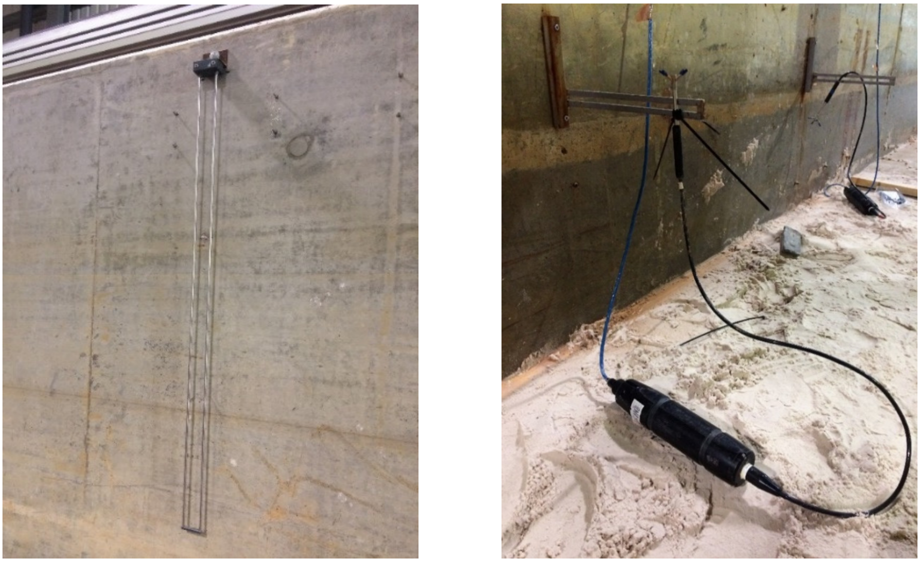

(a) Resistive wave gauge

(b) Vectrino velocimeter

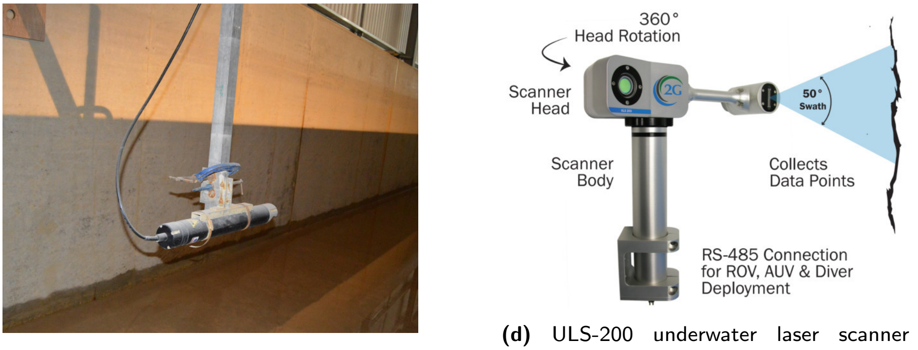

(c) Aquadopp profiler

(d) ULS-200 underwater laser scanner (2Grobotics, 2020)

Figure 5.2: Deployed measuring instruments in the PROTEUS test.

Figure 5.3 shows some pictures of the monopile (λ=1:16.67) and the installation of its scour protection. Before the installation, the sandpit is flattened and the instruments are fixed to the correct positions. Then the scour protection is installed for the inner ring (diameter of $2D_P$) with stones colored in red. The remaining area of the scour protection (using colored stones, diameter from $2D_P$ to $5D_P$) is finished sector by sector in order to achieve a good mixture of stones, as shown in Figure 5.3(a). Figure 5.3(b) shows the model ready for a test before the wave flume is filled. Figure 5.3(c) is the panorama of the monopile model in the FFF.

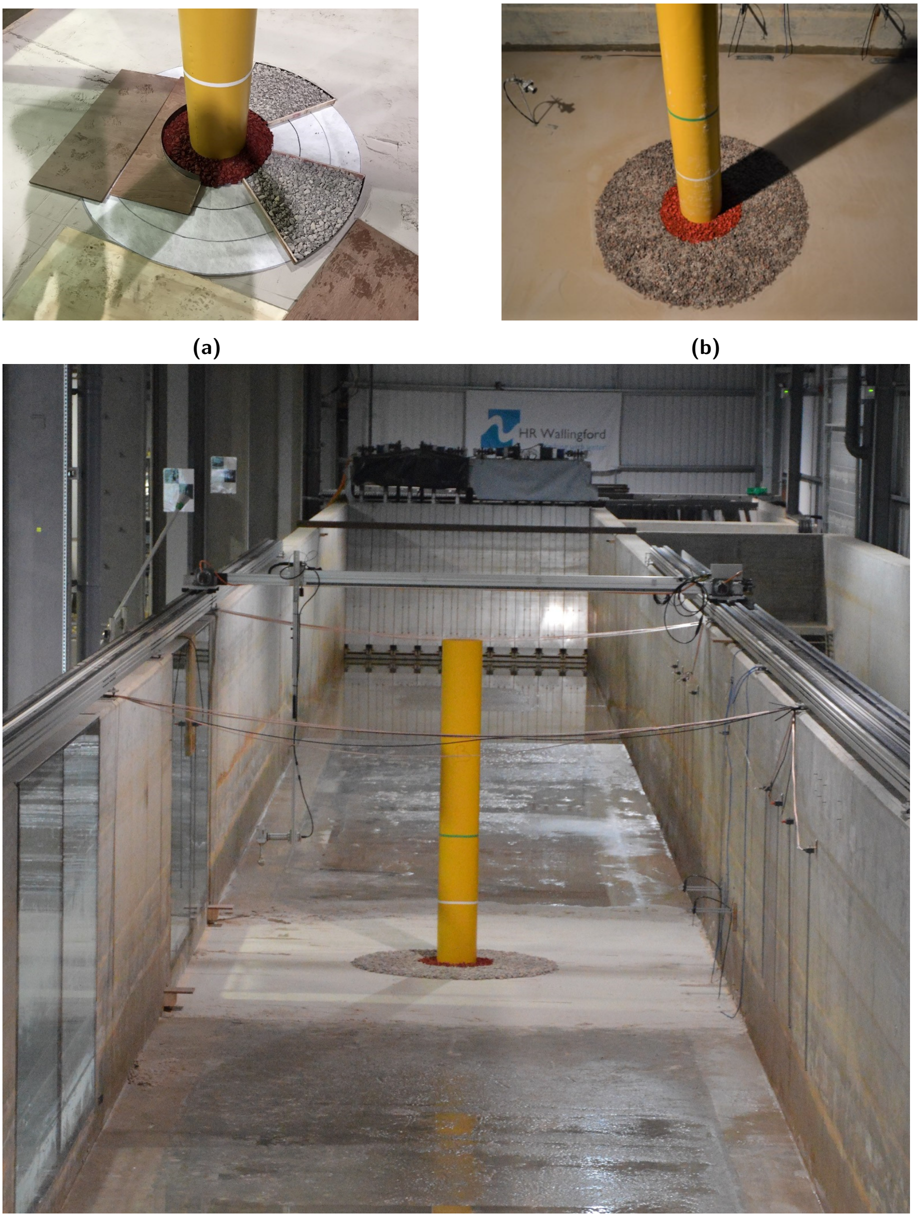

(a)

(b)

(c)

Figure 5.3: Experimental set-up in PROTEUS project: (a) Scour protection layer installation; (b) A physical model ready before filling the wave flume; (c) Monopile scour protection model in FFF.

5.2.2 Rock materials

In total six rock mixtures were used in the present experiments, with D_{50} varying from 6.75 mm to 13.5 mm. The density of the rocks is $\rho_s = 2650 kg/m^3$. Table 5.1 lists the information of the rock materials including the total weight of the rock materials and the average scour protection layer thickness of each case. The grading coefficient for all the listed rock mixtures is $D_{84}/D_{16} = 2.40$. The grading curves are shown in Figure 5.4 using sieve size D and in Figure 5.5 using nominal sieve size D_n.

Table 5.1: Conditions of rock materials in the test cases

Rock materials	Total weight [kg]	Median stone diameter D_{50} [mm]	Nominal stone diameter D_{n50} [mm]	Average layer thickness [mm]	Designed equivalent layers of D_{n50} [-]
RM1	76	12.5	10.5	24.6	2.5
RM2	76	12.5	10.5	30.0	2.5
RM3	145	6.75	5.67	49.6	9.0
RM4	85	6.75	5.67	31.8	5.3
RM5	145	6.75	5.67	51.4	9.0
RM6	1158	13.5	11.34	92.4	8.0
RM7	1158	13.5	11.34	93.9	8.0

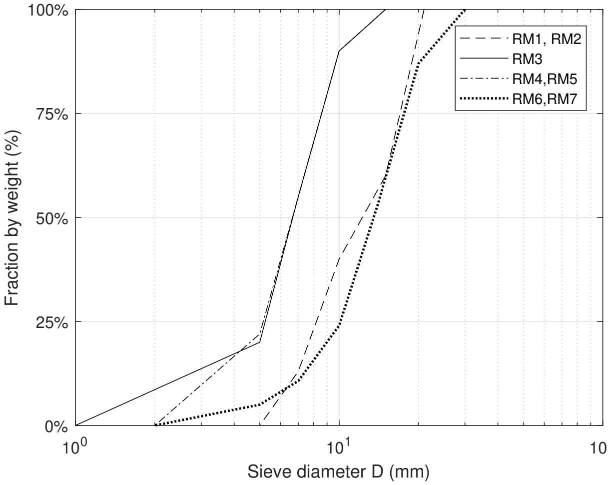

Figure 5.4: Grading curves of the model rock materials

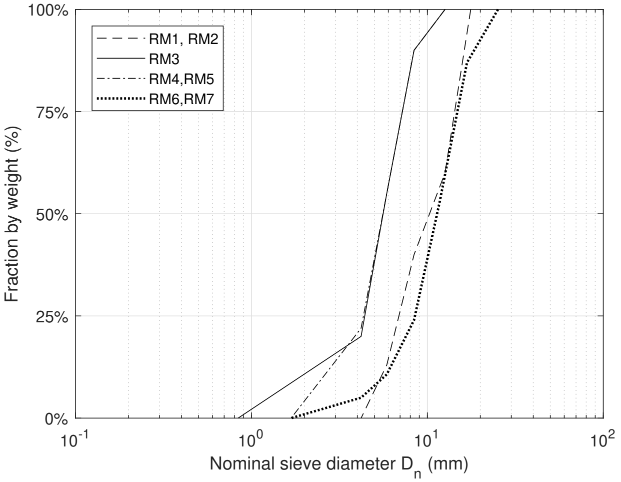

Figure 5.5: Grading curves of the model rock materials using nominal stone diameter

5.2.3 Test matrix

The test matrix presented in this chapter contains both static stability tests and dynamic stability tests of the monopile scour protection as listed in Table 5.2 and 5.3. Combined waves and currents conditions are used in every test. The static stability test cases are done with regular waves. In the dynamic stability test cases, the damage development is investigated after 1000 and 3000 irregular waves. JONSWAP spectra are used in the irregular wave tests. The direction of the flow is indicated by the sign of U_c. When $U_c > 0$, the current is following the wave propagation direction, and the cross angle between waves and current is $\varphi = 0°$. When $U_c < 0$, the current is opposing the wave propagation direction, and gives $\varphi = 180°$.

Table 5.2: Test conditions of large scale experiments of monopile scour protection: part I

Part I	Static Stability Tests, Using Regular Waves									
Test ID	Scale ratio	Pile diameter	Water depth	Regular wave height	Regular wave period	Current velocity	Median stone diameter	Nominal stone diameter	Rock mixture	Geotextile applied
	λ [-]	D_P [m]	d [m]	H [m]	T [s]	U_c [m/s]	D_{50} [mm]	D_{n50} [mm]	(-) [-]	Yes/No [-]
Test 03A	16.667	0.3	1.2	0.227	2.95	-0.250	12.5	10.5	RM2	Yes
Test 03B	16.667	0.3	1.2	0.283	2.94	-0.250	12.5	10.5	RM2	Yes
Test 03C	16.667	0.3	1.2	0.275	2.94	-0.250	12.5	10.5	RM2	Yes
Test 03D	16.667	0.3	1.2	0.331	2.47	-0.250	12.5	10.5	RM2	Yes
Test 03E	16.667	0.3	1.2	0.389	2.48	-0.250	12.5	10.5	RM2	Yes
Test 05A	16.667	0.3	1.5	0.204	2.92	0.277	6.75	5.67	RM3	No
Test 05B	16.667	0.3	1.5	0.228	2.93	0.277	6.75	5.67	RM3	No
Test 05C	16.667	0.3	1.5	0.28	2.94	0.277	6.75	5.67	RM3	No
Test 05D	16.667	0.3	1.5	0.318	2.94	0.277	6.75	5.67	RM3	No
Test 05E	16.667	0.3	1.5	0.348	2.94	0.277	6.75	5.67	RM3	No
Test 05F	16.667	0.3	1.5	0.326	2.51	0.277	6.75	5.67	RM3	No
Test 05G	16.667	0.3	1.5	0.369	2.48	0.277	6.75	5.67	RM3	No
Test 07A	16.667	0.3	1.2	0.257	2.95	-0.236	6.75	5.67	RM4	Yes
Test 07C	16.667	0.3	1.2	0.293	2.48	-0.236	6.75	5.67	RM4	Yes
Test 07D	16.667	0.3	1.2	0.329	2.48	-0.236	6.75	5.67	RM4	Yes
Test 09A	16.667	0.3	0.9	0.209	2.46	-0.239	6.75	5.67	RM5	No
Test 09B	16.667	0.3	0.9	0.22	2.07	-0.239	6.75	5.67	RM5	No
Test 09C	16.667	0.3	0.9	0.259	2.08	-0.239	6.75	5.67	RM5	No
Test 11A	8.333	0.6	1.8	0.509	3.5	-0.397	13.5	11.34	RM6	No
Test 11B	8.333	0.6	1.8	0.37	3.48	-0.397	13.5	11.34	RM6	No
Test 11C	8.333	0.6	1.8	0.422	3.48	-0.397	13.5	11.34	RM6	No
Test 11D	8.333	0.6	1.8	0.544	3.48	-0.397	13.5	11.34	RM6	No
Test 11E	8.333	0.6	1.8	0.409	2.84	-0.397	13.5	11.34	RM6	No
Test 11F	8.333	0.6	1.8	0.458	2.85	-0.397	13.5	11.34	RM6	No
Test 11G	8.333	0.6	1.8	0.501	2.83	-0.397	13.5	11.34	RM6	No
Test 11H	8.333	0.6	1.8	0.559	2.85	-0.397	13.5	11.34	RM6	No

Table 5.3: Test conditions of large scale experiments of monopile scour protection: part II

Part II	Dynamic Stability Tests, Using Irregular Waves										
Test ID	Scale ratio	Pile diameter	Water depth	Significant wave height	Peak period	Current velocity	Median stone diameter	Nominal stone diameter	Rock mixture	Geotextile applied	Number of waves
	λ	D_P	d	H_s	T_p	U_c	D_{50}	D_{n50}	(-)	Yes/No	N
	[-]	[m]	[m]	[m]	[s]	[m/s]	[mm]	[mm]	[-]	[-]	[-]
Test02A	16.667	0.3	1.2	0.188	2.49	0.377	12.5	10.5	RM1	Yes	1000
Test02B	16.667	0.3	1.2	0.188	2.49	0.377	12.5	10.5	RM1	Yes	3000
Test04A	16.667	0.3	1.2	0.272	2.52	-0.498	12.5	10.5	RM2	Yes	1000
Test04B	16.667	0.3	1.2	0.263	2.48	-0.498	12.5	10.5	RM2	Yes	3000
Test06A	16.667	0.3	1.5	0.281	2.30	0.367	6.75	5.67	RM3	No	1000
Test06B	16.667	0.3	1.5	0.286	2.28	0.367	6.75	5.67	RM3	No	3000
Test08A	16.667	0.3	1.2	0.208	2.52	-0.496	6.75	5.67	RM4	Yes	1000
Test08B	16.667	0.3	1.2	0.210	2.52	-0.496	6.75	5.67	RM4	Yes	3000
Test10A	16.667	0.3	0.9	0.191	2.00	-0.330	6.75	5.67	RM5	No	1000
Test10B	16.667	0.3	0.9	0.191	2.00	-0.330	6.75	5.67	RM5	No	3000
Test12A	8.333	0.6	1.8	0.438	2.89	-0.510	13.5	11.34	RM6	No	1000
Test12B	8.333	0.6	1.8	0.443	2.89	-0.510	13.5	11.34	RM6	No	3000
Test13A	8.333	0.6	1.5	0.372	2.28	-0.570	13.5	11.34	RM7	No	1000
Test13B	8.333	0.6	1.5	0.377	2.28	-0.570	13.5	11.34	RM7	No	3000

5.3 Results

5.3.1 Bed shear stress analysis

Methods for estimating bed shear stresses are introduced in Section 2.2.2. The bed shear stress analysis results for static and dynamic stability tests are presented in Table 5.4 and 5.5 respectively, where the bed shear stresses due to current and wave are evaluated by Eq. (2.23) and (2.29) respectively. The corresponding bed friction coefficients are provided as well. Above the scour protection area, the Nikuradse roughness is calculated by $k_s = 2.5D_{50}$. For the wave bed friction coefficient f_w, the differences between the Soulsby's formula (Eq. 2.24) and Dixen's formula (Eq. 2.25) are compared. The maximum bed shear stress is calculated by Eq. (2.37).

Table 5.4: Bed shear stress analysis results: static stability tests

Test ID	Bed friction coeff., current	Bed shear stress, current	Bed friction coeff., wave	Bed friction coeff., wave	Bed shear stress, wave	Bed shear stress, wave	Max. bed shear stress	Shear velocity, current	Shear velocity, wave	Max. shear velocity
	f_c	τ_c	f_w	f_w	τ_w	τ_w	τ_{max}	u_{*c}	u_{*w}	u_{*max}
	Eq. (2.26) [-]	Eq. (2.23) $[N/m^2]$	Eq. (2.35) [-]	Eq. (2.34) [-]	Eq. (2.29+2.35) $[N/m^2]$	Eq. (2.29+2.34) $[N/m^2]$	Eq. (2.37) $[N/m^2]$	Eq. (2.38) $[m/s]$	Eq. (2.39) $[m/s]$	Eq. (2.40) $[m/s]$
Test 03A	8.74×10^{-3}	0.273	1.07×10^{-1}	1.16×10^{-1}	3.700	4.029	4.568	0.017	0.063	0.068
Test 03B	8.74×10^{-3}	0.273	8.94×10^{-2}	1.04×10^{-1}	4.822	5.582	6.136	0.017	0.075	0.078
Test 03C	8.74×10^{-3}	0.273	9.15×10^{-2}	1.05×10^{-1}	4.659	5.350	5.902	0.017	0.073	0.077
Test 03D	8.74×10^{-3}	0.273	9.86×10^{-2}	1.10×10^{-1}	5.918	6.619	7.180	0.017	0.081	0.085
Test 03E	8.74×10^{-3}	0.273	8.63×10^{-2}	1.01×10^{-1}	7.185	8.422	8.991	0.017	0.092	0.095
Test 05A	6.74×10^{-3}	0.259	8.24×10^{-2}	9.82×10^{-2}	1.619	1.929	2.396	0.016	0.044	0.049
Test 05B	6.74×10^{-3}	0.259	7.49×10^{-2}	9.23×10^{-2}	1.850	2.279	2.758	0.016	0.048	0.053
Test 05C	6.74×10^{-3}	0.259	6.33×10^{-2}	8.27×10^{-2}	2.367	3.091	3.590	0.016	0.056	0.060
Test 05D	6.74×10^{-3}	0.259	5.72×10^{-2}	7.74×10^{-2}	2.757	3.732	4.242	0.016	0.061	0.065
Test 05E	6.74×10^{-3}	0.259	5.31×10^{-2}	7.38×10^{-2}	3.072	4.267	4.783	0.016	0.065	0.069
Test 05F	6.74×10^{-3}	0.259	6.99×10^{-2}	8.82×10^{-2}	2.788	3.518	4.025	0.016	0.059	0.063
Test 05G	6.74×10^{-3}	0.259	6.47×10^{-2}	8.39×10^{-2}	3.220	4.174	4.689	0.016	0.065	0.068
Test 07A	7.20×10^{-3}	0.201	5.89×10^{-2}	7.89×10^{-2}	2.622	3.514	3.917	0.014	0.059	0.063
Test 07C	7.20×10^{-3}	0.201	6.62×10^{-2}	8.51×10^{-2}	3.123	4.017	4.424	0.014	0.063	0.067
Test 07D	7.20×10^{-3}	0.201	6.02×10^{-2}	8.00×10^{-2}	3.590	4.773	5.185	0.014	0.069	0.072
Test 09A	7.87×10^{-3}	0.225	7.25×10^{-2}	9.03×10^{-2}	2.750	3.426	3.871	0.015	0.059	0.062
Test 09B	7.87×10^{-3}	0.225	8.75×10^{-2}	1.02×10^{-1}	2.941	3.430	3.875	0.015	0.059	0.062
Test 09C	7.87×10^{-3}	0.225	7.62×10^{-2}	9.33×10^{-2}	3.580	4.384	4.839	0.015	0.066	0.070
Test 11A	7.87×10^{-3}	0.620	6.15×10^{-2}	8.12×10^{-2}	6.959	9.181	10.405	0.025	0.096	0.102
Test 11B	7.87×10^{-3}	0.620	8.00×10^{-2}	9.63×10^{-2}	4.752	5.719	6.874	0.025	0.076	0.083
Test 11C	7.87×10^{-3}	0.620	7.20×10^{-2}	8.99×10^{-2}	5.564	6.948	8.134	0.025	0.083	0.090
Test 11D	7.87×10^{-3}	0.620	5.88×10^{-2}	7.88×10^{-2}	7.546	10.117	11.352	0.025	0.101	0.107
Test 11E	7.87×10^{-3}	0.620	9.70×10^{-2}	1.09×10^{-1}	5.357	6.028	7.192	0.025	0.078	0.085
Test 11F	7.87×10^{-3}	0.620	8.82×10^{-2}	1.03×10^{-1}	6.139	7.142	8.332	0.025	0.085	0.091
Test 11G	7.87×10^{-3}	0.620	8.28×10^{-2}	9.84×10^{-2}	6.828	8.121	9.329	0.025	0.090	0.097
Test 11H	7.87×10^{-3}	0.620	7.49×10^{-2}	9.23×10^{-2}	7.803	9.609	10.838	0.025	0.098	0.104

Table 5.5: Bed shear stress analysis results: dynamic stability tests

Test ID	Bed friction coeff., current	Bed shear stress, current	Bed friction coeff., wave	Bed friction coeff., wave	Bed shear stress, wave	Bed shear stress, wave	Max. bed shear stress	Shear velocity, current	Shear velocity, wave	Max. shear velocity
	f_c	τ_c	f_w	f_w	τ_w	τ_w	τ_{max}	u_{*c}	u_{*w}	u_{*max}
	Eq. (2.26) [-]	Eq. (2.23) $[N/m^2]$	Eq. (2.35) [-]	Eq. (2.34) [-]	Eq. (2.29+2.35) $[N/m^2]$	Eq. (2.29+2.34) $[N/m^2]$	Eq. (2.37) $[N/m^2]$	Eq. (2.38) $[m/s]$	Eq. (2.39) $[m/s]$	Eq. (2.40) $[m/s]$
Test02B	8.74 $\times 10^{-3}$	0.621	2.20 $\times 10^{-1}$	1.86 $\times 10^{-1}$	1.740	1.469	2.331	0.025	0.038	0.048
Test04B	8.74 $\times 10^{-3}$	1.084	1.70 $\times 10^{-1}$	1.57 $\times 10^{-1}$	2.601	2.407	3.887	0.033	0.049	0.062
Test06B	6.74 $\times 10^{-3}$	0.454	1.34 $\times 10^{-1}$	1.35 $\times 10^{-1}$	1.279	1.286	1.947	0.021	0.036	0.044
Test08B	7.20 $\times 10^{-3}$	0.886	1.21 $\times 10^{-1}$	1.26 $\times 10^{-1}$	1.217	1.267	2.348	0.030	0.036	0.048
Test10B	7.87 $\times 10^{-3}$	0.428	1.49 $\times 10^{-1}$	1.44 $\times 10^{-1}$	1.412	1.366	2.009	0.021	0.037	0.045
Test12B	7.87 $\times 10^{-3}$	1.023	1.28 $\times 10^{-1}$	1.31 $\times 10^{-1}$	3.400	3.470	5.030	0.032	0.059	0.071
Test13B	8.34 $\times 10^{-3}$	1.354	1.87 $\times 10^{-1}$	1.67 $\times 10^{-1}$	3.103	2.776	4.586	0.037	0.053	0.068

5.3.2 Static stability analysis

During the experiments, the threshold of motion is detected by visual observation via the underwater camera. This visual observation method has been used in both De Vos et al. (2011) and Nielsen and Petersen (2019), where the reliability is discussed in detail by the latter reference. However, for the visual assessment of the present experiments, the visibility is affected by the sand suspension, therefore only very clear rock movement is observed.

The static stability analysis approach is introduced in Section 3.2.3.1. According to De Vos et al. (2011), the regression formula for a pile model of $D_P = 0.1$ m is given in Eq. (3.11). For the tests using a $D_P = 0.3$ m model, the predicted critical bed shear stress $\tau_{cr,pred}$ can be calculated via Eq. (5.1). Further, for tests using a $D_P = 0.6$ m model, $\tau_{cr,pred}$ is calculated by Eq. (5.2).

$$\tau_{cr,pred} = 4.997 + 3.569\tau_c + 0.765\tau_w \tag{5.1}$$

$$\tau_{cr,pred} = 9.954 + 3.569\tau_c + 0.765\tau_w \tag{5.2}$$

Two forms of critical bed shear stress are applied in the analysis. One is the expression provided by Soulsby and Whitehouse (1997), τ_{cr}, adapted from Eq. (2.22) to Eq. (5.3), where θ_{cr} is obtained from Eq. (2.20). The other is suggested by De Vos et al. (2011), noted as $\tau_{cr,2}$, adapted from Eq. (3.13) to Eq. (5.4).

$$\tau_{cr} = \theta_{cr}\rho(s-1)gD_{50} \tag{5.3}$$

$$\tau_{cr,2} = 0.035\rho(s-1)gD_{67.5} \tag{5.4}$$

A comparison between Eq. (5.3) and Eq. (5.4) is introduced by Fazeres-Ferradosa et al. (2019). The experimental results and predicted shear stresses are presented in Table 5.6.

Table 5.6: Static stability analysis results

Test ID	Predicted critical shear stress	Critical bed shear stress (Soulsby and Whitehouse, 1997)	Critical bed shear stress (De Vos et al., 2011)	Critical Shields parameter (Soulsby and Whitehouse, 1997)	Max. Shields parameter (Soulsby, 1995)	STAB parameter	Dimensionless diameter	Clear rock motion noticed?
	$\tau_{cr,pred}$	τ_{cr}	$\tau_{cr,2}$	θ_{cr}	θ_{max}	$STAB$	D_*	Yes/No
	Eq. (5.1-5.2) $[N/m^2]$	Eq. (5.3) $[N/m^2]$	Eq. (5.4) $[N/m^2]$	Eq. (2.20) [-]	Eq. (3.10) [-]	Eq. (3.9) [-]	Eq. (2.21) [-]	- [-]
Test03A	8.803	11.268	8.943	0.056	0.022	0.397	290	No
Test03B	9.661	11.268	8.943	0.056	0.030	0.542	290	No
Test03C	9.536	11.268	8.943	0.056	0.029	0.524	290	No
Test03D	10.499	11.268	8.943	0.056	0.035	0.632	290	No
Test03E	11.469	11.268	8.943	0.056	0.044	0.794	290	No
Test05A	7.159	5.921	4.829	0.054	0.021	0.397	157	No
Test05B	7.336	5.921	4.829	0.054	0.026	0.476	157	No
Test05C	7.731	5.921	4.829	0.054	0.033	0.612	157	No
Test05D	8.030	5.921	4.829	0.054	0.039	0.726	157	Yes
Test05E	8.271	5.921	4.829	0.054	0.044	0.820	157	Yes
Test05F	8.053	5.921	4.829	0.054	0.037	0.688	157	No
Test05G	8.383	5.921	4.829	0.054	0.043	0.801	157	Yes
Test07A	7.719	5.921	4.829	0.054	0.036	0.662	157	No
Test07C	8.102	5.921	4.829	0.054	0.041	0.756	157	No
Test07D	8.459	5.921	4.829	0.054	0.048	0.887	157	Yes
Test09A	7.903	5.921	4.829	0.054	0.036	0.665	157	No
Test09B	8.049	5.921	4.829	0.054	0.036	0.665	157	Yes
Test09C	8.538	5.921	4.829	0.054	0.044	0.815	157	Yes
Test11A	17.490	12.170	9.659	0.056	0.048	0.853	313	No
Test11B	15.802	12.170	9.659	0.056	0.031	0.561	313	No
Test11C	16.423	12.170	9.659	0.056	0.038	0.671	313	No
Test11D	17.939	12.170	9.659	0.056	0.052	0.925	313	Yes
Test11E	16.264	12.170	9.659	0.056	0.032	0.579	313	No
Test11F	16.863	12.170	9.659	0.056	0.039	0.689	313	No
Test11G	17.390	12.170	9.659	0.056	0.043	0.762	313	No
Test11H	18.136	12.170	9.659	0.056	0.050	0.889	313	Yes

Figure 5.6(a) shows the difference between the critical bed shear stress and the predicted bed shear stress using the method of De Vos et al. (2011) (Eqs. (5.1), (5.2) and (5.4)). From the perspective of onset of motion, Figure 5.6(a) shows that the predicted critical bed shear stress for the small scale model introduced in De Vos et al. (2011) results in a conservative approach. For the cases with $D_P = 0.3$ m and $D_{50} = 6.75$ mm, the clear stone movement happens when $\tau_{cr,pred} \approx 1.66\tau_{cr,2}$. For the cases with $D_P = 0.6$ m and $D_{50} = 13.5$ mm, the clear stone movement happens when $\tau_{cr,pred} \approx 1.86\tau_{cr,2}$. It can be seen that the predicted critical bed shear stress will lead to a conservative value for the large scale ratio. Figure 5.6(b) shows the relationship between the local bed shear stress around the pile and the critical bed shear stress via the models of Soulsby and Whitehouse (1997). The local bed shear stress is calculated by Eq. (5.3) and determined by assuming a uniform amplification factor $\alpha = 1.8$ as was suggested by Whitehouse et al. (2014). It is seen that using $\alpha = 1.8$ results in a more scattered distribution of the local bed shear stress and a conservative estimation of the threshold of motion.

It should be noted that during the present large-scale tests, a live-bed situation was measured and the sediment suspension made the recorded image blurry after 2–3 waves, which clearly affects the recording quality and the possibility to see initiation of motion. Meanwhile, due to the great distance between the pile and the underwater camera, the motions of very small stones are not able to be captured. It is therefore possible that stone entrainment occurred before it was visually acknowledged, and it is not possible to develop a new formula based on these data. However, it can be noted that the predicted critical shear stress by De Vos et al. (2011) tends to be on the safe side.

Figure 5.7 shows the relationship between the STAB parameter (Opti-Pile) and the observed onset of motion based on the camera results. Most of the calculated STAB parameters are in the range of 0.4–0.8. These values, according to Den Boon et al. (2004), have exceeded the criteria of a static design, which should trigger the incipience of motion. However, the experimental results show that this judgement could also be conservative and safe, and no clear relationship between the STAB parameter and the threshold of motion was identified for this dataset. STAB parameters of 0.6–0.8 may give a result of either observed stone motion or no motion.

The deviations between the present results of the large scale tests and the existing static design method can be attributed to several reasons. Firstly, the Soulsby's curve (Figure 2.12) has a wide spreading for waves combined with current conditions in the range of $D_* > 100$. This makes it difficult to obtain an accurate analysis for the static analysis. Secondly, scale effects exist as the viscous forces cannot be scaled correctly, and the local amplification factor might be smaller as the model scale increases. Scale effects can also be seen from the Soulsby's curve. As can be seen in Figure 5.8, the D_* range for various experiments has been plotted. The critical bed shear stress for the present large scale tests are clearly larger than in the previous studies using small scale models, such as De Vos et al. (2011) and Whitehouse et al. (2014), which means the small scale experiments seem to be more conservative with regard to the incipience of stone motion.

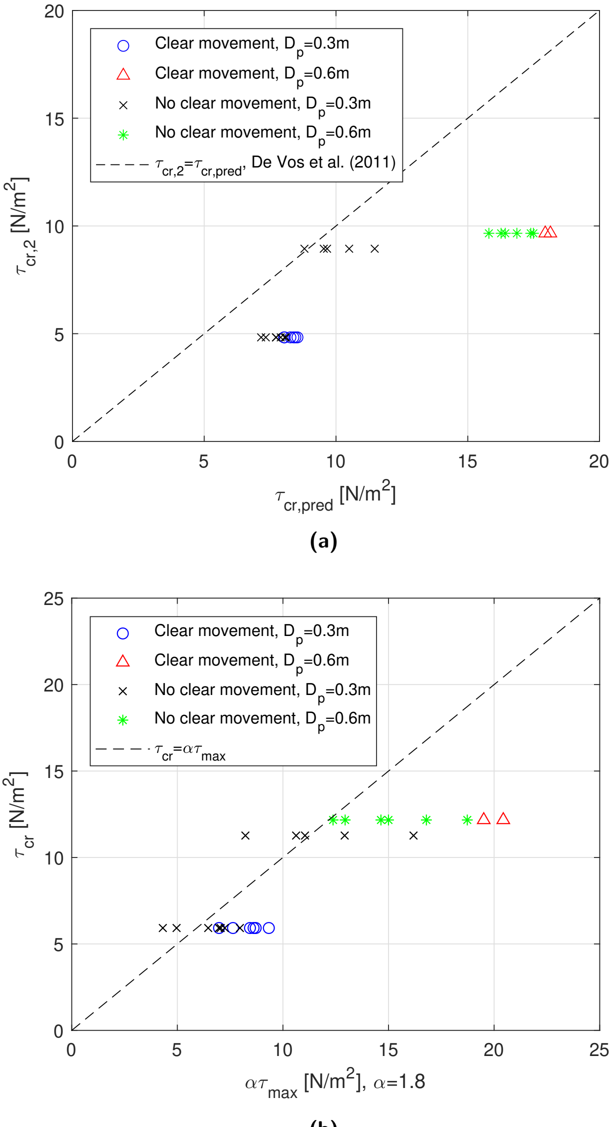

(a)

(b)

Figure 5.6: Comparison between the critical bed shear stress and predicted bed shear stress: (a) static design approach (De Vos et al., 2011); (b) τ_{cr} and τ_{max} are calculated using Soulsby and Whitehouse (1997).

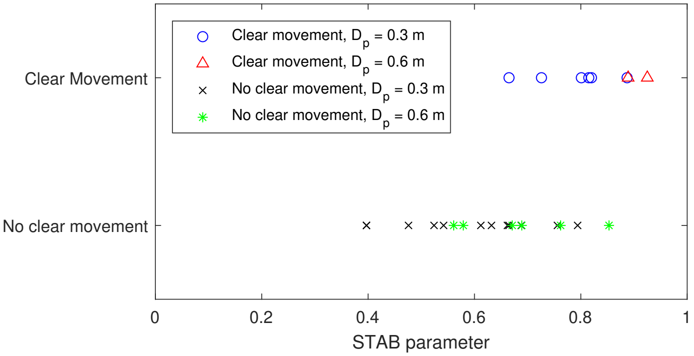

Figure 5.7: Relationship between the STAB parameter and the observed incipience of motion.

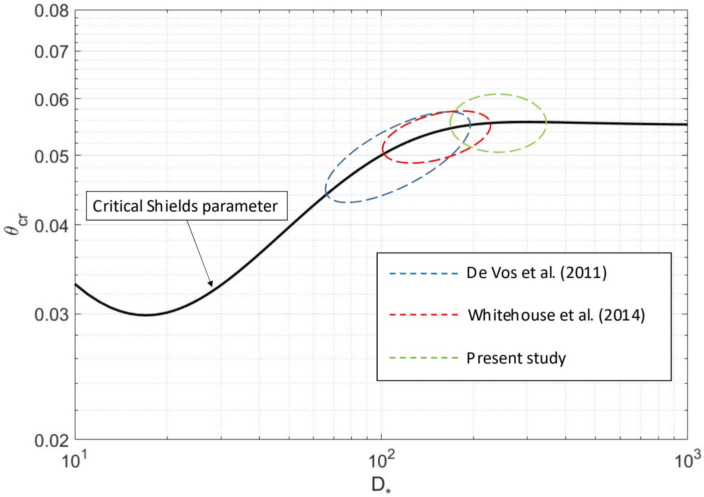

Figure 5.8: Range of D_* in different experiments on the Soulsby's critical Shields parameter diagram.

5.3.3 Dynamic stability analysis

Beside the study of the onset of motion, the dynamic stability of the scour protection layer is investigated. A dynamically stable scour protection will result in a much smaller stone size of the protection layer and significantly reduce the cost of the installation, depending on the volume of rock material for a proper thickness of the armor layer.

The large scale tests hereby have covered a wide range of environmental conditions, including different water depths, pile diameters and stone sizes. In order to have a clear insight, dimensionless expressions are necessary to depict the relationship among the combined conditions. The key dimensionless parameters in this situation include the Reynolds numbers for the pile (Eq. 5.5) and the stones (Eq. 5.6), the Froude number for the stones (Eq. 5.7), the Keulegan–Carpenter number (Eq. 5.8), the ratio between wave and current velocities (Eq. 5.9), the ratio between water depth and pile diameter (d/D_P) and the ratio between stone size and pile diameter (D_{n50}/D_P).

$$R_{e,D_P} = \frac{(U_m + |U_c|)D_P}{\upsilon} \tag{5.5}$$

$$R_{e,D_{n50}} = \frac{u_{*max}D_{n50}}{\upsilon} \tag{5.6}$$

$$F_{r,D_{n50}} = \frac{|U_c|}{\sqrt{gD_{n50}}} \tag{5.7}$$

$$KC = \frac{U_m T_p}{D_P} \tag{5.8}$$

$$U_{cw} = \frac{|U_c|}{|U_c| + U_m} \tag{5.9}$$

An overview of the values of these dimensionless parameters for the irregular wave tests are listed in Table 5.7. The dimensionless parameters can indicate the flow properties in the experiments which can determine the formation of flow separation, lee-wake vortexes and horseshoe vortexes. As seen from Table 5.7, the Reynolds numbers of the pile, R_{e,D_P}, are in the magnitude of $O(10^5)$, indicating the flow around the pile has a fully turbulent wake Sumer and Fredsøe (1997). The KC number reflects the effects of the oscillatory flows. In the present experiment, the range of KC number is $0.693 < KC < 1.448$, which means the oscillatory flow due to the waves will not lead to severe vortex shedding nor to the development of a horseshoe vortex, but might only introduce a pair of vortices at the wake side of the wave-induced flow, according to Sumer and Fredsøe (1997) and Sumer and Fredsøe (2002). The ratio between current and waves, U_{cw}, reflects the velocity components of the flow and the wave or current dominated regime, where $U_{cw} = 1$ gives a current only condition and $U_{cw} = 0$ is a wave only condition. For all cases shown in Table 5.7, $U_{cw} > 0.689$. This means the flow is dominated by the steady current.

The damage patterns after 3000 waves from the overhead cameras and the corresponding scanned bed surface elevations are displayed in Figure 5.9 and Figure 5.10. The red coloured stones in the inner ring can clearly show how they are transported by the flow around the pile due to the waves and the current. In most of the cases, significant horseshoe vortices and lee-wake vortices due to the current can be noticed as the inner ring stones are moved by the hydrodynamic loads and form a wake shape in the downstream of the pile. The removal of the inner ring stones leads to an erosion pattern nearby the pile at a $\pm$ 45° position towards the incoming current, for example, in Test 04B, 08B, 12B, and 13B. The observed phenomena are in accordance with Hjorth (1975), where the maximum amplification factor also occurs at $\pm$ 45° position towards to the incoming flow. For Test 08B, the protection fails as many inner ring rocks are removed and the geotextile is exposed. For Test 02B, the removal of inner ring rocks is not obvious as the hydrodynamic load is relatively week.

The STAB parameter (Eq. 3.9) and the measured and predicted S_{3D} (Eqs. 3.14 and 3.15) values are also given in Table 5.7. For the present cases, the STAB parameter is always less than 0.4. The protection layer is assumed to be statically stable Den Boon et al. (2004). However, it can be seen that most of the presented results are clearly not statically stable but dynamically stable. This shows the design limitation of using the predicted STAB parameter as an underestimation of the damage level.

A comparison is made between predicted and measured S_{3D} values after 3000 waves as shown in Figure 5.11. It can be noted that the predicted damage numbers are always larger than the measured damage numbers, regardless of whether waves are following or opposing current. It is defined by De Vos et al. (2012) that failure occurs when the estimated damage number is larger than 1. However, despite Test 08B, no clear failure is seen in Test 02B, 04B, 06B, 10B, 12B, and 13B, despite the predicted damage numbers $S_{3D,pred}$ being larger than 2. For Test 08B, the damage pattern shows a clear horseshoe vortex induced by the current, causing a large exposure area of the geotextile. The high damage number is mainly due to the high current condition, the small stone material, and a lower protection layer thickness.

Table 5.7: Dimensionless parameters for dynamic stability tests

Test ID	R_e number pile diameter	R_e number stone diameter	F_r number stone diameter	KC number	Ratio of velocities	Water depth to pile diameter ratio	Stone size to pile diameter ratio	STAB parameter	Predicted S_{3D} value	Measured S_{3D} value
	R_{e,D_P}	$R_{e,D_{n50}}$	$F_{r,D_{n50}}$	KC	U_{cw}	d/D_P	D_{n50}/D_P	$STAB$	$S_{3D,pred}$	S_{3D}
	Eq. (5.5)	Eq. (5.6)	Eq. (5.7)	Eq. (5.8)	Eq. (5.9)	-	-	Eq. (3.9)	Eq. (3.14)	Eq. (3.15)
Test02B	1.51×10^5	507	1.175	1.043	0.750	4.0	0.035	0.207	0.75	0.46
Test04B	2.02×10^5	655	1.552	1.448	0.740	4.0	0.035	0.345	3.09	0.68
Test06B	1.52×10^5	250	1.556	1.051	0.726	5.0	0.019	0.329	4.28	0.83
Test08B	1.91×10^5	275	2.103	1.191	0.778	4.0	0.019	0.397	11.52	2.47
Test10B	1.40×10^5	303	1.399	0.917	0.706	3.0	0.019	0.339	2.38	0.82
Test12B	4.44×10^5	804	1.529	1.109	0.689	3.0	0.019	0.413	4.22	2.35
Test13B	4.51×10^5	768	1.709	0.693	0.758	2.5	0.019	0.377	3.71	1.08

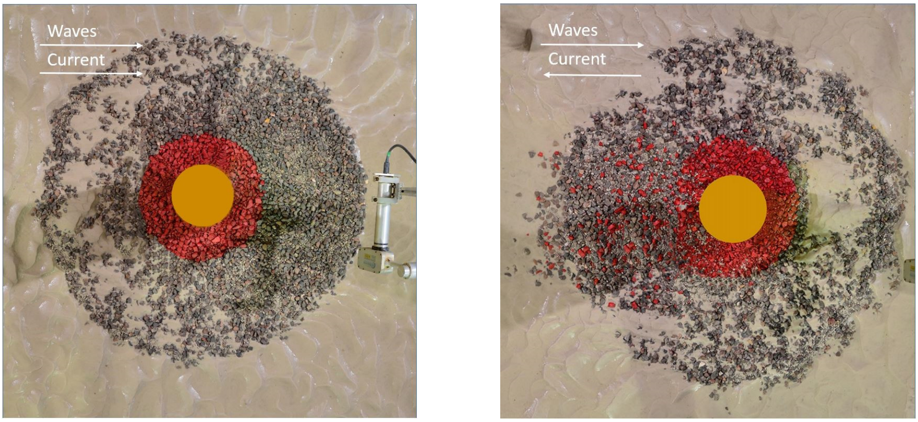

(a) Test 02B **(b)** Test 04B

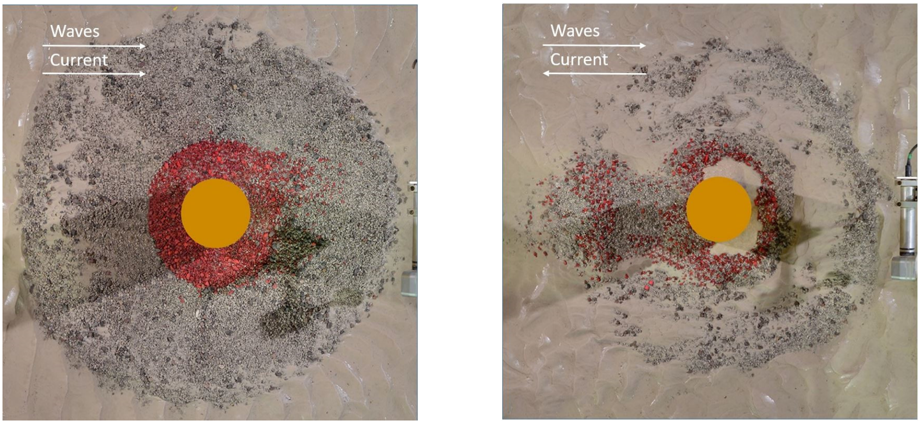

(c) Test 06B **(d)** Test 08B

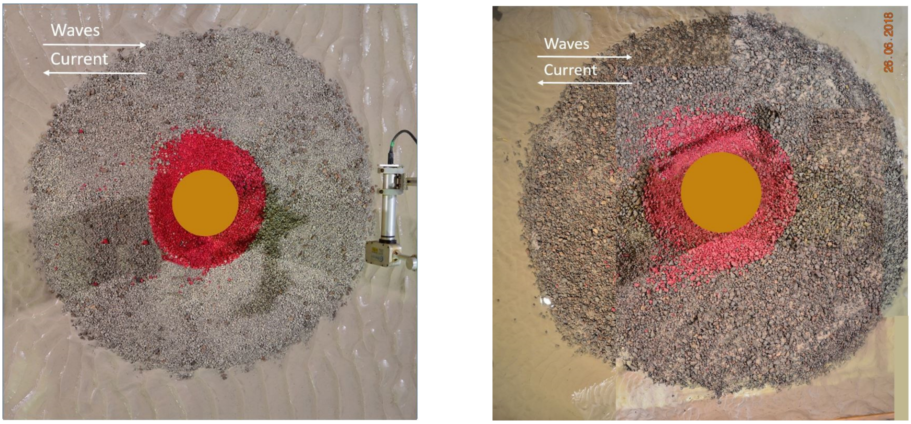

(e) Test 10B **(f)** Test 12B

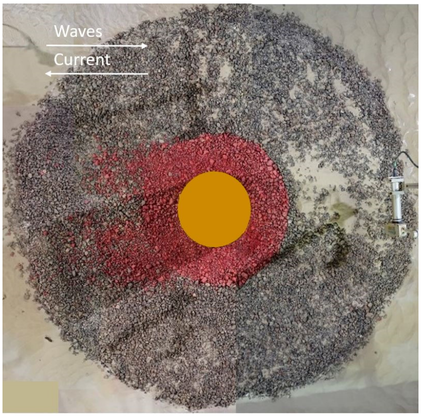

(g) Test 13B

Figure 5.9: Overhead photos of the scour protection layer after 3000 waves.

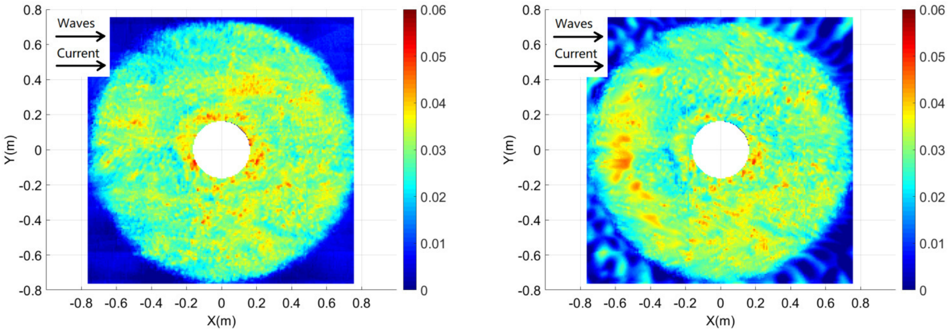

(a) Test 02B before waves

(b) Test 02B after 3000 waves

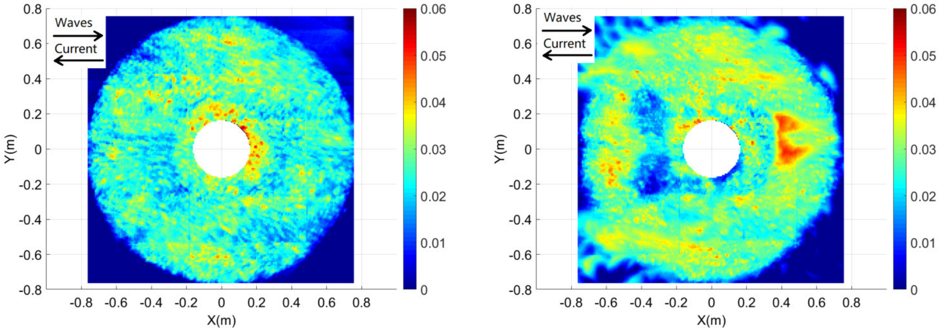

(c) Test 04B before waves

(d) Test 04B after 3000 waves

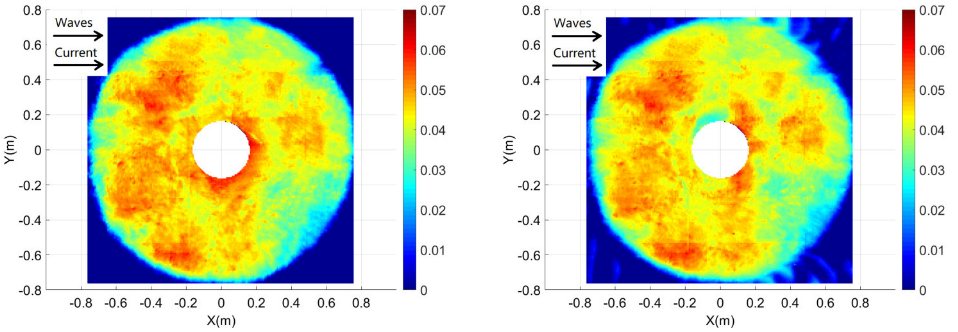

(e) Test 06B before waves **(f)** Test 06B after 3000 waves

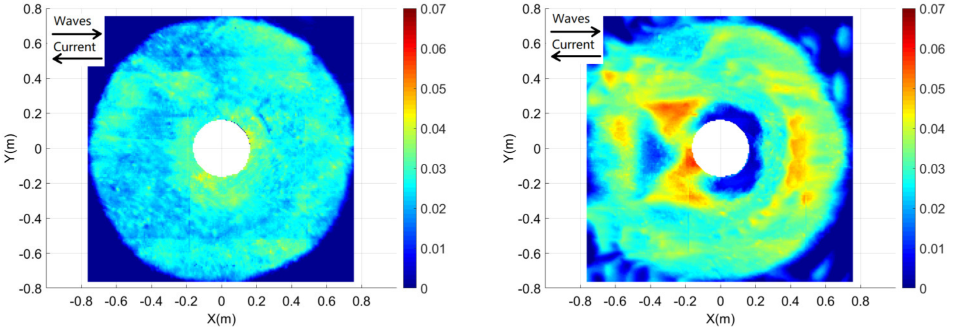

(g) Test 08B before waves **(h)** Test 08B after 3000 waves

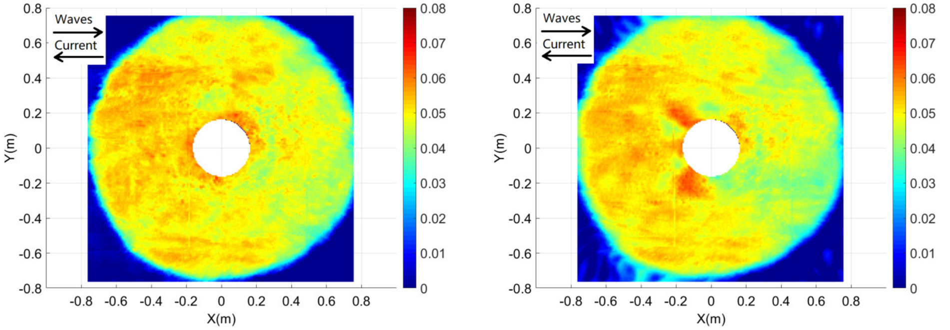

(i) Test 10B before waves **(j)** Test 10B after 3000 waves

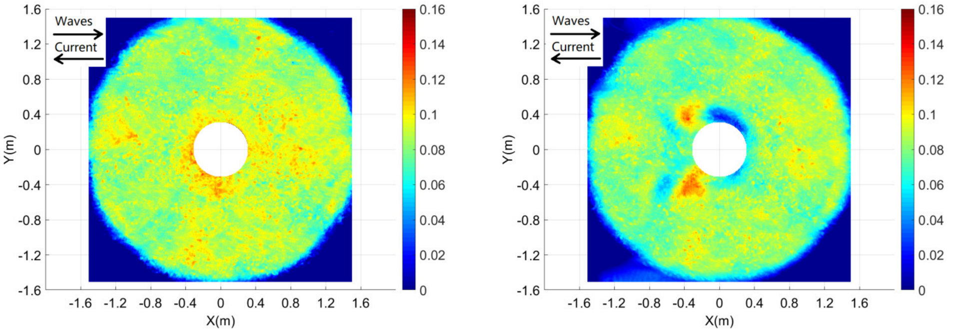

(k) Test 12B before waves **(l)** Test 12B after 3000 waves

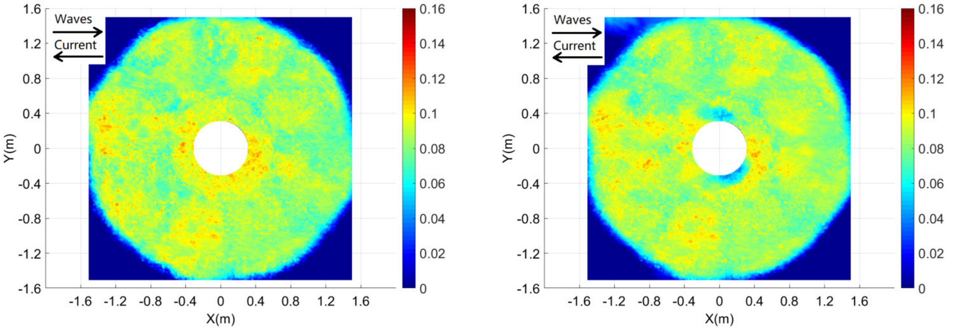

(m) Test 13B before waves **(n)** Test 13B after 3000 waves

Figure 5.10: Scanned profiles of the scour protection layer before and after 3000 waves. Colourbar stands for bed surface elevation in Z direction, unit in meter.

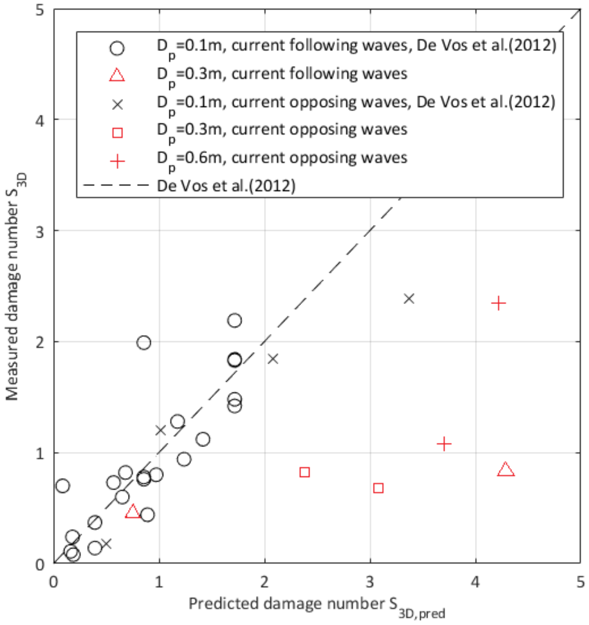

(a)

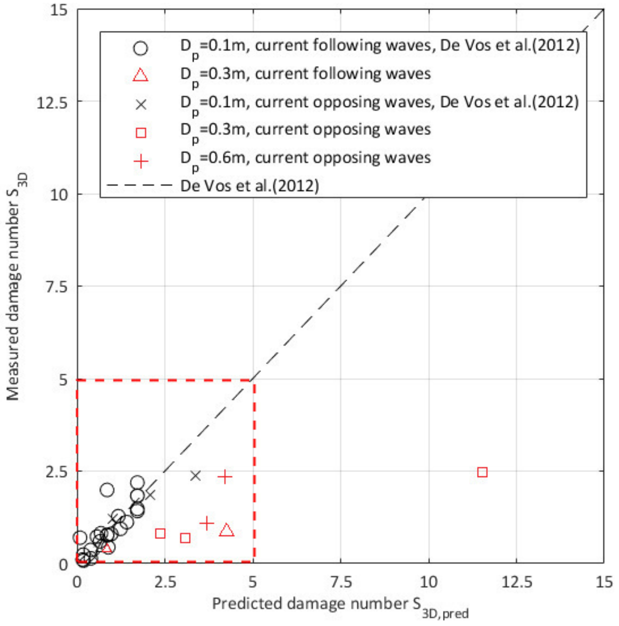

(b)

Figure 5.11: Comparison between predicted damage number $S_{3D,pred}$ and measured damage number S_{3D}: (a) zoom-in plot for $S_{3D} < 5$; (b) zoom-out plot for $S_{3D} < 15$. Red dashed box refers to the zoom-in plot of (a).

The results show that Eq. (3.15) will give a conservative prediction of the dynamic stability of the scour protection layer. Several reasons may lead to the deviations between the predicted values and the measured values. One key reason might be that the large scale experimental conditions are out of range for the input parameters in the regression formula (Eq. 3.15), especially the stone size (D_{50}) and the ratio between velocities (U_{cw}). Table 5.8 shows the difference between the parameters in the present experiments and the experiments of De Vos et al. (2012). The applied stone sizes in the present experiments are smaller than in the study of De Vos et al. (2012) and the experiments presented in this chapter focuses on the current dominated flow, $U_{cw} > 0.69$, which is larger than in most of the test cases in the experiments of De Vos et al. (2012). Another reason might be that the layer thicknesses exceeds the ones which were tested in De Vos et al. (2012). Other possible reasons can be the scale effects, model effects and experimental uncertainties.

Table 5.8: The median armour stone sizes D_{50} used in different scale tests

Test series	Pile diameter D_P [m]	Model D_{50} [mm]	Prototype D_{50} [mm]	U_{cw} [-]
De Vos et al. (2012)	0.1	4.2–8.6	208–430	0.26–0.70
Test 02B–10B	0.3	6.75–12.5	113–208	0.71–0.78
Test 12B, 13B	0.6	13.5	113	0.69–0.76

Nielsen and Petersen (2019) proposed a new estimation approach by considering the relationship between the maximum bed shear stress θ_{max}, the damage number S_{3D} and the relative velocity U_{cw}. The research suggests two estimated limits for low damage and failure, as the solid lines shown in Figure 5.12. θ_{max} is calculated using U_m in Figure 5.12(a) and using U_s (significant value) in Figure 5.12(b). To obtain these values, the small-scale experimental data of De Vos et al. (2012) are analysed for the estimated limits with $U_{cw} < 0.7$. As a complement to the dataset, the large scale experimental data with $0.69 < U_{cw} < 0.75$ presented in this paper are added to the figure. Although some differences exist when using different wave orbital velocities to calculate θ_{max}, the limit lines of θ_{max} for high U_{cw} conditions do not drop dramatically after $U_{cw} > 0.5$ as given by Nielsen and Petersen (2019), but stay stable even when $U_{cw} > 0.7$. This shows that the large scale scour protection can endure a relatively higher bed load than expected. As there is a lack of data regarding how small scale tests behave in very high U_{cw} conditions, it is not easy to draw a fair conclusion regarding the scale effects, and therefore more investigations are expected in a future study to overcome this lack of knowledge.

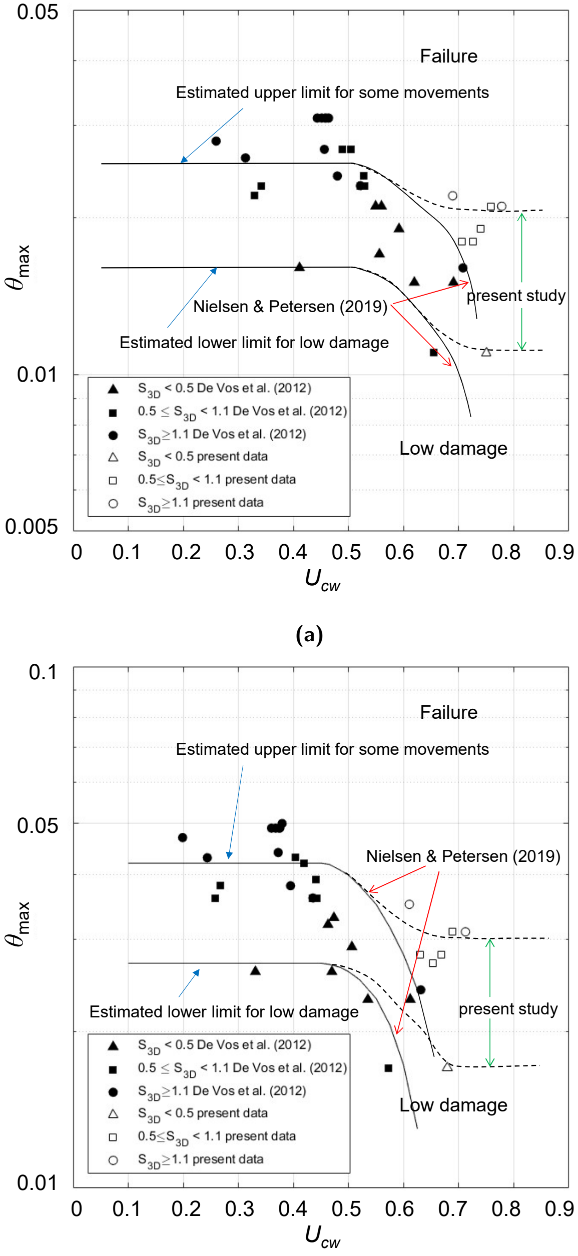

(a)

(b)

Figure 5.12: Limit lines for failure judgement using θ_{max} for different U_{cw} conditions: (a) θ_{max} is calculated using U_m; (b) θ_{max} is calculated using U_s and $U_{cw} = |U_c|/(|U_c|+U_s)$, $U_s = 2U_{rms}$.

5.3.4 Erosion depth analysis

The erosion depth is an important parameter to depict the damage of the scour protection. De Schoesitter et al. (2014) discussed that using more layers of smaller size stones will reduce the rate of failure of a scour protection. The failure is defined as the exposure of filter with an area of $4D_{50}^2$. This is equivalent to an area of four adjacent stones removed in the bottom of the armor layer. However, this definition is quite sensitive to the randomness of the observation, since the area of exposure is usually rather small compared to the whole area of protection. To the safe side of this definition, it can be understood as the moment when the maximum depth of damage exceeds the thickness of the protection layer. This approach varies from De Vos et al. (2012), as it focuses on erosion depth instead of erosion volume and because the protection layer thickness used in the present large scale test (up to $9D_{n50}$) is much larger than $3D_{n50}$. Therefore, an investigation of the maximum damage depth of the protection layer can give interesting results.

The estimation approaches for scour depth under combined current and wave condition is briefly described in Section 2.2.3.3. Basically the method from Sumer and Fredsøe (2001a) is more suitable for $KC \leq 4$ conditions, the method of Rudolph and Bos (2006) offers solutions for $1 < KC < 10$ conditions, while data analysis from Qi and Gao (2014) focuses more on an even lower KC number condition of $0.4 < KC < 4$. As the armour rock material is often quite large when compared to the fine sediments, the undisturbed bed shear stress must be smaller than the critical bed shear stress ($\theta \leq \theta_{cr}$), which is considered to be a "clear water" condition. The clear water condition scour depth under steady current was analysed by Raudkivi and Ettema (1983). However, for the damage depth of scour protection layer, there remains a scarcity of experimental data under low KC number, wave-plus-current, live-bed and clear water conditions.

With regards to the maximum damage depth of this scour protection layer, S, the definition is similar to that in scour problem. This depth is defined as the maximum eroded height of the scanned profile before and after actions of current and 3000 waves, as shown in Figure 5.13. In order to ascertain a better insight into the relationship between the maximum damage depth of the scour protection layer around a monopile and the hydrodynamic load due to combined waves and currents conditions, an analysis is carried out based on the large-scale experimental data. The results are shown in Table 5.9. As a complement of the data and a comparison between small scale and large scale results, the re-processed scanning data from De Vos (2008) is also added to the analysis, labelled with a prefix of "Ldv". The case number can be referred to Chapter 4 in De Vos (2008), where scans after 3000 waves are processed, $D_{n50} = 3.5$ mm and $D_{85}/D_{15} = 2.48$ for most of the cases.

Table 5.9: Maximum damage depth in present large scale test

Test ID	Average armour layer thickness	Max. damage depth of scour protection	Ratio between max. shear velocity and critical shear velocity	Dimensionless damage depth of scour protection	Ratio between max. scour depth and average layer thickness
	t_a	S	u_{*max}/u_{cr}	S/D_P	S/t_a
	[mm]	[mm]	[-]	[-]	[-]
Test 02B	24.6	24.2	0.455	0.081	0.984
Test 04B	30.0	34.3	0.587	0.114	1.143
Test 06B	49.6	20.8	0.573	0.069	0.419
Test 08B	31.8	37.5	0.630	0.125	1.179
Test 10B	51.4	18.4	0.582	0.061	0.358
Test 12B	92.4	82.9	0.643	0.138	0.897
Test 13B	93.9	76.2	0.614	0.127	0.812
Ldv6*	8.8	8.7	0.685	0.087	0.993
Ldv7	8.8	11.1	0.660	0.111	1.271
Ldv8	8.8	9.1	0.723	0.091	1.038
Ldv11	8.8	6.7	0.613	0.067	0.765
Ldv13	8.8	4.3	0.466	0.043	0.489
Ldv14	8.8	8.8	0.550	0.088	1.000
Ldv15	8.8	13.8	0.644	0.138	1.582
Ldv16	8.8	9.2	0.700	0.092	1.055
Ldv17	8.8	17.2	0.733	0.172	1.968
Ldv18	8.8	17.0	0.679	0.170	1.939
Ldv19	8.8	9.1	0.735	0.091	1.036
Ldv22	8.8	11.4	0.569	0.114	1.300
Ldv24	8.8	15.5	0.757	0.155	1.771
Ldv25	8.8	8.0	0.579	0.080	0.911
Ldv27	8.8	10.4	0.695	0.104	1.186
Ldv31**	8.8	7.4	0.647	0.074	0.841
Ldv32**	8.8	9.8	0.679	0.098	1.125
Ldv33**	8.8	13.1	0.789	0.131	1.500
Ldv34**	8.8	5.3	0.558	0.053	0.600
Ldv38	8.8	18.2	0.790	0.182	2.079
Ldv39	8.8	12.7	0.681	0.127	1.450
Ldv40	8.8	12.8	0.786	0.128	1.468
Ldv41	8.8	16.9	0.784	0.169	1.936

* Ldv stands for test cases from Table 4-6 in De Vos (2008)
** $D_{85}/D_{15} = 1.32$

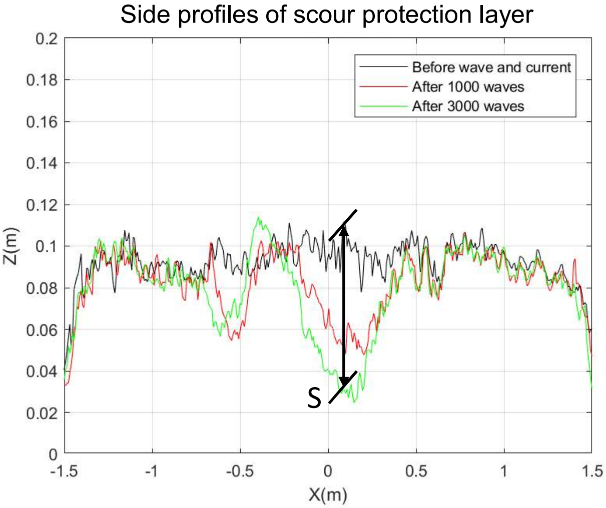

Figure 5.13: Definition of the maximum damage depth (S) of the scour protection layer.

The effect of the ratio between maximum shear velocity and critical shear velocity, u_{*max}/u_{cr} and the Reynolds number of stone size, $R_{e,D_{50}}$, are plotted in Figure 5.14 and Figure 5.15, respectively. It is clearly seen that the dimensionless maximum damage depth S/D_P increases as u_{*max}/u_{cr} increases, for both present result and data from De Vos (2008). The maximum depth to pile ratio, S/D_P, is mostly bounded between an upper limit and a lower limit with a range of 0.11, approximately. Using Eq. (3.9) and Eq. (2.40), it can be derived that $u_{*max}/u_{cr} = \sqrt{STAB}$. This shows that $STAB$ parameter can reflect the physics that S/D_P increases as the shear load increases, but is too rough when predicting the damage of the scour protection.

From another perspective, as shown in Figure 5.15 it is seen that the damage depth increases with the stone Reynolds numbers, $R_{e,D_{50}}$ ($R_{e,D_{50}} = 1.19R_{e,D_{n50}}$), based on the relationship between D_{n50} and D_{50}). This is easy to explain as a larger bed shear stress or shear velocity will physically introduce a larger amount of rock material removal. For the present large scale tests, $R_{e,D_P} \sim O(10^5)$, S/D_P increases slowly as $R_{e,D_{50}}$ increases, while for the small scale tests, $R_{e,D_P} \sim O(10^4)$, S/D_P increases sharply as $R_{e,D_{50}}$ slightly increases. This corresponds to Shields (1936) which stated that for $R_{e,D_{50}} > 400$, the critical bed shear stress is approaching a constant value and is much larger than when $R_{e,D_{50}} < 200$. Moreover, this may also be attributed to the horseshoe vortex behaviors in different scales. As in low Re number but turbulent flow condition, the turbulent boundary layer thickness to pile size (δ/D_P) is usually larger, which can cause a larger relative separation distance of the horseshoe vortex Sumer and Fredsøe (2002). As

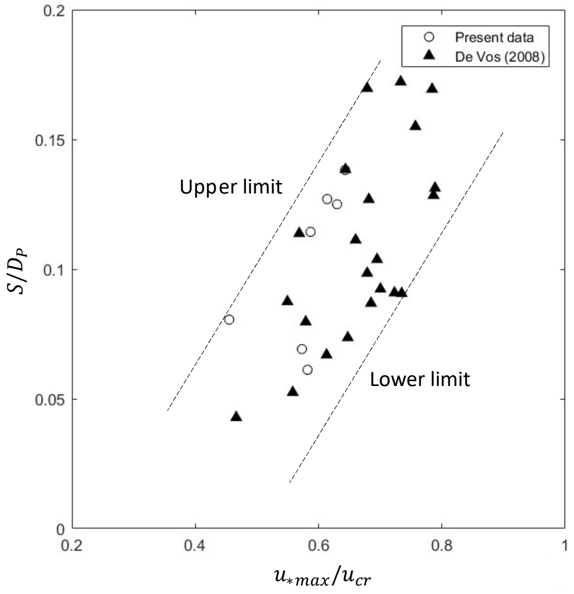

Figure 5.14: Relation between S/D_P and u_{*max}/u_{cr} after 3000 waves.

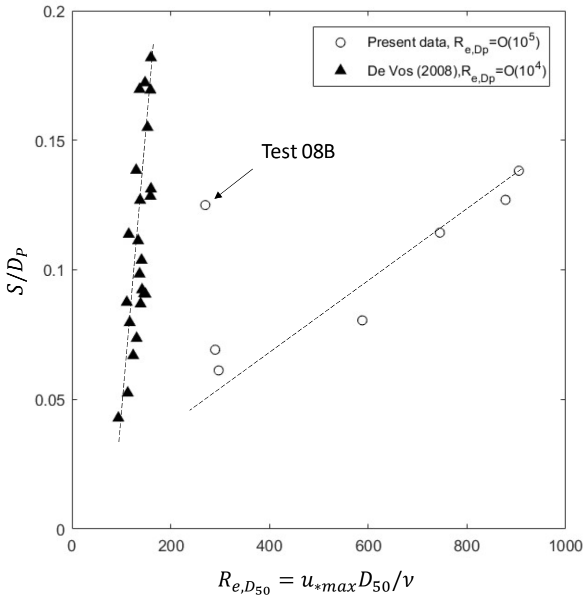

Figure 5.15: Relation between S/D_P and $R_{e,D_{50}}$ after 3000 waves.

the flow details are not captured in these experiments, more discussions related to the microscopic interactions between flow and rock material shall be addressed in the future. Nevertheless, the scale effects due to the pile Reynolds number (R_{e,D_P}) are clearly reflected. One exception is Test 08B which shows a significant failure. As listed in Table 5.7, the stone Froude number for Test 08B is $F_{r,D_{n50}} = 2.103$ and $U_{cw} = 0.778$. These values are much larger than the values of the other test cases and could be the reason for the large deviation of S/D_P in Figure 5.15.

In comparison with the existing models which predict the scour depth in sand under low KC number, the dimensionless damage depth versus U_{cw} is plotted in Figure 5.16. The regression lines from Sumer and Fredsøe (2001a), Rudolph and Bos (2006) and Qi and Gao (2014) are plotted as well for reference. The experimental data from the present large scale tests and De Vos (2008) are categorized by different KC number ranges. All of these data points are within the range of $KC < 3.5$. It can be seen from the figure that the measured S/D_P are mostly smaller than the predictions. When $U_{cw} < 0.4$, several data points can be well fitted to the three regression models, but when $U_{cw} > 0.4$, most of the data points are not able to be fitted ideally, especially for the conditions when $KC < 1.5$. There are several reasons which could explain the discrepancies between the present experimental data and the existing prediction models. In the first place, the existing formulas are mostly valid for live-bed conditions. It is not clear yet whether the prediction methods are also valid for the scour protection materials in clear water conditions. However, according to the study of Raudkivi and Ettema (1983) on the current-only scour depth in clear water conditions, the scour depth in clear water conditions is less than that in live-bed conditions. This conclusion could be reasonably expanded to the combined waves and current conditions. Secondly, the sediments used in Sumer and Fredsøe (2001a), Rudolph and Bos (2006) and Qi and Gao (2014) are fine or coarse sands with small diameters, which results in a different scaling factor for sediment, $N_{d_s} = N_L^{0.25}$. This is different from the present study where the armor stones are scaled geometrically, $N_{d_s} = N_L$ (Sutherland and Whitehouse, 1998). Therefore, the existing theories are prone to give a higher damage depth. Thirdly, it was discussed in Looseveldt and Vannieuwenhuyse (2012) that the damage of the scour protection may still develop after 3000 waves, which indicates that the equilibrium damage depth might not have been reached. However, this effect is considered to be minor as the damage depth is almost ten times smaller than the predicted value. In addition, according to the prediction formulas, for scour depth around pile, S/D_P will be larger in a higher U_{cw} or higher KC condition. But for a scour protection, Figure 5.16 shows that the damage depth S/D_P does not necessarily increase when U_{cw} or KC increases.

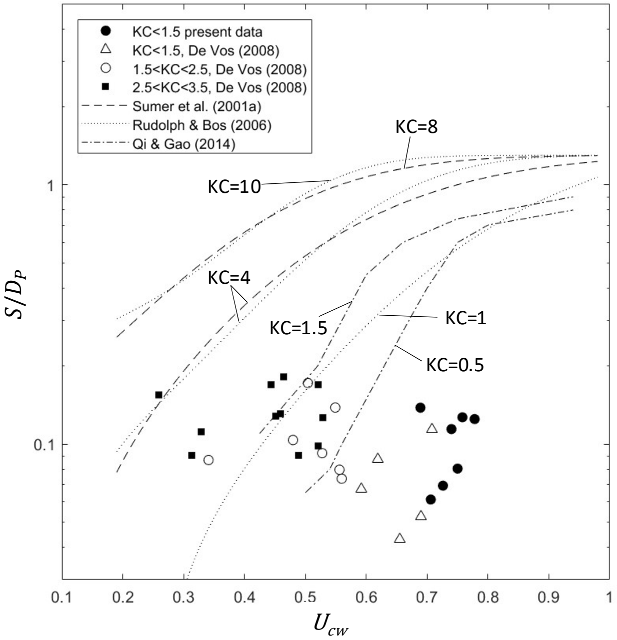

Figure 5.16: Relation between S/D_P, U_{cw} and KC after 3000 waves.

5.4 Conclusions

Regarding the scour protection of a monopile, various design approaches have been proposed based on small scale tests. However, the literature shows a scarcity of large-scale physical modelling and full-scale tests data to validate such approaches, especially in combined wave and current conditions. In the PROTEUS project, a series of large scale experiments of monopile scour protections under combined waves and currents conditions were carried out. This chapter mainly focuses on the data analysis regarding the issues of: (1) bed shear stress, (2) static stability of the scour protection, (3) dynamic stability of the scour protection, and (4) damage depth of the scour protection.

The following conclusions can be drawn:

- The work attempts to apply two static design approaches given in Den Boon et al. (2004) and De Vos et al. (2011) in estimating the scour protection performance of large scale tests. Both methods show deviations when compared to the experimental results. For the first method, the same Stab parameter will give either statically stable or unstable results. For the second method, the predicted bed shear stress values seem overestimated in the large scale experiments, causing a relatively conservative design. The model and scale effects are considered to be a primary reason for the deviation.

- The dynamic design approach given in De Vos et al. (2012) is applied to predict the damage numbers for the large scale test cases. The predictions are usually larger than the measured damage results. The range of the prediction formula, scale effects, and model effects can be reasons for the deviation. For high U_{cw} conditions, more investigations are needed to obtain a better prediction of damage numbers. Practically, the design methodologies based on a geometric scale ratio between 1:100 to 1:35 can be considered safe in light of the results obtained here. For the readers' interests, the quantification of model effects will be introduced in Chapter 6 while the scale effects will be analysed in Chapter 8.

- The damage depths of the scour protection after 3000 waves are analysed and compared to the existing prediction methods for low KC numbers conditions, such as Rudolph and Bos (2006) and Qi and Gao (2014). It is found that S/D_P increases with u_{*max}/u_{cr} or $STAB$ parameter, but with a quite wide range between the upper limit prediction and the lower limit prediction. S/D_P also increases with the stone Reynolds number ($R_{e,D_{50}}$), but a different pile Reynolds number (R_{e,D_P}) will introduce different trends between S/D_P and $R_{e,D_{50}}$, indicating scale effects in the experimental modelling. Furthermore, S/D_P of the scour protection are usually smaller than the predicted values. The deviation may be caused by the applicability in clear water conditions for scour protection cases. It is also found that the damage depth of the scour protection is not obviously related to U_{cw} and KC number.

Chapter 6

Small scale scour protection test - quantification of measurement & model effects

6.1 Objectives

Though scale effects are usually perceived as the primary cause of differences between scale and prototype model test results, it is crucial to identify the scale effects can only be validated and analysed when the measurement effects and the model effects are clearly quantified a priori. This chapter, with an objective of quantitatively assessing the measurement and model effects, introduces a series of repeated small scale laboratory experiments to investigate erosion damage of monopile scour protection under combined wave and current. Three main tasks are performed: (1) the repeatability of test conditions are discussed using statistic analysis method; (2) the measurement effects due to bed profiler are analysed by repetitive measurements; (3) The model effects are revealed through repeated tests in the same hydraulic conditions. Statistical analysis of the experimental uncertainties associated with model effects is carried out using the three dimensional damage number (S_{3D}) and provides valuable data for estimating the experimental standard deviations of the local and global damage number in such tests.

6.2 Experimental set-up and focus

6.2.1 Description

The present work adopts a small scale riprap monopile scour protection model made by armour stones and tries to elaborate the causes and impacts on the armour layer damage of measurement, model and scale effects using three groups of tests so as to compare with the large scale PROTEUS model. The three test groups, TG1 to TG3, are applied in this study. The target conditions are respectively scaled down from the PROTEUS tests Test 10B, Test 13B and Test 14 (as listed in Table 5.3). Firstly, the measurement effects are quantified by performing repeated measurements of the same damage profile of the scour protection from TG1. Then, the model effects for TG1 and TG2 are obtained through statistical analysis for seven repeated tests. In this chapter, the focus will be on the dataset of TG1 and TG2. Test group TG3 has two repeated cases, which is specially used for the analysis of scale effects and will be introduced in Chapter 8. The geometrical scaling is used for the pile model and the Froude scaling is used for the wave and current conditions, therefore, resulting in the target conditions presented in Table 6.1, where d is the water depth, D_P is the pile diameter, U_c is the current velocity (negative value indicates a current opposing following waves), H_s is the significant wave height, T_p is the peak wave period and N is the number of waves. The scale ratios in Table 6.1 are the geometrical scale ratios between model and prototype, where the pile diameter of the prototype is D_P= 5 m.

Table 6.1: Target wave and current conditions of the present tests

Test ID	Scale ratio	d [m]	D_P [m]	U_c [m/s]	H_s [m]	T_p [s]	N [-]
PROTEUS Test 10B	1:16.67	0.9	0.3	-0.330	0.191	2.00	3000
TG1	1:50	0.3	0.1	-0.191	0.064	1.16	3000
PROTEUS Test 13B	1:8.33	1.5	0.6	-0.570	0.377	2.28	3000
TG2	1:50	0.25	0.1	-0.233	0.063	0.93	3000
PROTEUS Test 14 *	1:8.33	1.8	0.6	-0.510	0.443	2.89	5000
TG3	1:50	0.3	0.1	-0.208	0.073	1.180	5000

* PROTEUS Test 14 applies rock materials of D_{50}=13.5mm and $D_{85}/D_{15} = 6$, total weight is 1351kg (Arboleda Chavez et al., 2019).

6.2.2 Facility and test setup

The experiments have been carried out in the wave flume of the Civil Engineering Department, Coastal Engineering Research Group at Ghent University (Ghent University, 2020). The dimensions of the wave flume are 30 m × 1 m × 1.2 m and the maximum operational water depth is $d = 0.8$ m. A uni-directional current system is installed in the wave flume which can create a steady current against the incoming wave. Active wave absorption is used in the wave generation system and passive wave absorption is used at the beach side of the wave flume to absorb any reflected waves from the beach. The test setup is displayed in Figure 6.1 and a well installed model is plotted in Figure 6.2. A 2.5 m long and 5 cm deep sandbox is installed in the middle of the wave flume while the pile model (D_P= 0.1 m) is fixed amid the sandbox. The extended radius of the armour layer is 2.5D_P (0.25 m).

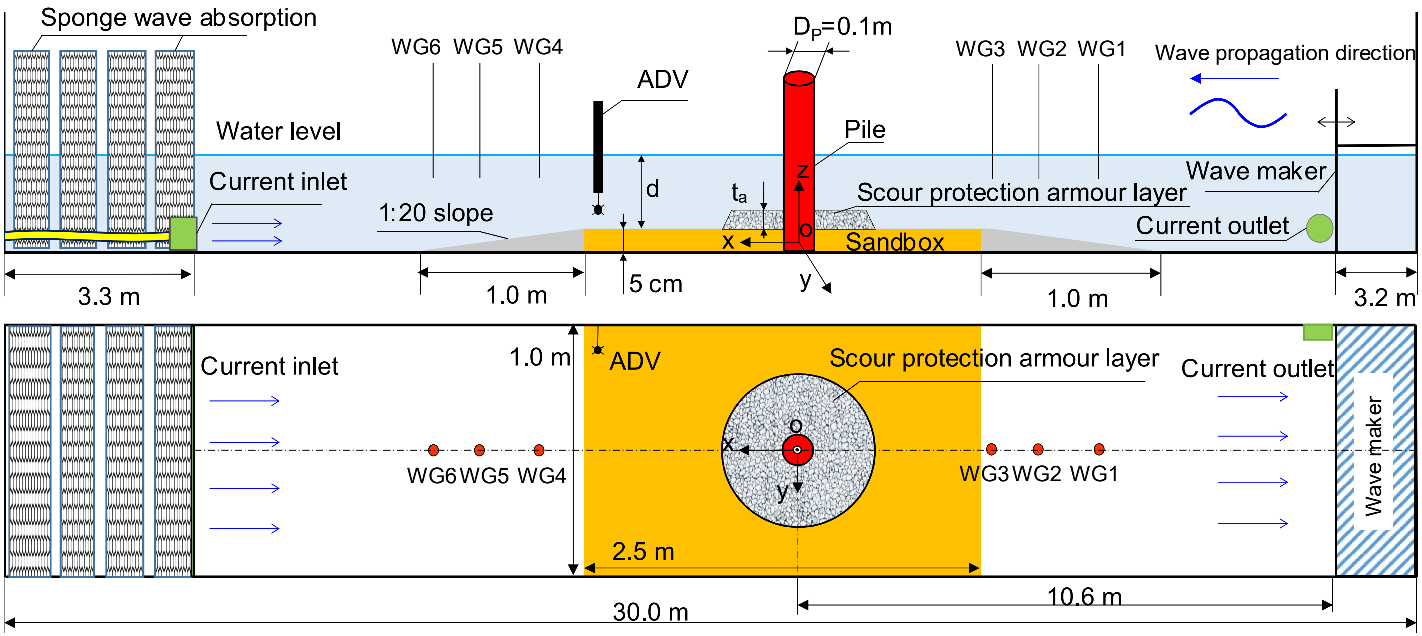

Figure 6.1: Layout of wave flume setup of small scale monopile scour protection model.

Figure 6.2: Installed model in Ghent University wave flume.

Six resistive wave gauges (abbreviated as WGs) are deployed in the wave flume, in which WG1-WG3 are located in the wave incoming side for collecting the wave signals and WG4-WG6 are near the passive wave absorption system for measuring the reflection. The accuracy of this type wave gauge is 1 mm and the sampling frequency is 40 Hz. A Vectrino (Nortek Group, 2017) Acoustic Doppler Velocity meter (ADV) is employed to measure the depth-average current velocity at the vertical location of $z = 0.4d$. The sampling frequency is 25 Hz and the measurement resolution is 1 mm/s. The locations of all probes are listed in Table 6.2.

Table 6.2: Locations of probes in small scale test

Probe location	TG1		TG2	
	X [m]	Y [m]	X [m]	Y [m]
Pile centre	0.00	0.00	0.00	0.00
WG1	-2.59	0.00	-2.59	0.00
WG2	-2.18	0.00	-2.18	0.00
WG3	-1.88	0.00	-1.88	0.00
WG4	9.20	0.00	9.41	0.00
WG5	9.37	0.00	9.53	0.00
WG6	9.70	0.00	9.70	0.00
ADV	0.80	-0.45	0.80	-0.45

The armour stones of TG1 and TG2 are scaled using the Best Model described in Section 4.3.6. The sieve diameters and the grading curve of armour layer stones are provided in Table 6.3 and Figure 6.3. The material density is $\rho_s = 2650 kg/m^3$ and the total mass of armour stones is 5.36 kg. The target average armour layer thickness is t_a = 17 mm, which equals 9 layers of armour stones ($9D_{n50}$). The construction of the armour layer applies a single-layer configuration where no geotextile nor granular filter is used. The relatively fine armour stone size ($D_{50} = 2.26$ mm) strives for a dynamically stable scour protection at the end state under designated wave and current condition. TG3 applies the same armour stones with TG1 and TG2, which maintains a correctly scaled D_{50}, but the grading coefficient similarity is discarded. The reason for doing so is because the fine rock materials ($D_s < 5mm$) in PROTEUS Test 14 takes a considerable portion of 25% in the total material mass as the grading coefficient is large. These small materials will be improperly scaled to less than 1 mm in small scale models. Uniform and fine sands are used to model the bed sediment, the median size is $d_s = 100\mu m$. Applying the scaling rule for sediment described in Eq. (4.20) and Eq. (4.21), the prototype sediment size is estimated to 375 μm.

Table 6.3: Size and grading coefficient of applied armour stones

Sieve size	D_{16}[mm]	D_{50} [mm]	D_{84} [mm]	D_{n50}	D_{84}/D_{16}
Values	1.38	2.26	3.17	1.90	2.30

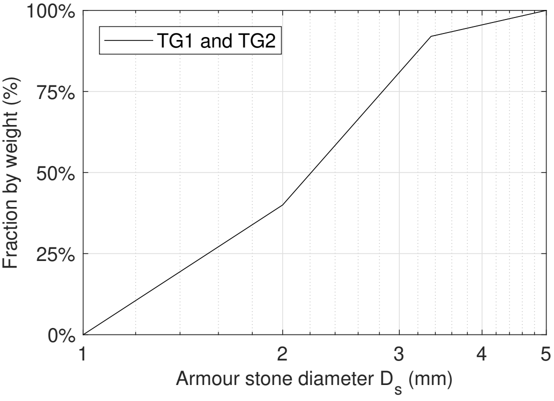

Figure 6.3: Armour stones applied in small scale experiment

The intact and damaged profiles of the scour protection layer before and after wave and current action are measured by means of the FARO®Freestyle 3D handheld laser scanner (FARO Technologies Inc, 2017) (Figure 6.4). The raw scanned data is post-processed into an orthogonally gridded format by means of an averaging filter. The grid resolution is 2 mm, which is close to the size of the armour stone and can well depict the deformation of the armour layer. A validation case is done in dry conditions by measuring a cuboid of 90 mm × 45 mm × 45 mm, see

Figure 6.5. The theoretical volume of the cuboid is 182250 mm^3 and the measured volume is 182125 mm^3, the relative error is 0.06% (Debaveye and De Riemacker, 2020). However, due to the system randomness in calibration and data collection, the measurement effect is unavoidable and will be analysed in this work through repeated measurements. More details regarding the facility and the test set-up can be referred in Appendix A.

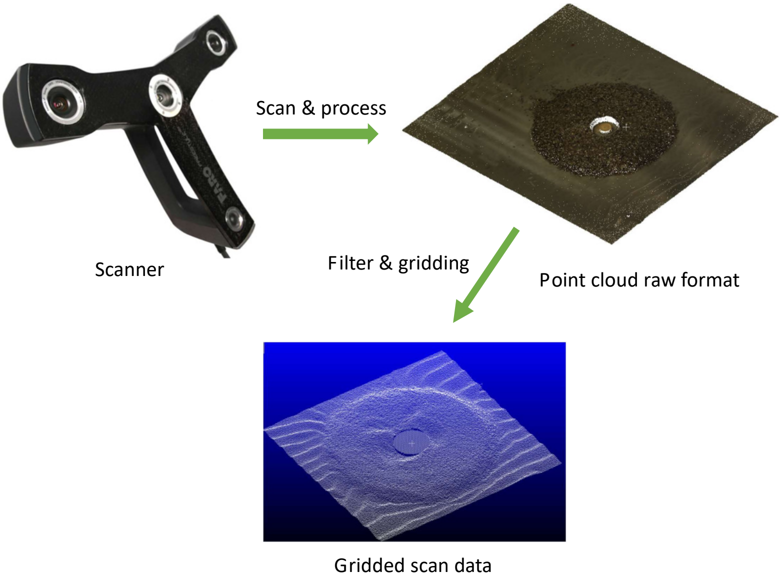

Figure 6.4: FARO®Freestyle 3D handheld laser scanner and data post-processing.

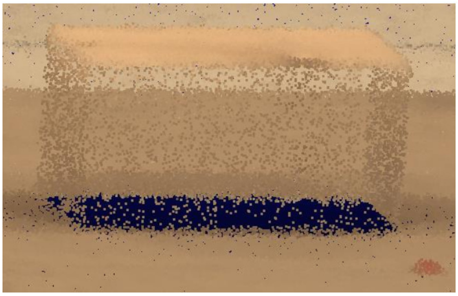

Figure 6.5: Cuboid model used for validation purpose, from Debaveye and De Riemacker (2020).

6.2.3 Test matrix

The measured conditions for each repeated test in all test groups are listed Table 6.4, including water depth d, depth-averaged current velocity U_c, significant wave height H_s, 1/10 wave height $H_{1/10}$, maximum wave height H_{max}, peak period T_p and mean energy periods $T_{m-1,0}$. For test groups TG1 and TG2, seven repeated tests are performed, while in TG3, two repeated tests are conducted. Irregular waves using Jonswap spectra and peak enhancement factor $\gamma = 3.3$ are applied in each test. For test groups TG1 and TG2, the wave duration sets to 3000T_p. For TG3, the wave duration is 5000T_p while damaged profiles are scanned after 1000, 3000 and 5000 waves. The same wave trains are applied for TG1_1 to TG1_3 and TG2_1 to TG2_3 with the purpose to investigate the differences of armour layer damage between using the same and distinct wave trains.

Table 6.4: Test matrix

Test ID	d [m]	U_c [m/s]	H_s [m]	$H_{1/10}$ [m]	H_{max} [m]	T_p [s]	$T_{m-1,0}$ [s]
TG1_1	0.3	-0.187	0.063	0.080	0.214	1.182	1.074
TG1_2	0.3	-0.190	0.064	0.081	0.279	1.147	1.072
TG1_3	0.3	-0.183	0.063	0.079	0.236	1.164	1.072
TG1_4	0.3	-0.183	0.064	0.080	0.224	1.164	1.065
TG1_5	0.3	-0.186	0.063	0.080	0.273	1.164	1.073
TG1_6	0.3	-0.185	0.062	0.079	0.224	1.138	1.071
TG1_7	0.3	-0.187	0.063	0.079	0.211	1.138	1.072
TG2_1	0.25	-0.222	0.063	0.078	0.195	0.978	0.922
TG2_2	0.25	-0.221	0.062	0.077	0.204	0.954	0.923
TG2_3	0.25	-0.221	0.063	0.078	0.228	0.954	0.920
TG2_4	0.25	-0.219	0.062	0.078	0.174	0.973	0.923
TG2_5	0.25	-0.217	0.063	0.078	0.193	0.985	0.923
TG2_6	0.25	-0.221	0.061	0.076	0.191	0.985	0.927
TG2_7	0.25	-0.217	0.062	0.078	0.177	0.964	0.922
TG3_1	0.3	-0.202	0.075	0.093		1.219	1.118
TG3_2	0.3	-0.203	0.075	0.093		1.219	1.117

6.2.4 Repeatability of waves and current conditions generated in the laboratory

Repeatability of employed hydrodynamic conditions is crucial for evaluating the model effects. The inherent system randomness in wave and current generation causes the instantaneous flow varies between each repetitive test, no matter whether the waves and/or current generation inputs are manually or automatically controlled. The repeatability can be evaluated by considering the same location, the same experimental tools, the same observer, the same measuring instrument, the same conditions and the same objectives, and be quantified with the dispersion characteristics of the results, such as the standard deviation of the measuring result (Eq. 6.1) and the standard deviation of the mean (Eq. 6.2), according to JCGM (2008),

$$\sigma(q) = \sqrt{\sigma^2(q)} = \sqrt{\frac{1}{n-1}\sum_{i=1}^{n}(q-\bar{q})^2} \tag{6.1}$$

$$\sigma(\bar{q}) = \sqrt{\frac{1}{n}\sigma^2(q)} = \sqrt{\frac{1}{n}}\sigma(q) \tag{6.2}$$

where q is the measured quantity, $\bar{q}$ is the arithmetic mean value of q, as defined in Eq. (6.3),

$$\bar{q} = \frac{1}{n}\sum_{i=1}^{n} q_i \tag{6.3}$$

n is the number of measurements and $\sigma^2(q)$ is the variance of measurements. $\sigma(q)$ reflects the degree of data dispersion and the $\sigma(\bar{q})$ expresses the precision of the mean value. Ideal repeatability requires $\sigma(q)$ and $\sigma(\bar{q})$ to be as small as possible.

For the tests with the same wave trains, the measured wave surface elevations of TG_1 to TG_3 are plotted in Figure 6.6, where the wave peaks and troughs and up/down crossings are well repeated through visual assessment. However, differences can still be noticed as a result of the randomness due to the flow turbulence and the interaction with current. The wave statistical characteristics are apparently not sensitive to the wave train repeatability, as seen in the plotted measured wave spectra (Figure 6.7) and wave height exceeding probability distributions (Figure 6.8). Figure 6.9 show the current flow turbulent energy spectra respectively. Prior to analysing the turbulence the measured velocity signals were despiked and detrended. The turbulence of the current in longitudinal flow direction is analysed using the spectral method of Richard et al. (2013) taking into account the noise of the ADV. According to Richard et al. (2013) the turbulence intensity (T_i) is defined as Eq. (6.4),

$$T_i = \frac{\sqrt{u'^2 - {\sigma_{noise}}^2}}{\mu(U_c)} \times 100[\%] \tag{6.4}$$

where u'^2 is the square sum of the velocity perturbation, $\mu(U_c)$ is the mean velocity and ${\sigma_{noise}}^2$ is the variance due to noise of the ADV. The variance due to noise is derived from a two parameter best-fit line (dotted black line in Figure 6.9) as proposed by Richard et al. (2013). When the best-fit line plateaus towards the right end of Figure 6.9 the turbulence noise floor is reached. Towards the left of Figure 6.9 the best-fit line aligns well with the $f_t^{-5/3}$ line indicating the inertial subrange. It can be seen that the measurements from repeated tests cover the same range in the spectral plot (Figure 6.9).

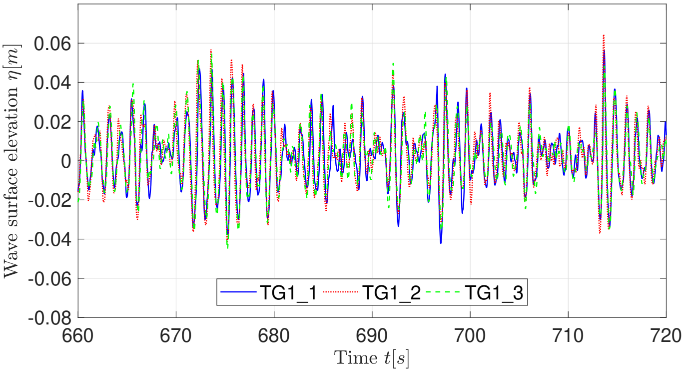

(a) TG1

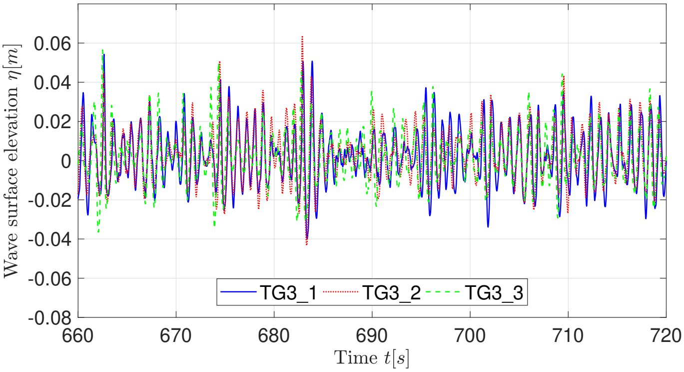

(b) TG2

Figure 6.6: Repeatability of measured wave surface elevation.

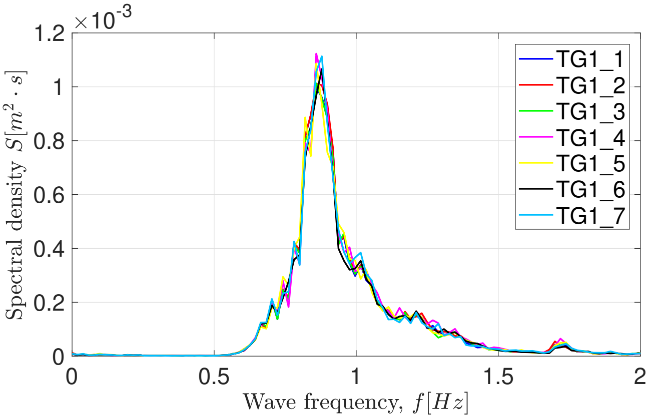

(a) TG1

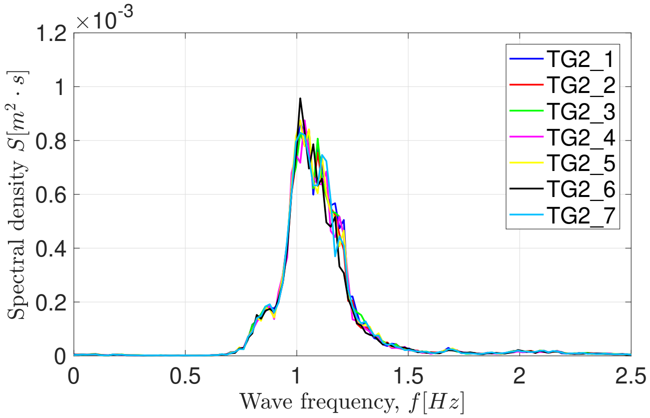

(b) TG2

Figure 6.7: Repeatability of measured wave spectra.

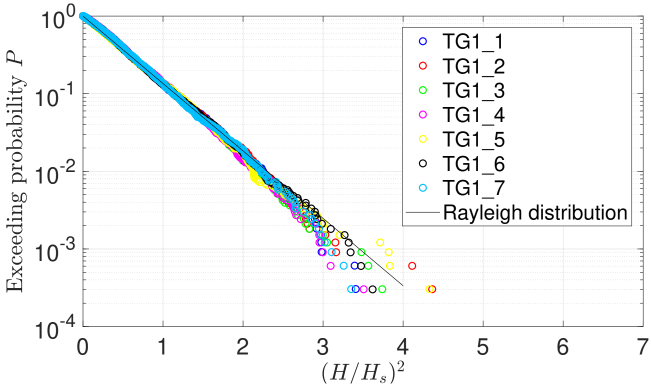

(a) TG1

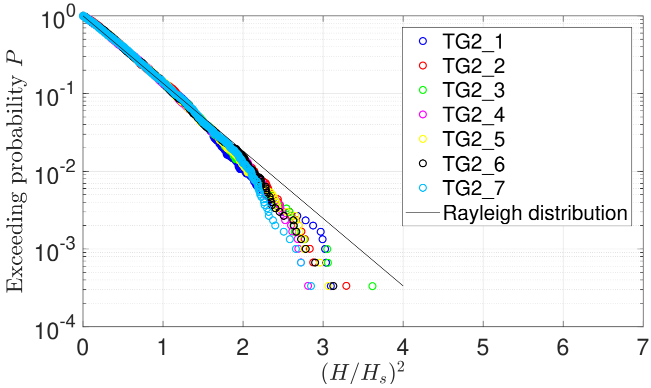

(b) TG2

Figure 6.8: Wave height distributions.

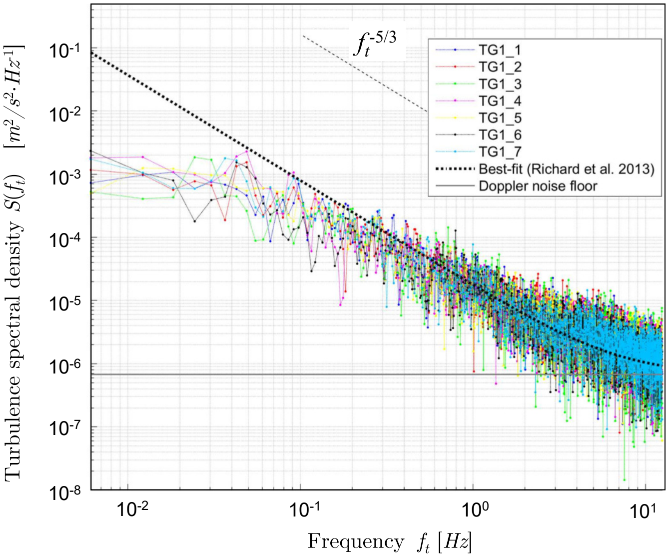

(a) TG1

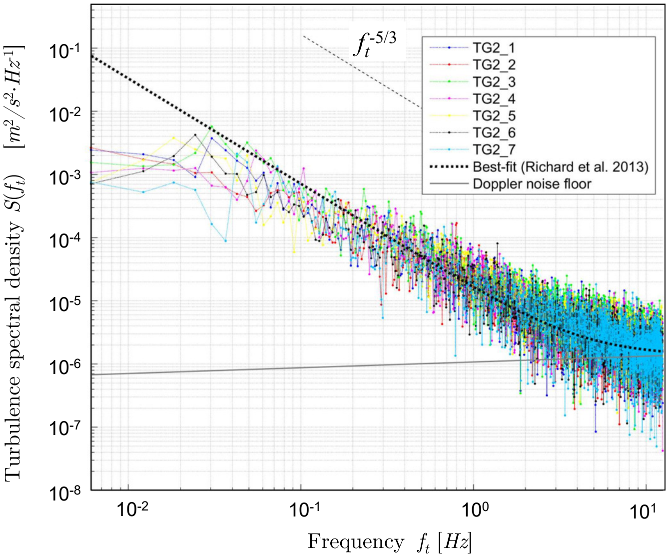

(b) TG2

Figure 6.9: Measured current turbulent energy spectra.

Table 6.5 lists the repeatability analysis results for the measured wave and current conditions. The standard deviations and standard deviations of the mean are both ideally small for the repeated tests, except for H_{max}. H_{max} records the maximum wave height in 3000 waves, which corresponds to an exceeding probability of approximately 0.03% in the present tests. Compared with H_s and $H_{1/10}$, H_{max} has a higher standard deviation, as it is affected by the instantaneous superposition of the incoming waves, reflected waves from the absorption structure, diffracted waves from the pile and the interactions between waves and currents. Further, the measured turbulent intensities of repeated tests show a standard deviation below 0.53%. This leads to the conclusion that uncertainties in turbulence intensity for repeated tests are limited.

Table 6.5: Repeatability of measured wave and current parameters

TG1	H_s [m]	$H_{1/10}$ [m]	H_{max} [m]	T_p [s]	$T_{m-1,0}$ [s]	U_c [m/s]	T_i [%]
$\bar{q}$	0.063	0.080	0.237	1.16	1.07	-0.186	6.57
$\sigma(q)$	0.0007	0.0008	0.0275	0.0163	0.0029	0.0025	0.32
$\sigma(\bar{q})$	0.0003	0.0003	0.0104	0.006	0.0010	0.0009	0.13
TG2	H_s [m]	$H_{1/10}$ [m]	H_{max} [m]	T_p [s]	$T_{m-1,0}$ [s]	U_c [m/s]	T_i [%]
$\bar{q}$	0.062	0.078	0.195	0.97	0.92	-0.220	6.57
$\sigma(q)$	0.0008	0.0007	0.0180	0.0133	0.0021	0.0021	0.53
$\sigma(\bar{q})$	0.0003	0.0003	0.0068	0.005	0.0009	0.0008	0.20

6.2.5 Repeatability of armour layer flatness

The manual placement of armour stones makes it difficult to build a perfectly flat armour layer. The armour stones are randomly distributed and form a rough and rugged surface, as sketched in Figure 6.10. The averaged armour layer thickness and the flatness of the initial profile compose an important source of uncertainty in model building. Given the bed surface elevation in each grid point in the armour layer area (noted as Z), and the flatness (noted as F) can be expressed by a ratio between the standard deviation of bed surface elevation and the averaged layer thickness t_a, as Eq. (6.5),

$$F = \frac{\sigma(Z)}{t_a} \tag{6.5}$$

where, $\sigma(Z)$ is given in Eq. (6.6),

$$\sigma(Z) = \sqrt{\frac{1}{m-1}\sum_{k=1}^{m}(Z-\overline{Z})^2} \tag{6.6}$$

m is the number of grid points, F=0 represents a flat surface. The edge of the scour protection (the outer ring as shown in Figure 3.5) contains reposed armour stones and will result in a high standard deviation of layer thickness, thus is neglected in computing $\sigma(Z)$ and F. The results of layer thickness and flatness are shown in Table 6.6. The F value for each test is approximately 0.1, representing the surface coarseness is 10% of the thickness. The standard deviation of $\sigma(Z)$ is around 2 mm, which reasonably matches the stone size. The standard deviations of the layer thickness $\sigma(t_a)$ and of the flatness $\sigma(F)$ can be calculated through Eq. (6.1). The standard deviations of the mean values, $\sigma(\overline{t_a})$ and $\sigma(\overline{F})$, are calculated through Eq. (6.2). Statistically, for TG1 and TG2, $\sigma(t_a) \approx$ 0.6 mm and $\sigma(F) \approx$ 0.011 to 0.021, as listed in Table 6.7. The results indicate a reasonable repeatability of the armour layer construction with regard to the thickness, but repeatability for the flatness is not ideal. Meanwhile, there remain several factors that are not strictly treated within the present work, such as the edge repose angles and the exact armour stone volume of each subarea. Overall, the manual construction of armour layer is one important source of randomness and uncertainty herein the experimental conditions.

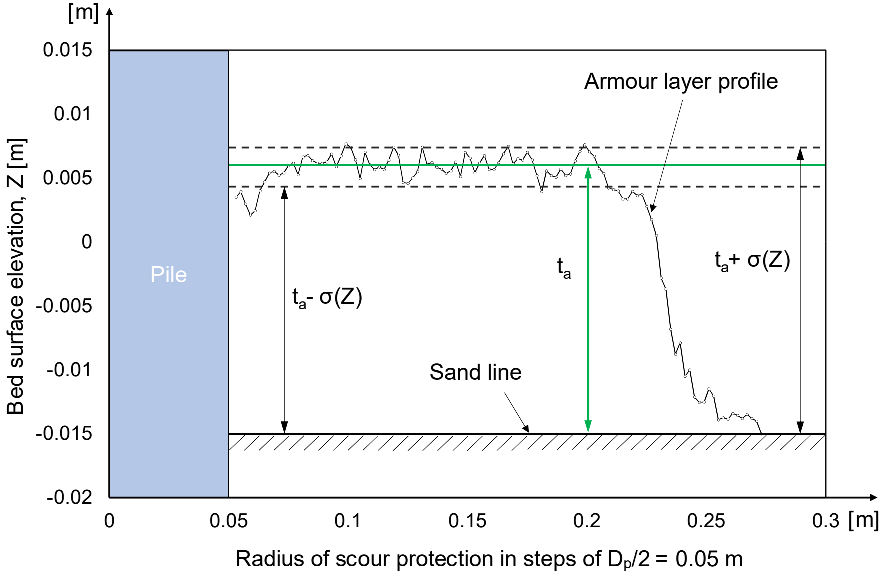

Figure 6.10: Sketch of flatness of armour layer thickness.

6.3 Results

The damage of scour protection is quantified based on the S_{3D} number (Eq. 3.14). Besides the global S_{3D} number, the damage number in each subarea is given in

Table 6.6: Layer thickness (t_a) and flatness (F) from initial scans of the armour layer

Test ID	t_a [mm]	$\sigma(Z)$ [mm]	F [-]	Test ID	t_a [mm]	$\sigma(Z)$ [mm]	F [-]
TG1_1	16.5	1.7	0.11	TG2_1	18.5	1.8	0.10
TG1_2	18.4	1.6	0.08	TG2_2	18.5	1.7	0.09
TG1_3	17.6	1.4	0.08	TG2_3	18.1	2.0	0.11
TG1_4	17.6	2.5	0.14	TG2_4	18.4	1.6	0.08
TG1_5	17.5	1.9	0.11	TG2_5	17.1	1.8	0.11
TG1_6	18.1	1.5	0.09	TG2_6	17.8	1.9	0.11
TG1_7	18.1	2.1	0.11	TG2_7	17.2	1.5	0.09

Table 6.7: Repeatability of flatness of initial scans

Test group	$\overline{t_a}$ [mm]	$\overline{F}$ [-]	$\sigma(t_a)$ [mm]	$\sigma(F)$ [-]	$\sigma(\overline{t_a})$ [mm]	$\sigma(\overline{F})$ [-]
TG_1	17.7	0.103	0.62	0.021	0.24	0.008
TG_2	17.9	0.099	0.60	0.011	0.23	0.004

Eq. (6.7),

$$S_{3D,i} = \frac{V_i}{D_{n50} \cdot S_P} \tag{6.7}$$

where i is the index of the subarea, see Figure 3.5. and V_i is the eroded volume of the i-th subarea.

6.3.1 Measurement effects due to handheld laser scanner

The scan measurement quality of a handheld laser scanner will significantly affect the S_{3D} result mainly attributed to the disturbances from calibration, scanning speed and angle, scanning dark area, and, scanning area immersed in water. Firstly, the Cartesian system needs to be calibrated during each measurement, which can introduce small relative translation and rotation between the initial and the end profiles. Secondly, the scanning angle and speed can affect the data collection. As the handheld laser scanner captures and processes reflected infrared light to generated points in space, the scanning area needs to be slowly swept in different angles in order to avoid shadow effect. Thirdly, the quality of measurement can deteriorate when scanning dark stones and dark areas, which is attributed to the surface absorption of light. As the armour stones are sometimes blocked with each other, the scanned profile misses points unavoidably in dark gaps between the stones despite the specific colouring of stones. This can be handled in post processing by adopting a grid resolution close to the stone diameter to maintain the best scan quality. Additionally, the scanned area should not be immersed in water as errors could be introduced due to the light refraction in water. In general, it is necessary to manipulate the handheld laser scanner and process the data carefully to minimize the inaccuracy in calibration and measurement.

The quantification of the measurement effects relies on repeated scans of the same profile in TG1_4. The end profile of this case has been scanned for five times (measurement 1 - 5 in Figure 6.11) and the damage numbers $S_{3D,i}$ are processed using Equation (6.7) and are plotted in Figure 6.11.

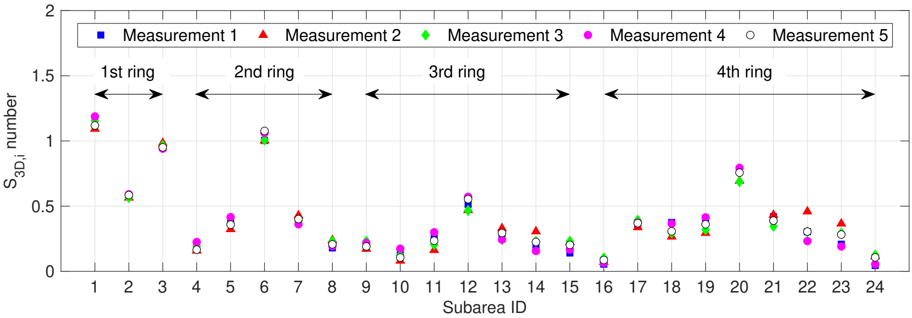

Figure 6.11: Results of repetitive damage measurement in case TG1_4.

By means of a statistic analysis, the standard deviation of global damage number is $\sigma(S_{3D}) = 0.039$, the maximum difference of S_{3D} between the five measurements is 0.095. Taking into account that the layer thickness contains approximately 9 layers of armour stones, the S_{3D} difference between measurements is much less than the layer number of armour stones (0.095/9=1%). The maximum standard deviation of subarea damage number is $\sigma(S_{3D,i}) = 0.083$, which happens in subarea 22 in the 4th ring. The higher inaccuracy of measurement in the 4th ring is attributed to the reason that the scanning vision was not complete enough to cover the reposed armour layer stones at the edge where the shadow effect was relatively strong. The results show a limited uncertainty due to measurement effects in the present experiment based on case TG1_4.

6.3.2 Damage patterns

The initial and damaged profiles of the scour protection layers for TG1 are visualized in Figure 6.12. Through a visual evaluation, the damage profiles exhibit similar patterns between each case. The erosion happens mainly at two regions: (1) the two sides near the pile towards the current incoming direction (45° to 90° and 270° to 315°); (2) the lee-side (135° to 225°) and away from the pile, and forms a butterfly-like shape as observed in all end profiles presented in Figure 6.12. The accretion of armour stones occurs mostly in the current downstream direction (90° to 135° and 225° to 270°), which is formed due to the transport process of the armour stones from the eroded regions. The damage and accretion are not symmetrical in the two sides. Meanwhile, rare erosion occurs in the incoming current upstream side (315° to 360° and 0° to 45°, where 360° coincides with 0° in Figure 6.12). The erosion pattern matches the shear stress distribution around a cylinder pile in steady current provided in Hjorth (1975). Accordingly, the damage profiles for TG2 are visualized in Figure 6.13. Similar to the patterns in TG1, TG2 shows that more damage occurs in the areas near the pile towards the incoming current direction (45° to 90° and 270° to 315°). The lee-side between 135° and 225° also suffers erosion damage, however, different from the patterns in TG1, the damaged areas in TG2 stretch longer in the wake and lead to significant erosions in the edge ring. Meanwhile, the accretions of armour stones in areas from 90° to 135° and from 225° to 270° are not obvious. This is attributed to the fact that the stones that are initiated from the side of pile by the high flow velocity around the pile are moved to the lee-side area, where strong lee-wake vortex brings them further to out of the edge. The photos of the end states of TG1_4 and TG2_4 presented in Figure 6.14 directly reflect the damage areas. Through visual assessment, the scour protections are dynamically stable in these tests, as there are no exposure of sediment beneath the scour protection layer.

Under the applied hydraulic conditions in TG1, the armour layer remains intact in the pure current action scenario. It is asserted that the presence of wave induced bottom velocity triggers the erosion. Regarding the conditions of waves opposing current, it is observed that the armour stones near the pile start to roll upward when a low wave trough passes the pile and stop rolling or fall down when a following wave crest passes. The high wave crest can also entrain some armour stones back towards the current incoming direction. The motion modes of the transported armour stones are mainly rolling and flipping, while a small amount of fine grains float and suspend for a very short time, usually within one second. However, with the high current boundary condition used in TG2, some armour stones are already moved by the pure action of the current within the current acceleration stage (5 minutes for every test), leading to a higher erosion in the wake region and at the edge of the armour layer. Small sand ripples are observed everywhere out of the scour protection region in the sandbox, but the bed deformation is relatively small to the pile size and the erosion failure due to large bed deformation is not observed in the present experiments.

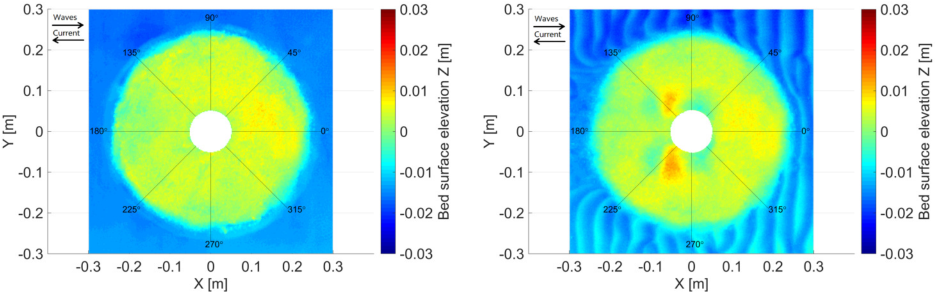

(a) TG1_1 start profile **(b)** TG1_1 end profile

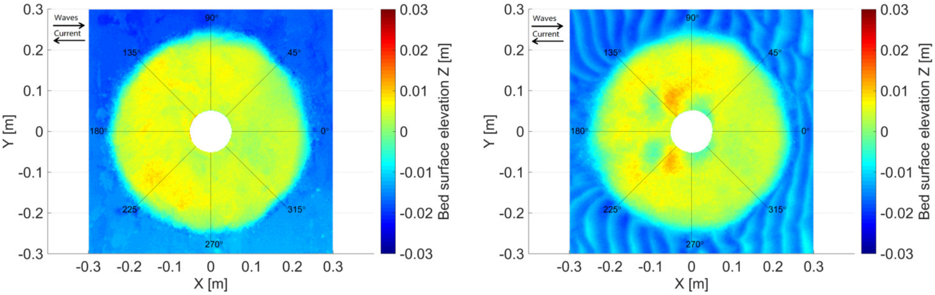

(c) TG1_2 start profile **(d)** TG1_2 end profile

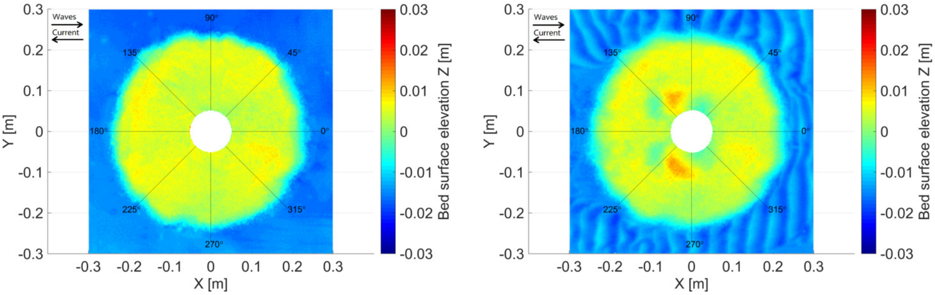

(e) TG1_3 start profile **(f)** TG1_3 end profile

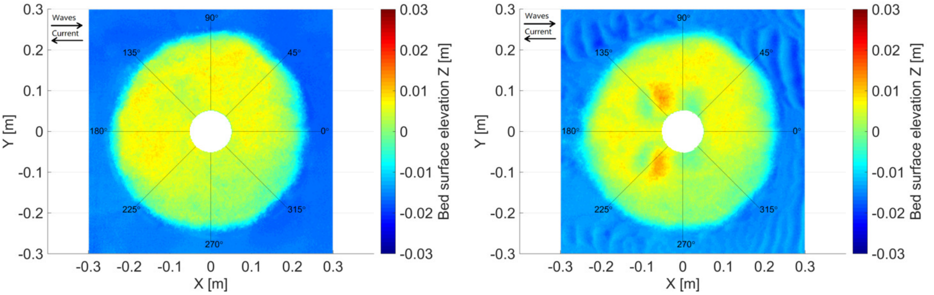

(g) TG1_4 start profile **(h)** TG1_4 end profile

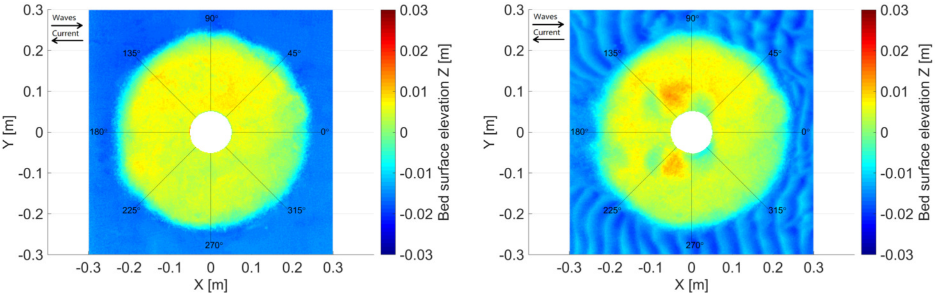

(i) TG1_5 start profile **(j)** TG1_5 end profile

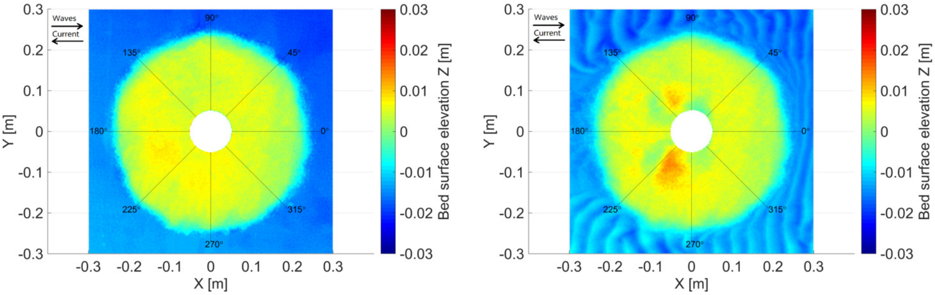

(k) TG1_6 start profile **(l)** TG1_6 end profile

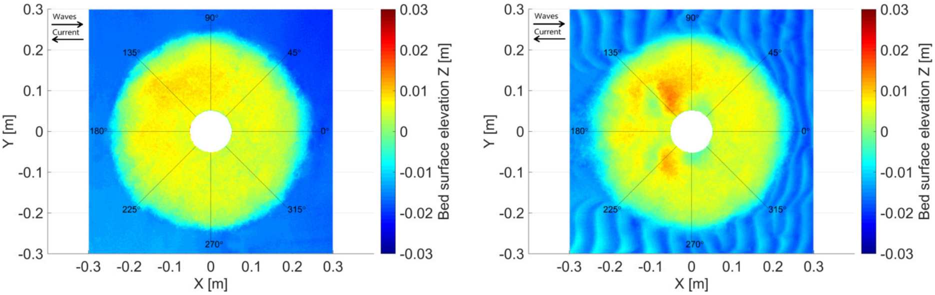

(m) TG1_7 start profile **(n)** TG1_7 end profile

Figure 6.12: Initial and end profiles of TG1.

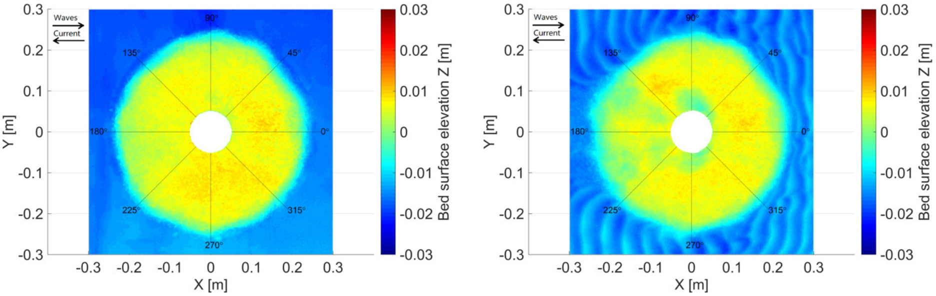

(a) TG2_1 start profile **(b)** TG2_1 end profile

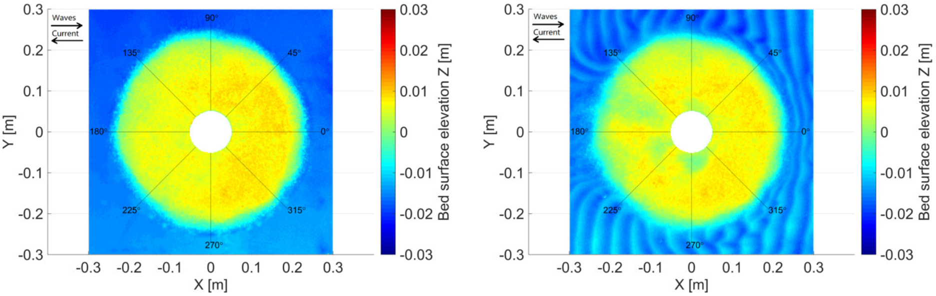

(c) TG2_2 start profile **(d)** TG2_2 end profile

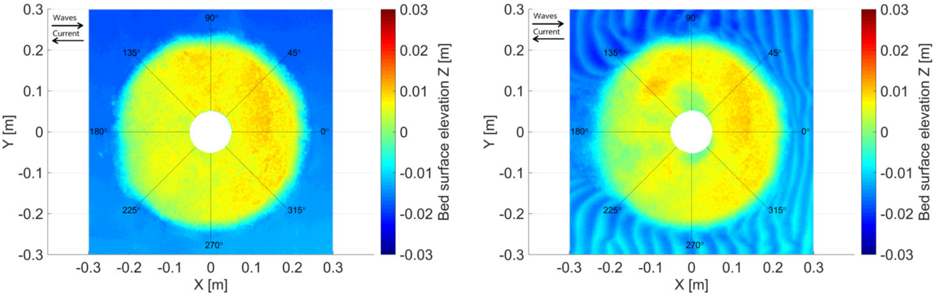

(e) TG2_3 start profile **(f)** TG2_3 end profile

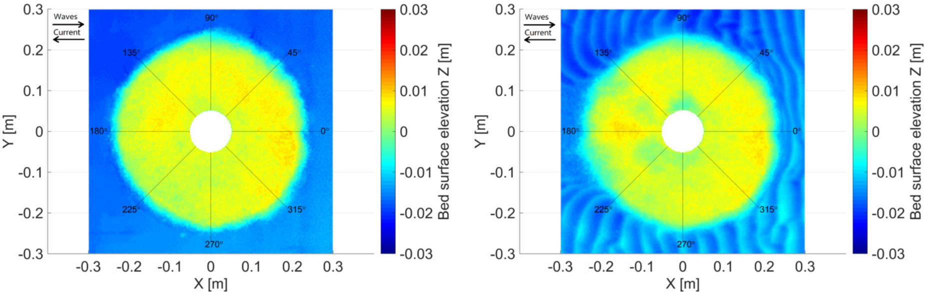

(g) TG2_4 start profile **(h)** TG2_4 end profile

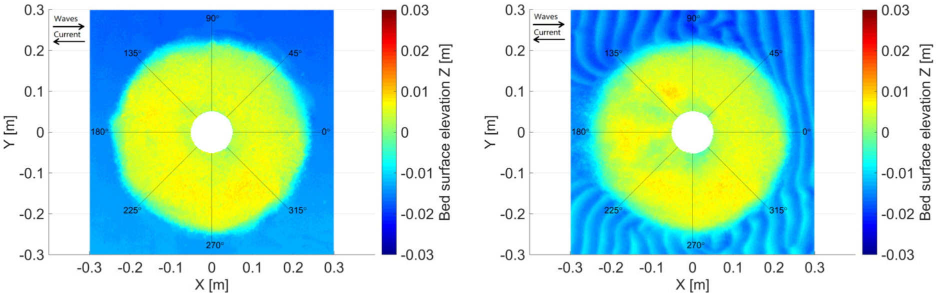

(i) TG2_5 start profile **(j)** TG2_5 end profile

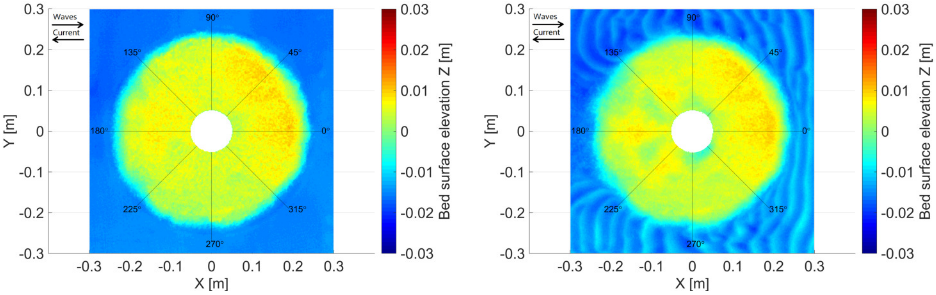

(k) TG2_6 start profile **(l)** TG2_6 end profile

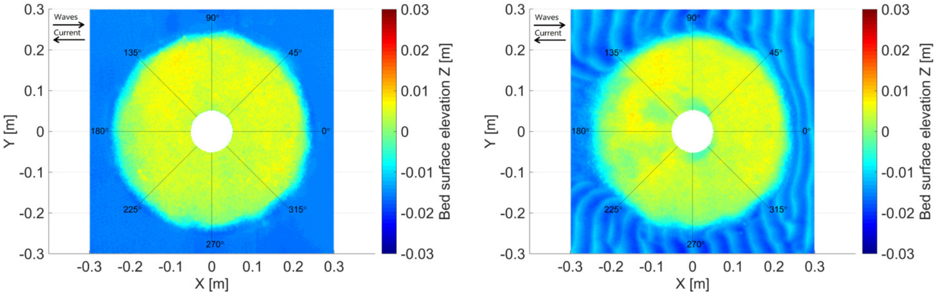

(m) TG2_7 start profile **(n)** TG2_7 end profile

Figure 6.13: Initial and end profiles of TG2.

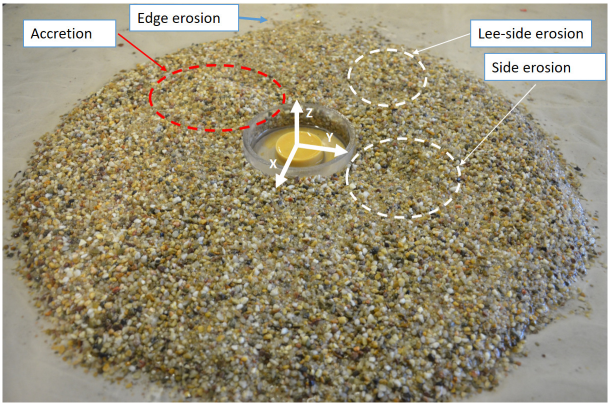

(a) TG1_4 end state

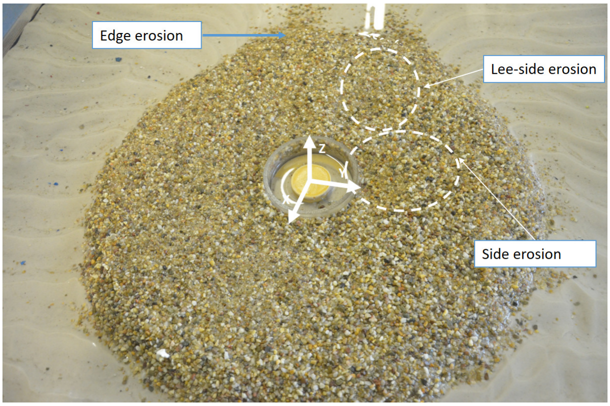

(b) TG2_4 end state

Figure 6.14: Photo visualisation of erosion and accretion areas in the end profiles: **(a)** TG1_4 end state; **(b)** TG2_4 end state.

6.3.3 Model effects analysis

As pure visual assessment is difficult to highlight the subtle differences of the repeated tests, quantitative analysis of the measured global damage results is essential for the discussion of model effects. Firstly, the measured global damage numbers are calculated with Eq. (3.14) and are listed in Table 6.8. For TG1, the mean of S_{3D} is $\overline{S_{3D}} = 1.208$ and the standard deviation of S_{3D} is $\sigma(S_{3D}) = 0.125$. The standard deviation of the mean $\sigma(\overline{S_{3D}}) = 0.047$. For TG2, $\overline{S_{3D}} = 1.269$, $\sigma(S_{3D}) = 0.257$ and $\sigma(\overline{S_{3D}}) = 0.097$. Though the S_{3D} result exhibits a satisfactory repeatability in terms of both S_{3D} and $\overline{S_{3D}}$, it should be noted that the maximum damages happen in different subareas (subarea 1, 3 and 6). Here, subarea 1 and 3 are located in the inner ring and subarea 6 is located in the current downstream side and in the second ring (see Figure 3.5). Despite the asymmetrical pattern of the armour layer damage around the pile that causes the maximum $S_{3D,i}$

is located alternatively between subarea 1 and subarea 3, one can observe that the maximum damage does not necessarily occur close to the pile but possibly meters far in the prototype scenario. This is because the lee-wake vortex can introduce higher bed shear stress than the horseshoe vortex, where the former can affect the entire wake area and the latter affects only the areas very close to the pile as shown in Figure 2.9. The phenomenon that the lee-wake vortex induced damage being higher than the horseshoe vortex induced damage is also presented in Nielsen and Petersen (2019) and in Appendix A.

Table 6.8: Damage numbers of scour protection armour layer and associated subarea of where maximum erosion is located

Test ID	S_{3D}	Max $S_{3D,i}$ in subarea i	Test ID	S_{3D}	Max $S_{3D,i}$ in subarea i
TG1_1	1.382	1	TG2_1	1.628	3
TG1_2	1.250	6	TG2_2	1.317	3
TG1_3	1.241	3	TG2_3	1.540	1
TG1_4	1.173	1	TG2_4	1.140	1
TG1_5	1.304	3	TG2_5	1.196	6
TG1_6	1.020	6	TG2_6	1.196	3
TG1_7	1.087	6	TG2_7	0.865	3

Assuming the damage in each subarea follows a normal distribution, the 95% confidence interval of the subarea damage $S_{3D,i}$ is $[\overline{S_{3D,i}} - 2\sigma(S_{3D,i}), \overline{S_{3D,i}} + 2\sigma(S_{3D,i})]$. A narrow range of the 95% confidence interval of $S_{3D,i}$ indicates a good repeatability of the scour protection armour layer damage and a low uncertainty level. In Figure 6.15 the damage numbers in subareas 1 to 15 and the corresponding 95% confidence intervals for TG1 and TG2 are plotted. The results show that the uncertainty level of the local damage strongly depends on the mean subarea damage number $\overline{S_{3D,i}}$. Referring to Figure 3.5, the subareas which are located in the current incoming side have both low $\overline{S_{3D,i}}$ and uncertainty level $\sigma(S_{3D,i})$. For subareas 1, 3, 6 and 12, the local damage level is high, correspondingly, $\sigma(S_{3D,i})$ is significantly higher. The relationships between $\overline{S_{3D,i}}$ and $\sigma(S_{3D,i})$ are visualized in Figure 6.16. As references, the standard deviations of $S_{3D,i}$ due to measurement and the standard deviations of global damage number S_{3D} in each test group are provided. Clearly, compared with the uncertainty due to measurement and the uncertainty of global S_{3D}, the subarea damage numbers $S_{3D,i}$ show a much higher uncertainty level. The maximum $\sigma(S_{3D,i})$ is up to 0.42 for TG2, which is 1.6 times of $\sigma(S_{3D})$. In terms of the local damage, the results obtained in the small scale test are hardly repeatable, which show strong model effects that are inherent in such experiments.

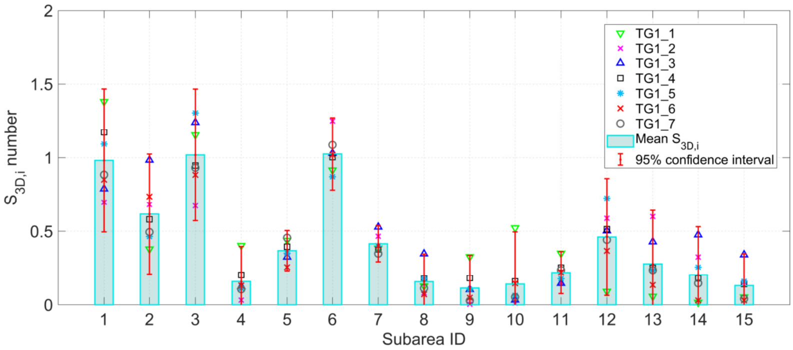

(a) TG1

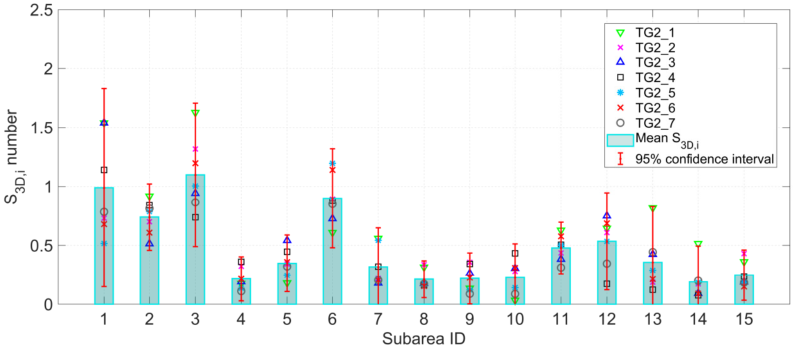

(b) TG2

Figure 6.15: Damage numbers in each subarea along with the 95% confidence interval.

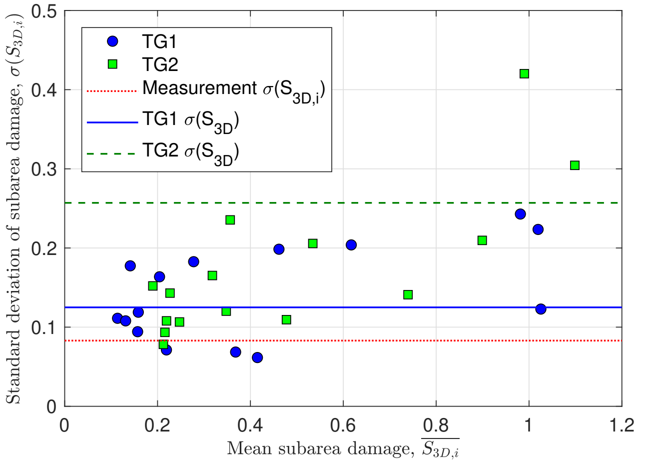

Figure 6.16: Relationship between the mean subarea damage $\overline{S_{3D,i}}$ and the standard deviation $\sigma(S_{3D,i})$.

6.4 Discussion

An overview of the relative uncertainties of both the model inputs and outputs (global and subarea damage numbers) is listed in Table 6.9. For TG1, the ratio between the standard deviation of the global damage and its mean is $\sigma(S_{3D})/\overline{S_{3D}} = 10.3\%$, which is comparable to those obtained from statistical analysis of the repeated tests given in De Vos et al. (2012) (see Table 6.10), where $\sigma(S_{3D})/\overline{S_{3D}} \approx 11\%$. For TG2, the standard deviation of the global damage, $\sigma(S_{3D})$, is up to 20.3%·$\overline{S_{3D}}$. The $\sigma(S_{3D})/\overline{S_{3D}}$ value is larger than those from De Vos et al. (2012), which is mainly due to the limited number of repeated tests in the study of De Vos et al. (2012). The standard deviation of the local damage is even higher, where $\sigma(S_{3D,i}) = 33.1\% \cdot \overline{S_{3D}}$. As the physics of sediment transport under wave and current contains various stochastic processes due to the presence of waves, turbulence and non-uniformly distributed sediment particles, considerably high uncertainty level and significant model effects are inevitable as a result of (1) non-repeatability of instantaneous flow field velocity distribution and (2) non-repeatability of shape, orientation and distribution of the armour stones. This leads us to a further discussion of the possible sources of uncertainties and ways to reduce the model effects.

Table 6.9: Summary of expression of model effects

	$\overline{S_{3D}}$	$\sigma(S_{3D})$	$\frac{\sigma(U_c)}{U_c}$	$\frac{\sigma(H_s)}{H_s}$	$\frac{\sigma(T_p)}{T_p}$	$\frac{\sigma(t_a)}{t_a}$	$\frac{\sigma(F)}{F}$	$\frac{\sigma(S_{3D})}{\overline{S_{3D}}}$	$\frac{max[\sigma(S_{3D,i})]}{\overline{S_{3D}}}$
TG1	1.208	0.125	1.3%	1.1%	1.4%	3.5%	20.2%	10.3%	19.9%
TG2	1.269	0.257	0.9%	1.2%	1.4%	3.3%	10.7%	20.3%	33.1%

Table 6.10: S_{3D} and $\sigma(S_{3D})/\overline{S_{3D}}$ results from repeated tests in De Vos et al. (2012).

	S_{3D} of Test no. 15 in De Vos et al. (2012)	S_{3D} of Test no. 20 in De Vos et al. (2012)
Repeat 1	0.37	1.84
Repeat 2	0.31	1.53
Repeat 3	0.38	1.55
$\sigma(S_{3D})/\overline{S_{3D}}$	10.7%	10.6%

- Incoming waves and current.
  Under the conditions of the same wave spectra parameters, the model effects from the same and distinct wave trains are negligible. Referring to the measured wave conditions (Table 6.4) and the damage results (Table 6.8), the same wave train cases (TG1_1 to TG1_3, TG2_1 to TG2_3) can neither contribute to a same global damage nor a same subarea damage, indicating that the influence of same or distinct wave trains on the armour layer dynamic stability is weak. As discussed in Section 6.2.4, the measured wave spectra and

wave height exceeding probabilities are not sensitive to the randomness of a specific wave train, except for the maximum wave height H_{max}. As listed in Table 6.9, the relative standard deviations, $\sigma(H_{max})/\overline{H_{max}}$ are 11.6% for TG1 and 9.2% for TG2, which indicates that $\sigma(H_{max})/\overline{H_{max}}$ could be a major contributor to $\sigma(S_{3D})/\overline{S_{3D}}$ compared to other wave parameters. The relationship between recorded H_{max} and S_{3D} is plotted in Figure 6.17. The fitted trend lines show that higher H_{max} could give rise to higher S_{3D} number, which is reasonable as higher H_{max} introduces larger wave bottom orbital velocity acting on the armour stones. However, the correlation for the two fitted lines are weak ($R^2 < 0.52$). Despite H_{max}, no clear evidence in this study can prove the links between the low uncertainty level of other measured wave parameters and the high uncertainty of local scour protection damage. For the incoming current, the uncertainty levels of depth-averaged current velocity and turbulence intensity weakly affect the uncertainty of local damage.

- Thickness (t_a) and flatness (F) of the armour layer.
  The uncertainty due to the flatness of the armour layer is the highest among the discussed model inputs. Understandably, it contributes to high uncertainty of damage outputs. Reducing the F value and the uncertainty of F value is beneficial for lowering the model effects. This may be achieved by using moulds to build the armour layer or via machine aided model construction instead of inaccurate handwork in laboratory. In real engineering, it is impossible to build ideally flat armour layers in a wind farm. Therefore, conservatively, at least $\sigma(S_{3D}) = 20\% S_{3D}$ is suggested to be considered when designing a monopile scour protection made up with multiple layers of small grains. However, it is not yet clear how much the total model effects can be reduced with such an approach. However, it can be seen that $\sigma(F)/\overline{F}$ is lower for TG2, but the relative uncertainty of S_{3D} in TG2 is higher than in TG1. This results in less evidence that the relative uncertainty of S_{3D} is strongly dependent on the flatness of the armour layer.

Despite the uncertainty of wave and current conditions around the model for each test as well as the armour layer model construction, the uncertainty level of global or subarea damage are closely associated with the expected damage level. Taking an ideal situation where the scour protection is static, the uncertainty of S_{3D} will only be attributed to the measurement uncertainty. When a high wave or high current condition is applied, the vortices and flow field around the pile can be more chaotic, which will eventually lead to both high damage and high uncertainty of damage.

6.5 Conclusions

In this Chapter, two groups of small scale repeated tests of monopile scour protection in combined wave and current conditions are introduced. The aim is to quantitatively analyse the measurement effects and model effects regarding ero-

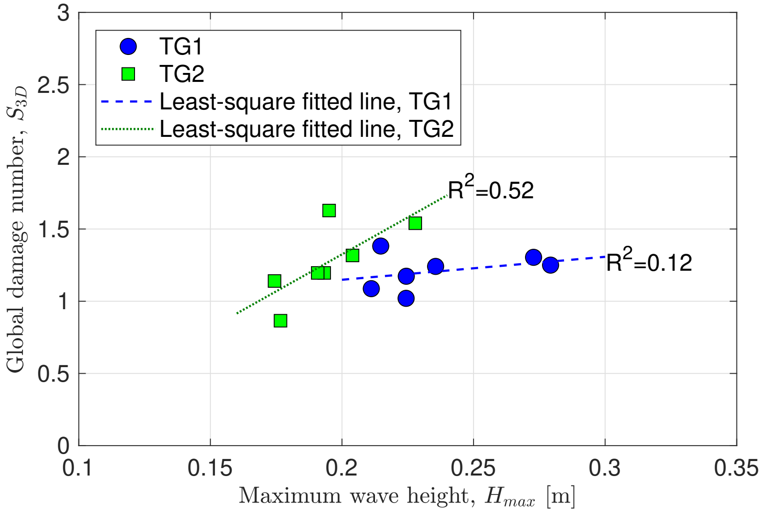

Figure 6.17: Relationship between maximum wave height H_{max} and global damage number S_{3D}.

sion damage in monopile scour protection experiments. The study arrives in the conclusions as below:

- Measurement effects due to the application of the handheld laser scanner contribute limited to the total uncertainty, the standard deviation of the global damage number is $\sigma(S_{3D}) = 0.039$ for five repeated measurements. The maximum difference of S_{3D} among the measurements is 0.095. The maximum standard deviation of the subarea damage number is $\sigma(S_{3D,i}) = 0.083$. The results show a limited impact from measurement effects to the total uncertainty.

- The model effects are analysed by means of two groups of repeated tests. In the two test groups, the wave and current conditions are well replicated as listed in Table 6.9. The damage profiles have shown a repeatable damage distribution. The standard deviation of the global damage number is up to $\sigma(S_{3D}) = 0.257$ and $\sigma(S_{3D}) = 20.3\% \cdot \overline{S_{3D}}$. The standard deviation of the subarea damage number $\underline{\sigma(S_{3D,i})}$ reaches even larger values of $\sigma(S_{3D,i}) = 0.42$ and $\sigma(S_{3D,i}) = 33.1\% \cdot \overline{S_{3D}}$. The low repeatability of the maximum wave height H_{max} and the flatness of the armour layer thickness due to the irregular armour stones distribution are two important sources of the total uncertainty. The irreproducible and chaotic flow field around the pile is considered to be the key reason for the large standard deviation of scour protection damage number. As for the future design, a standard deviation $\sigma(S_{3D})$ up to $20\%S_{3D}$ is conservatively expected regarding a dynamically stable monopile scour protection made up with multiple layers of small grains.

The obtained results on measurement effects and model effects provides a valid data support for the future work on the analysis of scale effects that exist between small and large scale experiments of monopile scour protection erosion. The standard deviation of the armour layer damage can be applied to the design of a dynamically stable monopile scour protection considering a reasonably sufficient safety margin. The achieved data can also form the basis in the development of other novel design methodologies for monopile scour protection, e.g., the reliability based design considering the whole life cycle of OWT Fazeres-Ferradosa et al. (2018b). In the meantime, it should be addressed that the results may be limited to the dynamically stable scour protection with multiple layer small grains and the specific wave and current conditions. More investigations are anticipated for other environmental conditions and other scour protection configurations.

Chapter 7

Analysis of experimental uncertainty in measurement

7.1 Sources of uncertainties in measurement

In Chapter 6, the model effects analysis has shown that under the conditions of repeatable wave and current conditions, the experimental uncertainties of local and global damage of scour protection can still be high. The unrepeatable physical process and armour layer model building are believed to be the main reasons. However, the uncertainties from measured conditions can still propagate to the final result thanks to the highly nonlinear hydraulic model. Taking a further look into the S_{3D} prediction formula (Eq. 3.15) by De Vos et al. (2012), the predictions are fitted to cubic of the wave and current induced velocities and square of the wave period. In this sense, a formal analysis of uncertainties due to measurement can help us to investigate how much uncertainties are propagated to the final damage result. This work has been carried out based on the guidelines of JCGM (2008).

An initial step of the analysis is to identify the sources of uncertainty in the experiment. In the experiment described in Chapter 6, the sources of uncertainty can be categorised as:

- Randomness due to probe installation and calibration, which mainly refers to the probes such as water depth sensor, wave gauges, ADV and hand laser scanner.

- Randomness due to wave and current condition in wave flume. The wave and current interaction process is stochastic and unrepeatable. In addition randomness also is also derived from generation, reflection and absorption of waves.

- Randomness due to data-processing. The parameters in post-processing can affect value of the obtained wave characteristics, such as the wave height and period, hence, this leads to a minor deviation between the real value and processed value.

- Randomness due to scour protection modelling. As seen from last Chapter, this randomness can cause a very large standard deviation of the local and global S_{3D}.

Let's rewrite the scour protection damage number formula (Eq. 3.15) of De Vos et al. (2012) as Eq. (7.1),

$$S_{3D,pred} = N^{b_0} \times \left(a_0 \frac{{U_m}^3 T_{m-1,0}^2}{\sqrt{gd}(s-1)^{3/2} D_{n50}^2} + a1 \left(a2 + a3 \frac{\left(\frac{U_c}{w_s}\right)^2 \left(|U_c| + a_4 U_m\right)^2 \sqrt{d}}{g {D_{n50}}^{3/2}} \right) \right) \tag{7.1}$$

The sources of uncertainty can be distinguished as: (1) number of waves N; (2)mean wave orbital velocity U_m; (3) wave period $T_{m-1,0}$; (4) current velocity U_c; (5) water depth d; (6) stone diameter D_{n50}; (7) rock density s. The expression for U_m as given Eq. (2.32) is a function of wave spectrum and can be rewritten as Eq. (7.2) while applying a two parameter Jonswap spectrum,

$$U_m = f(H_s, T_p) \tag{7.2}$$

Thus, H_s and T_p can be seen as two sources of uncertainties. In addition, the coefficient $a_4 = U_r/6.4$ in wave opposing current condition, is a function of $T_{m-1,0}$ and wave height H_s as given in Eq. (3.16).

For the sake of simplification, the analysis only focuses on the measurement uncertainties of four parameters related to wave and current conditions, H_s, $T_{m-1,0}$, T_p and U_c, so Eq. (7.3) reduces to

$$S_{3D} = f(H_s, T_{m-1,0}, T_p, U_c) \tag{7.3}$$

Therefore, an uncertainty from wave and current measurements which propagates to S_{3D} can be obtained as a combined uncertainty according to the law of propagation (Eq. 4.8) assuming the four measured parameters are independent, as Eq. (7.4),

$$\begin{aligned} u_C^2(S_{3D}) = {} & \left(\frac{\partial S_{3D}}{\partial H_s}\right)^2 u^2(H_s) + \left(\frac{\partial S_{3D}}{\partial T_{m-1,0}}\right)^2 u^2(T_{m-1,0}) + \\ & \left(\frac{\partial S_{3D}}{\partial T_p}\right)^2 u^2(T_p) + \left(\frac{\partial S_{3D}}{\partial U_c}\right)^2 u^2(U_c) \end{aligned} \tag{7.4}$$

where u_C is the combined uncertainty and u is the standard uncertainty of each parameter. For the rest parameters, the water depth d and the number of waves N should have smaller contributions to the combined uncertainties as their power coefficients are smaller than 1 in Eq. (7.1). The stone size D_{n50} and density s may cause relatively higher uncertainties due to their quadratic and sub-quadratic contributions in Eq. (7.1).

7.2 Uncertainty in individual test

The uncertainty in an individual test is mainly affected by single measurement and data processing. For wave properties H_s, T_p and $T_{m-1,0}$, the measured values are determined by the accuracy of the wave gauges and the parameters used in the spectral analysis. The wave surface elevation data collection is continuous during a test case, therefore a repetitive measurement is not possible, the uncertainty of wave height due to wave gauge accuracy can be estimated by the Type B evaluation. The accuracy of meter reading is $\epsilon_{H_s} = 1$ mm, where a rectangular distribution between $-\epsilon_{H_s}$ and $+\epsilon_{H_s}$ mm is assumed. This gives $u(H_s)$ as Eq. (7.5).

$$u(H_s) = u_B(H_s) = \frac{\epsilon_{H_s}}{\sqrt{3}} = 0.577mm = 5.77 \times 10^{-4}m \tag{7.5}$$

The spectral analysis of a wave series is based on a Fast Fourier Transformation (FFT) of the wave signal from time domain to frequency domain (Welch, 1967). It is important to mention that the quality of obtained spectrum $S(f)$ relies on the selection of the FFT parameters, which are mainly the total time of recorded data (T_r), the data number in a subseries (M_s), the length of subseries overlapping and tapering (T_d). Sand (1986) pointed out that the confidence interval of the estimated spectrum narrows as the number of subseries and the total time increase at the same time. When the total time of the recorded data is determined, the number of subseries (p_s) is then calculated by Eq. (7.6),

$$p_s = \frac{T_r - T_d}{M_s - T_d} \tag{7.6}$$

M_s is an integer of 2^n and T_d usually equals to 10%M - 20%M.

The FFT analysis results in a frequency band width on the wave spectrum of $\Delta f = f_s/M_s$, f_s is the sampling frequency and is 40 Hz for the wave gauges used in the small scale tests (see Section 6). According to Sand (1986), smaller Δf can maintain more frequency resolution but will lead to large variance of spectrum and a lot of spectral spikes, while large Δf will result in a low frequency resolution and an underestimated energy density near the peak frequency. This produces a deviance between the post-processed and the real T_p, which is considered as a source of uncertainty.

In this study, a wave train from small scale test TG1_1 is analysed so as to determine the uncertainties of T_p. The FFT analysis is done via the software of WaveLab (Frigaard and Lykke Andersen, 2014). The total data number in this wave train is approximately 92000 after cutting off of wave ramp up and ramp down, which is around 2000 waves. In order to achieve a smooth spectrum, the data number in each FFT subseries is 1024. The tapering and overlapping length is 20% of the subseries length. Figure 7.1 shows the comparison between the smoothed measured wave spectrum and the target JONSWAP wave spectrum with $\gamma = 3.3$.

The analysis results in a frequency resolution of Δf= 0.0396 Hz and the peak frequency is f_p= 0.8594 Hz. Conservatively, we assume the real f_p randomly

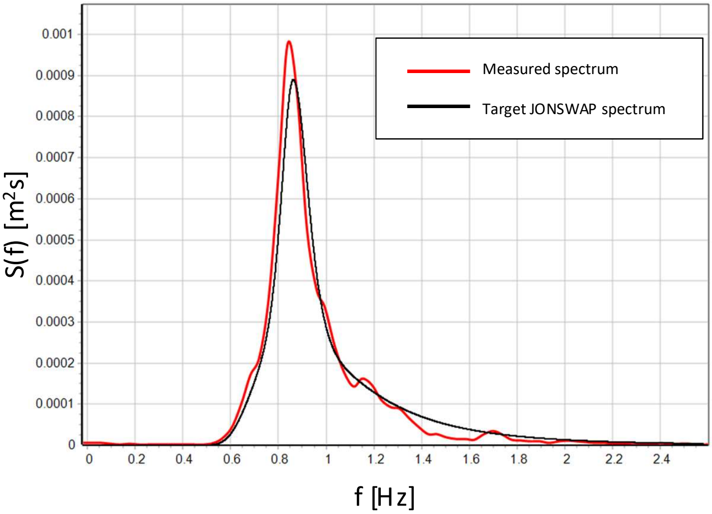

Figure 7.1: Smoothed measured wave spectrum in comparison with target JONSWAP spectrum.

locates in $[f_p - 0.5\Delta f, f_p + 0.5\Delta f]$, the real peak period therefore is 1.137 s $\leq T_p \leq$ 1.191 s. Assume the error of T_p is distributed averagely, we have the error of $\epsilon_{T_p} = 0.027$ s, the Type B uncertainty of T_p therefore is,

$$u(T_p) = u_B(T_p) = \frac{\epsilon_{T_p}}{\sqrt{3}} = 0.0157s \tag{7.7}$$

For the energy period $T_{m-1,0}$, it is less affected by the frequency resolution than T_p. To conservative estimate the uncertainty, the approximate relationship, $T_{m-1,0} = 0.9T_p$, can be applied (Hofland et al., 2017). This gives,

$$u_(T_{m-1,0}) = u_B(T_{m-1,0}) = 0.9u_B(T_p) = 0.0141s \tag{7.8}$$

The estimation in Eq. (7.8) does not represent a definite correlation between T_p and $T_{m-1,0}$ from the physics. The approximate relationship is only valid when an analytical JONSWAP spectrum is applied.

The current velocity uncertainty is analysed with a current time series obtained from TG1_1. The turbulence of current velocity results in a fluctuation of current velocity bounded within -0.238 m/s $\leq U_c \leq$ -0.135 m/s as displayed in Figure 7.2. The occurrence probability histogram is plotted in Figure 7.3, with a bin width of 0.002 m/s. The distribution of the occurrence probability can be fitted to a normal distribution of $U_c \sim N(\mu(U_c), \sigma^2(U_c))$, with $\mu(U_c) = -0.0187$ m/s and $\sigma(U_c) = 0.0137$ m/s. The coverage of 99% confidence interval is estimated to $\mu(U_c) - 2.58\sigma(U_c) \leq U_c \leq \mu(U_c) + 2.58\sigma(U_c)$, which is numerically -0.222 m/s

$\leq U_c \leq$ -0.151 m/s. Hence, the uncertainty due to the fluctuation can be obtained from a Type B uncertainty evaluation, as Eq. (7.9).

$$u_{B1}(U_c) = \sigma(U_c) = 0.0137m/s \tag{7.9}$$

In addition, the accuracy of ADV is $\epsilon_{U_c} = 1$ mm/s, which produces an uncertainty in measurement of $u_{B2}(U_c)$ (Eq. 7.10).

$$u_{B2}(U_c) = \frac{\epsilon_{U_c}}{\sqrt{3}} = 0.0003m/s \tag{7.10}$$

The uncertainty of U_c can be combined as Eq. (7.11),

$$u(U_c) = \sqrt{u_{B1}^2(U_c) + u_{B2}^2(U_c)} = 0.0137m/s \tag{7.11}$$

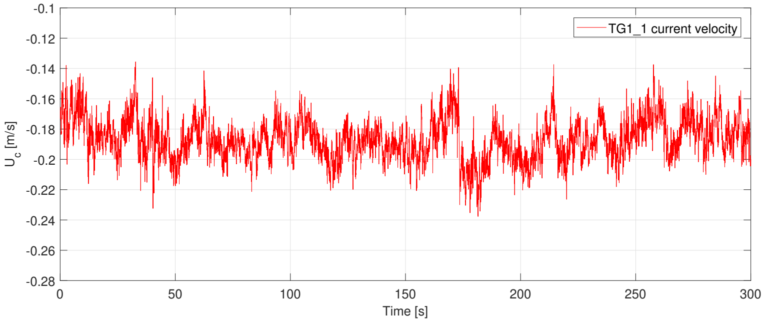

Figure 7.2: Fluctuation of current velocity in TG1_1.

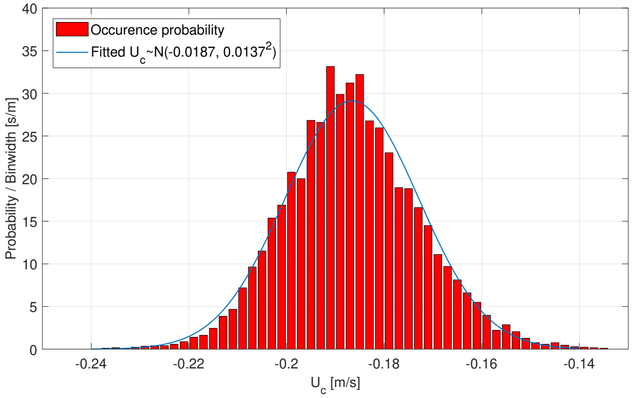

Figure 7.3: Occurence probability distribution and a fitted normal distribution

The total combined uncertainty of S_{3D} in an individual measurement then can be evaluated using Eq. (7.4). Table 7.1 listed the sensitivity coefficients of the inputs to S_{3D} result as well as the standard uncertainty of the inputs.

Table 7.1: Experimental uncertainties due to wave and current measurement in an individual test

Quantity q_i	H_s	T_p	$T_{m-1,0}$	U_c
$\frac{\partial S_{3D}}{\partial q_i}$	57.02 $[m^{-1}]$	4.96 $[s^{-1}]$	0.45 $[s^{-1}]$	-40.25 $[(m/s)^{-1}]$
$u(q_i)$	$5.77\times10^{-4}[m]$	$1.56\times10^{-2}[s]$	$1.40\times10^{-2}[s]$	$1.37\times10^{-2}[m/s]$
$\left(\frac{\partial S_{3D}}{\partial q_i}\right)^2 u^2(q_i)$	1.06×10^{-3}	6.30×10^{-3}	3.97×10^{-5}	3.04×10^{-1}

The numerical result yields,

$$u(S_{3D}) = u_C(S_{3D}) = \left[\sum_{i=1}^{4}\left(\frac{\partial S_{3D}}{\partial q_i}\right)^2 u^2(q_i)\right]^{\frac{1}{2}} = 0.558 \tag{7.12}$$

Therefore, in an individual test, the estimated uncertainty of S_{3D} due to measurement is approximately 0.558. This indicates that a considerable amount of uncertainty from measurement can propagate to the final uncertainty of the scour protection damage number. The major contributor to the uncertainty is the current velocity U_c due to the high standard uncertainty level of $u(U_c)$ and the quadratic relationship of U_c in Eq. (3.15). T_p and H_s are also important as they determine the cubic item U_m in Eq. (3.15).

7.3 Uncertainties in repeated test

The uncertainties in repeated test can be estimated using the Type A evaluation approach. Referring to the measured small scale test conditions listed in Table 6.4, the uncertainties can be obtained through Eq. (7.13) to (7.16), in which $n = 7$ is the number of repetition.

$$u(H_s) = \sqrt{\frac{1}{n}}\sigma(H_s) \tag{7.13}$$

$$u(T_p) = \sqrt{\frac{1}{n}}\sigma(T_p) \tag{7.14}$$

$$u(T_{m-1,0}) = \sqrt{\frac{1}{n}}\sigma(T_{m-1,0}) \tag{7.15}$$

$$u(U_c) = \sqrt{\frac{1}{n}}\sigma(U_c) \tag{7.16}$$

Table 7.2: Experimental uncertainties due to wave and current measurement in repeated tests

Uncertainties of TG1				
Quantity q_i	H_s	T_p	$T_{m-1,0}$	U_c
$\frac{\partial S_{3D}}{\partial q_i}$	51.38 $[m^{-1}]$	4.66 $[s^{-1}]$	0.45 $[s^{-1}]$	-38.11 $[(m/s)^{-1}]$
$u(q_i)$	2.61×$10^{-4}[m]$	6.16×$10^{-3}[s]$	1.11×$10^{-3}[s]$	9.37×$10^{-4}[m/s]$
$\left(\frac{\partial S_{3D}}{\partial q_i}\right)^2 u^2(q_i)$	1.80×10^{-4}	8.24×10^{-4}	2.50×10^{-7}	1.27×10^{-3}
$u(S_{3D})$	0.0478			
Uncertainties of TG2				
Quantity q_i	H_s	T_p	$T_{m-1,0}$	U_c
$\frac{\partial S_{3D}}{\partial q_i}$	30.45 $[m^{-1}]$	4.16 $[s^{-1}]$	0.19 $[s^{-1}]$	-45.95 $[(m/s)^{-1}]$
$u(q_i)$	2.86×$10^{-3}[m]$	5.05×$10^{-3}[s]$	8.00×$10^{-4}[s]$	7.78×$10^{-4}[m/s]$
$\left(\frac{\partial S_{3D}}{\partial q_i}\right)^2 u^2(q_i)$	7.57×10^{-5}	4.41×10^{-4}	2.25×10^{-8}	1.28×10^{-3}
$u(S_{3D})$	0.0424			

The sensitivity coefficients and uncertainty results of small scale tests TG1 and TG2 are derived in Table 7.2. The value of $u(S_{3D})$ represents the uncertainties which propagate from the input conditions to the damage result.

As for the measurement of damaged profiles, the uncertainty can be separated into two components, one is the uncertainty due to the measurement of the same scan, the other is sourced from repetitive test results. For the first component, as analysed in Chapter 6, the standard deviation of five repetitive measurements of one scan is $\sigma(S_{3D}) = 0.039$, therefore the Type A uncertainty evaluation leads,

$$u_{A1}(S_{3D}) = \sqrt{\frac{1}{5}}\sigma(S_{3D}) = 0.0174 \tag{7.17}$$

The second component can be estimated based on the Type A evaluation of the repetitive test results, from Table 6.8. The results for TG1 and TG2 are given in Eq. (7.18) and Eq. (7.19) separately.

$$u_{A2}(S_{3D}) = \sqrt{\frac{1}{7}}\sigma(S_{3D}) = 0.0472 \qquad for \quad TG1 \tag{7.18}$$

$$u_{A2}(S_{3D}) = \sqrt{\frac{1}{7}}\sigma(S_{3D}) = 0.0971 \qquad for \quad TG2 \tag{7.19}$$

The uncertainty of the scans are combined using Eq. (7.20).

$$u(S_{3D}) = \left[u_{A1}^2(S_{3D}) + u_{A2}^2(S_{3D})\right]^{\frac{1}{2}} \tag{7.20}$$

The results are listed in Table 7.3. As a reference, the uncertainties propagated from input conditions are listed as well. It is seen that the uncertainty component which is propagated from wave and current measurement takes a significant proportion. This also explains why high model effects exist in monopile scour protection damage test.

Table 7.3: Experimental uncertainties due to measurement in repeated tests

$u(S_{3D})$	Propagated from input conditions	Damage profile scanning
TG1	0.0478	0.0503
TG2	0.0424	0.0986

7.4 Conclusion and discussions

This chapter analyses the experimental uncertainty in small scale monopile scour protection experiment using a formal methodology recommended by JCGM (2008). For the sake of a reasonable simplification, the analysis focuses on four major influential parameters, H_s, T_p, $T_{m-1,0}$ and U_c, due to their high uncertainty levels and their high-order nonlinear relationships with the predicted S_{3D} as described in Eq. (3.15). The results clearly reflect the uncertainty level of such hydraulic modelling in an individual test and in a repeated test. Main conclusions are summarised as follows:

- The uncertainty in an individual test is $u(S_{3D}) = 0.558$. This value is assessed purely based on a propagation of uncertainties from the input parameters, and is considerably high compared with the obtained damage result. The major contributor is the uncertainty due to the current measurement.
- With repeated tests, the uncertainties of input parameters are assessed using Type A evaluation method. The results show much lower estimated $u(S_{3D})$ than an individual test for both TG1 and TG2. Compared with the uncertainties of measured S_{3D}, the propagated uncertainties are not negligible at all though the input repeatability is ideal as seen in Table. 6.5. This causes the difficulties of achieving a stable and reliable experimental result in such hydraulic modelling.

However, it is also necessary to mention that the predicted S_{3D} equation (Eq. 3.15) basically overestimates the damage results for TG1 and TG2 as the results listed in Table 7.4. The applicability of the prediction formula is not ideal for stone sizes and model scales out of range, as found in Looseveldt and Vannieuwenhuyse (2012) and Chapter 5. This in the meantime will over-predict the uncertainties that are propagated from the inputs. Nevertheless, in addition to the scour protection model construction, the uncertainties from measured wave and current conditions should be concerned for the model effects.

Table 7.4: Comparison between predicted and measured mean of S_{3D}

$\overline{S_{3D}}$	Predicted value	Measured value
TG1	2.163	1.208
TG2	2.654	1.269

Chapter 8

Analysis of scale effects

8.1 Scale effects of damage of monopile scour protection

As introduced in Chapter 4, applying a scaling rule in scaled down test, such as the Best Model, will lead to scale effects as a result of discarding some similarities. To have a clear insight of the scale effects on the basis of obtained experimental dataset, this chapter only focuses on the erosion damage of the monopile scour protection. Both small and large scale experimental data are applied for the analysis. The detailed descriptions of the experiments can be found in Chapter 5 for large scale experiments and in Chapter 6 for small scale experiments. The test conditions are summarised in Table 6.1, where, the cases TG1, TG2 and TG3 use 1:50 small scale models; PROTEUS Test 10B uses a 1:16.667 large scale model; PROTEUS Test 13B and Test 14 use 1:8.333 large scale models. Due to the limitation of the experimental setups, the scale effects of armour stone sinking and edge scour were not able to be discussed in this chapter.

Assuming the pile surface is smooth for both the small and large scale models, the equilibrium $S_{3D,i}$ can be simplified as a function of Eq. (8.1).

$$S_{3D,i} = \Theta_i\left(\frac{U}{\sqrt{gD_P}}, \frac{UD_P}{\upsilon}, \frac{U_mT_p}{D_P}, \frac{d}{D_P}, \frac{t_a}{D_P}, \frac{t_a}{D_{n50}}, \frac{D_{84}}{D_{16}}, \frac{\theta_{max}}{\theta_{cr}}\right) \tag{8.1}$$

The first two terms in Eq. (8.1) are respectively the Froude number F_{r,D_P} and the Reynolds number R_{e,D_P}. Considering the combination of wave and current, $U = U_m + |U_c|$, where U_m is the mean wave orbital velocity obtained from Eq. (2.32). The third term is the KC number in irregular wave condition. The 4th to the 7th terms are characterising the model geometry including both the pile and the scour protection layer. The last term depicts the relationship between the hydrodynamic load and the armour stone resistance, where θ_{max} is the maximum Shields parameter in combined wave and current condition, obtained by Eqs. (2.19) and (2.37), θ_{cr} is the critical shear stress calculated from Eq. (2.20).

8.1.1 Comparison between small and large scale test results

By processing the intact and damaged profiles of a monopile scour protection, the dimensionless armour layer deformation can be obtained for a fair comparison between similar small and large scale experiments. Figure 8.1 and Figure 8.2 show the dimensionless deformation ($\Delta Z/D_P$) of the armour layers for TG1 vs PROTEUS Test 10B and TG2 vs PROTEUS Test 13B, respectively. Repeated tests are all visualised in Figure 8.1 and Figure 8.2.

Comparing the results of TG1 and PROTEUS Test 10B displayed in Figure 8.1, similar trends of the erosion and accretion distribution are observed. For example, erosions are found in upstream side of the incoming current (45° to 90° and 270° to 315°) and accretions are located in the downstream side of the current (90° to 135° and 225° to 270°). The similarities qualitatively reflect a similar distribution pattern of the pressure gradient and bed shear stress amplification between the two scaled models, which can be attributed to the application of similar Froude numbers. It is seen in Figure 8.1 that the local damage level for the large scale test is less than that in the small scale tests in terms of both the depth and extension of the erosion area.

As for the comparison between TG2 and PROTEUS Test 13B, the damage patterns of small and large scale tests are similar with regard to the erosions in the areas from 45° to 135° and from 225° to 315° at the two sides of the pile. From Figure 8.2, the large scale test case PROTEUS Test 13B has a similar damage level as the small scale test TG2.

In the lee-side from 135° to 225° of the scour protection, significant erosions are found in the small scale tests TG1 and TG2 due to the lee-wake vortexes, but rare lee-side erosions exist for the large scale tests. This is attributed to the different lee-wake vortex strength appearing in different sized models. The deformation behaviours at the edge are also very different between small and large scale tests. In TG1 and TG2, the edge area near 180° has an accretion deformation, which is mainly caused by the armour stone transported from the other eroded areas in upper stream, as visualised with the overhead photo in Figure 8.3a. In the large scale test PROTEUS Test 10B, the accretion in lee-side edge area is mainly due to the sediment settling. Very limited armour stones are displaced at the edge area, as shown in Figure 8.3b.

Figure 8.4 plots the quantitative comparisons of subarea damage numbers $S_{3D,i}$ between large and small scale experiments, where for small scale tests TG1 and TG2, average values and 95% confidence intervals (95% CI) of each $S_{3D,i}$ are provided on the presumptions that $S_{3D,i}$ follows a normal distribution. As the calculation of damage numbers in edge areas (subarea 16 to 24 in Figure 3.5) may be affected by the edge sediment transport or settling, $S_{3D,16}$ to $S_{3D,24}$ are not considered in analysis. Through the results of small scale experiments TG1 and TG2, it is found that the most vulnerable subareas are: (i) subarea 1,2 and 3 which are close to the pile; (ii) subarea 6 and 12, which are located in the wake of the pile. These subareas have both high $S_{3D,i}$ and high uncertainties of $S_{3D,i}$. For large scale tests PROTEUS Test 10B and PROTEUS Test 13B, maximum damage numbers occur in subareas 1 and 3. From Figure 8.4, significant scale effects can be observed:

(a) For the two tested scenarios, in the most damaged areas (subarea 1, 2, 3, 6 and 12), large scale models always show less damage than small scale models.

(b) From the comparison between PROTEUS Test 13B vs. TG2, in weakly damaged areas, large scale models show less damage compared to small scale models.

(c) From the comparison between PROTEUS Test 10B vs. TG1, in some weakly damaged areas, large scale models may also give larger damager numbers than small scale models. This mainly occur in subarea 4, 8, 9, 10 and 15, which are located in the incoming current direction.

The findings (a) and (b) are reasonable as the results are in accordance with what was observed for scour around pile. According to Ettema et al. (2006), larger pile size introduces relatively shallower scour depth around pile compared to smaller pile size. For (c), the conclusions are not definite and maybe explained with several reasons. The large scale test PROTEUS Test 10B is not repeated and the average damage values and repeatability are not well known, so it is possible that a randomly large erosion damage occurs in this test. Meanwhile, the relative scale ratio between TG1 and PROTEUS Test 10B is only 1:3, therefore, the differences in some weakly damaged areas due to scale effects are not as obvious as they appear PROTEUS Test 13B vs. TG2.

8.1.2 Discussions

Table 8.1 lists the characterising dimensionless parameters and local damage in subarea 1, 2, 3 and 6. The listed subarea damage numbers for small scale tests contain both the means and 95% confidence intervals. Taking a look into the dimensionless parameters, the major differences between the small and large scale tests exist in R_{e,D_P} and θ_{max}/θ_{cr}. These two parameters can be regarded as major sources that lead the scale effects.

8.1.2.1 Influence of R_{e,D_P}

Firstly, the Reynolds number R_{e,D_P} for TG1 is approximately 2.3×10^4 and for TG2 is 2.6×10^4. The values are lower than the commonly used critical Reynolds number of 3.0×10^4 and the flow regimes around the pile in the small scale tests are subcritical. The R_{e,D_P} numbers for PROTEUS Test 10B and Test 13B are $R_{e,D_P} = 1.2 \times 10^5$ and 4.0×10^5, separately. Referring to the Strouhal number diagram (S_t) for flow around smooth pile (Figure 8.5), PROTEUS Test 10B is close to the low transition region and PROTEUS Test 13B is in the supercritical region. The larger Reynolds numbers feature the large scale tests in two ways: (i) the boundary layer separation can be turbulent and (ii) the vortex shedding frequencies are different from that in the small scale tests.

For (i), the turbulent boundary layer is usually thinner than the laminar boundary layer and can withstand higher pressure gradient, which leads the boundary layer

Table 8.1: Overview of scale effects on subarea damage in monopile scour protection experiments

Parameters	Small scale TG1	Large scale PROTEUS Test 10B	Small scale TG2	Large scale PROTEUS Test 13B
R_{e,D_P}	2.33×10^4	1.23×10^5	2.61×10^4	3.97×10^5
F_{r,D_P}	0.267	0.272	0.30	0.310
KC	0.912	0.917	0.751	0.693
θ_{max}/θ_{cr}	0.722	0.466	0.809	0.494
S_t	0.20	0.20	0.20	0.48
d/D_p	3.0	3.0	2.5	2.5
t/D_p	0.18	0.17	0.18	0.16
t/D_{n50}	9.4	9.1	9.5	8.3
D_{85}/D_{15}	2.5	2.3	2.5	2.3
$S_{3D,1}$ (95% CI)	0.981 (0.496 - 1.467)	0.481	0.990 (0.149 - 1.830)	0.712
$S_{3D,2}$ (95% CI)	0.617 (0.209 - 1.025)	0.397	0.739 (0.457 - 1.021)	0.328
$S_{3D,3}$ (95% CI)	1.019 (0.573 - 1.466)	0.602	1.099 (0.490 - 1.707)	1.082
$S_{3D,6}$ (95% CI)	1.025 (0.780 - 1.271)	0.217	0.899 (0.480 - 1.318)	0.108

separation point on the pile further downstream compared to a laminar boundary layer separation (Hjorth, 1975). But this has more influences on the drag force acting on the cylinder rather than the armour stones, due to the fact that the surface roughness of the armour layer significantly thickens the boundary layer, reduces the flow velocity approaching the pile base and advances the boundary layer separation point. Therefore in both the large and small scale tests, the erosion regions near the pile seem to be dominated by the pressure gradient and not affected by the theoretically different separation regimes.

For (ii), the vortex shedding frequency can be calculated using $f_v = S_t \cdot U/D_P$. Combining $U = \upsilon R_{e,D_P}/D_P$, $f_v = \upsilon S_t R_{e,D_P}/{D_P}^2$. S_t can be looked up through Figure 8.5. It is obtained that $f_v = 0.47$ for TG1, $f_v = 0.27$ for PROTEUS Test 10B, $f_v = 0.52$ for TG2 and $f_v = 0.53$ for PROTEUS Test 13B. The results lead to an interesting and coincidental conclusion that the local damage level is closely linked to the vortex shedding frequency. This phenomenon is also found in Ettema et al. (2006), who have stated that lower vortex shedding frequency can reduce the scour depth around a pile. Considering that the vortex shedding originates from the side of the pile, which overlaps with the higher erosion area (subarea 1 and 3), the reason could be that the amount of stone movement in a period is more in a higher f_v condition than in a lower f_v condition. Though, the conclusions are not definite due to the unknown model effects in the large scale tests and the lack of data of vortex shedding measurement over a scour protection.

8.1.2.2 Influence of θ_{max}/θ_{cr}

The difference of θ_{max}/θ_{cr} in the small and large scale tests is another reason for the scale effects. According to the studies in Den Boon et al. (2004), θ_{max}/θ_{cr} is defined as the STAB parameter, which can be used to describe the damage level of the scour protection. Understandably, higher STAB parameter leads to higher damage level of scour protection due to the higher bed load, though not very precise in the range of $0.4 < \theta_{max}/\theta_{cr} < 0.5$ according to De Vos et al. (2012). In the present study, θ_{max}/θ_{cr} for small scale tests TG1 and TG2 are around 0.7 to 0.8, while for large scale tests are 0.45-0.5. The difference is big enough for an observable scale effect, for example, one can see a much higher armour stone transport level that creates larger side erosion area, higher armour stone accretion and higher lee-wake induced erosion level in small scale tests.

One reason for the different θ_{max}/θ_{cr} is that θ_{max} is scaled with a scale factor of 1 as given by Eq. (4.45), while θ_{cr} is a function of the stone size Reynolds number, which is not correctly scaled in the small scale model by the adopted Best Model scaling. The dimensionless armour stone diameter D_* for TG1 and TG2 is $20 < D_* < 120$, for PROTEUS Test 10B is $90 < D_* < 240$ and for PROTEUS Test 13B is $180 < D_* < 460$. Plotting these D_* ranges in the threshold of motion curve (Figure 8.6), it is seen that the armour stones in the large scale tests have higher θ_{cr} than small scale tests. However, as is shown in Figure 8.6, the uncertainty for θ_{cr} is considerably high where the differences between the upper bound value and the lower bound value can be up to tenfold. This is due to the strong model effects in the sediment threshold of motion tests, which has been thoroughly discussed in van Rijn (1993). Therefore, it is difficult to clearly identify the impact of θ_{max}/θ_{cr}. It should be noted in this paper that the stone sizes are indeed very small in the small scale tests, which might not be an ideal engineering solution. This is because for the purpose of knowing the scale effects the scour protection damage needs to happen in both the small and large scale tests. During the large scale tests, it was found that applying large sized armour stones may lead to an over stable scour protection layer with the facility's extreme capability where no damage could be detected. Hence a compromised solution is made accordingly. Nevertheless, applying a larger stone size can mitigate the scale effects caused by θ_{max}/θ_{cr}, since θ_{cr} is approaching a constant value (θ_{cr}=0.056) when D_* is larger than 100.

8.1.2.3 Other factors

Besides, several other factors can be minor sources of the scale effects, which are shortly discussed below.

- Horseshoe vortex.
  The horseshoe vortex is a key factor for the formation of scour hole around a pile. The horseshoe vortex exists in a steady current condition and in a $KC > 6$ oscillating flow condition, which amplifies the bed shear stress in front of the pile. Although the horseshoe vortex scale is governed by R_{e,D_P}, the associated scale effect is not clearly observed probably due to the bed shear stress amplification is not large enough to introduce an erosion in front of the pile (according to Sumer and Fredsøe (2002), the horseshoe vortex induced bed shear stress in front of the pile can be half or one-third of the bed shear stress at the side of the pile). Considering the relatively lower current velocity in marine environment and the larger armour stones used

practically, the influence of the horseshoe vortex can be even smaller. The occurrence of horseshoe vortex induced erosion may also result in a dynamic failure of the scour protection.

- Incoming flow turbulence.
  In the present study, the turbulence intensity of the incoming flow is considered to a minor factor. For both the small and large scale tests, the turbulence intensities are above 5% and below 10%, showing that the flow conditions are fully turbulent. But this effect can be significant if the model scale is even smaller when the incoming flow becomes slow and the turbulence is not fully developed, which should be avoided in experiments.

- Sediment size.
  The sediment size to armour stone size ratio d_s/D_{50} for TG1 and TG2 is 4.4×10^{-2}, for PROTEUS Test 10B is 3.1×10^{-2} and for PROTEUS Test 13B is 1.6×10^{-2}. The sinking is not obvious for both the present large and small scale experiments because the sediment layers were found to be well protected when the model were demolished after each test. The sediment size in the present study is thought to be a minor factor for scale effects of the erosion damage. But it is clearly seen that the ripples of sand are different in the small and large scale experiments, and the edge scour property is significantly different. Referring to Table 8.2, d_s/D_{50} in prototype is $3\times10^{-3}-4\times10^{-3}$, the ability of sand penetration is much higher. This makes the sediment size an important factor for scale effects when considering the sinking and edge scour in full scale tests.

Table 8.2: Sediment sand sizes in small scale and large scale tests

d_s [μm]	TG1 and TG2	PROTEUS Test 10B	PROTEUS Test 13B
Model	100	210	210
Prototype	375	325	465

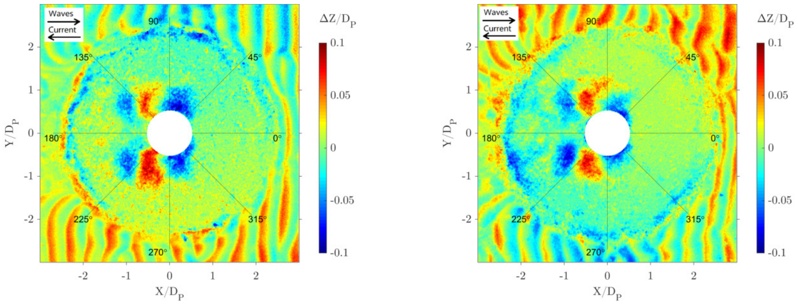

(a) TG1_1 **(b)** TG1_2

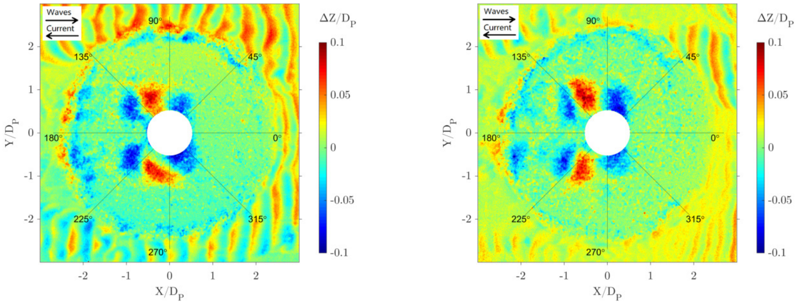

(c) TG1_3 **(d)** TG1_4

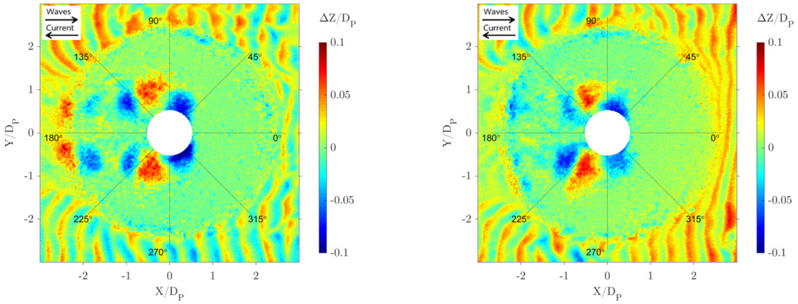

(e) TG1_5 **(f)** TG1_6

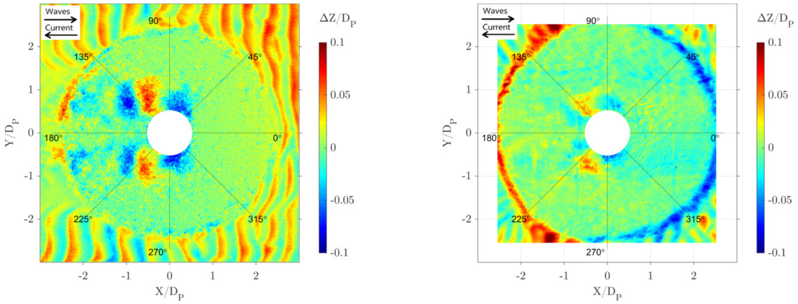

(g) TG1_7 **(h)** PROTEUS Test 10B

Figure 8.1: Comparisons of dimensionless deformation of armour layer after 3000 waves between small scale and large scale test, TG2 vs. PROTEUS Test10B, relative scale ratio is 1:3.

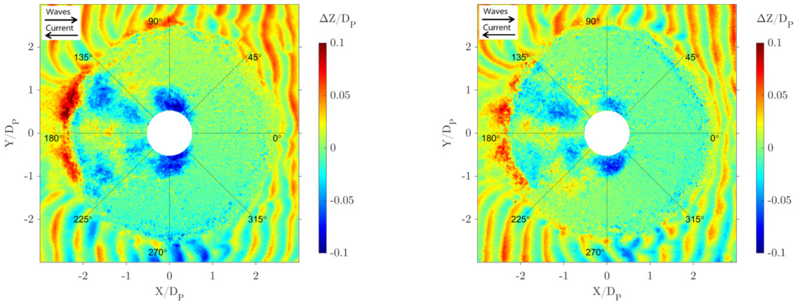

(a) TG2_1 **(b)** TG2_2

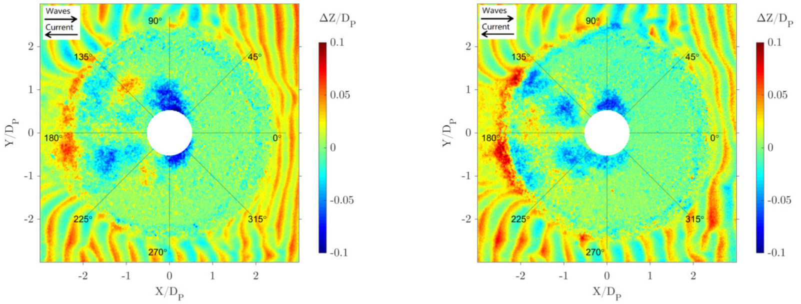

(c) TG2_3 **(d)** TG2_4

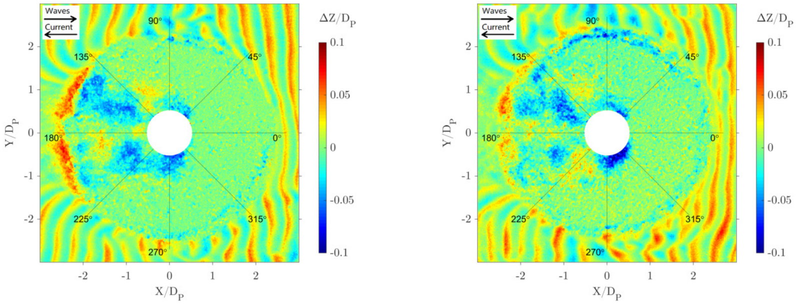

(e) TG2_5 **(f)** TG2_6

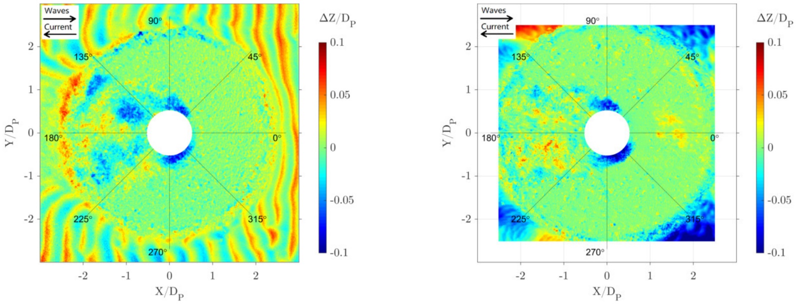

(g) TG2_7 **(h)** PROTEUS Test 13B

Figure 8.2: Comparisons of dimensionless deformation of armour layer after 3000 waves between small scale and large scale test, TG2 vs. PROTEUS Test13B, relative scale ratio is 1:6.

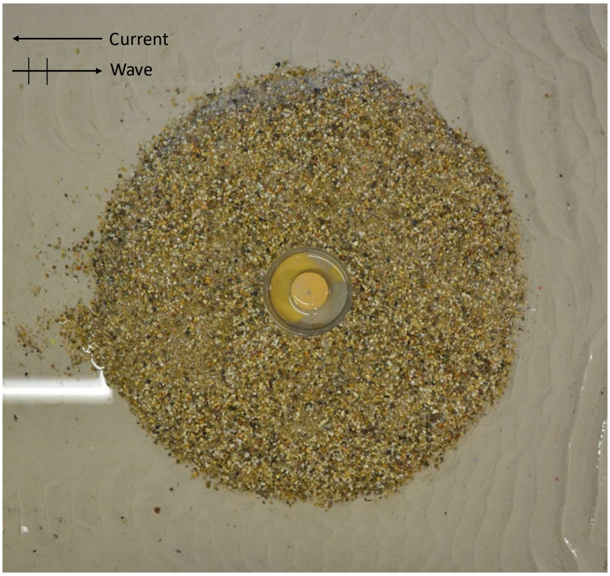

(a) small scale test case TG1_4;

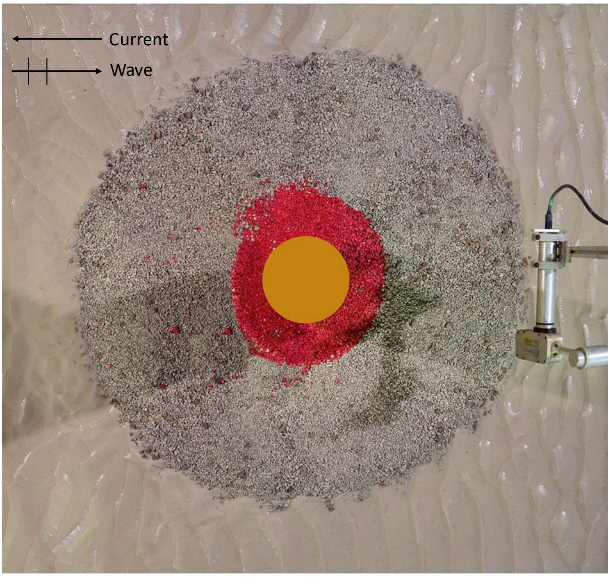

(b) large scale test case PROTEUS Test 10B.

Figure 8.3: Overhead photos of scour protection layer after 3000 waves.

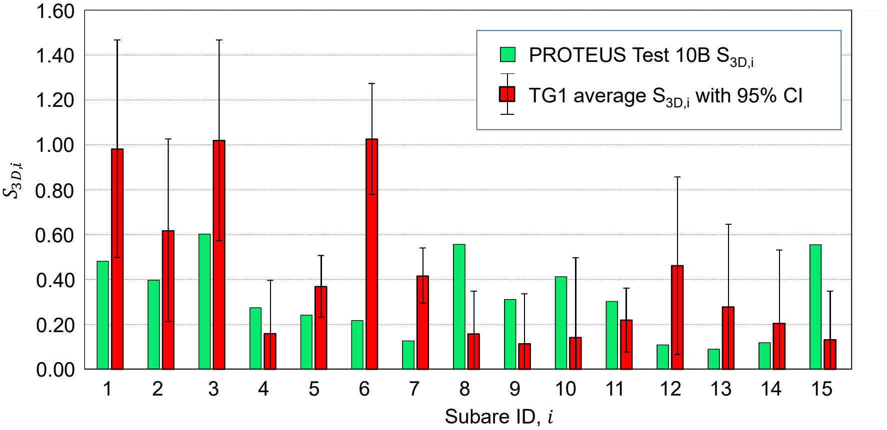

(a) TG1 vs. PROTEUS Test 10B

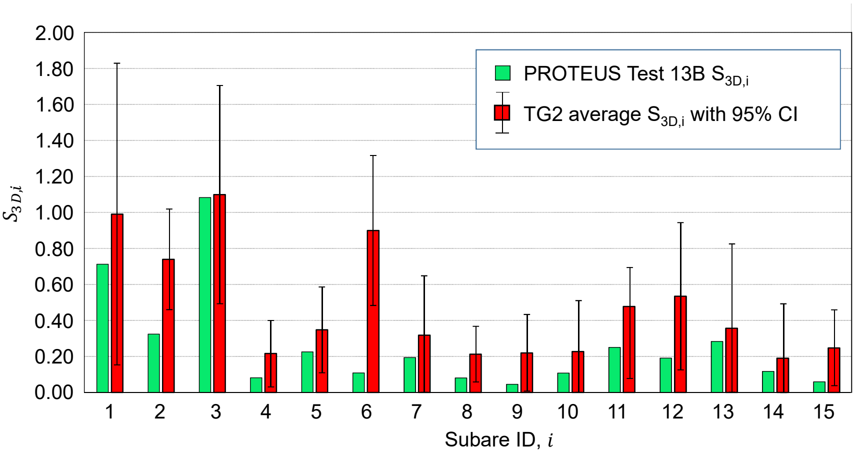

(b) TG2 vs. PROTEUS Test 13B

Figure 8.4: Subarea damage numbers $S_{3D,i}$ for large and small scale tests.

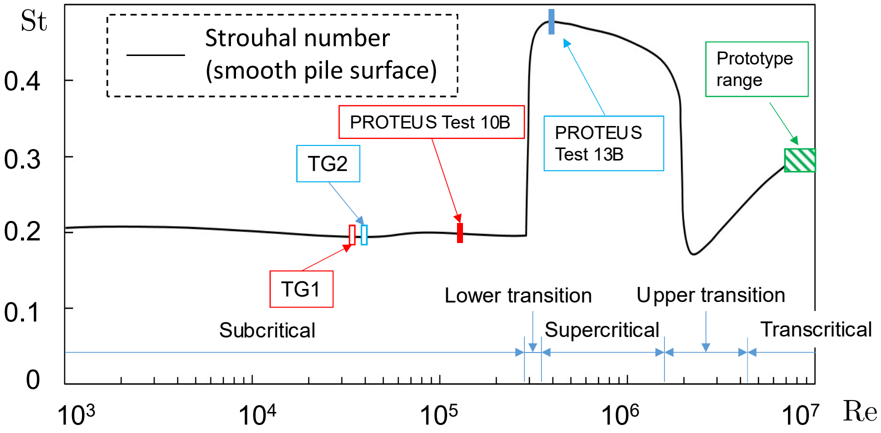

Figure 8.5: The Strouhal numbers of small scale and large scale tests displayed in the S_t-R_e diagram, modified from Sumer and Fredsøe (1997).

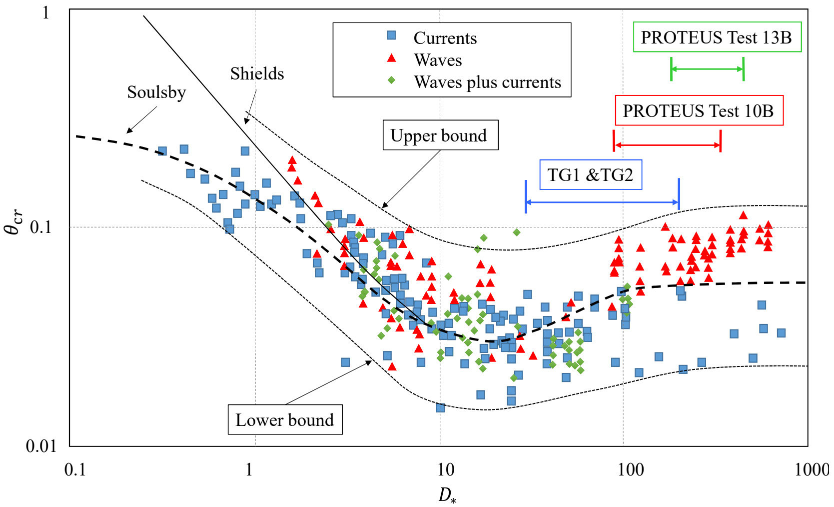

Figure 8.6: Comparison of the dimensionless armour stone sizes used in small scale and large tests in the critical Shields parameter diagram, modified from Soulsby (1997). Upper and lower bound lines are eye-ball fitted by the author.

8.2 Time scale

The development of monopile scour protection damage is investigated through the cases of large scale test PROTEUS Test 14 and small scale test TG3 by scanning the intact and damaged profiles after 1000, 3000 and 5000 waves. For the test conditions, a reference to Table 6.1 and Table 6.4 is made. This section focuses on the different time scale behaviours between different scale models.

8.2.1 Damage profiles

The scour protection damage profiles of PROTEUS Test 14 after 1000, 3000 and 5000 waves are visualized in Figure 8.7. The wave propagates to positive X direction and the current flows to negative X direction.

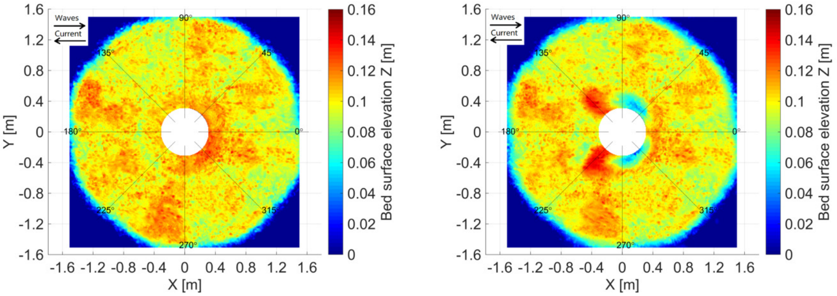

(a) Start profile **(b)** Profile after 1000 waves

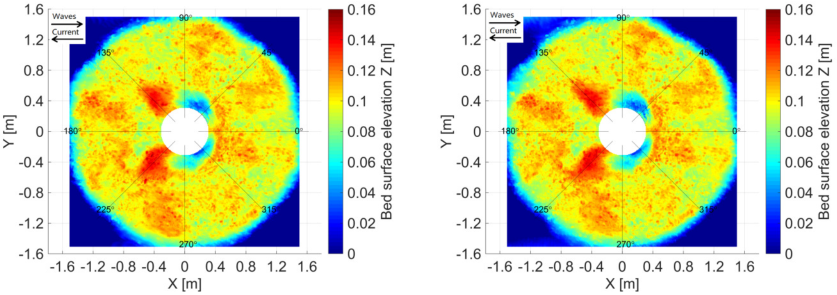

(c) Profile after 3000 waves **(d)** Profile after 5000 waves

Figure 8.7: Damage development of PROTEUS Test 14 after 1000, 3000 and 5000 waves.

As a visual comparison, the damage profiles of TG3_1 and TG3_2 are plotted in Figure 8.8. From these figures, common phenomena for the two scale models are seen: the scour protection deforms fast during 0-3000 waves, creates damage zones to the current incoming direction and creates accretion zones to the current wake side.

Differences are also obvious. For PROTEUS Test 14, the profile after 5000 waves shows very close pattern with that after 3000 waves, which indicates an

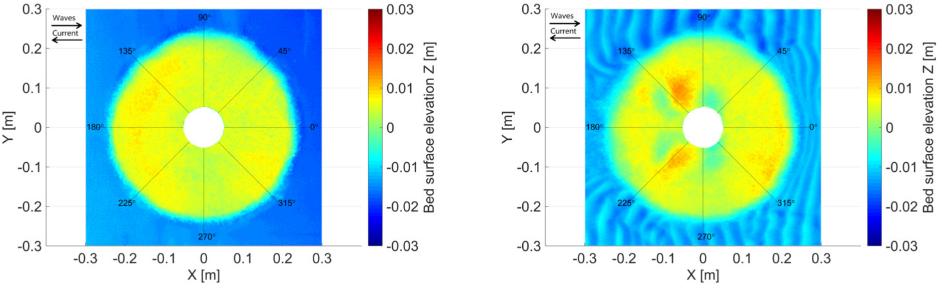

(a) TG3_1 start profile

(b) TG3_1 profile after 1000 waves

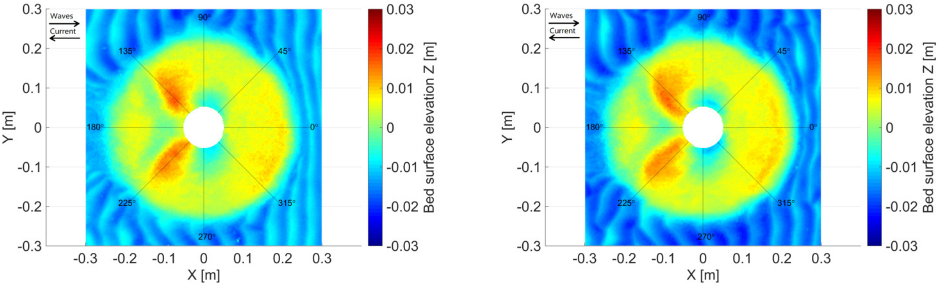

(c) TG3_1 profile after 3000 waves

(d) TG3_1 profile after 5000 waves

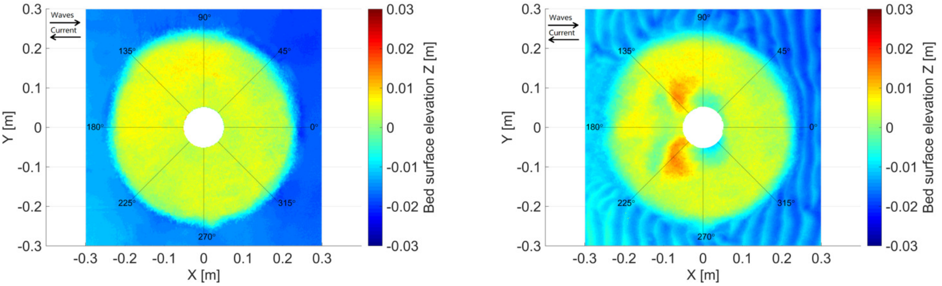

(e) TG3_2 start profile

(f) TG3_2 profile after 1000 waves

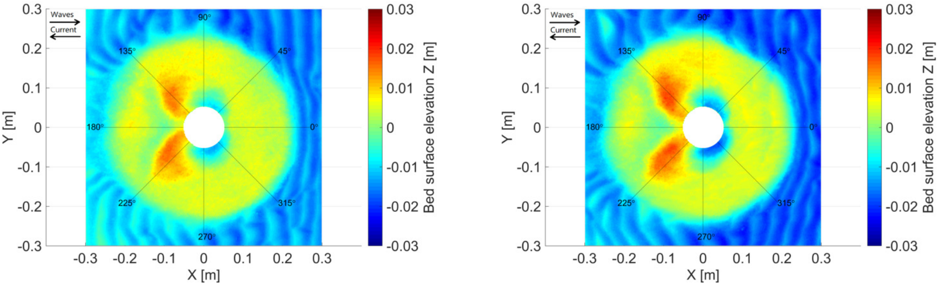

(g) TG3_2 profile after 3000 waves

(h) TG3_2 profile after 5000 waves

Figure 8.8: Damage development of TG3_1 and TG3_2 after 1000, 3000 and 5000 waves.

approximate equilibrium state. For TG3_1 and TG3_2, 3000 waves are apparently not enough for obtaining an equilibrium. This result corresponds to the findings in Looseveldt and Vannieuwenhuyse (2012) and is mainly attributed to the wave against current hydrodynamic condition. Meanwhile, compared with the damage profiles in TG3 which contain large lee-side erosion areas, PROTEUS Test 14 only has accretion in the lee-side from 135° to 225°, while the lee-side erosion is almost negligible. The small lee-side erosion is also found in PROTEUS Test 13B. The provided evidence shows a better stability performance of the large scale model under the similar hydrodynamic loading.

8.2.2 Damage numbers

The damage numbers for small scale TG3 and large scale PROTEUS Test 14 after 1000, 3000 and 5000 waves are analysed. The subarea damage variations are plotted in Figure 8.9 and Figure 8.10.

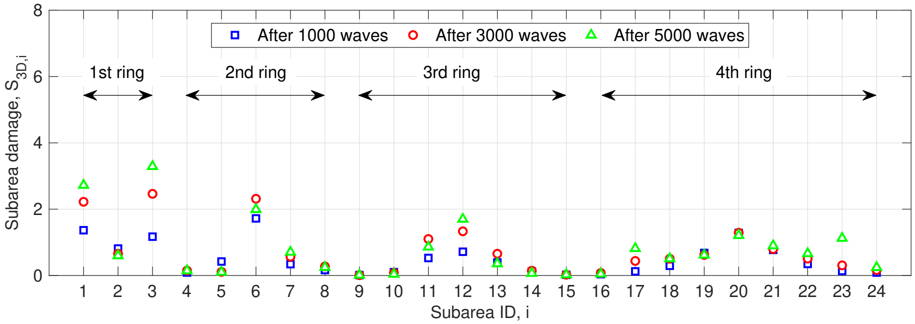

(a) TG3_1

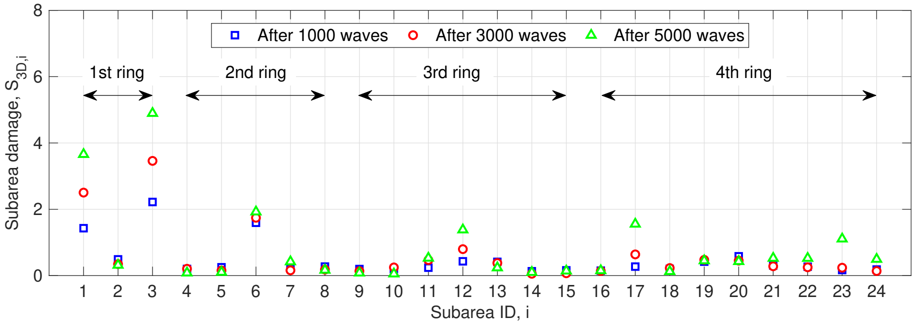

(b) TG3_2

Figure 8.9: Subarea damage numbers development of TG3_1 and TG3_2 after 1000, 3000 and 5000 waves.

The subarea damage of TG3 plotted in Figure 8.9 shows that progressive damage in long duration waves mainly occurs in the side erosion zones - subarea 1 and 3. The lee-side erosion zone in the second ring, subarea 6, is weakly affected

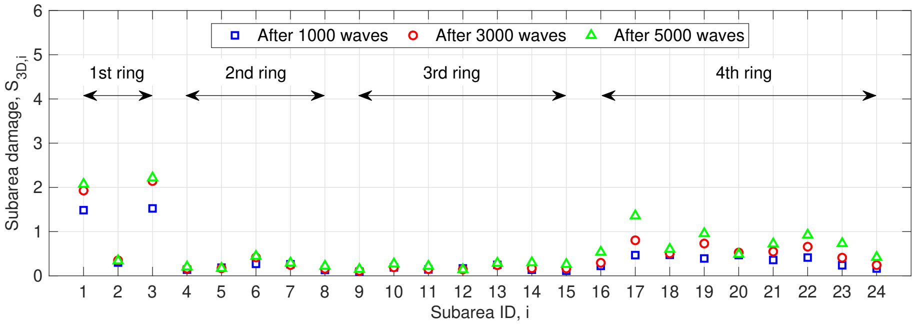

Figure 8.10: Subarea damage numbers development of PROTEUS Test 14 after 1000, 3000 and 5000 waves.

by the wave duration after 1000 waves. The reason is that after some wave actions, subarea 6 is sheltered by the accumulated stones and the pile against the wake vortexes, where the hydrodynamic loading significantly decreases in this area. Those areas where no significant damages occur after 1000 waves will not suffer progressive damage for longer wave duration. As a comparison, Figure 8.9 shows that subarea damages in the first to the third ring of the large scale model are almost stable after 3000 waves. However, the edge erosion of the armour layer in the fourth ring progresses as wave duration increases, this is explained as a strong blockage effect due to the narrow gap between the scour protection and the wave flume wall.

Table 8.3 lists the global S_{3D} after 1000, 3000, 5000 waves. The dimensionless damage numbers of the large scale model are smaller than those of the small scale model with different wave durations. As PROTEUS Test 14 and TG3 are using different grading coefficients, the impact on S_{3D} needs to be further considered. In the PROTEUS tests, Test 12A, Test 12B and Test 14 are using the same wave and current conditions referring to Table 5.3 and Table 6.1, while $D_{85}/D_{15} = 2.48$ for Test 12A and Test 12B, and $D_{85}/D_{15} = 6$ for Test 14. Scan analysis shows $S_{3D} = 1.57$ for Test 12A after 1000 waves and $S_{3D} = 2.35$ for Test 12B after 3000 waves (see Table 5.7). The results show quite limited impacts of D_{85}/D_{15} on the damage results.

Table 8.3: S_{3D} after 1000, 3000 and 5000 waves

Test ID	TG3_1	TG3_2	PROTEUS Test 14
S_{3D} after 1000 waves	1.712	2.220	1.524
S_{3D} after 3000 waves	2.462	3.459	2.144
S_{3D} after 5000 waves	3.290	4.895	2.217

The time scale factor F_N for damage development after N waves is proposed by De Vos et al. (2012), which reads in Eq. (8.2),

$$F_N = N^{b_0} \tag{8.2}$$

and adapted by Raaijmakers et al. (2010) as Eq. (8.3).

$$F_N = b_1 \left[1 - \exp\left(-\frac{N}{N_{char}} \right) \right] \tag{8.3}$$

The coefficients are explained after Eq. (3.19) in Section 3.

A normalised time scale factor can be written as a ratio of F_N/F_{1000}, and $N =$ 1000, 3000 and 5000 for the present discussion. As a fair comparison, the measured normalised time scale factor is $S_{3D,N}/S_{3D,1000}$. The predicted and measured time scale factors are displayed in Figure 8.11.

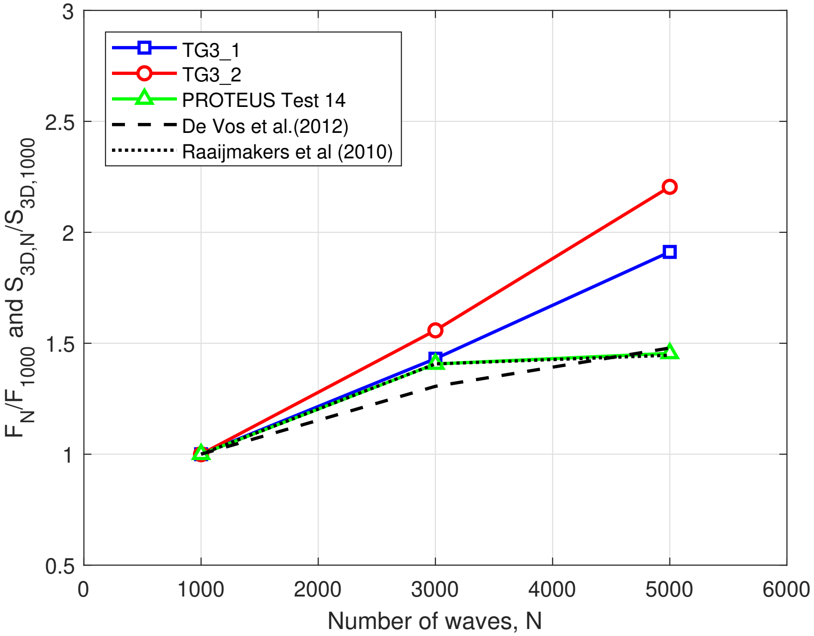

Figure 8.11: Comparison between prediced and measured normalised time scale factors.

The results show a very good agreement between the measured values of PROTEUS Test 14 and the predicted values using Eq. (8.3) after Raaijmakers et al. (2010), and verify the applicability of Eq. (8.3) to large scale model. Both Eq. (8.2) and Eq. (8.3) underestimate the damage development in small scale tests for 3000 and 5000 waves.

8.3 Conclusions

This chapter describes the scale effects that exist in monopile scour protection experiments in a way of comparing experimental results between similar small scale and large scale model tests using the Best Model scaling rule. Results of three comparison groups are presented through damage pattern visualisation and analysis of global and subarea damages. Clear scale effects can be observed and are concluded as below:

- Small scale model tests result in larger damage numbers and eroded areas than the large scale tests, excluding the impact from model effects. The trend is valid for both global damage number S_{3D} and subarea damage number $S_{3D,i}$. The reasons are mainly related to the limitations of the Best Model scaling rule. Using this scaling rule, the similarities of R_e number and θ_{max}/θ_{cr} cannot be satisfied. Large scale PROTEUS Test 13B has a lower local damage than the mean level of its similar small scale test TG2, but the global damage S_{3D} is close to that in TG2, which is probably due to the similar vortex shedding frequencies f_v between the two models. Though scale effects could not be totally removed as the Reynolds numbers R_e are very different between scale models and prototype, extra experiments are indispensable to prove that other optional scaling rules can perform better in mitigating the scale effects in such experiments.

- Regarding the time scale of scour protection damage, the large scale model has a faster equilibrium time and a more stable performance. PROTEUS Test 14 reaches an approximate equilibrium after 3000 waves, while the similar small scale test TG3 gives progressive S_{3D} after 5000 waves. Damage numbers after 1000, 3000 and 5000 waves for TG3 are all larger than those in PROTEUS Test 14. For PROTEUS Test 14, the time scale factor well matches the prediction from Raaijmakers et al. (2010). The result indicates the conservativeness of small scale experiments in predicting the damage development for prototype.

However, it is still a challenge to predict how much the damage results obtained from small scale tests deviate from prototype. Firstly, the large scale experimental data and field test data are still scarce, which is mainly due to the high cost of such experiments. It is also difficult to achieve the metocean conditions in prototype fully similar to that in laboratory experiments. Secondly, a more comprehensive understanding of scale effects in monopile scour protection experiment requires series scaled tests. It is crucial to find the asymptotic trend of the damage results with respect to the model scale ratios. The critical Reynolds numbers should be analysed through series scale tests to set a minimum scale ratio to avoid strong scale effects. Thirdly. such investigations should also be carried out by means of high-fidelity numerical simulation tools in the future.

Chapter 9

Synthetic analysis of existing experimental datasets

9.1 Dataset description

As was introduced in Chapter 3, different monopile scour protection experiments have been carried out to investigate the engineering feasibility of using dynamically stable scour protection around monopile (De Vos et al., 2012; Looseveldt and Vannieuwenhuyse, 2012; De Schoesitter et al., 2014; Whitehouse et al., 2014; Arboleda Chavez et al., 2019), which have applied various pile sizes, armour stone sizes, armour layer thicknesses and hydrodynamic conditions. Clear damage levels are defined via visual observation during these tests. A synthetic analysis of these experimental data is necessary to further investigate the governing characteristic dimensionless parameters in describing the scour protection failure status.

Many valuable discussions were made regarding the affecting parameters in previous experimental studies of monopile scour protection. Typically, De Vos et al. (2012) provide an explicit relationship between the dynamic stability index (S_{3D}) and several dimensional parameters. Whitehouse et al. (2014) characterise the relationships between the scour protection stable or failure behaviours and identify three main dimensionless characteristic parameters: θ_{max}/θ_{cr} ($STAB$ parameter) for armour stones, D_* for armour stones and layers of stones n_a ($n_a = t_a/D_{n50}$). As shown in Figure 9.1, it was noticed that D_* and critical Shields parameter can be used to identify failure cases from stable cases. The long dashed line in Figure 9.1 is the critical Shields parameter generated from Soulsby (1997). The short dashed line indicates that the damage status of the armour layer is affected by the amplification factor of bed shear stress (α) near the pile. This amplification factor is fitted to $\alpha = 1.8$. Fazeres-Ferradosa et al. (2018a) pointed out that layers of stones n_a plays an important role when assessing the damage of armour layer. When n_a increases to 8, $S_{3D} > 3$ may still indicate a stable scour protection. Nielsen and Petersen (2019) use two dimensionless numbers, KC and U_{cw}, to identify the boundaries between stable and failed cases for the data presented by

De Vos et al. (2012).

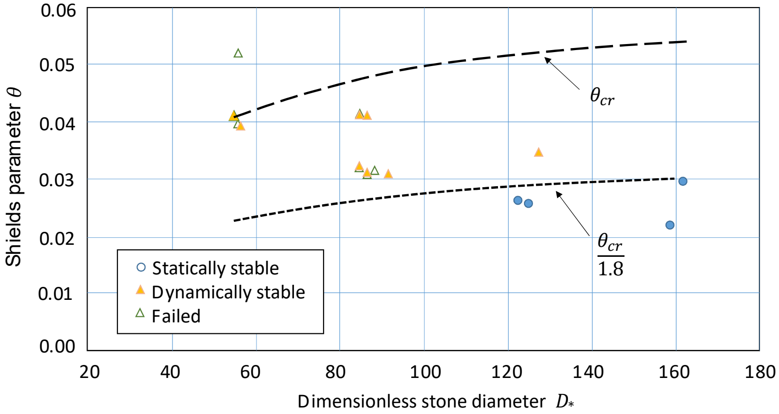

Figure 9.1: Monopile scour protection damage status expressed by θ and D_*.

Unlike the scour depth prediction, where KC and U_{cw} are the only dominant parameters (Sumer and Fredsøe, 2002), the stability of a monopile scour protection is affected by more parameters, which involve, for example, the pile diameter D_P, the stone size D_{50} and the layer thickness t_a, as seen in Eq. (8.1). An analysis of the dominant factors is a prerequisite based on the compilation of available experimental results, as listed in Table B.1 in Appendix B. In Table B.1, 143 irregular wave test datasets are gathered from various sources, where IDs 1–69 are extracted from De Vos et al. (2012) (named as "LDV" in later text), IDs 70–111 are from Looseveldt and Vannieuwenhuyse (2012) (named as "KN" in later text), IDs 112–134 are from De Schoesitter et al. (2014) (named as "SC" in later text) and IDs 135–143 are from the PROTEUS experiments (Arboleda Chavez et al., 2019) (named as "PR" in later text). In the last column, the abbreviation "SDF" stands for whether the scour protection is statically stable (S), dynamically stable (D) or failure (F). The judgement of SDF is based on the S_{3D} evaluation approach. Minor modifications are introduced on the basis of the original method presented by De Vos et al. (2012), which are: (1) S for $S_{3D} < 0.1 \cdot t_a/D_{n50}$, (2) D for $0.1 \cdot t_a/D_{n50} \leq S_{3D} \leq 0.4 \cdot t_a/D_{n50}$ and (3) F for $S_{3D} > 0.4 \cdot t_a/D_{n50}$. In addition, to have a fair evaluation, the judgement is made after 5000 wave as it reaches an approximate equilibrium according to Looseveldt and Vannieuwenhuyse (2012). For the cases where the S_{3D} are measured after 3000 waves, the results are extrapolated to 5000 waves using the time evolution relationship expressed in Eq. (3.15), which gives S_{3D} after 5000 waves calculated by Eq. (9.1), where $b_0 = 0.243$. For the SC data, 5000 waves were employed. Though the S_{3D} number was not clearly specified, the SDF results are stated by De Schoesitter et al. (2014). However, it should be noted that De Schoesitter et al. (2014) apply a failure criterion that the filter layer has an exposure area of $4D_{n50}^2$.

$$S_{3D,5000} = S_{3D,3000}\frac{5000^{b_0}}{3000^{b_0}} \tag{9.1}$$

In Table B.1 in Appendix B, test cases with ID 91, 94, 97, 99 and 101 are using 1:100 scale ratio, which yields D_P =0.05 m. This may cause significant scale effects. Therefore, these cases are categorised as "KNs" (indicating KN small scale) in the following analysis.

9.2 Data analysis

As assumed in Eq. (8.1), the damage of monopile scour protection is governed by a set of dimensionless parameters, which describe the hydrodynamic loading (F_r number, R_e number, KC number), the geometrical characteristics (dimensionless water depth d/D_P, dimensionless armour layer thickness t_a/D_P, layers of armour stones t_a/D_{n50} and grading coefficients D_{84}/D_{16}) and the relative mobility of armour stones θ_{max}/θ_{cr}.

The Froude and Reynolds number around a pile should be calculated by Eq. (9.2) and (9.3), where U_c is the depth averaged current velocity, U_m is the mean wave orbital velocity. The KC number is written as $KC = U_mT_p/D_P$, U_m is calculated by Eq. (2.32). With U_c and U_m, U_{cw} is calculated by Eq. (2.45).

$$F_{r,D_P} = \frac{|U_c| + U_m}{\sqrt{gD_P}} \tag{9.2}$$

$$R_{e,D_P} = \frac{(|U_c| + U_m)D_P}{\upsilon} \tag{9.3}$$

The Shields parameter θ_{max} is calculated using Eq. (3.10) and θ_{cr} is obtained using the Soulsby's method (Eq. 2.20).

9.2.1 Impacts of KC, U_{cw} and θ_{max}/θ_{cr} numbers

The KC and U_{cw} numbers are governing factors for the pile scour process for the reason that large KC and U_{cw} numbers can trigger horseshoe vortex near the pile. θ_{max}/θ_{cr} is the STAB parameter, which is used to define the failure of scour protection. These three parameters are presumed to be crucial for the stability of monopile scour protection, which provide a good start to the analysis.

Figure 9.2 shows the influences of KC number and U_{cw} on the SDF behaviours of scour protections. This figure reflects a trend that the failure cases in higher U_{cw} conditions ($U_{cw} > 0.4$) have relatively lower KC numbers, which physically means that in high current velocity component conditions, the ability of resisting wave induced erosion is lowered. However, unlike what has been explained in pile scour, such as Eq. (2.42) and Eq. (2.46), it is difficult to clearly separate the stable cases and failure cases based on KC and U_{cw}. When $2 < KC < 4$, failure cases can occur within a wide range of U_{cw}. And it is very often seen that failure cases have lower KC numbers than stable cases under the same U_{cw} conditions. A main reason for this unclear boundary is that the armour stone resistances, θ_{max}/θ_{cr}, are different. Figure 9.3 and Figure 9.4 depict the influences of θ_{max}/θ_{cr} along with KC and U_{cw}, separately.

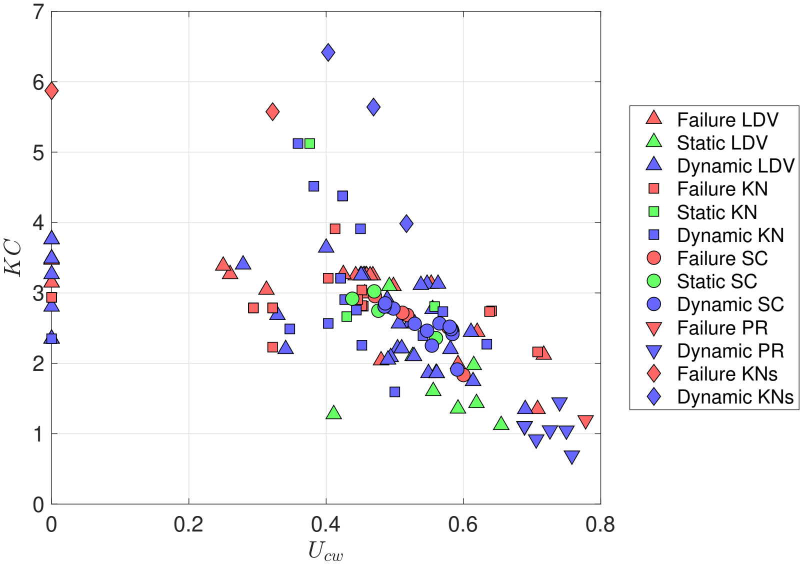

Figure 9.2: SDF results versus U_{cw} and KC.

From these two figures, it is observed that the SDF results are more dependent on the value of θ_{max}/θ_{cr}. Figure 9.3 shows that when $1 < KC < 2.5$, failure can happen when $\theta_{max}/\theta_{cr} > 0.321$, while for other KC numbers, failure occurs when $\theta_{max}/\theta_{cr} > 0.438$. Similarly, in Figure 9.4, failure cases occur mostly when $\theta_{max}/\theta_{cr} > 0.438$ and $U_{cw} < 0.6$, and, $\theta_{max}/\theta_{cr} > 0.321$ and $U_{cw} > 0.592$. The results highlight the importance of θ_{max}/θ_{cr} in a stable scour protection design, and concerns should be paid to wave and current conditions when $1 < KC < 2.5$ and $U_{cw} > 0.592$. However, it is also difficult to have a clear threshold line to distinguish the failure and non-failure cases. More parameters need to be investigated.

9.2.2 Impacts of Froude numbers

The Froude numbers are used to describe the intensity of flow compared to the size of the geometry, which can be defined using the pile size and stone size. Specifically, the densimetric Froude number form takes the relative density into account. For the sake of identifying the impacts from either wave or current, the Froude numbers are separated into two components, one depicts the wave velocity, the other depicts the current velocity. For the Froude numbers around the pile,

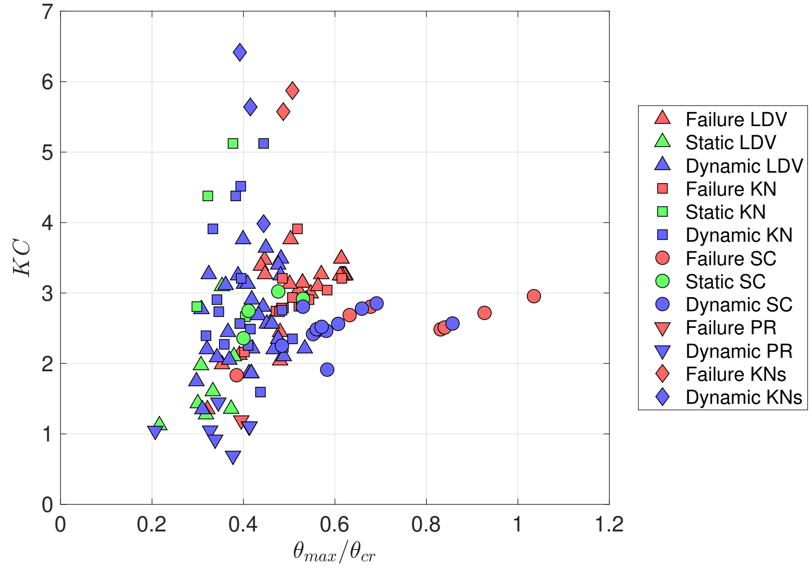

Figure 9.3: SDF results versus θ_{max}/θ_{cr} and KC.

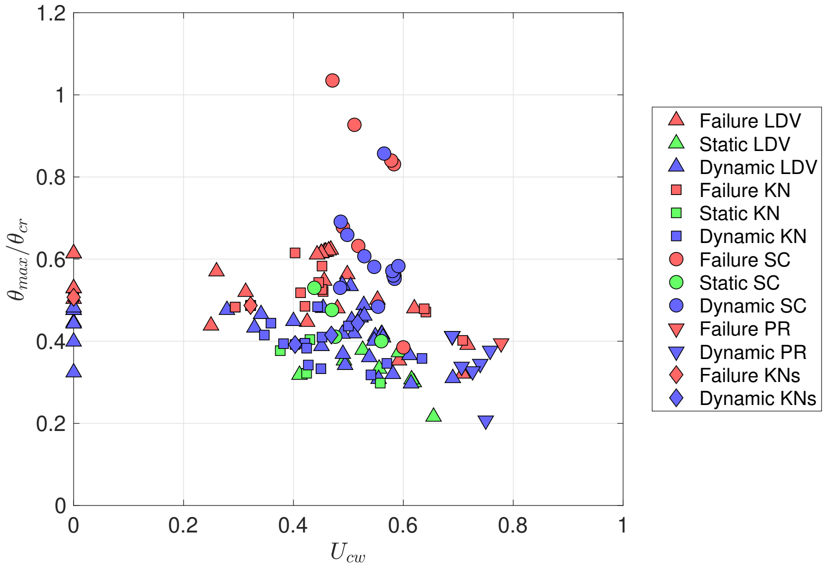

Figure 9.4: SDF results versus U_{cw} and θ_{max}/θ_{cr}.

the two components due to wave and current are respectively defined in Eq. (9.4) and Eq. (9.5).

$$F_{rw,D_P} = \frac{U_m}{\sqrt{gD_P}} \tag{9.4}$$

$$F_{rc,D_P} = \frac{U_c}{\sqrt{gD_P}} \tag{9.5}$$

To describe the near-bed flow, the densimetric Froude numbers considering the wave and current shear velocities u_{*w} and u_{*c} are also defined (Eq. 9.6 and 9.7).

$$F_{r,u_{*w}} = \frac{u_{*w}}{\sqrt{(s-1)gD_{50}}} \tag{9.6}$$

$$F_{r,u_{*c}} = \frac{u_{*c}}{\sqrt{(s-1)gD_{50}}} \tag{9.7}$$

In addition, another form of densimetric Froude numbers which directly use U_m and U_c instead of shear velocities are defined in Eq. (9.4) and Eq. (9.5)

$$F_{r,U_m} = \frac{U_m}{\sqrt{(s-1)gD_{50}}} \tag{9.8}$$

$$F_{r,U_c} = \frac{U_c}{\sqrt{(s-1)gD_{50}}} \tag{9.9}$$

Figure 9.5, Figure 9.6 and Figure 9.7 separately visualise the influences due to the combinations of F_{rw,D_P}–F_{rc,D_P}, $F_{r,u_{*w}}$–$F_{r,u_{*c}}$ and F_{r,U_m}–F_{r,U_c}. In these figures, a negative current velocity indicates a current opposing wave condition and a positive current velocity means wave propagates co-directionally with current.

The data distribution displayed in Figure 9.5 shows that F_{rw,D_P} and F_{rc,D_P} are not crucial for identifying SDF results as the failure cases and stable cases are mixed together. Instead, Figure 9.6 and Figure 9.7 both have clear boundaries to distinguish failure cases from stable cases, especially, the statically stable cases can be separated from the failure cases. The results show that with an increase of current load, the armour layer can only attain a stable state with lower wave load acting on. The boundaries between failure and stable cases are tentatively fitted in Figure 9.6 and Figure 9.7 with dashed lines. A further look into Figure 9.7 and Figure 9.6 shows that using F_{r,U_m} and F_{r,U_c} can help to better categorise the results since less stable cases would be mixed with failure cases compared to using the shear velocities densimetric Froude numbers, $F_{r,u_{*w}}$ and $F_{r,u_{*c}}$. The results highlight the importance of F_{r,U_m} and F_{r,U_c} in assessing the stability of monopile scour protection.

However, a few issues which need to be addressed when discussing the boundary lines in Figure 9.7. Firstly, the results show that the abilities to resist wave loads under current actions are not symmetric in wave following or against current conditions. And in contrast to the conclusion drawn in Looseveldt and Vannieuwenhuyse (2012) that wave opposing current conditions would introduce more damage and tend to destabilise the scour protection layer, Figure 9.7 shows that the scour protection layer may gain the ability to resist wave loads in current opposing wave conditions. This asymmetrical behaviour is not definite for the reason that there are a lot less test cases using current opposing wave conditions than those using current following wave conditions. Secondly, the data compilation has covered different armour layer thicknesses, which may play an important role to affect the stability results. More discussions should be made regarding the layer thickness parameter, t_a/D_P.

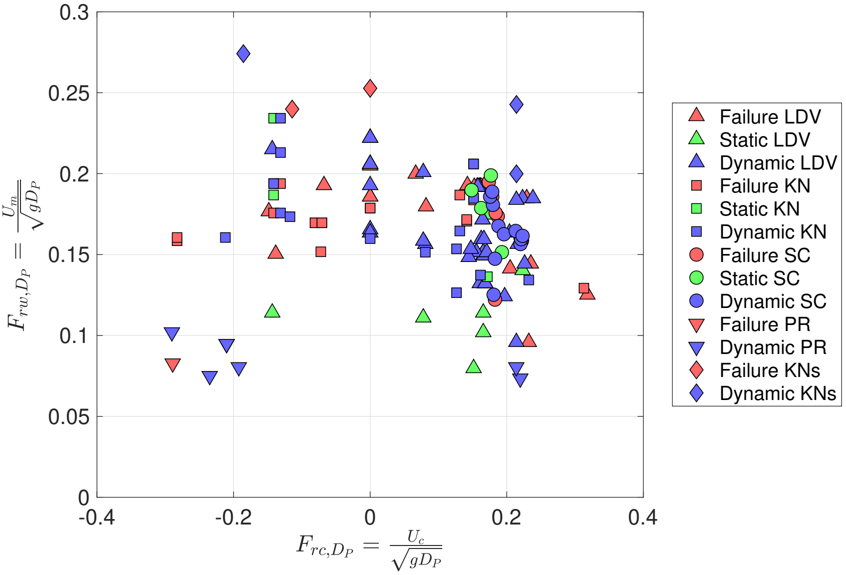

Figure 9.5: SDF results versus F_{rw,D_P} and F_{rc,D_P}.

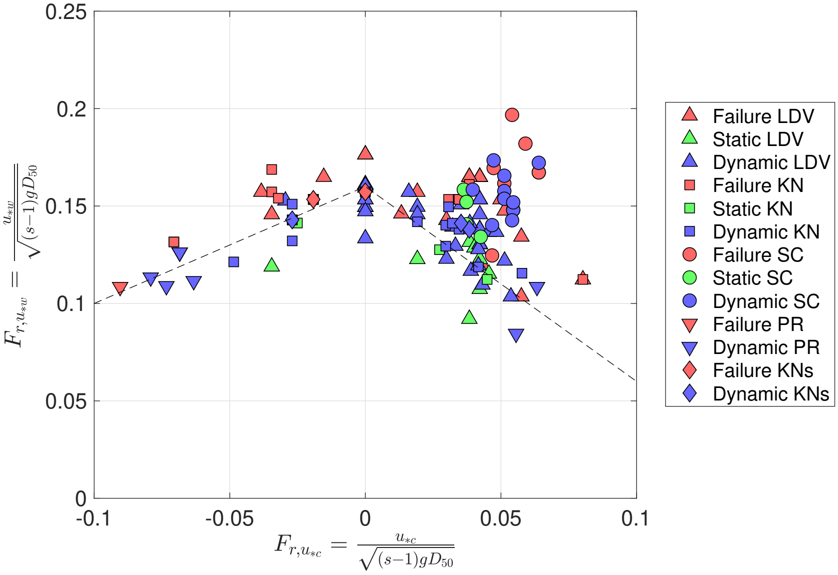

Figure 9.6: SDF results versus $F_{r,u_{*w}}$ and $F_{r,u_{*c}}$. The dashed line is an approximate boundary between failure and stable cases.

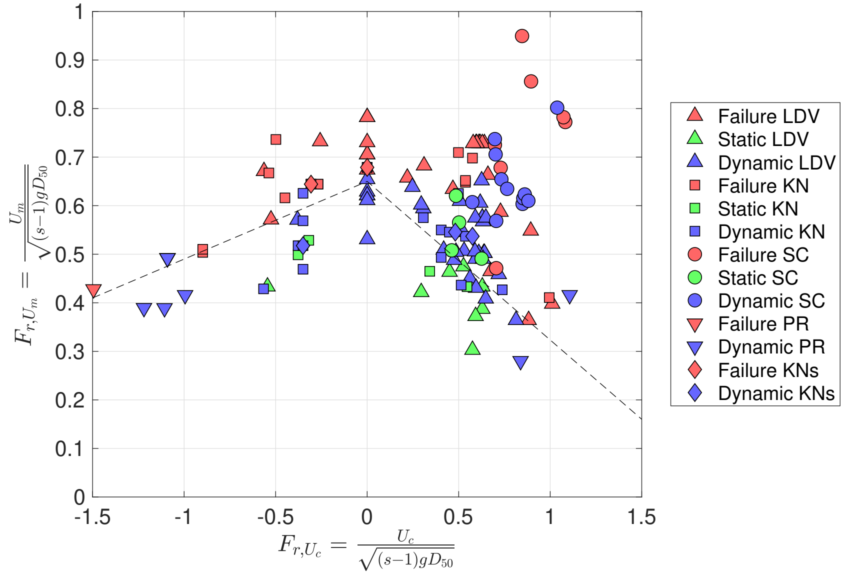

Figure 9.7: SDF results versus F_{r,U_m} and F_{r,U_c}. The dashed line is an approximate boundary between failure and stable cases.

9.2.3 Impact of armour layer thickness

Figure 9.8 shows the SDF results with various dimensionless armour layer thicknesses t_a/D_P and θ_{max}/θ_{cr}. Figure 9.9 is a zoom-in perspective for Figure 9.8. Figure 9.8 and Figure 9.9 show that the increase of armour layer can improve the ability to resist erosive shear load and enhance the stability of the armour layer. The dashed lines in the figures can be approximated to distinguish stable cases from failure cases. Failure mainly occurs when armour layer thickness is thin and θ_{max}/θ_{cr} is relatively high. However, it is noticed from Figure 9.8 that when $0.125 \leq t_a/D_P \leq 0.215$, the approximate boundary is dominated by two KNs failure cases. As described, these two D_P =0.05 m cases contain strong scale effects and lead to a very conservative boundary to separate failure cases from stable cases. The conservativeness means that a scour protection which is assumed to fail based on this boundary line may actually bear more bed loads and be stable. If these two cases are discarded, the allowable θ_{max}/θ_{cr} for a stable scour protection would significantly increase.

Instead of using θ_{max}/θ_{cr}, Figure 9.10 plots the SDF results varying with t_a/D_P using θ_{max} as an input parameter. A boundary can also be observed to separate failure cases from statically or dynamically stable cases. Similarly, this boundary line is affected by the two failure cases from KN2 data and is prone to be conservative. However, using θ_{max} does not have more advantages compared to using θ_{max}/θ_{cr}, because an individual θ_{max} value can only reflect the load acting on an armour stone. It is not able to reflect the threshold of motion status of an armour stone, which loses a physical significance.

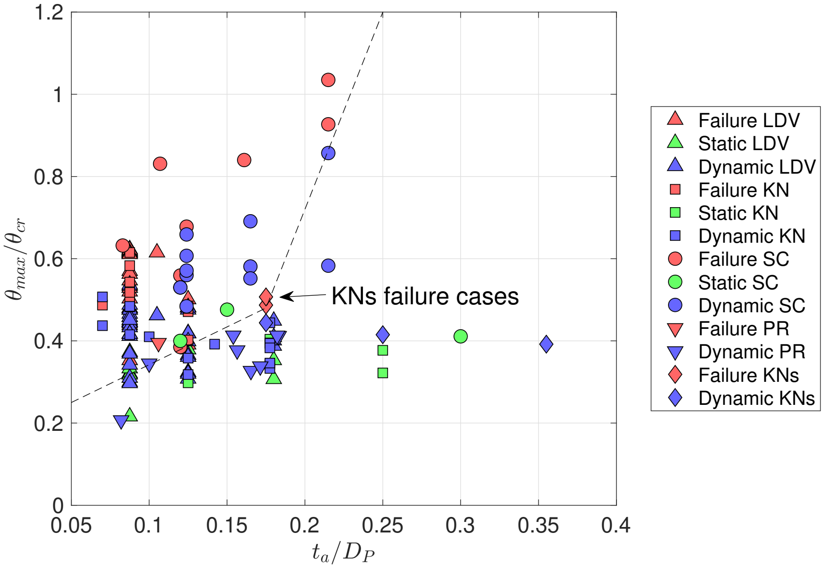

Figure 9.8: SDF results versus t_a/D_P and θ_{max}/θ_{cr}. The dashed line is an approximate boundary between failure and stable cases.

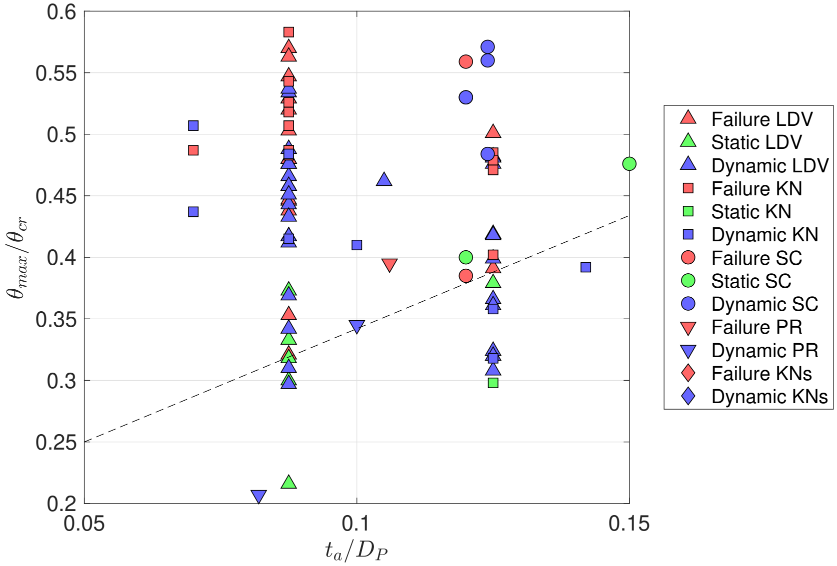

Figure 9.9: SDF results versus t_a/D_P and θ_{max}/θ_{cr}: zoom-in view of $0.05 < t_a/D_P < 0.15$ and $0.2 < \theta_{max}/\theta_{cr} < 0.6$. The dashed line is an approximate boundary between failure and stable cases.

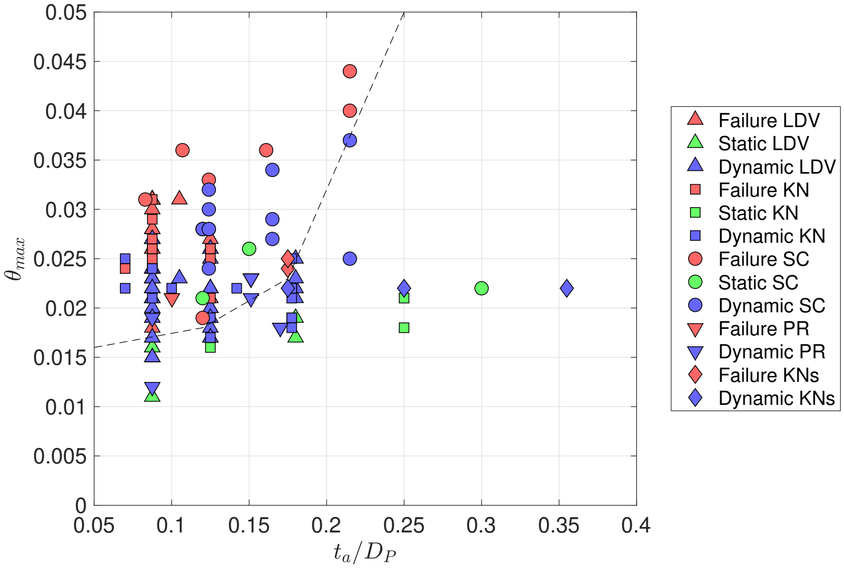

Figure 9.10: SDF results versus t_a/D_P and θ_{max}. The dashed line is an approximate boundary between failure and stable cases.

From the results, it is seen that the layer thickness of a monopile scour protection is an important design parameter. Thicker layer thickness could not only enhance the performance of the erosion stability but also alleviate sinking problems, however it may raise the construction cost as well since a bigger volume of rocks will be transported. An optimisation between the applied armour stone size and volume has to be taken into consideration for a purpose of achieving a low-cost engineering feasibility.

9.2.4 Impact of Reynolds number

As discussed in Chapter 8, one of the important factors which leads to scale effects is the Reynolds numbers that characterise the flow around pile. It is confirmed that a geometrically similar large scale monopile scour protection model has a better stability performance compared to a small scale model under similar environmental loads. In order to discuss the influence from Reynolds number (R_{e,D_P}), Figure 9.11, Figure 9.12 and Figure 9.13 plot the SDF results with various R_{e,D_P} against θ_{max}/θ_{cr}, KC and Ucw, respectively. Unfortunately the influence due to R_{e,D_P} is not obvious, which is mainly attributed to the limited data resources of using large scale model ($R_{e,D_P} > O(10^5)$).

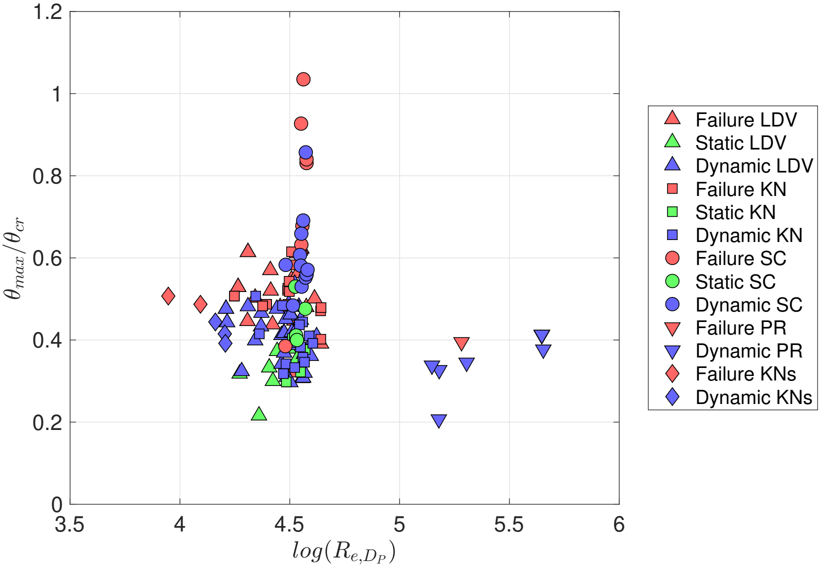

Figure 9.11: SDF results versus R_{e,D_P} and θ_{max}/θ_{cr}.

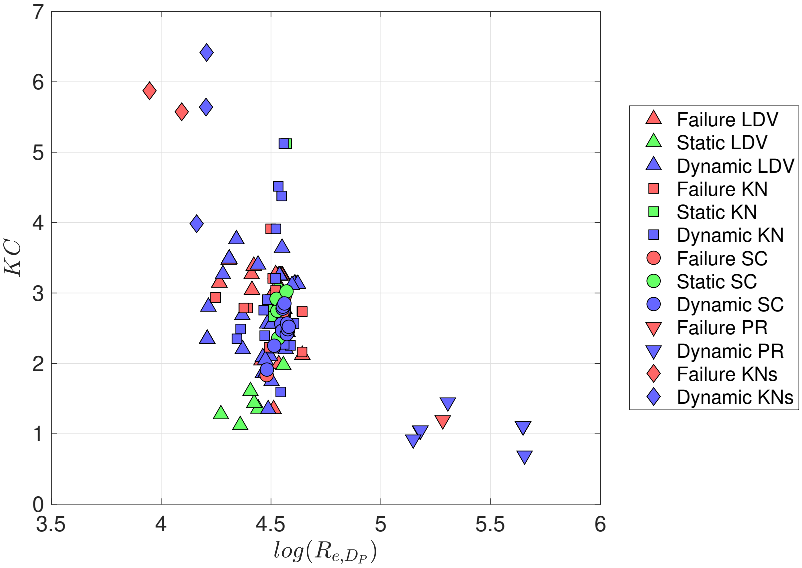

Figure 9.12: SDF results versus R_{e,D_P} and KC.

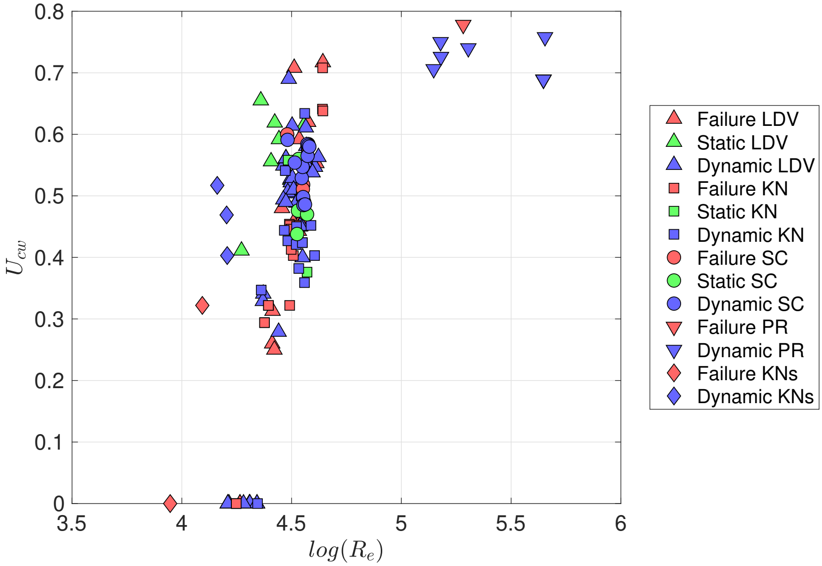

Figure 9.13: SDF results versus R_{e,D_P} and Ucw.

9.3 Potential application on scour protection design

Through the discussion on the dimensionless parameters which may contribute to the monopile scour protection stability performance (SDF), three key conclusions can be drawn.

(1) Wave and current velocities have major impacts on the SDF results. The armour layer can withhold less wave loads when current co-exists. The influence of the current direction is not obvious due to the scarcity of data. The boundary between failure and stable cases can be represented by Froude numbers F_{r,U_m} and F_{r,U_c}. Compared with other Froude numbers, these two parameters are very close to the expression used in Izbash formula (Izbash, 1935).

(2) The ratio between Shields parameter and critical Shields parameter (θ_{max}/θ_{cr}, also used as the STAB parameter), which represents the mobility of armour stones, is very important for the SDF results. Failures frequently occur when $\theta_{max}/\theta_{cr} > 0.438$ and occasionally occur when $\theta_{max}/\theta_{cr} > 0.321$ and $U_{cw} > 0.592$.

(3) The dimensionless thickness of armour layer, t_a/D_P, is one key parameter. Increasing t_a/D_P will improve the stability of monopile scour protection.

The conclusions hint a possibility of using these dimensionless parameters to predict the erosion failure of a monopile scour protection.

9.3.1 Failure prediction

Firstly, the criterion for a stable armour layer accounting F_{r,U_m} and F_{r,U_c} is regressed into Eq. (9.10). The stable and failure regions are plotted in Figure 9.14.

$$3F_{r,U_m} + |F_{r,U_c}| \leq 2 \tag{9.10}$$

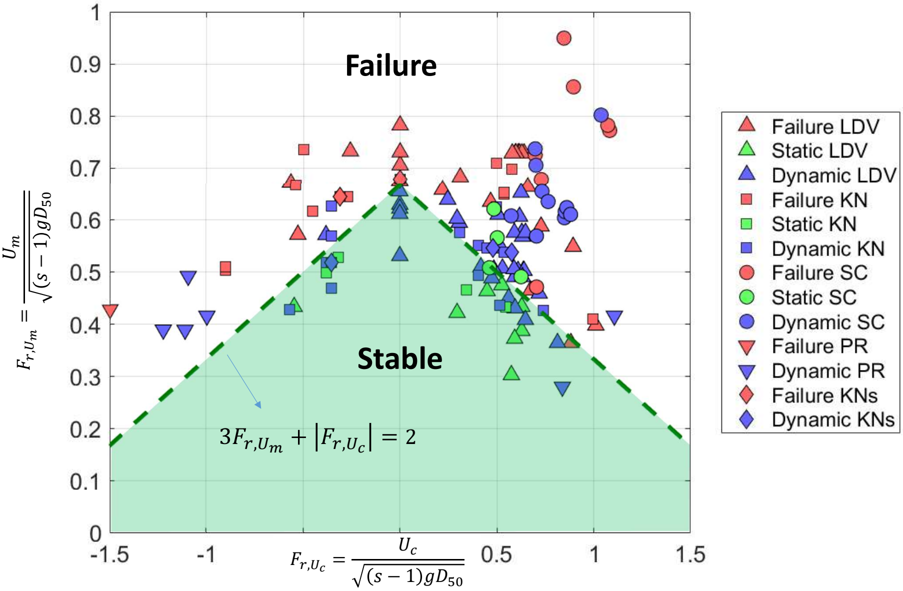

Figure 9.14: Stable and failure regions determined by Eq. (9.10).

Eq. (9.10) is simplified to a criterion number K_1, as defined in Eq. (9.11). If $K_1 < 1$, the scour protection tends to fail under the specific hydrodynamic loading.

$$K_1 = \frac{2}{3F_{r,U_m} + |F_{r,U_c}|} \tag{9.11}$$

A second criterion number, K_2, is assumed to be related to θ_{max}/θ_{cr} of the armour stones. Figure 9.15 plots the relationship between θ_{max}/θ_{cr} and U_{cw} and the stable/failure regions. Achieving a stable scour protection will require to satisfy the conditions in Eq. (9.12). Based on Eq. (9.12), K_2 is defined as a piecewise function by Eq. (9.13). If $K_2 < 1$, the scour protection tends to fail under the specific hydrodynamic loading. For this criterion, the KC number is not taken into account for the reason that the experimental data within the range of $KC > 2$ and $U_{cw} > 0.6$ are not enough for arriving in a reliable conclusion.

$$\frac{\theta_{max}}{\theta_{cr}} \leq \begin{cases} 0.438, & 0 \leq U_{cw} < 0.425 \\ -0.509U_{cw} + 0.6543, & 0.425 \leq U_{cw} \leq 0.8 \end{cases} \tag{9.12}$$

$$K_2 = \begin{cases} \frac{0.438}{\theta_{max}/\theta_{cr}}, & 0 \leq U_{cw} < 0.425 \\ \\ \frac{-0.509U_{cw}+0.6543}{\theta_{max}/\theta_{cr}}, & 0.425 \leq U_{cw} \leq 0.8 \end{cases} \tag{9.13}$$

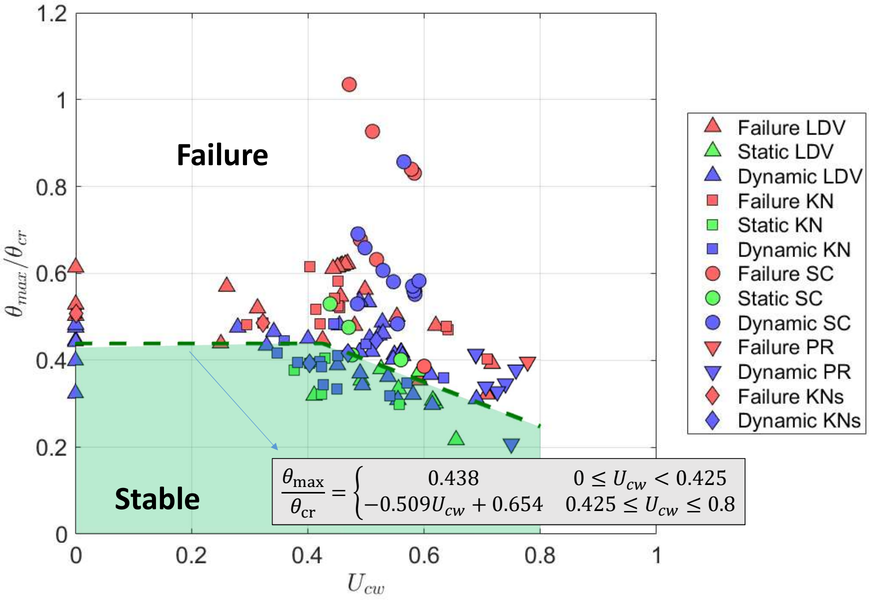

Figure 9.15: Stable and failure regions determined by Eq. (9.12).

Thirdly, the dimensionless armour layer thickness t_a/D_P is determined by fitting a piecewise function using θ_{max}/θ_{cr} as input. When $\theta_{max}/\theta_{cr} < 0.391$, a quadratic relationship between t_a/D_P and θ_{max}/θ_{cr} is used, as expressed in Eq. (9.14). This ensures the asymptotic property that $t_a/D_P = 0$ when $\theta_{max}/\theta_{cr} = 0$. When $0.391 \leq \theta_{max}/\theta_{cr} \leq 0.857$, a simple linear relationship is fitted, where the two small scale failure cases from KNs dataset are not taken into consideration. This is because using KNs failure data will significantly increase the required layer thickness or the stone size due to high scale effects. Figure 9.16 shows the division of failure and stable regions using Eq. (9.14) and Figure 9.17 is the zoom-in view of the parameter ranges of $0.2 \leq \theta_{max}/\theta_{cr} \leq 0.6$ and $0.05 \leq t_a/D_P \leq 0.2$. Therefore, an other criterion number K_3 can be defined using Eq. (9.15). When $K_3 < 1$, the scour protection tends to fail with the applied thickness of armour layer. K_3 reflects the physics that a thick armour layer can be beneficial for the stability of monopile foundation scour protection, but this number is only valid for the range that $t_a/D_P \geq 0.05$ and $\theta_{max}/\theta_{cr} \leq 0.857$. It is very difficult to extrapolate the applicability to a thinner layer or a larger θ_{max}/θ_{cr} condition due to the scarcity of test data. When $\theta_{max}/\theta_{cr} > 0.857$, it is likely that all armour stones are under the risk of being moved by the amplified bed shear stress around pile. In addition, it should also be noted that this armour layer thickness excludes the thickness of a filter layer.

$$\frac{t_a}{D_P} \geq \begin{cases} 0.673\left(\frac{\theta_{max}}{\theta_{cr}}\right)^2 + 0.0566\frac{\theta_{max}}{\theta_{cr}}, & 0 \leq \frac{\theta_{max}}{\theta_{cr}} < 0.391 \\ 0.1679\left(\frac{\theta_{max}}{\theta_{cr}}\right) + 0.0593, & 0.391 \leq \frac{\theta_{max}}{\theta_{cr}} \leq 0.857 \end{cases} \tag{9.14}$$

$$K_3 = \begin{cases} \frac{t_a/D_P}{0.673\left(\frac{\theta_{max}}{\theta_{cr}}\right)^2+0.0566\left(\frac{\theta_{max}}{\theta_{cr}}\right)}, & 0 \leq \frac{\theta_{max}}{\theta_{cr}} < 0.391 \\ \frac{t_a/D_P}{0.1679\left(\frac{\theta_{max}}{\theta_{cr}}\right)+0.0593}, & 0.391 \leq \frac{\theta_{max}}{\theta_{cr}} \leq 0.857 \end{cases} \tag{9.15}$$

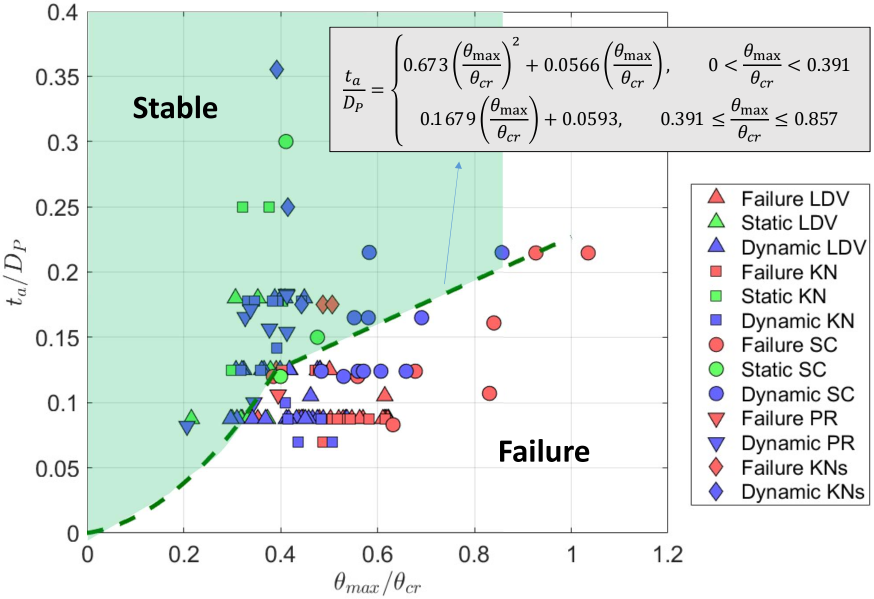

Figure 9.16: Stable and failure regions determined by Eq. (9.14).

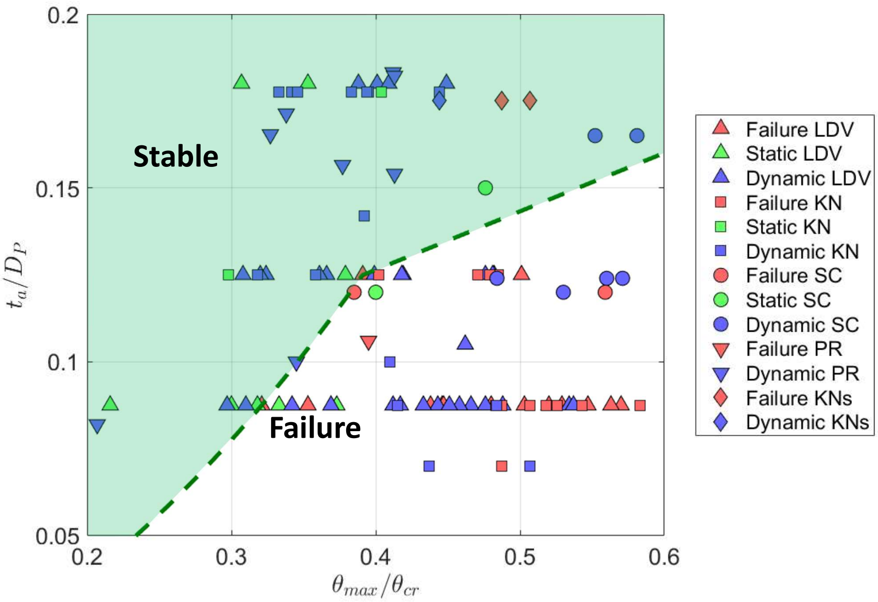

Figure 9.17: Stable and failure regions determined by Eq. (9.14): zoom-in view of $0.2 \leq \theta_{max}/\theta_{cr} \leq 0.6$ and $0.05 \leq t_a/D_P \leq 0.2$

Finally, a product of all criterion numbers is defined by Eq. (9.16),

$$K = K_1 K_2 K_3 \tag{9.16}$$

when $K < 1$, the scour protection tends to fail.

Figure 9.18 plots the SDF results against the K value. In this figure it is seen that nearly a half of dynamically stable cases are with and only five statically stable cases are with $K < 1$. This shows that the K value can well identify possible failure cases from a conservative view. It should be noted that small scale KNs data has been discarded in 9.18.

9.3.2 Comparison with existing design methods

In order to have an insight of the K value in predicting monopile scour protection failure, a comparison between different methods is discussed. For a fair comparison excluding scale effects of very small scale model, the KNs data is discarded. Figure 9.19 illustrates the SDF results presented by using only θ_{max}/θ_{cr} (STAB parameter). The comparison between Figure 9.19 and Figure 9.18 shows that the K value has a better performance to identify failure and stable cases compared with the STAB criteria ($STAB < 0.415$ for statically stable, $0.415 \leq STAB \leq 0.46$ for dynamically stable and $STAB > 0.46$ for failure).

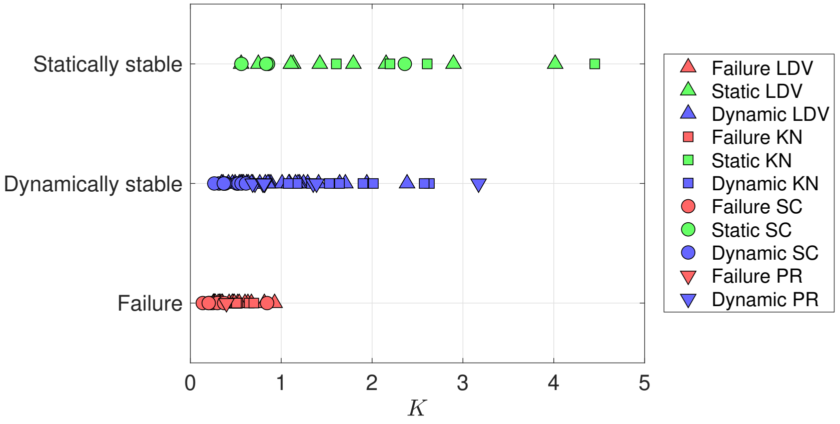

Figure 9.18: SDF results versus K value.

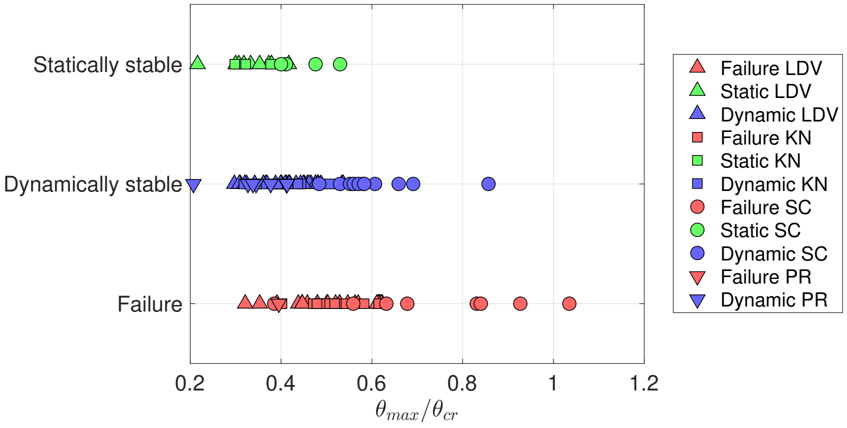

Figure 9.19: SDF results versus θ_{max}/θ_{cr} value.

Figure 9.20 plots the SDF results against the $S_{3D,pred}$ values obtained from De Vos et al. (2012). Though the $S_{3D,pred}$ values are able to identify statically stable and failure cases with a threshold of $S_{3D,pred} > 1$, the limitations are obvious: (1) it is not applicable to a thick layer thickness when $t_a/D_{n50} > 3$; (2) it may result in very large $S_{3D,pred}$ number when D_{50} is small and out of proposed range, therefore excludes many actual dynamically stable cases. Compared with the S_{3D} method by De Vos et al. (2012), the K values can be applied to wider ranges of stone size and armour layer thickness. With a merit of both K value and S_{3D}, a plot of stable and failure cases using the two parameters is provided in Figure 9.21. It is seen that the if both K and $S_{3D,pred}$ are considered, the failure cases will be better identified when the two conditions are satisfied simultaneously: $K < 1$ and

$S_{3D,pred} > 1$.

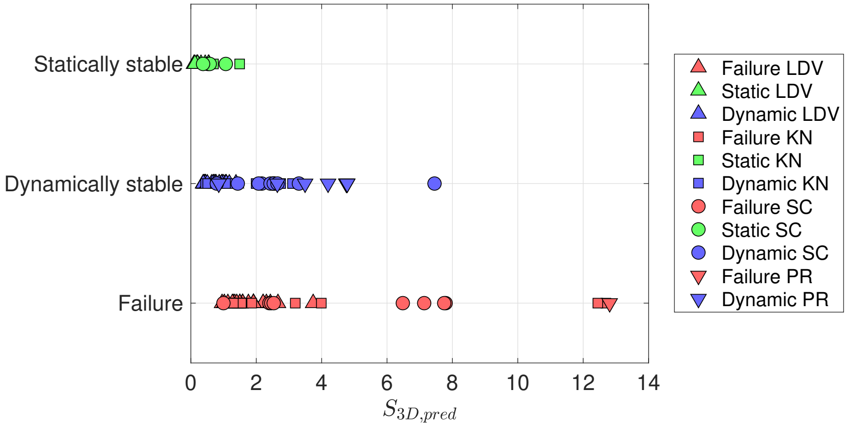

Figure 9.20: SDF results versus $S_{3D,pred}$ value.

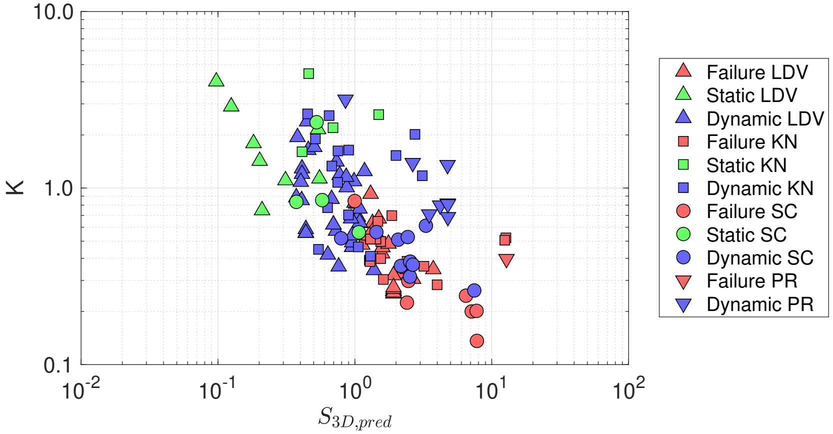

Figure 9.21: SDF results represented by both K and $S_{3D,pred}$.

9.4 Design case study

9.4.1 Existing wind farms

For the purpose of validating the applicability of K value in monopile scour protection design, four wind turbine foundations are evaluated. The design conditions and armour layer parameters are listed in Table 9.1. The data is extracted from Esteban et al. (2019b), where detailed technical parameters of the listed foundations, including the metocean, location, soil, armour layer and filter layer, are presented. The design wave and current conditions given in Table 9.1 are using 50 year returning period.

Table 9.1: Parameters of wind turbine foundations and design conditions

Case name	d [m]	D_P [m]	U_m [m/s]	U_c [m/s]	D_{n50} [mm]	t_a [m]	t_a/D_{n50} [-]	ρ_s [kg/m^3]
Egmond aan Zee	20	4.6	0.73	0.6	400	1.8	4.5	2800
Horns Rev 1	14	4.2	1.15	1.17	550	1.8	3.3	2600
Princess Amelia	24	4	1.61	1.3	500	1.5	3.0	2800
Scroby Sands	12	4.2	1.08	1.68	450	1.3	2.9	2600

Using the prediction formulas of K value (Eqs. 9.11, 9.13, 9.15 and 9.16), the results are listed in Table 9.2. The K values are all larger than 1, indicating that all the four turbine foundations have stable armour layers to protect scouring under the design conditions.

Table 9.2: Evaluation results

Case name	θ_{max}/θ_{cr}	K_1	K_2	K_3	K	Evaluation result
Egmond aan Zee	0.171	2.040	2.479	13.292	67.226	Stable
Horns Rev 1	0.385	1.360	1.032	3.518	4.937	Stable
Princess Amelia	0.460	1.038	0.928	2.747	2.646	Stable
Scroby Sands	0.389	1.156	0.885	2.497	2.555	Stable

As a comparison, Table 9.3 and Table 9.4 respectively list the designed median stone weights (W_{n50}) and median stone sizes (D_{50}) using different methods. The results of using Izbash method (Izbash, 1935) and using De Vos method (De Vos et al., 2012) are provided by Esteban et al. (2019b). The fourth columns in the two tables list the optimised D_{50} and W_{n50} via the K value, where $K = 1$ is used as the design constraint for a stable scour protection against erosion. The calculation is done by iteratively solving D_{50} until $K = 1$. W_{n50} is calculated by Eq. (9.17) using $D_{n50} = 0.84D_{50}$. The armour layer thickness is kept the same with the real design.

$$W_{n50} = \rho_s {D_{n50}}^3 = 0.593\rho_s {D_{50}}^3 \tag{9.17}$$

The comparison shows that the designs based on $K = 1$ are more economic compared to other existing design method under an assumption that the armour layer thickness is fixed. The Izbash method is the most conservative as it focuses more on the critical status of the armour stone, which yields a statically stable scour protection. The De Vos method can achieve much smaller stones due to the fact that it allows some armour stones movements and aims for a dynamically stable status. The K value method gives the smallest stone sizes because it takes the advantage of the layer thickness. In De Vos method, the results are valid for

Table 9.3: Median stone weight results using different design methods, W_{50} unit in kg

Case name	Izbash method	De Vos method	K value method	Real weight
Egmond aan Zee	0.77	1.03	0.09	179.2
Horns Rev 1	21.44	11.27	10.91	432.6
Princess Amelia	84.34	78.95	36.82	350.0
Scroby Sands	61.43	50.44	27.09	236.9

Table 9.4: Median stone sizes results using different design methods, D_{50} unit in mm

Case name	Izbash method	De Vos method	K value method	Real size
Egmond aan Zee	78	86	38	477
Horns Rev 1	241	194	192	655
Princess Amelia	371	363	281	596
Scroby Sands	342	320	260	536

a layer thickness of $t_a = 2.5D_{n50}$, but the listed wind farms were using $t_a = 2.9D_{n50}$ to $4.0D_{n50}$, which means the $\theta_{max}/\theta cr$ of the armour stones could be larger. This the main reason of the differences between the design results. The design stone sizes of all design methods are smaller than that were applied in real engineering, which is mainly attributed to two reasons: (1) the real engineering cases have to consider enough safety margins to improve the functionality of the scour protection; (2) the construction of the four wind farms can be dated back to year 2003 to 2005, while very limited data resources could be referred in the early era of offshore wind. Recent resources have shown that more and more dynamically stable scour protections are being applied to prototype, and the armour stone sizes are significantly reduced Fazeres-Ferradosa et al. (2021).

9.4.2 New wind turbine foundation

As the offshore wind technology growing quickly in recent years, the pile size for new generation wind turbine may exceed 10 m. Regarding the large sized new wind turbine foundation, a design example considering an optimisation of both armour stone size and armour layer thickness is provided in this section.

The design case is assumed to be a newly designed large size wind turbine foundation, which is located in Fairybank of the Belgian Part of North Sea and has a pile diameter of $D_P = 9m$. The target water depth in the zone is $d = 25m$ and the median bed sediment grain size is 200 μm. A fifty year extreme wave and current conditions are applied to the design, which gives $H_s = 5.91m$, $T_p = 10.09s$ and $U_c = 1.7m/s$. The armour layer has a fixed diameter of $5D_P$ (45 meters). The armour stone density is fixed to $\rho_s = 2650kg/m^3$.

The objective is set to be the minimum cost of applied armour stones, noted as C. C is assumed to be a function of both the unit stone weight and the total volume of the stones, as expressed in Eq. (9.18). The coefficient 24 indicates the total scour protection area is 24 times the pile diameter.

$$C = f(W_{50}, \frac{\pi}{4} 24 D_P^2 t_a) \tag{9.18}$$

To further simplify the objective, the cost function is assumed to be proportional to W_{n50}, which is also proportional to D_{50}^3. Meanwhile, as D_P is a fixed value, the cost function can be simplied to be proportional to t_a. Therefore, a simple relationship is established as Eq. (9.19),

$$C = C_1 D_{50}^3 t_a \tag{9.19}$$

where C_1 is constant number in this design.

The design ranges are limited to $0.01m \leq D_{50} \leq 0.6m$ and $1.0D_{50} \leq t_a \leq 8.0D_{50}$. For the K value, a safety factor is necessary. Tentatively, $K = 2$ is set as to ensure a safe design. Hence, the optimisation model deteriorates to Eq. (9.20),

$$\begin{array}{ll} \text{Objective} & min(C) = min(C_1 D_{50}^3 t_a) \\ \text{Subjected to} & D_{50} \in [0.01, 0.6] \quad \text{and} \\ & t_a \in [1.0D_{50}, 8.0D_{50}] \quad \text{and} \\ & K \geq 2 \end{array} \tag{9.20}$$

Solving this optimisation problem returns the design results as listed in Table 9.5. For this case, reasonable stone sizes, stone weights and armour layer thickness are obtained. It is seen that the optimisation process tries to push the designed armour layer thickness to the upper boundary while reduce the armour stone size as much as possible. This is mainly due to the fact that the assumed cost function is more sensitive to D_{50} and less sensitive to t_a. In reality, the cost function can be more complicated other than simple cubic or linear relationship of two parameters. However, the given example shows that the proposed K value may provide an option to optimise monopile scour protection layer in practise under various real engineering restrictions and objectives.

Table 9.5: Design results of large size wind turbine scour protection

t_a (m)	D_{50} (mm)	D_{n50} (mm)	W_{50} (kg)	$\frac{t_a}{D_{n50}}$ (-)	$\frac{t_a}{D_{50}}$ (-)	K (-)
1.87	240	202	21.7	7.79	9.28	2.0

9.5 Conclusions

This chapter mainly discusses two issues based on the data analysis of experimental results. Firstly, a compilation of existing experimental data of monopile scour protection model test is presented. This compilation considers only the erosion failure mode of the scour protection and covers various pile sizes and model scales. Different armour layer configurations are involved in this compilation, such as 2–3 layers of large sized armour stones and 8–10 layers of small sized armour stones. A synthetic analysis of the influencing parameters is carried out. The following parameters have shown significant impacts on the SDF results, which are

(1) densimetric Froude number of depth-averaged current velocity F_{r,U_c},

(2) densimetric Froude number of mean wave orbital velocity F_{r,U_m},

(3) ratio between the maximum Shields parameter and the critical Shields parameter, θ_{max}/θ_{cr},

(4) ratio between velocities U_{cw},

(5) dimensionless layer thickness t_a/D_P.

Secondly, a K value is proposed to evaluate the erosion failure of a monopile scour protection considering all the influencing parameters. K is a criterion number, which is a product of three criterion numbers (K_1, K_2 and K_3), $K = K_1K_2K_3$. When $K \geq 1$, the monopile scour protection is stable. $K < 1$ indicates the scour protection is prone to fail. The K value may also be applied to the design of monopile scour protection. Design examples are presented for some existing wind farms and a presumed new generation wind turbine. For the existing wind farms, smaller armour stone sizes are obtained using $K \geq 1$ as a design restrain constraint compared with using other existing design methods. For the new wind turbine, reasonable stone sizes and armour layer thickness are obtained through an optimisation process under the assumptions: (1) the minimum cost function is the objective, (2) the cost function is proportional to $D_{50}^3 t_p$. The results show that it is promising to apply the K value in real engineering design for new generation monopile foundation scour protection.

Some important issues and limitations have to be addressed regarding the applicability of the K value in practical design of monopile scour protection.

- Using the K value in design does not consider the extension width of the scour protection due to the reason that the shear failure usually occurs near the pile. However, from the existing experience, the scour protection extension width (W_a in Figure 3.1) should be at least $5D_P$ to $8D_P$ (De Vos, 2008; Esteban et al., 2019b).

- The K value is fitted based on conditions that the wave duration is less than 5000 waves. This duration is supposed to be adequate for a scour protection reaching an equilibrium state, according to laboratory observation. However, the real sea conditions might be more complex than expected, therefore, concerns needs to be paid by using sufficient safety margins.

- The K value should be calculated when the inputs are bounded within the range of the compilation, which involves: $0.07 \leq t_a/D_P \leq 0.35$, $0.02 \leq$

$D_{50}/D_P \leq 0.17$, $|F_{r,U_c}| < 1.5$, $F_{r,U_w} < 1$ and $\theta_{max}/\theta_{cr} < 0.857$. The applicability of extrapolating design results to out-of-range data input is one of the interests for future study.

- The grading of the armour stones are not considered due to the limited data resources. The result would be valid for a grading coefficient range of $1.3 \leq D_{84}/D_{16} \leq 4.0$. However, more investigations are needed for the sake of optimising the gradings of armour materials.

Chapter 10

Conclusions and outlook

Scour protections around offshore wind foundations are important to the engineering safety of the offshore wind turbine system, especially for monopile, jacket and gravity-based structure. It attracts vast concerns from both the academia and the industry throughout decades so as to understand the failure mechanisms of the scour protection and to achieve reliable and economical design methods. This thesis, on the basis of differently scaled laboratory experimental studies, discusses issues related to the erosion failure of monopile scour protection under current and wave conditions. The main conclusions are drawn as follows.

Firstly, the present study analyses the experimental data obtained from the unique large scale tests of monopile scour protection (PROTEUS project) and compares the experimental results to the existing design methods. The large scale models are scaled down from a prototype pile diameter $D_P = 5$ m using geometrical scale ratios of $\lambda =$ 1:16.667 and 1:8.333. For the static stability, both the STAB parameter method (Den Boon et al., 2004) and the static design method (De Vos et al., 2011) conservatively predict the static stability of the large scale model. For the dynamic stability, design methods from De Vos et al. (2012) and Nielsen and Petersen (2019) report higher predicted damage levels of the scour protection than the measurement. The main reason for the conservativeness is that the existing design methods are developed based on small scale experiments, therefore the associated model and scale effects will lead to an overestimated failure risk for large scale models or prototypes. The other reason is that the applied wave-current conditions and the armour stone sizes are out of range of the S_{3D} design formula (Eq. 3.15) given by De Vos et al. (2012). As for the erosion depth, the maximum eroded depth of monopile scour protection is compared to the traditional scour depth prediction formulas. The erosion depth S/D_P increases as u_{*max}/u_{cr} increases and tends to be lower than the prediction. The results indicate a necessity of a systematic investigation on the inherent scale effects.

Secondly, with the Best Model scaling scheme (Hughes, 1993), a series of small scale experiments (λ= 1:50), which are down scaled from the PROTEUS project test cases Test 10B and Test 13B, are performed so as to investigate the scale effects in the monopile scour protection experiment. In order to clearly reflect the physics, the analysis procedure follows the sequence of measurement effects – model effects – scale effects as suggested by Kortenhaus et al. (2005) such that to exclude the interference due to measurement and model setup when comparing the two scaled models. The study of measurement and model effects are carried out with repeated tests. The results show that with the applied hand laser scanner, the standard deviation of global S_{3D} due to measurement accuracy is limited to $\sigma(S_{3D}) = 0.039$. While the standard deviation of global S_{3D} due to model setup is up to $\sigma(S_{3D}) = 20.3\%\overline{S_{3D}}$, and for subarea damage $S_{3D,i}$ the standard deviation reaches $\sigma(S_{3D,i}) = 33.1\%\overline{S_{3D}}$. The non-repeatability of flow field around pile due to turbulence and the non-repeatability of scour protection installation and flatness are assumed to be the primary causes of the model effects.

Thirdly, a formal analysis of uncertainties due to wave and current measurement is carried out according to the guidelines from JCGM (2008). The analysis reports a high uncertainty in individual experiment of monopile scour protection, the uncertainty of S_{3D} is $u(S_{3D})$= 0.558, which is mainly attributed to the high fluctuation of incoming current as well as its quadratic contribution to the predicted S_{3D}. In repeated experiments, the uncertainty is much lower as more knowledge of such experiments has been gained. For TG1 and TG2, the predicted uncertainties of S_{3D} due to measurement are separately 0.0478 and 0.0427. These values are with the same orders to the measured uncertainties of S_{3D} and show that considerable uncertainties will propagate from wave and current measurement to S_{3D} results. This is mainly due to the highly nonlinear relationship between U_m, U_c and predicted S_{3D}. The over-prediction of S_{3D} will also lead to an overestimation of experimental uncertainties.

In the fourth, the scale effects are analysed by comparing the two different scaled model test results. The comparison clearly reflects the differences of damage patterns, especially the eroded area and the $S_{3D,i}$ values. The large scale test results exhibit smaller damage numbers as well as the areas of erosion and accretion than the small scale test results. The primary reasons for the observed scale effects are attributed to the impossibility of reproducing similar flow regimes and the incorrect reproduction of sediment transport properties. For the time scale of damage development, the large scale model reaches an equilibrium state at around 3000 waves, while small scale model has not obtained an equilibrium at 5000 waves under a similar wave and current condition. The results show that small scale experiment will result in a less stable scour protection. The study reveal the limits of applying the Best Model scaling laws as significant scale effects appear, and indicates the necessity of further investigation on more appropriate scaling laws.

At last, an synthetic analysis of the compilation of existing laboratory experiments is carried out. From the study, the most influencing parameters for the stability of armour layer are: Froude numbers F_{r,U_c} and F_{r,U_m}, ratio between the maximum Shields parameter and critical Shields parameter θ_{max}/θ_{cr}, ratio between current and wave velocities U_{cw} and dimensionless armour layer thickness t_a/D_P. A K value is defined to evaluate whether the scour protection is stable or failure under the designated wave and current condition, considering only the shear erosion failure mode. The stability status of the armour layer when $K \geq 1$ can be either statically stable or dynamically stable, which allows a possibility of using smaller grains to build the armour layer. Design examples are presented using both the existing wind farm data and the new generation large wind turbine data. The results show that smaller armour stone sizes can be obtained by using the K value than by using other existing design methods. This indicates a possible reduction of foundation installation cost.

The thesis proves the importance of using large scaling modelling for monopile scour protection and provides the model and scale effects associated to such experiment. As an outlook for the future work, a few suggestions can be given. (1) The design of new generation scour protection layer should consider the scale effects as the small scale experiment based design will lead to extra investment. (2) At least 20% of standard deviation of predicted S_{3D} should be added to the practical dynamic design method. (3) More systemic investigations are still required to obtain a more precise design formula taking account more influencing factors such as the grading of armour stones, wider range of armour stone size and armour layer thickness, edge scour, sinking, and, more complex seabed conditions. Field data is extremely important for the development of new design methods. As pure experimental studies, especially large scale experiments, are expensive to be applied in practical design, the Simulation-Based-Design (SBD) is promising to be an alternative in frontline with the fast development of novel high-efficiency and high-resolution numerical simulation techniques in the near future.

Appendix A

Additional information of small scale experiments

This appendix shows some details of the small scale experiments performed in the wave flume at the Coastal Engineering Research Group of Ghent University and introduces the current generation system, wave generation and absorption system, performance comparison of applied scanners and some photos during the experiments.

A.1 Current system

The current is generated via a fixed speed pump as shown in Figure A.1. The current velocity is adjusted by a manual valve. The pipe connects the inlet in the end of wave flume, as seen in Figure A.2

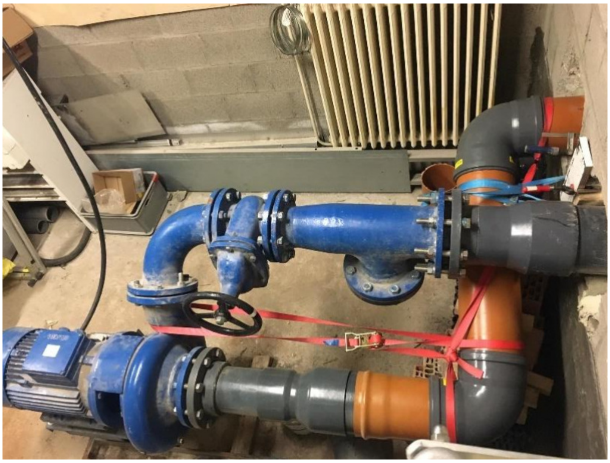

Figure A.1: Current generating pumps.

Figure A.2: Pipe connected to the current inlet.

The current profiles for TG1 (d=0.3 m) and TG2 (d= 0.25 m) are measured by the ADV in various height above the bottom, shown in Figure A.3. The results indicate a proper measurement height for the depth averaged current velocity at $z = 0.4d$.

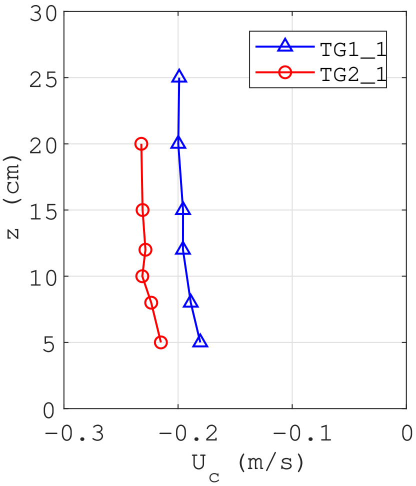

Figure A.3: Current profiles for TG1 and TG2.

A.2 Wave generation and absorption system

The waves are generated using a piston-type wave paddle. The implementation of wave generation and active wave absorption is introduced in Troch (2000). The passive wave absorption system in the present test utilises four layers of honeycomb sponge blocks, as shown in Figure A.4. The current inlet screen is installed beneath the wave absorption system.

Figure A.4: Passive wave absorption and current inlet.

The reflection coefficient of the passive wave absorption is analysed using the WaveLab software, which is based on a time-domain method for Separating the Incident waves and the Reflected Waves (SIRW-method) (Frigaard and Lykke Andersen, 2014). The reflection rate is then defined as Eq. (A.1),

$$K_r = \frac{H_{s,r}}{H_{s,i}} \tag{A.1}$$

Where $H_{s,r}$ is the reflected significant wave height, and $H_{s,i}$ is the incident significant wave height.

For the wave and current condition used in TG1, K_r= 0.23 for an empty wave flume condition and K_r=0.25 with the pile at presence. The magnitudes of the reflection coefficients are reasonably high due to the interactions between wave and current, which are comparable to the values obtained from Draycott et al. (2018). The diffraction due to the presence of the pile leads to a higher K_r than the empty wave flume condition.

A.3 Performance comparison between scanners

In the previous studies from De Vos (2008) and Looseveldt and Vannieuwenhuyse (2012), the single-beam laser profiler, EPro (Meinert, 2004), was applied to record the bed profiles (Figure A.5) This non-contact erosion profile consists mainly of a motion servo system, a laser beam shooter and a receiver, and a post-processing software. Thanks to the waterproof setting, the EPro profiler can measure the bed deformations in an underwater condition. The scanning resolution is defined by the user, but a trade-off between the measuring resolution and speed has to be considered. Practical user experience from De Vos (2008) suggests to use grid size of 5 mm × 5 mm as the measurement resolution. A complete measurement of a monopile scour protection area of 0.7m × 0.7m takes approximately 30 minutes.

Figure A.5: EPro laser scanner.

However, problems exist in the measurement of monopile scour protection damage due to the relatively low accuracy compared to the stone size. According to the setting introduced in De Vos (2008), the accuracy in all directions is 1 mm. Debaveye and De Riemacker (2020) has tentatively analysed the possible errors in measured eroded volumes and $S_{3D,i}$ with this measurement accuracy. A part of the results is shown in Figure A.6. It is found that the calibration of the EPro in Z direction can significantly affect the S_{3D} value, the error of S_{3D} due to 1 mm shift of Z origin can be high up to 0.41 and the relative error of S_{3D} reaches 68%.

Figure A.7 shows a bed form plot of the EPro raw data. The exact location of centre of the pile is difficult to judge, which introduces the errors mentioned above. Further, De Vos (2008) and Looseveldt and Vannieuwenhuyse (2012) have mentioned that the colouring of stones will affect the quality of the scan due to the laser absorption effect. De Vos (2008) and Debaveye and De Riemacker (2020)

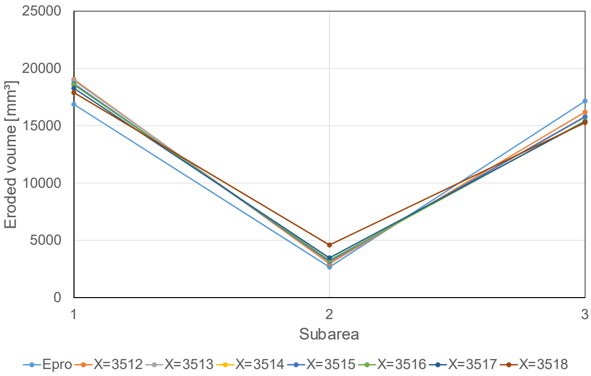

(a) Errors due to X origin shift.

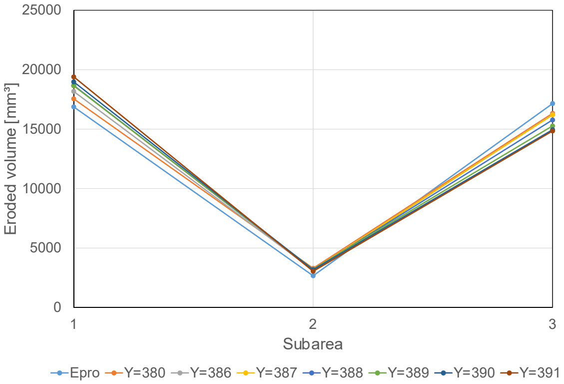

(b) Errors due to Y origin shift.

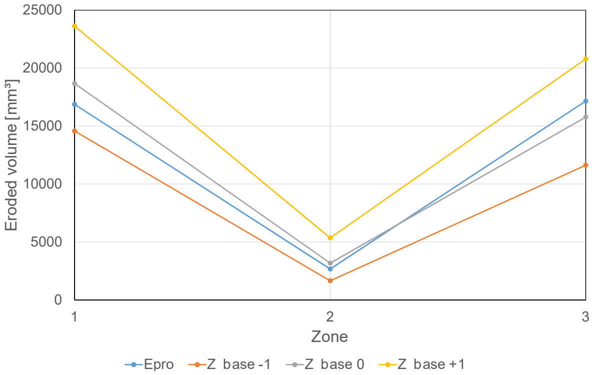

(c) Errors due to Z origin shift.

Figure A.6: Sensitivity of obtained subarea eroded volumes to measurement accuracy.

point out that the scanning quality around pile can be poor as extraordinary data spikes occur due to the laser reflection effect.

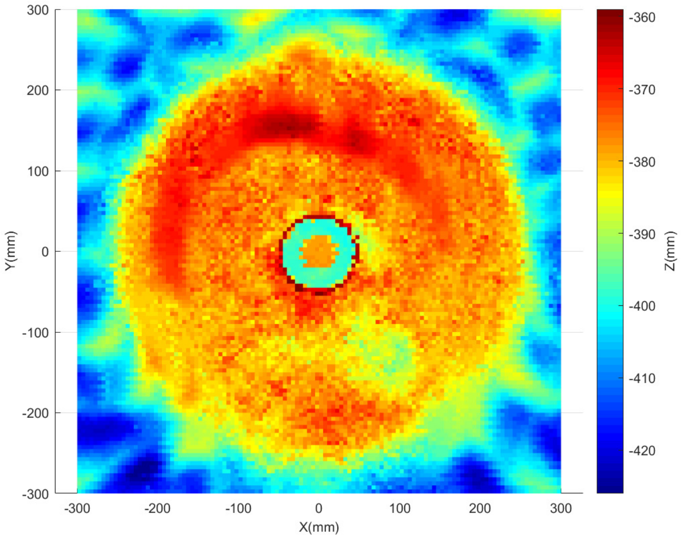

Figure A.7: EPro raw data plot scour protection, grid resolution 5 mm × 5 mm.

For the present small scale tests, the hand held laser scanner is applied as an alternative scanning tool, which maintains relatively high resolution with regard to the stone size. As displayed in Figure A.8, the centre of the pile can be found easily. This gives a possibility of assessing the damage of the scour protection with a high accuracy.

Comparing the performance of the two devices, the pros and cons are summarised shortly. The advantages of the EPro profiler are: (1) It is convenient to use and post-process after well installed. The designated software provides a direct visualisation of damage patterns and calculates the damage number automatically. (2) The servo system ensures a good horizontal levelling. (3) It supports underwater scanning. The disadvantages are: (1) The high resolution scanning takes a long time and reduces the efficiency. (2) The accuracy is relatively low when the stone sizes are small. (3) The device has a large size and is heavy to install. The advantages of the Faro hand laser scanner are: (1) It can preserve high resolution scan within a short scanning time. (2) It is light, small and convenient to take and move. Meanwhile the drawbacks are: (1) The device is not waterproof and the water level has to be lowered to below the scanning area before each scan. This causes extra wave flume time and lowers the efficiency. (2) Though the device is not sensitive to different light colours of stones, dark colours such as black, dark blue and dark brown should be avoided. (3) The post-processing is complicated and time-consuming.

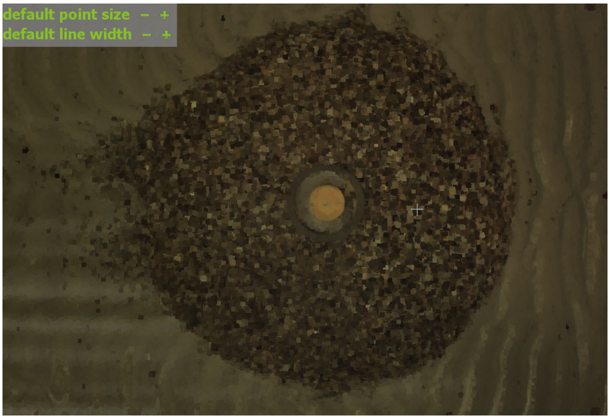

(a) Zoom-out view

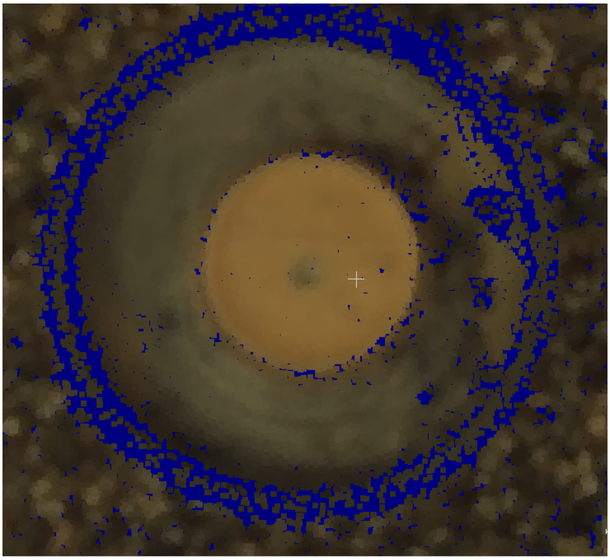

(b) Zoom-in view close to pile centre

Figure A.8: Faro hand laser scanner raw data plot scour protection.

A.4 Photos

This section provides a few details of the scour protection performance by camera photos. Figure A.9 is an intact scour protection before wave and current action. Figure A.10 shows the status of sediment beneath the scour protection when the model is demolished. It is seen that the sediments around pile are not embedded to the scour protection layer. No significant sinking is observed because of the fine armour material in the present test acting as a filter layer.

Figure A.11 and Figure A.12 show the scour protection deformation after a two hour pure current condition. The current velocity is U_c=-0.23 m/s. Under

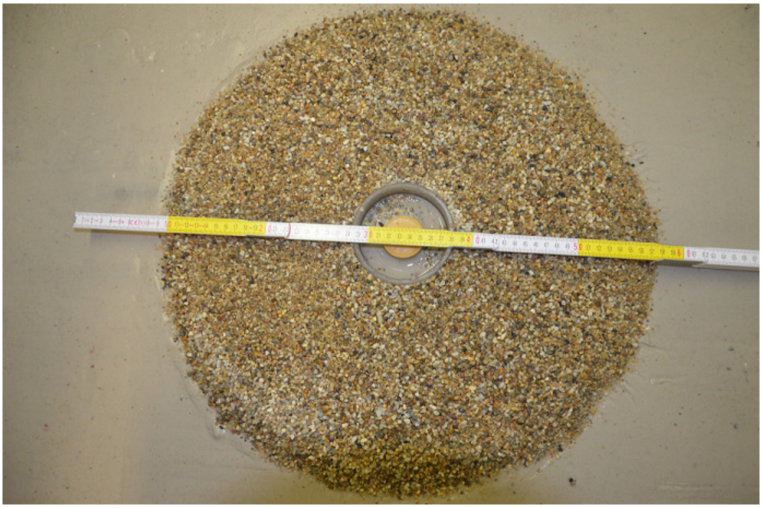

Figure A.9: An intact scour protection around monopile.

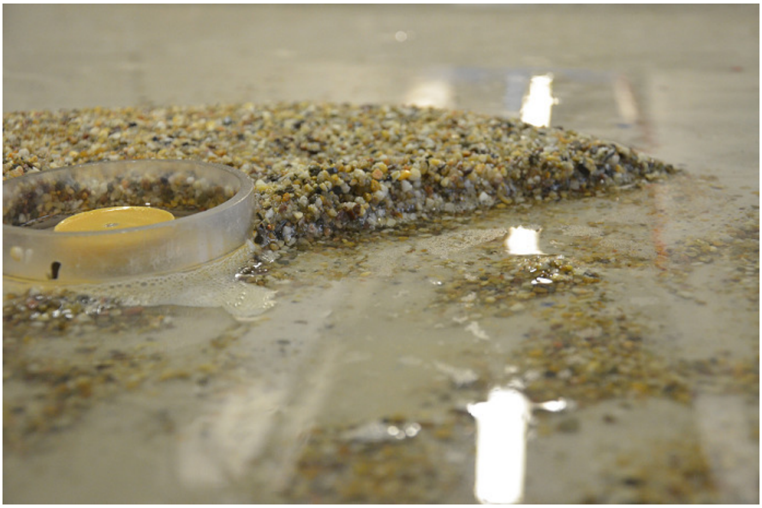

Figure A.10: Scour protection demolishing (TG1_6)

this condition, the scour protection is unstable as significant erosions happen in the wake region. The sediments in the wake region are also disturbed by the wake flow, forming two streaks of ripples. Different from the edge scour and edge failure, the erosion does not occur as a falling apron, but purely driven by the shear stress. This can be observed from A.13 that the edge scour happens not directly behind the scour protection but around 20 cm further downstream. The phenomenon highlights that under this specific condition, the impact due to the wake vortex can be greater than that due to the horseshoe vortex. This agrees with the findings of Nielsen and Petersen (2019), who concludes the reasons that the critical shear stress for lee-wake vortex induced stone motion is smaller than that for the horseshoe vortex induced motion.

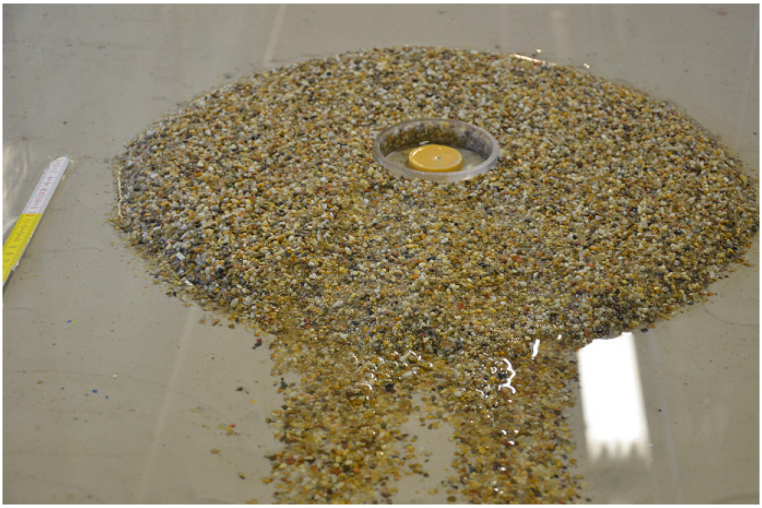

Figure A.11: Scour protection after 2 hour current, U_c=-0.23 m/s

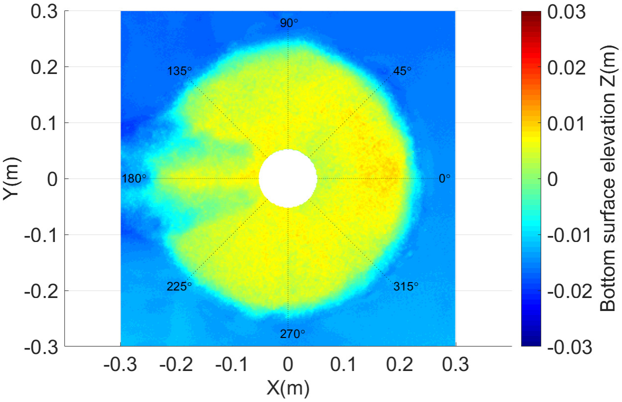

Figure A.12: Scan of scour protection after 2 hour current, U_c=-0.23 m/s

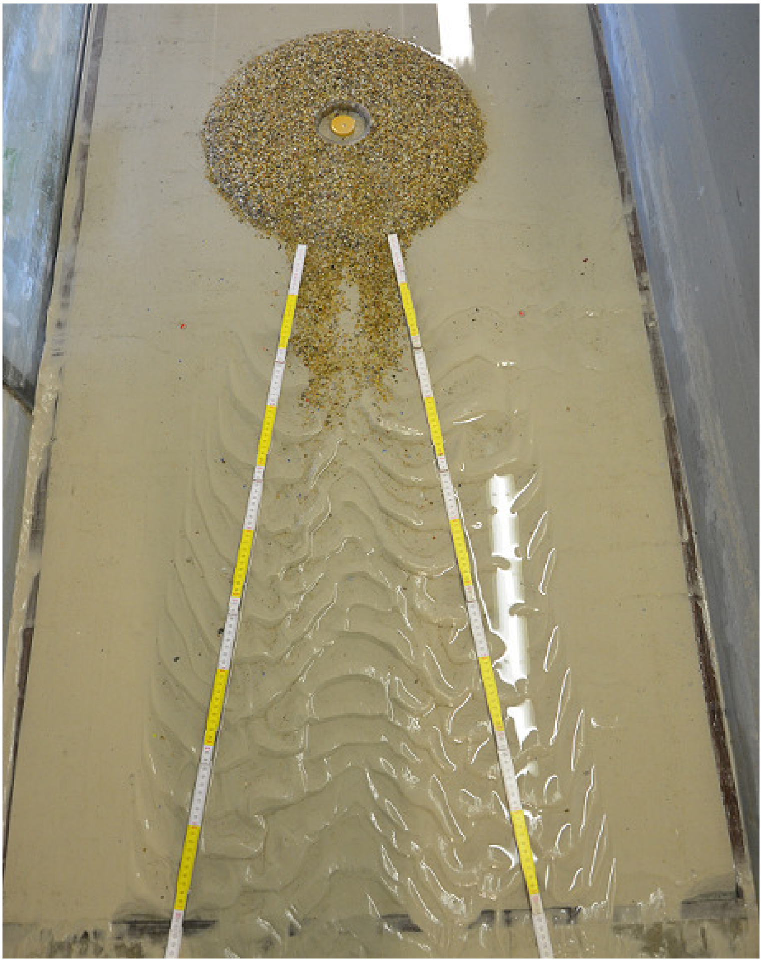

Figure A.13: Scour at wake region.

Appendix B

Available monopile scour protection experimental dataset

Table B.1: Collection of test conditions and results in various monopile scour protection experiments: irregular waves

ID	Test Name	Water depth	Pile diameter	Significant Wave height	Peak period	Current velocity	Median stone diameter	Nominal stone diameter	Relative density	Grading coefficient	Armour layer thickness	Filter	SDF
		d	D_P	H_s	T_p	U_c	D_{50}	D_{n50}	s	D_{85}/D_{15}	t_a		
		[m]	[m]	[m]	[s]	[m/s]	[mm]	[mm]	[-]	[-]	[mm]		
1	LDV1	0.4	0.1	0.139	1.45	0	4.1667	3.5	2.65	2.48	8.75	Geotextile	D
2	LDV2	0.4	0.1	0.125	1.71	0	4.1667	3.5	2.65	2.48	8.75	Geotextile	D
3	LDV3	0.4	0.1	0.141	1.71	0	4.1667	3.5	2.65	2.48	8.75	Geotextile	F
4	LDV4	0.4	0.1	0.156	1.71	0	4.1667	3.5	2.65	2.48	8.75	Geotextile	F
5	LDV5	0.4	0.1	0.12	1.16	0.077	4.1667	3.5	2.65	2.48	8.75	Geotextile	S
6	LDV6	0.4	0.1	0.135	1.42	0.08	4.1667	3.5	2.65	2.48	8.75	Geotextile	D
7	LDV7	0.4	0.1	0.12	1.71	0.077	4.1667	3.5	2.65	2.48	8.75	Geotextile	D
8	LDV8	0.4	0.1	0.136	1.71	0.081	4.1667	3.5	2.65	2.48	8.75	Geotextile	F
9	LDV11	0.4	0.1	0.118	1.2	0.164	4.1667	3.5	2.65	2.48	8.75	Geotextile	S
10	LDV13	0.4	0.1	0.069	1.42	0.15	4.1667	3.5	2.65	2.48	8.75	Geotextile	S
11	LDV14	0.4	0.1	0.088	1.42	0.164	4.1667	3.5	2.65	2.48	8.75	Geotextile	S
12	LDV15	0.4	0.1	0.114	1.42	0.159	4.1667	3.5	2.65	2.48	8.75	Geotextile	D
13	LDV15_r1	0.4	0.1	0.114	1.42	0.167	4.1667	3.5	2.65	2.48	8.75	Geotextile	D
14	LDV15_r2	0.4	0.1	0.114	1.42	0.167	4.1667	3.5	2.65	2.48	8.75	Geotextile	D
15	LDV16	0.4	0.1	0.129	1.42	0.165	4.1667	3.5	2.65	2.48	8.75	Geotextile	D
16	LDV17	0.4	0.1	0.14	1.4	0.161	4.1667	3.5	2.65	2.48	8.75	Geotextile	D
17	LDV18	0.4	0.1	0.115	1.71	0.164	4.1667	3.5	2.65	2.48	8.75	Geotextile	F
18	LDV19	0.4	0.1	0.13	1.71	0.163	4.1667	3.5	2.65	2.48	8.75	Geotextile	D
19	LDV20	0.4	0.1	0.145	1.71	0.16	4.1667	3.5	2.65	2.48	8.75	Geotextile	F
20	LDV20_r1	0.4	0.1	0.145	1.71	0.167	4.1667	3.5	2.65	2.48	8.75	Geotextile	F
21	LDV20_r2	0.4	0.1	0.145	1.71	0.159	4.1667	3.5	2.65	2.48	8.75	Geotextile	F
22	LDV22	0.4	0.1	0.083	1.42	0.23	4.1667	3.5	2.65	2.48	8.75	Geotextile	F
23	LDV24	0.4	0.1	0.146	1.71	-0.067	4.1667	3.5	2.65	2.48	8.75	Geotextile	F
24	LDV25	0.4	0.1	0.099	1.42	-0.142	4.1667	3.5	2.65	2.48	8.75	Geotextile	S
25	LDV27	0.4	0.1	0.134	1.37	-0.137	4.1667	3.5	2.65	2.48	8.75	Geotextile	F
26	LDV28	0.4	0.1	0.139	1.45	0	4.1667	3.5	2.65	1.32	8.75	Geotextile	D
27	LDV29	0.4	0.1	0.141	1.71	0	4.1667	3.5	2.65	1.32	8.75	Geotextile	F
28	LDV30	0.4	0.1	0.156	1.71	0	4.1667	3.5	2.65	1.32	8.75	Geotextile	F
29	LDV31	0.4	0.1	0.114	1.42	0.166	4.1667	3.5	2.65	1.32	8.75	Geotextile	S
30	LDV32	0.4	0.1	0.115	1.71	0.164	4.1667	3.5	2.65	1.32	8.75	Geotextile	D

ID	Test Name	Water depth	Pile diameter	Significant Wave height	Peak period	Current velocity	Median stone diameter	Nominal stone diameter	Relative density	Grading coefficient	Armour layer thickness	Filter	SDF
		d	D_P	H_s	T_p	U_c	D_{50}	D_{n50}	s	D_{85}/D_{15}	t_a		
		[m]	[m]	[m]	[s]	[m/s]	[mm]	[mm]	[-]	[-]	[mm]		
31	LDV33	0.4	0.1	0.145	1.71	0.161	4.1667	3.5	2.65	1.32	8.75	Geotextile	F
32	LDV34	0.4	0.1	0.083	1.42	0.212	4.1667	3.5	2.65	1.32	8.75	Geotextile	D
33	LDV35	0.4	0.1	0.109	1.71	0.233	4.1667	3.5	2.65	1.32	8.75	Geotextile	F
34	LDV36	0.4	0.1	0.134	1.71	-0.147	4.1667	3.5	2.65	1.32	8.75	Geotextile	F
35	LDV37	0.4	0.1	0.115	1.71	0.154	4.1667	3.5	2.65	2.48	8.75	No	D
36	LDV38	0.4	0.1	0.145	1.71	0.164	4.1667	3.5	2.65	2.48	8.75	No	F
37	LDV38_r1	0.4	0.1	0.145	1.71	0.155	4.1667	3.5	2.65	2.48	8.75	No	F
38	LDV39	0.4	0.1	0.115	1.71	0.169	4.1667	3.5	2.65	2.48	10.5	No	D
39	LDV40	0.4	0.1	0.145	1.71	0.156	4.1667	3.5	2.65	2.48	10.5	No	F
40	LDV41	0.4	0.1	0.145	1.71	0.151	4.1667	3.5	2.65	2.48	8.75	Granular	F
41	LDV43	0.2	0.1	0.08	1.79	0.172	4.1667	3.5	2.65	2.48	8.75	Geotextile	F
42	LDV44	0.4	0.1	0.156	1.71	0	5.9524	5	2.65	4	12.5	Geotextile	D
43	LDV45	0.4	0.1	0.152	1.71	0.077	5.9524	5	2.65	4	12.5	Geotextile	D
44	LDV46	0.4	0.1	0.129	1.42	0.164	5.9524	5	2.65	4	12.5	Geotextile	S
45	LDV47	0.4	0.1	0.14	1.4	0.165	5.9524	5	2.65	4	12.5	Geotextile	D
46	LDV48	0.4	0.1	0.13	1.71	0.163	5.9524	5	2.65	4	12.5	Geotextile	D
47	LDV49	0.4	0.1	0.145	1.71	0.158	5.9524	5	2.65	4	12.5	Geotextile	D
48	LDV50	0.4	0.1	0.109	1.71	0.224	5.9524	5	2.65	4	12.5	Geotextile	D
49	LDV51	0.4	0.1	0.14	1.71	0.227	5.9524	5	2.65	4	12.5	Geotextile	F
50	LDV52	0.2	0.1	0.058	1.71	0.315	5.9524	5	2.65	4	12.5	Geotextile	F
51	LDV53	0.4	0.1	0.145	1.71	0.156	8.5714	7.2	2.65	1.39	18	Geotextile	D
52	LDV54	0.4	0.1	0.121	1.42	0.221	8.5714	7.2	2.65	1.39	18	Geotextile	S
53	LDV55	0.4	0.1	0.14	1.71	0.221	8.5714	7.2	2.65	1.39	18	Geotextile	D
54	LDV56	0.2	0.1	0.08	1.79	0.168	8.5714	7.2	2.65	1.39	18	Geotextile	S
55	LDV58	0.4	0.1	0.163	1.71	-0.142	8.5714	7.2	2.65	1.39	18	Geotextile	D
56	LDV59	0.4	0.1	0.14	1.71	0.236	8.5714	7.2	2.65	1.39	18	No	D
57	LDV71	0.4	0.1	0.168	1.71	0	4.1667	3.5	3.2	2.48	8.75	Geotextile	F
58	LDV72	0.4	0.1	0.155	1.71	0	4.1667	3.5	3.2	2.48	8.75	Geotextile	F
59	LDV73	0.4	0.1	0.151	1.71	0.066	4.1667	3.5	3.2	2.48	8.75	Geotextile	F
60	LDV74	0.4	0.1	0.128	1.42	0.143	4.1667	3.5	3.2	2.48	8.75	Geotextile	D

ID	Test Name	Water depth d [m]	Pile diameter D_P [m]	Significant Wave height H_s [m]	Peak period T_p [s]	Current velocity U_c [m/s]	Median stone diameter D_{50} [mm]	Nominal stone diameter D_{n50} [mm]	Relative density s [-]	Grading coefficient D_{85}/D_{15} [-]	Armour layer thickness t_a [mm]	Filter	SDF
61	LDV75	0.4	0.1	0.139	1.35	0.146	4.1667	3.5	3.2	2.48	8.75	Geotextile	D
62	LDV76	0.4	0.1	0.146	1.71	0.141	4.1667	3.5	3.2	2.48	8.75	Geotextile	F
63	LDV77	0.4	0.1	0.122	1.42	0.203	4.1667	3.5	3.2	2.48	8.75	Geotextile	F
64	LDV78	0.4	0.1	0.107	1.42	0.195	4.1667	3.5	3.2	2.48	8.75	Geotextile	D
65	LDV81	0.4	0.1	0.168	1.71	0	5.9524	5	3.2	4	12.5	Geotextile	D
66	LDV82	0.4	0.1	0.146	1.71	0	5.9524	5	3.2	4	12.5	Geotextile	D
67	LDV83	0.4	0.1	0.124	1.71	0.202	5.9524	5	3.2	4	12.5	Geotextile	D
68	LDV84	0.4	0.1	0.135	1.42	0.214	5.9524	5	3.2	4	12.5	Geotextile	D
69	LDV85	0.4	0.1	0.139	1.71	0.212	5.9524	5	3.2	4	12.5	Geotextile	D
70	KN1	0.4	0.1	0.138	1.659	0	4.1667	3.5	2.65	2.48	8.75	Geotextile	F
71	KN2	0.4	0.1	0.131	1.664	0.14	4.1667	3.5	2.65	2.48	8.75	Geotextile	F
72	KN3	0.4	0.1	0.141	1.671	0.15	4.1667	3.5	2.65	2.48	8.75	Geotextile	F
73	KN4	0.2	0.1	0.06	1.689	0.31	5.9524	5	2.65	4	12.5	Geotextile	F
74	KN5	0.4	0.1	0.131	1.659	-0.08	4.1667	3.5	2.65	2.48	8.75	Geotextile	F
75	KN6	0.4	0.1	0.131	1.659	-0.08	4.1667	3.5	2.65	2.48	8.75	Geotextile	F
76	KN7	0.4	0.1	0.132	1.659	0.14	4.1667	3.5	2.65	2.48	8.75	Geotextile	F
77	KN8	0.4	0.1	0.131	1.659	-0.07	4.1667	3.5	2.65	2.48	8.75	Geotextile	F
78	KN9	0.4	0.1	0.135	1.67	-0.14	4.1667	3.5	2.65	2.48	8.75	Geotextile	F
79	KN10	0.4	0.1	0.149	1.671	-0.13	4.1667	3.5	2.65	2.48	8.75	Geotextile	F
80	KN11	0.4	0.1	0.117	1.659	0.08	4.1667	3.5	2.65	2.48	8.75	Geotextile	D
81	KN12	0.4	0.1	0.149	1.671	-0.14	5.9524	5	2.65	4	12.5	Geotextile	F
82	KN13	0.4	0.1	0.16	1.44	-0.14	8.4524	7.1	2.65	1.39	17.75	Geotextile	S
83	KN14	0.4	0.1	0.135	1.67	-0.13	8.4524	7.1	2.65	1.39	17.75	Geotextile	D
84	KN15	0.4	0.1	0.149	1.671	-0.14	8.4524	7.1	2.65	1.39	17.75	Geotextile	D
85	KN16	0.4	0.1	0.145	2.14	-0.13	8.4524	7.1	2.65	1.39	17.75	Geotextile	D
86	KN17	0.4	0.1	0.158	2.208	-0.13	8.4524	7.1	2.65	1.39	17.75	Geotextile	D
87	KN18	0.4	0.1	0.126	2.137	0.15	8.4524	7.1	2.65	1.39	17.75	Geotextile	D
88	KN19	0.4	0.1	0.14	2.146	0.15	8.4524	7.1	2.65	1.39	17.75	Geotextile	D
89	KN20	0.4	0.1	0.158	2.208	-0.14	11.905	10	2.65	1.32	25	Geotextile	S
90	KN21	0.4	0.1	0.14	2.146	0.15	11.905	10	2.65	1.32	25	Geotextile	S

ID	Test Name	Water depth	Pile diameter	Significant Wave height	Peak period	Current velocity	Median stone diameter	Nominal stone diameter	Relative density	Grading coefficient	Armour layer thickness	Filter	SDF
		d [m]	D_P [m]	H_s [m]	T_p [s]	U_c [m/s]	D_{50} [mm]	D_{n50} [mm]	s [-]	D_{85}/D_{15} [-]	t_a [mm]		
91*	KNs22	0.4	0.05	0.131	1.659	-0.08	4.1667	3.5	2.65	2.48	8.75	Geotextile	F
92	KN23	0.4	0.1	0.131	1.659	-0.07	4.1667	3.5	2.65	2.48	8.75	Geotextile	F
93	KN24	0.4	0.125	0.131	1.659	-0.08	4.1667	3.5	2.65	2.48	8.75	Geotextile	F
94*	KNs25	0.4	0.05	0.138	1.659	0	4.1667	3.5	2.65	2.48	8.75	Geotextile	F
95	KN26	0.4	0.1	0.138	1.659	0	4.1667	3.5	2.65	2.48	8.75	Geotextile	F
96	KN27	0.4	0.125	0.138	1.659	0	4.1667	3.5	2.65	2.48	8.75	Geotextile	D
97*	KNs28	0.4	0.05	0.122	1.423	0.15	4.1667	3.5	2.65	2.48	8.75	Geotextile	D
98	KN29	0.4	0.125	0.122	1.423	0.14	4.1667	3.5	2.65	2.48	8.75	Geotextile	D
99*	KNs30	0.4	0.05	0.132	1.659	0.15	5.9524	5	2.65	4	12.5	Geotextile	D
100	KN31	0.4	0.125	0.132	1.659	0.14	5.9524	5	2.65	4	12.5	Geotextile	D
101*	KNs32	0.4	0.05	0.149	1.671	-0.13	8.4524	7.1	2.65	1.39	17.75	Geotextile	D
102	KN33	0.4	0.125	0.149	1.671	-0.13	8.4524	7.1	2.65	1.39	17.75	Geotextile	D
103	KN34	0.5	0.1	0.151	1.691	0.13	4.1667	3.5	2.65	2.48	8.75	Geotextile	D
104	KN35	0.5	0.1	0.15	2.114	0.13	4.1667	3.5	2.65	2.48	8.75	Geotextile	F
105	KN36	0.2	0.1	0.073	1.748	-0.28	5.9524	5	2.65	4	12.5	Geotextile	F
106	KN37	0.2	0.1	0.074	1.72	-0.28	5.9524	5	2.65	4	12.5	Geotextile	F
107	KN38	0.2	0.1	0.063	1.76	0.16	5.9524	5	2.65	4	12.5	Geotextile	D
108	KN39	0.2	0.1	0.06	2.079	0.17	5.9524	5	2.65	4	12.5	Geotextile	S
109	KN40	0.2	0.1	0.062	1.708	0.23	5.9524	5	2.65	4	12.5	Geotextile	D
110	KN41	0.2	0.1	0.074	1.72	-0.21	8.4524	7.1	2.65	1.39	17.75	Geotextile	D
111	KN42	0.2	0.1	0.057	2.022	0.23	8.4524	7.1	2.65	1.39	17.75	Geotextile	S
112	S1001	0.24	0.1	0.097	1.552	0.161	7.5	6.3	2.65	Not specified	30	Granular	S
113	S1002	0.24	0.1	0.103	1.552	0.147	6.015	5.0526	2.56	Not specified	12	Granular	S
114	S1003	0.24	0.1	0.098	1.552	0.178	4.135	3.4734	2.60	Not specified	12.4	Granular	D
115	S1004	0.24	0.1	0.094	1.562	0.185	4.1345	3.473	2.60	Not specified	8.3	Granular	F
116	S1005	0.24	0.1	0.095	1.562	0.182	2.686	2.2562	2.56	Not specified	21.5	Granular	F
117	S1006	0.24	0.1	0.091	1.543	0.186	4.135	3.4734	2.60	Not specified	12.4	Granular	D
118	S2001	0.36	0.1	0.148	1.534	0.175	7.5	6.3	2.65	Not specified	15	Granular	S
119	S2002	0.36	0.1	0.139	1.525	0.174	6.015	5.0526	2.56	Not specified	12	Granular	D
120	S2003	0.36	0.1	0.139	1.525	0.177	4.135	3.4734	2.60	Not specified	12.4	Granular	F

ID	Test Name	Water depth	Pile diameter	Significant Wave height	Peak period	Current velocity	Median stone diameter	Nominal stone diameter	Relative density	Grading coefficient	Armour layer thickness	Filter	SDF
		d [m]	D_P [m]	H_s [m]	T_p [s]	U_c [m/s]	D_{50} [mm]	D_{n50} [mm]	s [-]	D_{85}/D_{15} [-]	t_a [mm]		
121	S2004	0.36	0.1	0.141	1.525	0.177	4.1345	3.473	2.60	Not specified	16.5	Granular	D
122	S2005	0.36	0.1	0.145	1.531	0.172	2.686	2.2562	2.56	Not specified	21.5	Granular	F
123	S2006	0.36	0.1	0.121	1.53	0.194	4.135	3.4734	2.60	Not specified	16.5	Granular	D
124	S3001	0.5	0.1	0.148	1.572	0.191	6.0714	5.1	2.56	Not specified	12	Granular	S
125	S3002	0.5	0.1	0.155	1.565	0.22	4.1667	3.5	2.60	Not specified	12	Granular	F
126	S3003	0.5	0.1	0.154	1.559	0.218	4.1667	3.5	2.60	Not specified	16.5	Granular	D
127	S3004	0.5	0.1	0.155	1.573	0.219	4.1667	3.5	2.60	Not specified	12.4	Granular	D
128	S3005	0.5	0.1	0.16	1.575	0.211	2.7381	2.3	2.56	Not specified	21.5	Granular	D
129	S3006	0.5	0.1	0.154	1.582	0.22	2.7381	2.3	2.56	Not specified	10.7	Granular	F
130	S3007	0.5	0.1	0.156	1.579	0.218	2.7381	2.3	2.56	Not specified	16.1	Granular	F
131	S3008	0.5	0.1	0.157	1.575	0.221	4.1667	3.5	2.60	Not specified	12.4	Granular	D
132	S3009	0.5	0.1	0.146	1.542	0.181	4.1667	3.5	2.60	Not specified	12.4	Granular	D
133	S3010	0.5	0.1	0.123	1.515	0.181	4.1667	3.5	2.60	Not specified	12	Granular	F
134	S3011	0.5	0.1	0.124	1.542	0.179	2.7381	2.3	2.56	Not specified	21.5	Granular	D
135	Test02	1.2	0.3	0.188	2.49	0.377	12.5	10.5	2.65	2.5	24.6	Geotextile	D
136	Test04	1.2	0.3	0.263	2.48	-0.498	12.5	10.5	2.65	2.5	30	Geotextile	D
137	Test06	1.5	0.3	0.286	2.28	0.367	6.75	5.67	2.65	2.5	49.6	No filter	D
138	Test08	1.2	0.3	0.21	2.52	-0.496	6.75	5.67	2.65	2.5	31.8	Geotextile	F
139	Test10	0.9	0.3	0.191	2	-0.33	6.75	5.67	2.65	2.5	51.4	No filter	D
140	Test12	1.8	0.6	0.443	2.89	-0.51	13.5	11.34	2.65	2.5	92.4	No filter	D
141	Test13	1.5	0.6	0.377	2.28	-0.57	13.5	11.34	2.65	2.5	93.9	No filter	D
142	Test14	1.8	0.6	0.442	2.89	-0.51	13.5	11.34	2.65	6.0	109.9	No filter	D
143	Test15	1.8	0.6	0.443	2.89	-0.51	13.5	11.34	2.65	12.0	109.3	No filter	D

* The cases are using D_P =0.05 m. Significant scale effects exist in these cases.

References

2Grobotics (2020). ULS-200 mid-range underwater laser scanner. `https://www.2grobotics.com/products/underwater-laser-scanner-uls-200/`, Accessed on 2020-12-30.

Arany, L., Bhattacharya, S., Macdonald, J. H., and Hogan, S. J. (2016). Closed form solution of eigen frequency of monopile supported offshore wind turbines in deeper waters incorporating stiffness of substructure and ssi. *Soil Dynamics and Earthquake Engineering*, 83:18–32.

Arboleda Chavez, C. E., Stratigaki, V., Wu, M., Troch, P., Schendel, A., Welzel, M., Villanueva, R., Schlurmann, T., De Vos, L., Kisacik, D., Taveira Pinto, F., Fazeres-Ferradosa, T., Rosa Santos, P., Baelus, L., Szengel, V., Bolle, A., Whitehouse, R., and Todd, D. (2019). Large-scale experiments to improve monopile scour protection design adapted to climate change—the proteus project. *Energies*, 12(9):1709.

Asgarpour, M. (2016). 17 - assembly, transportation, installation and commissioning of offshore wind farms. In *Offshore Wind Farms, Technologies, Design and Operation*, pages 527 – 541. Woodhead Publishing.

Baker, C. J. (1979). The laminar horseshoe vortex. *Journal of Fluid Mechanics*, 95:347–367.

Baker, C. J. (1980). The turbulent horseshoe vortex. *Journal of Wind Engineering and Industrial Aerodynamics*, 6:9–23.

Baker, C. J. (1985). The position of points of maximum and minimum shear stress upstream of cylinders mounted normal to flat plates. *Journal of Wind Engineering and Industrial Aerodynamics*, 18:263–274.

Baker, C. J. (1991). The oscillation of horseshoe vortex systems. *Journal of Fluids Engineering*, 113:489–495.

Bakker, K. J., Verheij, H. J., and de Groot, M. B. (1994). Design relationship for filters in bed protection. *Journal of Hydraulic Engineering*, 120(9):1082–1088.

Bakker, W. T. and van Doorn, T. (1978). Near-bottom velocities in waves with a current. In *Proceedings of 16th Conference on Coastal Engineering*, volume 2, pages 1394–1413, Hamburg, Germany.

Baykal, C., Sumer, B. M., Fuhrman, D. R., Jacobsen, N. G., and Fredsøe, J. (2015). Numerical investigation of flow and scour around a vertical circular cylinder. *Philosophical Transactions of the Royal Society A*, 373:20140104.

Bearman, P. W. (1969). On vortex shedding from a circular cylinder in the critical reynolds number régime. *Journal of Fluid Mechanics*, 37(3):577–585.

Bearman, P. W., Downie, M. J., Graham, J. M. R., and Obasaju, E. D. (1985). Force on cylinders in viscous oscillatory flow at low keulegan-carpenter numbers. *Journal of Fluid Mechanics*, 154:337–356.

Breusers, H. N. C., Nicollet, G., and Shen, H. W. (1977). Local scour around cylindrical piers. *Journal of Hydraulic Research*, 15(3):211–252.

Breusers, H. N. C. and Raudkivi, A. J. (1991). *Scouring — Hydraulic Structures Design Manual*. IAHR A.A. Balkema, Rotterdam, the Netherlands.

Burcharth, H. F., Liu, Z., and Troch, P. (1999). Scaling of core material in rubble mound breakwater model tests. In *Proceedings 5th International Conference on Coastal and Port Engineering in Developing Countries (COPEDEC)*, pages 1518–1528.

Burcharth, H. F. and Lykke Andersen, T. (2009). Scale effects related to small scale physical modelling of overtopping of rubble mound breakwaters. In *Coastal Structures 2007*, pages 1532–1541.

Chen, H.-H., Yang, R.-Y., and Hwung, H.-H. (2014). Study of hard and soft countermeasures for scour protection of the jacket-type offshore wind turbine foundation. *Journal of Marine Science and Engineering*, 2:551–567.

Chiew, Y. M. (1995). Mechanics of riprap failure at bridge piers. *Journal of Hydraulic Engineering*, 121(9):635–643.

Chiew, Y. M. (2002). Failure mechanisms of riprap layer around bridge piers. In *First International Conference on Scour of Foundations (ICSF-1)*, pages 70–91, Texas, USA.

Chiew, Y. M. (2004). Local scour and riprap stability at bridge piers in a degrading channel. *Journal of Hydraulic Engineering*, 130(3):218–226.

Chiew, Y. M. and Lim, F. H. (2000). Failure behavior of riprap layer at brdige piers under live-bed conditions. *Journal of Hydraulic Engineering*, 126(1):43–55.

Christoffersen, J. B. and Jonsson, I. G. (1985). Bed friction and dissipation in a combined current and wave motion. *Ocean Engineering*, 12(5):387–423.

CIRIA (2007). *The Rock Manual. The Use of Rock in Hydraulic Engineering, 2nd ed.* CIRIA, CUR and CETMEF, London, UK.

Colmenar-Santos, A., Perera-Perez, J., Borge-Diez, D., and dePalacio Rodríguez, C. (2016). Offshore wind energy: A review of the current status, challenges and future development in spain. *Renewable and Sustainable Energy Reviews*, 64:1 – 18.

Corvaro, S., Marini, F., Mancinelli, A., and Lorenzoni, C. (2018). Scour protection around a single slender pile exposed to waves. In *Proceedings of the 36th Conference on Coastal Engineering (ICCE)*, volume 1, papers.6, Baltimore, Maryland, USA.

Dai, Y. B. and Kamel, A. M. (1969). *Scale effects tests for rubble mound breakwaters*. Research Report, U.S. Army Engineer Waterways Experiment Station, CORPS OF ENGINEERS, Vicksburg, USA.

Dargahi, B. (1989). The turbulent flow field around a circular cylinder. *Experiments in Fluids*, 8:1–12.

Davies, A. G., Soulsby, R. L., and King, H. L. (1988). A numerical model of the combined wave and current bottom boundary layer. *Journal of Geophysical Research*, 93(C1):491–508.

De Schoesitter, P., Audenaert, S., Baelus, L., Bolle, A., Brown, A., Das Neves, L., Ferradosa, T., Haerens, P., T.Pinto, F., Troch, P., and Whitehouse, R. (2014). Feasibility of a dynamically stable rock armour layer scour protection for offshore wind farms. In *Proceedings of the 33rd International conference on ocean, offshore and arctic engineering (OMAE)*, San Francisco, CA, USA.

De Vos, L. (2008). *Optimisation of scour protection design for monopiles and quantification of wave run-up*. PhD thesis, Ghent University, Belgium.

De Vos, L., De Rouck, J., Troch, P., and Frigaard, P. (2011). Empirical design of scour protections around monopile foundations: Part 1: Static approach. *Coastal Engineering*, 58(6):540 – 553.

De Vos, L., De Rouck, J., Troch, P., and Frigaard, P. (2012). Empirical design of scour protections around monopile foundations. part 2: Dynamic approach. *Coastal Engineering*, 60:286 – 298.

Debaveye, R. and De Riemacker, B. (2020). Data analysis of the 3d damage number in small-scale monopile scour protection experiments. Master's thesis, Ghent University, Belgium.

Delany, N. K. and Sorensen, N. E. (1953). Low-speed drag of cylinders of various shapes, NACA Tech. Note 3038.

Deltares (1972). *Systematic investigation of two-dimensional and three dimensional scour.* Report M648/M893 (In Dutch), Delft, the Netherlands.

Den Boon, J. H., Sutherland, J., Whitehouse, R. J. S., Soulsby, R. L., Stam, C. J. M., Verhoeven, K., Høgedal, M., and Hald, T. (2004). Scour behavior and scour protection for monopile foundations of offshore wind turbines. In *Proceedings of the European Wind Energy Conference (EWEC)*, London, UK.

DHI (2019). Innovative design lowers costs of offshore wind farm scour protection systems by 30%. https://www.dhigroup.com/global/news/2019/06/innovative-design-lowers-costs-of-offshore-wind-farm-scour-protection-systems, Accessed on 2021-11-06.

Dixen, M., Hatipoglu, F., Sumer, B. M., and Fredsøe, J. (2008). Wave boundary layer over a stone-covered bed. *Coastal Engineering*, 55(1):1–20.

DNV (2014). Det Norske Veritas AS, Design of offshore wind turbine structures, Offshore standard DNV-OS-J101.

Draycott, S., Steynor, J., Davey, T., and Ingram, D. M. (2018). Isolating incident and reflected wave spectra in the presence of current. *Coastal Engineering Journal*, 60(1):39–50.

Engelund, F. (1953). On the laminar and turbulent flows of ground water through homogeneous sand. *Danish Academey of Technical Sciences / Transactions*, 3(4).

Esteban, M. D., López-Gutiérrez, J.-S., and Negro, V. (2019a). Gravity-based foundations in the offshore wind sector. *Journal of Marine Science and Engineering*, 7(64).

Esteban, M. D., López-Gutiérrez, J.-S., Negro, V., and Sanz, L. (2019b). Riprap scour protection for monopiles in offshore wind farms. *Journal of Marine Science and Engineering*, 7(12):440.

Ettema, R., Kirkil, G., and Muste, M. (2006). Similitude of large-scale turbulence in experiments on local scour at cylinders. *Journal of Hydraulic Engineering*, 132(1):33–40.

Ettema, R., Melville, B. W., and Barkdoll, B. (1996). Scale effect in pier-scour experiments. *Journal of Hydraulic Engineering*, 124(6):639–642.

Ettema, R., Mostafa, E. A., Melville, B. W., and Yassin, A. A. (1998). Local scour at skewed piers. *Journal of Hydraulic Engineering*, 124(7):756–759.

FARO Technologies Inc (2017). Freestyle3d and software user manual. `https://faro.app.box.com/s/pkfiiyeom0kwx722cff4yh01lwyspxu2/file/314135742270`, Accessed on 16/02/2021.

Fazeres-Ferradosa, T. (2018). *Reliability analysis applied to the optimization of dynamic scour protections for offshore windfarm foundations*. PhD thesis, University of Porto, Portugal.

Fazeres-Ferradosa, T., Chambel, J., Taveira-Pinto, F., Rosa-Santos, P., Taveira-Pinto, F. V. C., Giannini, G., and Haerens, P. (2021). Scour protections for offshore foundations of marine energy harvesting technologies: A review. *Journal of Marine Science and Engineering*, 9(3):297.

Fazeres-Ferradosa, T., Taveira-Pinto, F., Reis, M. T., and das Neves, L. (2018a). Physical modelling of dynamic scour protections: analysis of the damage number. *Proceedings of the Institution of Civil Engineers - Maritime Engineering*, 171(1):11–24.

Fazeres-Ferradosa, T., Taveira-Pinto, F., Romão, X., Vanem, E., Reis, M., and das Neves, L. (2018b). Probabilistic design and reliability analysis of scour protections for offshore windfarms. *Engineering Failure Analysis*, 91:291–305.

Fazeres-Ferradosa, T., Taveira-Pinto, F., Rosa-Santos, P., and Chambel, J. (2019). Probabilistic comparison of static and dynamic failure criteria of scour protections. *Journal of Marine Science and Engineering*, 7(11):400.

Fazeres-Ferradosa, T., Welzel, M., Schendel, A., Baelus, L., Santos, P. R., and Pinto, F. T. (2020). Extended characterization of damage in rubble mound scour protections. *Coastal Engineering*, 158:103671.

Frigaard, P. and Lykke Andersen, T. (2014). *Analysis of waves, Technical documentation for WaveLab 3 - DCE lecture notes No. 33*. Department of Civil Engineering, Aalborg University, Aalborg, Denmark.

Gaster, M. (1971). Vortex shedding from circular cylinders at low reynolds numbers. *Journal of Fluid Mechanics*, 46(4):749–756.

Gazi, A. H. and Afzal, M. S. (2020). A review on hydrodynamics of horseshoe vortex at a vertical cylinder mounted on a flat bed and its implication to scour at a cylinder. *Acta Geophysica*, 68:861–875.

Ghent University (2020). Large physical wave flume. `https://www.ugent.be/ea/civil-engineering/en/research/coastal-bridges-roads/coastal-engineering/infrastructure-services/overview`, Accessed on 16/02/2021.

Gonzalez-Rodriguez, A. G. (2017). Review of offshore wind farm cost components. *Energy for Sustainable Development*, 37:10 – 19.

Graf, W. H. and Yulistiyanto, B. (1998). Experiments on flow around a cylinder; the velocity and vorticity fields. *Journal of Hydraulic Research*, 36(4):637–654.

Grant, W. D. and Madsen, O. S. (1979). Combined wave and current interaction with a rough bottom. *Journal of Geophysical Research*, 84(C4):1797–1808.

Heller, V. (2011). Scale effects in physical hydraulic engineering models. *Journal of Hydraulic Research*, 49(3):293–306.

Hermans, K. W. and Peeringa, J. (2016). Future xl monopile foundation design for a 10 mw wind turbine in deep water. `https://publicaties.ecn.nl/PdfFetch.aspx?nr=ECN-E--16-069`, Accessed on 2021-11-06.

Hjorth, P. (1975). *Studies on the nature of local scour*. Lund Institute of Technology/Lund University, Department of Water Resources Engineering, Lund, Sweden.

Hoffman, G. J. C. M. and Verheij, H. J. (1997). *Scour Manual*. A.A.Balkema, Rotterdam, The Netherlands.

Hofland, B., Chen, X., Altomare, C., and Oosterlo, P. (2017). Prediction formula for the spectral wave period tm-1,0 on mildly sloping shallow foreshores. *Coastal Engineering*, 123:21 – 28.

HRWallingford (2021). Fast flow facility (FFF). `https://www.hrwallingford.com/facilities/fast-flow-facility`, Accessed on 2020-12-30.

Hughes, S. A. (1993). *Physical models and laboratory techniques in coastal engineering. Advanced series on ocean engineering - Volume 7*. World Scientific Publishing, Singapore.

IEA (2020). International Energy Agency, Renewables 2020, Analysis and Forecase to 2025. `https://www.iea.org/reports/renewables-2020`, Accessed on 2021-11-06.

Izbash, S. V. (1935). Construction of dams and other structures by dumping stones into flowing water - design and practice (in Russian). *Transactions of the Scientific Research Institute of Hydrotechnics*, XVII(2):12–66.

JCGM (2008). JCGM 100:2008 Evaluation of measurement data - guide to the expression of Uncertainty in Measurement (GUM).

Juul Jensen, O. and Klinting, P. (1983). Evaluation of scale effects in hydraulic models by analysis of laminar and turbulent flows. *Coastal Engineering*, 7(4):319–329.

Kamphuis, J. W. (1996). Physical modelling of coastal processes. In *Advances in Coastal and Ocean Engineering*, pages 79–114.

Kemp, P. H. and Simons, R. R. (1982). The interaction between waves and a turbulent current: waves propagating with the current. *Journal of Fluid Mechanics*, 116:227–250.

Kemp, P. H. and Simons, R. R. (1983). The interaction between waves and a turbulent current: waves propagating against the current. *Journal of Fluid Mechanics*, 130:73–89.

Kirby, A. M., Roca, M., Kitchen, A., Escarameia, M., and Chesterton, O. J. (2015). *Manual on Scour at Bridges and Other Hydraulic Structures, second edition*. CIRIA, London, UK.

Kortenhaus, A., Van der Meer, J., Burcharth, H. F., Geeraerts, J., Pullen, T., Ingram, D., and Troch, P. (2005). *D40 Report on conclusions of scale effects, Workpackage 7, Quantification of measurement errors, model and scale effects related to wave overtopping*. Leichtweiß-Institute for Hydraulic Engineering, Germany.

Lagasse, P. F., Clopper, P. E., Zevenbergen, L. W., and Ruff, J. F. (2006). *NCHRP Report 568, Riprap design criteria, recommended specifications and quality control. National Cooperative Highway Research Program*. Transport Research Board, Washington, D.C., USA.

Lauchlan, C. S. (1999). *Pier scour countermeasures*. PhD thesis, University of Auckland, Auckland, New Zealand.

Lauchlan, C. S. and Melville, B. W. (2001). Riprap protection at bridge piers. *Journal of Hydraulic Engineering*, 127(5):412–418.

Le Méhauté, B. (1957). Perméabilité des digues en enrochements aux ondes de gravité périodiques (in French). *Houlille Blanche*, 6:903–919.

Lim, F. H. and Chiew, Y. M. (2001). Parametric study of riprap failure around bridge piers. *Journal of Hydraulic Research*, 39(1):61–72.

Looseveldt, N. and Vannieuwenhuyse, K. (2012). Experimental validation of empirical design of a scour protection around monopiles under combined wave and current loading. Master's thesis, Ghent University, Belgium.

Mayall, R. O., McAdam, R. A., Whitehouse, R. J. S., Burd, H. J., Byrne, B. W., Heald, S. G., Sheil, B. B., and Slater, P. L. (2020). Flume tank testing of offshore wind turbine dynamics with foundation scour and scour protection. *Journal of Waterway, Port, Coastal, and Ocean Engineering*, 146(5):04020033.

Meinert, P. (2004). *EPro user manual*. Aalborg University, Aalborg, Denmark.

Melville, B. (2008). The physics of local scour at bridge piers. In *Proceedings of the 4th International Conference on Scour and Erosion (ICSE-4)*, Tokyo, Japan.

Melville, B. W. and Coleman, S. E. (2000). *Bridge Scour*. Water Resources Publication, Highlands Ranch, CO, USA.

Miles, J., Martin, T., and Goddard, L. (2017). Current and wave effects around windfarm monopile foundations. *Coastal Engineering*, 121:167–178.

Myrhaug, D. and Slaattelid, O. H. (1990). A rational approach to wave-current friction coefficients for rough, smooth and transitional turbulent flow. *Coastal Engineering*, 14:265–293.

Negro, V., López-Gutiérrez, J. S., Esteban, M. D., and Matutano, C. (2013). Uncertainties in the design of support structures and foundations for offshore wind turbines. *Renewable Energy*, 63:125–132.

Nielsen, A. W. (2011). *Scour Protection of Offshore Wind Farms*. PhD thesis, Technical University of Denmark, Lyngby, Denmark.

Nielsen, A. W., Liu, X., Sumer, B. M., and Fredsøe, J. (2013). Flow and bed shear stresses in scour protections around a pile in a current. *Coastal Engineering*, 72:20 – 38.

Nielsen, A. W., Mutlu Sumer, B., Fredsøe, J., and Christensen, E. D. (2011). Sinking of armour layer around a cylinder exposed to a current. *Proceedings of the Institution of Civil Engineers - Maritime Engineering*, 164(4):159–172.

Nielsen, A. W. and Petersen, T. U. (2018). Onset of motion of sediment underneath scour protection around a monopile. *Journal of Marine Science and Engineering*, 6(3):100.

Nielsen, A. W. and Petersen, T. U. (2019). Stability of cover stones around a vertical cylinder under the influence of waves and current. *Coastal Engineering*, 154:103563.

Nielsen, A. W., Probst, T., Petersen, T. U., and Sumer, B. M. (2015). Sinking of armour layer around a vertical cylinder exposed to waves and current. *Coastal Engineering*, 100:58 – 66.

Nielsen, A. W., Sumer, B. M., Ebbe, S. S., and Fredsøe, J. (2012). Experimental study on the scour around a monopile in breaking waves. *Journal of Waterway, Port, Coastal, and Ocean Engineering*, 138(6):501–506.

Nielsen, A. W., Sumer, B. M., Fredsøe, J., and Christensen, E. D. (2010). Scour protection around offshore wind turbines. monopiles. In *Proceedings of the 5th International Conference on Scour and Erosion (ICSE-5)*, pages 440–449, San Francisco, CA, USA.

Nielsen, P. (1992). *Coastal bottom boundary layers and sediment transport. Advanced Series on Ocean Engineering - Volume 4*. World Scientific Publishing, Singapore.

Nortek Group (2017). Nortek quick guide - vectrino profiler. `https://www.nortekgroup.com/assets/software/N3015-012-NQG_VECTRINPROO_1017.pdf`, Accessed on 16/02/2021.

NREL (2016). National Renewable Energy Laboratory, a spatial-economic costreduction pathway analysis for u.s. offshore wind energy development from 2015–2030. `https://www.nrel.gov/docs/fy16osti/66579.pdf`, Accessed on 2021-11-06.

Olabarrieta, M., Medina, R., and Castanedo, S. (2010). Effects of wave–current interaction on the current profile. *Coastal Engineering*, 57(7):643 – 655.

Oumeraci, H. (1994). Scour in front of vertical breakwaters - review of problems. In *Proceeding of International Workshop on Wave Barriers in Deepwaters, PHRI*, pages 281–317, Japan.

Parola, A. C. (1993). Stability of riprap at bridge piers. *Journal of Hydraulic Engineering*, 119(10):1080–1093.

Petersen, T. U. (2014). *Scour around offshore wind turbine foundation.* PhD thesis, Technical University of Denmark, Lyngby, Denmark.

Petersen, T. U., Mutlu Sumer, B., Fredsøe, J., Raaijmakers, T. C., and Schouten, J.-J. (2015). Edge scour at scour protections around piles in the marine environment — laboratory and field investigation. *Coastal Engineering*, 106:42 – 72.

Petersen, T. U., Nielsen, A. W., Hansen, D. A., Pedersen, A., Christensen, E. D., and Fredsøe, J. (2018). Stability of single-graded scour protection around a monopile in current. In *Proceedings of the 9th International Conference on Scour and Erosion (ICSE-9)*, Taipei, Taiwan.

Qi, W. G. and Gao, F. P. (2014). Physical modelling of local scour development around a large-diameter monopile in combined waves and current. *Coastal Engineering*, 83:72–81.

Qiu, W., Sales Junior, J., Lee, D., Lie, H., Magarovskii, V., Mikami, T., Rousset, J.-M., Sphaier, S., Tao, L., and Wang, X. (2014). Uncertainties related to predictions of loads and responses for ocean and offshore structures. *Ocean Engineering*, 86:58–67.

Quazi, M. E. and Peterson, A. W. (1973). A method for bridge pier riprap design. In *Proceedings of the 1st Canadian Hydraulics Conference*, pages 96–106, University of Alberta, Canada.

Raaijmakers, T. (2009). Evaluation of performance of scour protection and edge scour development—offshore windpark egmond aan zee. `http://publications.deltares.nl/1200160_002.pdf`, Accessed on 2020-12-30.

Raaijmakers, T. C., van Oeveren, M. C., Rudolph, D., Leenders, V., and Sinjou, W. C. P. (2010). Field performance of scour protection around offshore monopiles. In *Proceedings of the 5th International Conference on Scour and Erosion (ICSE-5)*, San Francisco, CA, USA.

Raudkivi, A. J. (1986). Functional trends of scour at bridge piers. *Journal of Hydraulic Engineering*, 112(1):1–13.

Raudkivi, A. J. and Ettema, R. (1983). Clear-water scour at cylindrical piers. *Journal of Hydraulic Engineering*, 109(3):338–350.

Richard, J. B., Thomson, J., Polagye, B., and Bard, J. (2013). Method for identification of doppler noise levels in turbulent flow measurements dedicated to tidal energy. *International Journal of Marine Energy*, 3-4:52–64.

Riezebos, H., Raaijmakers, T., Tönnies-Lohmann, A., Waßmuth, S., and Van Steijn, P. (2016). Scour protection design in highly morphodynamic environments. In *Proceedings of the 8th International Conference on Scour and Erosion (ICSE-8)*, Oxford, UK.

Rogelj, J., Shindell, D., Jiang, K., Fifita, S., Forster, P., Ginzburg, V., Handa, C., Kheshgi, H., Kobayashi, S., Kriegler, E., Mundaca, L., Séférian, R., and Vilariño, M. (2018). Mitigation pathways compatible with 1.5°c in the context of sustainable development. in: Global warming of 1.5°c. an ipcc special report on the impacts of global warming of 1.5°c above pre-industrial levels and related global greenhouse gas emission pathways, in the context of strengthening the global response to the threat of climate change, sustainable development, and efforts to eradicate poverty. `https://www.ipcc.ch/sr15/`, Chapter 2, Accessed on 2021-11-06.

Roshko, A. (1961). Experiments on the flow past a circular cylinder at very high reynolds number. *Journal of Fluid Mechanics*, 10(3):345–356.

Roulund, A., Sumer, B. M., Fredsøe, J., and Michelsen, J. (2005). Numerical and experimental investigation of flow and scour around a circular pile. *Journal of Fluid Mechanics*, 534:351–401.

Rudolph, D. and Bos, K. J. (2006). Scour around a monopile under combined wave-current conditions and low KC-numbers. In *Proceedings of the 3rd International Conference on Scour and Erosion (ICSE-3)*, Amsterdam, the Netherlands.

Sand, S. E. (1986). *Stochastic processes: practical computation of spectra*. Danish Hydraulic Institute (DHI), Hørsholm, Denmark.

Sarpkaya, T. (1976). Vortex shedding and resistance in harmonic flow about smooth and rough circular cylinder at high reynolds numbers. Technical report.

Sarpkaya, T. (1986). Force on a circular cylinder in viscous oscillatory flow at low keulegan-carpenter numbers. *Journal of Fluid Mechanics*, 165:61–71.

Schendel, A., Goseberg, N., and Schlurmann, T. (2014). Experimental study on the performance of coarse grain materials as scour protection. In *Proceedings of the 34th conference on Coastal Engineering, (ICCE)*, Seoul, Korea.

Schendel, A., Goseberg, N., and Schlurmann, T. (2016). Erosion stability of wide-graded quarry-stone material under unidirectional current. *Journal of Waterway, Port, Coastal, and Ocean Engineering*, 142(3):04015023.

Sheppard, D. M. and Glasser, T. (2004). Sediment scour at piers with complex geometries. In *Proceedings of the 2nd International Conference on Scour and Erosion (ICSE-2)*, Singapore.

Shields, A. (1936). *Anwendung der aehnlichkeitsmechanik und der turbulenzforschung auf die geschiebebewegung.* PhD thesis, Technical University of Berlin, Berlin, Germany.

Sánchez, S., López-Gutiérrez, J.-S., Negro, V., and Esteban, M. D. (2019). Foundations in offshore wind farms: Evolution, characteristics and range of use. analysis of main dimensional parameters in monopile foundations. *Journal of Marine Science and Engineering*, 7(441).

Soulsby, R. L. (1994). *Manual of marine sands*. HR Wallingford Report No. SR351, Wallingford, UK.

Soulsby, R. L. (1995). Bed shear-stresses due to combined waves and currents. In *Advances in Coastal Morphodynamics*, pages 4–20 to 4–23, Delft Hydraulics, the Netherlands.

Soulsby, R. L. (1997). *Dynamics of marine sands, a manual for practical applications*. Thomas Telford Publications, London, UK.

Soulsby, R. L., Hamm, L., Klopman, G., Myrhaug, D., Simons, R. R., and Thomas, G. P. (1993). Wave-current interaction within and outside the bottom boundary layer. *Coastal Engineering*, 21:41–69.

Soulsby, R. L. and Whitehouse, R. J. S. (1997). Threshold of sediment motion in coastal environments. In *Proceedings of the Pacific Coasts and Ports Conference*, volume 1, pages 149–154, Christchurch, New Zealand.

Spurk, J. H. and Aksel, N. (2020). *Fluid Mechanics, 3rd Eds*. Springer, Cham.

Sørensen, S. P. H. and Bo Ibsen, L. (2013). Assessment of foundation design for offshore monopiles unprotected against scour. *Ocean Engineering*, 63:17 – 25.

Steelwind Nordenham (2020). Beyond xxl – slim monopiles for deep-water wind farms. `https://www.offshorewind.biz/2020/05/11/beyond-xxl-slim-monopiles-for-deep-water-wind-farms/`, Accessed on 2021-11-06.

Subcon (2021). Subcon scour collar. `https://subcon.com/portfolio/scour-collar/`, Accessed on 2021-01-02.

Sumer, B. M., Christiansen, N., and and, J. F. (1993). Influence of cross section on wave scour around piles. *Journal of Waterway, Port, Coastal, and Ocean Engineering*, 119(5):477–495.

Sumer, B. M., Christiansen, N., and Fredsøe, J. (1997). The horseshoe vortex and vortex shedding around a vertical wall-mounted cylinder exposed to waves. *Journal of Fluid Mechanics*, 332:41–70.

Sumer, B. M. and Fredsøe, J. (1997). *Hydrodynamics around cylindrical structures, Advanced Series on Ocean Engineering - Volume 12*. World Scientific Publishing, Singapore.

Sumer, B. M. and Fredsøe, J. (2001a). Scour around pile in combined waves and current. *Journal of Hydraulic Engineering*, 127(5):403–411.

Sumer, B. M. and Fredsøe, J. (2001b). Wave scour around a large vertical circular cylinder. *Journal of Waterway, Port, Coastal, and Ocean Engineering*, 127(3):125–134.

Sumer, B. M. and Fredsøe, J. (2002). *The mechanics of scour in the marine environment. Advanced Series on Ocean Engineering - Volume 17*. World Scientific Publishing, Singapore.

Sumer, B. M., Fredsøe, J., and Christiansen, N. (1992). Scour around pile in combined waves and current. *Journal of Waterway, Port, Coastal, and Ocean Engineering*, 118(1):15–31.

Sumer, B. M. and Nielsen, A. W. (2013). Sinking failure of scour protection at wind turbine foundation. *Proceedings of the Institution of Civil Engineers - Energy*, 166(4):170–188.

Sutherland, J. and Whitehouse, R. J. S. (1998). *Scale effects in the physical modelling of seabed scour, Report TR64, Technical Report*. HR Wallingford, Wallingford, UK.

Tafarojnoruz, A., Gaudio, R., and Calomino, F. (2012). Evaluation of flow-altering countermeasures against bridge pier scour. *Journal of Hydraulic Engineering*, 138(3):297–305.

Terzaghi, K. and Peck, R. B. (1948). *Soil Mechanics in Engineering Practice*. John Wiley and Sons, New York.

Thomsen, A. L., Wohlt, P. E., and Harrison, A. S. (1972). *Riprap stability on earth embankments tested in large- and small-scale wave tanks, Technical Memorandum No. 37*. Coastal Engineering Research Center and Missouri River Division, U.S. Army, CORPS OF ENGINEERS.

Troch, P. (2000). *Experimentele studie en numerieke modellering van golfinteractie met stortsteengolfbrekers (in Dutch)*. PhD thesis, Ghent University, Zwijnaarde, Beglium.

UNFCCC (2015). United Nations Framework Convention on Climate Change, Paris Agreement. `https://unfccc.int/files/essential_background/convention/application/pdf/english_paris_agreement.pdf`, Accessed on 2021-11-06.

Unger, J. and Hager, W. H. (2006). Riprap failure at circular bridge piers. *Journal of Hydraulic Engineering*, 132(4):354–362.

Unger, J. and Hager, W. H. (2007). Down-flow and horseshoe vortex characteristics of sediment embedded bridge piers. *Experiments in Fluids*, 42(1):1–19.

van der Meer, J. W. (1988). *Rock slopes and gravel beaches under wave attack*. PhD thesis, Delft Hydraulics Laboratory, Delft, The Netherlands.

Van Gent, M. R. A., Smale, A. J., and Kuiper, C. (2003). Stability of rock slops with shallow foreshores. In *Coastal Structures 2003, J.A.Melby (ed), Proceedings of the Conference*, Portland, OR, USA. ASCE.

van Rijn, L. C. (1984). Sediment transport, part ii: suspended load transport. *Journal of Hydraulic Engineering*, 110(11):1613–1641.

van Rijn, L. C. (1993). *Principles of sediment transport in rivers, estuaries and coastal seas*. Aqua publications, Amsterdam, The Netherlands.

van Rijn, L. C. (2019). Critical movement of large rocks in currents and waves. *International Journal of Sediment Research*, 34(4):387–398.

Vandepitte, D. (1979). *Berekening van constructies: bouwkunde en civiele techniek*. Story-Scientia, Ghent, Belgium.

Vanneste, D. and Troch, P. (2014). A revision of the scaling method for core material in rubble-mound breakwaters. In *From Sea to Shore – Meeting the Challenges of the Sea: (Coasts, Marine Structures and Breakwaters 2013)*. ICE Publishing.

Verheij, H., Hoffmans, G., Dorst, K., and Vandesande, S. (2012). Interface stability of granular filter structures under currents. In *Proceedings of the 6th International Conference on Scour and Erosion (ICSE-6)*, Paris, France.

von Kármán, T. and Rubach, H. (1912). Über den mechanismus des flüssigkeits und luftwiderstandes. *Physikalische Zeitschrift XIII*.

Wahlin, B., Wahl, T., Gonzalez-Castro, J. A., Fulford, J., and Robeson, M. (2005). Task committee on experimental uncertainty and measurement errors in hydraulic engineering: an update. In *Proceedings of World Water and Environmental Resources Congress 2005: Impacts of Global Climate Change, EWRI*, Anchorage, Alaska.

Welch, P. D. (1967). The use of Fast Fourier Transform for the estimation of power spectra: a method based on time averaging over short, modified periodograms. *IEEE Transaction on Audio and Electroacoustics*, 15(2):70–73.

Welzel, M., Schendel, A., Hildebrandt, A., and Schlurmann, T. (2019). Scour development around a jacket structure in combined waves and current conditions compared to monopile foundations. *Coastal Engineering*, 152:103515.

Whitehouse, R. J. S. (1998). *Scour at Marine Structures: A Manual for Practical Applications*. Thomas Telford Publications, London, UK.

Whitehouse, R. J. S. (2004). Marine scour at large foundations. In *Proceedings of the 2nd International Conference on Scour and Erosion (ICSE-2)*, Singapore.

Whitehouse, R. J. S., Brown, A., Audenaert, S., Bolle, A., de Schoesitter, P., Haerens, P., Baelus, L., Troch, P., das Neves, L., Ferradosa, T., and Pinto, F. (2014). Optimising scour protection stability at offshore foundation. In *Proceedings of the 7th International Conference on Scour and Erosion (ICSE-7)*, Perth, Australia.

Whitehouse, R. J. S., Harris, J. M., Sutherland, J., and Rees, J. (2011). The nature of scour development and scour protection at offshore windfarm foundations. *Marine Pollution Bulletin*, 62(1):73 – 88.

Williamson, C. H. K. (1985). Sinusoidal flow relative to circular cylinders. *Journal of Fluid Mechanics*, 155:141–174.

Williamson, C. H. K. (1989). Oblique and parallel modes of vortex shedding in the wake of a circular cylinder at low reynolds numbers. *Journal of Fluid Mechanics*, 206:579–627.

WindEurope (2020a). Offshore wind in europe, key trends and statistics 2019. `https://windeurope.org/about-wind/statistics/offshore/european-offshore-wind-industry-key-trends-statistics-2019/`, Accessed on 2021-11-06.

WindEurope (2020b). Wind energy in europe in 2019, trends and statistics. `https://windeurope.org/about-wind/statistics/european/wind-energy-in-europe-in-2019/`, Accessed on 2021-11-06.

Wörman, A. (1989). Riprap protection without filter layers. *Journal of Hydraulic Engineering*, 115(12):1615–1630.

Wu, X., Hu, Y., Li, Y., Yang, J., Duan, L., Wang, T., Adcock, T., Jiang, Z., Gao, Z., Lin, Z., Borthwick, A., and Liao, S. (2019). Foundations of offshore wind turbines: A review. *Renewable and Sustainable Energy Reviews*, 104:379 – 393.

Yang, B., Wei, K., Yang, W., Li, T., and Qin, B. (2021). A feasibility study of reducing scour around monopile foundation using a tidal current turbine. *Ocean Engineering*, 220:108396.

Yang, B., Wei, K., Yang, W., Li, T., Qin, B., and Ning, L. (2019). A feasibility study for using fishnet to protect offshore wind turbine monopile foundations from damage by scouring. *Applied Sciences*, 9(5023).

Experimental study on stability of scour protection around offshore monopile foundations.